2nd Southwest Energy Science and Engineering Symposium

March 24, 2012
Double Tree Hotel
600 North El Paso Street
El Paso, TX 79901

Department of Mechanical Engineering
College of Engineering
University of Texas El Paso
500 W. University Ave.
El Paso, Texas 79968
Phone: (915)-747-5450 Fax: (915)-747-5019
rses@utep.edu

Web Link: http://engineering.utep.edu/seses/

FOREWARD

Welcome to the Southwest Energy Science and Engineering Symposium sponsored by Shell. The purpose of the symposium is to encourage communication among the engineers and scientists in and around the El Paso area's universities and industries.

The following individuals and organizations are acknowledged for their assistance with the symposium.

Conference Chair:	Dr. Ahsan Choudhuri University of Texas El Paso
Technical Chairs:	Dr. Norman Love Dr. Yirong Lin University of Texas El Paso
Logistics Committee:	Laura Barnum, University of Texas El Paso Carmen Medellin, University of Texas El Paso Laura Orozco, University of Texas El Paso
Hosted By:	College of Engineering Department of Mechanical Engineering & Center for Space Exploration and Technology Research (cSETR) University of Texas El Paso
Welcome and Introduction:	Dr. Richard Schoephoerster Dean, College of Engineering University of Texas El Paso
Session Chairs:	Dr. Yirong Lin, University of Texas El Paso Dr. Ishrap Shabib, University of Texas El Paso Dr. Evgeny Shafirovich, University of Texas El Paso Dr. Vinod Kumar, University of Texas El Paso Dr. C.V. Ramana, University of Texas El Paso Dr. Jose Espiritu, University of Texas El Paso Dr. Norman Love, University of Texas El Paso Dr. Mujibur Khan, University of Texas El Paso
Keynote Address:	Robert Romanosky, Jr., Ph.D Technology Manager for Power Systems Advanced Research National Energy Technology Laboratory U.S. Department of Energy

Southwest Energy Science and Engineering Symposium

UNIVERSITY OF TEXAS EL PASO
MARCH 24, 2012

7:00 am	**REGISTRATION**	Double Tree Hotel	Main Lobby
8:00 am	**BREAKFAST**	Double Tree Hotel	Sky Lounge
8:00 am	**OPENING NOTES**	Dr. Ahsan Choudhuri Professor and Chair, Department of Mechanical Engineering University of Texas El Paso	Sky Lounge
8:05 am	**WELCOME**	Dr. Richard Schoephoerster Dean, College of Engineering University of Texas El Paso	Sky Lounge
8:30 am	**POSTER SET UP**		
9:00 am	**PARALLEL TECHNICAL SESSIONS I**		
	Session 1-A	Energy Materials Technology I	Room: Salon I
	Session 1-B	Combustion and Propulsion I	Room: Salon II
	Session 1-C	Modeling and Emerging Technologies I	Room: Salon III
	Session 1-D	Sustainable and Renewable Energy	Room: Discovery
	Session 1-E	Materials and Design	Room: Voir Dire
	Session 1-F	Advanced Aerospace Systems	Room: Justice
10:15 am	**BREAK**		
10:30 am	**PARALLEL TECHNICAL SESSIONS II**		
	Session 2-A	Energy Materials Technology II	Room: Salon I
	Session 2-B	Novel Testing and Materials	Room: Salon II
	Session 2-C	Modeling and Emerging Technologies II	Room: Salon III
	Session 2-D	Heat Transfer and Sustainability	Room: Discovery
	Session 2-E	Materials and Sensor Design	Room: Voir Dire
	Session 2-F	Energy Enabling Technologies	Room: Justice
11:30 am	**LUNCH**		Sky Lounge
11:30 pm	**KEYNOTE PRESENTATION**		Sky Lounge

Robert Romanosky, Jr.,Ph.D
Technology Manager for Power Systems Advanced Research
National Energy Technology Laboratory
U.S. Department of Energy

1:00 pm	**ANNOUNCEMENT OF BEST POSTER AWARDS**	
1:15 pm	**ADJOURN**	

ABOUT THE SPEAKER

Robert Romanosky received both his M.S. and Ph.D. from West Virginia University in analytical chemistry/instrumentation. He has been with the U.S. Department of Energy, National Energy Technology Laboratory, since 1978, spending 18 years working in the in-house research area. He has been involved in all aspects of both laboratory and process research dealing with advanced instrumentation and process analysis.

Currently, Dr. Romanosky is the Technology Manager for Power Systems Advanced Research. This technology area encompasses research activities in Materials, Coal Utilization Science, Bioprocessing, University Research, and Computational Energy Sciences. The Materials Program fosters exploratory research whose aim is to generate new materials, ideas and concepts which have the potential to significantly improve the performance or cost of existing fossil systems or enable the development of new systems and capabilities. The Coal Utilization Program is concerned with fundamental development efforts in advanced sensors and controls, and development of models for power generation. This modeling development effort works in conjunction with the Computation Energy Science Program, whose goal is to provide simulation and computational resources to speed the development and reduce the cost of new power generation technologies. This work entails a broad spectrum of computational work including development of science based models of fossil fuel conversion phenomenon, simulation capabilities that couple unit processes in advanced power generation technologies, and virtual power plant simulations.

PARALLEL TECHNICAL SESSIONS I

Session 1-A: **Energy Materials Technology I** — Room: Salon I
Session Chair: Yirong Lin, UTEP — Double Tree El Paso

9:00 am	**Residential Photovoltaic Application in El Paso: Does it Promote Electricity Sustainability?** *M. Cole, UTEP*
9:15 am	**Combustion of Lunar Regolith/Magnesium Mixtures in Different Environments** *A. Delgado, E. Shafirovich, UTEP*
9:30 am	**Hydrogen Generation From Water Using Activated Aluminum** *A. K. Swamy, E. ShafirovichUTEP*
9:45 am	**Microgravity Combustion of Thermite Mixtures for Welding in Space** *J. Frias, A. Delgado, E. Shafirovich UTEP*
10:00 am	**Effect of Growth Temperature on the Structure, Strain and Surface Morphology of Nanocrystalline, Monoclinic HfO_2 Coatings** *C. Barraza, A. Garcia and C.V. Ramana, UTEP*

Session 1-B: **Combustion and Propulsion I** — Room: Salon II
Session Chair: Evgeny Shafirovich, UTEP — Double Tree El Paso

9:00 am	**Effect of Bidisperse Particles on Pressure Drop in a Gas-Solid Fluidized Bed** *M. Sarker, R.Chowdhury, N. Love, A. Choudhuri, UTEP*
9:15 am	**Development of an Optically Accessible High Pressure Tubine Combustor** *S. Sarker, J. Nunez, C. Valdez, N. Love, A. Choudhuri, UTEP*
9:30 am	**Goddard Laboratory Data Acquisition and Remote Control System** *J. Barragan, J. Flores, UTEP*
9:45 am	**Effect of Dilutents on Flame Radiation and Structures of Oxy-Fuel Flames** *M. De La Torre, B. Dam, V. Ardha, N. Love, A. Choudhuri, UTEP*
10:00 am	**Molecular Dynamics Simulation of Strained, Nanoscale CDTE Crystal Growth Using Bond-Order Potentials** *X. W. Zhou, D.K. Ward, J.L. Cruz-Campa, G.N. Nielson, D. Zubia, J. McClure, J.J. Chavez, UTEP, Sandia National Laboratories*

Session 1-C: **Modeling and Emerging Technologies I** — Room: Salon III
Session Chair: Vinod Kumar, UTEP — Double Tree El Paso

9:00 am	**A Finite Element Damage Model for Cohesive Failure of Matrix in Asphalt Mix** *M. Hossain, R. Tarefder, UNM*
9:15 am	**Application of System Dynamics to Select the Most Optimum Airport Pavement Maintenance** *M. Rahman, R. Tarefder, UNM*
9:30 am	**Comparison of Two Maintenance Strategies of Airfields using LCCA** *M. Ahmed, R. Tarefder,UNM*
9:45 am	**Optimal Siting of Wind Turbines Using Viral Systems Algorithm** *C. Ituarte-Villareal, C. S. Valles, J. F. Espiritu, UTEP*
10:00 am	**Using Genetic Algorithms to Solve Component Replacement Problems in Power Industry** *A. Aguirre, J. F. Espiritu,UTEP*

PARALLEL TECHNICAL SESSIONS I

Session 1-D: **Sustainable and Renewable Energy** Session Chair: Jose Espiritu, UTEP	Room: Discovery Double Tree El Paso
9:00 am	**Short-Term Prediction of Wind Farm Power Output Using a Hybrid Intelligent Algorithm Based on Meteorological Information** *P. Mandal, A. Haque, B. Tseng, UTEP*
9:15 am	**Wind Speed Prediction Using a Combined Intelligent Approach** *P. Mandal, A. Haque, B. Tseng, UTEP*
9:30 am	**Parallel Stochastic Multiscale Modeling of Single Phase Flow Through a Porous Media for Carbon Sequestration Risk Assessment** *P. Delgado, V. Kumar, UTEP*
9:45 am	**Studying Heuristics to Reduce Power Consumption in Peer-to-Peer Networks** *G. Perera, UTEP*
10:00 am	**Energy Efficiency and Conservation: A Case Study at the University of Texas at El Paso** *O. Moreno, H. Taboada, J. Villalobos, UTEP*
Session 1-E: **Materials and Design** Session Chair: C.V. Ramana, UTEP	Room: Voir Dire Double Tree El Paso
9:00 am	**Stress-Strain Responses of an I-40 Pavement Section in New Mexico** *M. Islam, R. A. Tarefder, UNM*
9:15 am	**Sample Size Effect on HMA Permeability and Determination of 3D Permeability** *M. Ahmad, R. Tarefder, UNM*
9:30 am	**Development of Wireless Thermoelectric Temperature Sensors** *J. Kuchle, Kazi Hassan, Norman Love, Ahsan Choudhuri, UTEP*
9:45 am	**Preparation and Characterization of GA_2O_3** *S. Sampath, K. Abhilash, C. V Ramana, UTEP*
10:00 am	**Thermal Barrier Coatings (TBC's) for High Heat Flux Thrust Chambers** *C. Bradley, UTEP*
Session 1-F: **Advanced Aerospace Systems** Session Chair: Norman Love, UTEP	Room: Justice Double Tree El Paso
9:00 am	**Thrust Measurement and Propellant Feed Systems Development for Testing LOX/Methane Reaction Control Thrusters** *D. Hernandez, G. Martinez, A. Acosta-Zamora, A. Choudhuri, UTEP*
9:15 am	**Test and Development of a Carbo-Thermal Rig to Study Liquid Methane Heat Transfer Characteristics** *M. Galvan, A. Trujillo, C.P. Garcia, A. Choudhuri, UTEP*
9:30 am	**Production of Cold Gas Methane for Use in Ignition Physics Research** *R. Ellis, J. Flores, UTEP*
9:45 am	**The Development of Methane and Oxygen Bi-Propellant 1 to 5 Newton Class Thrusters** *A. Vargas, M.A. Ingle, A. Acosta, D.H. Hernandez, A.Choudhuri, UTEP*
10:00 am	**Growth of Thin Film Cadmium Telluride and Zinc Telluride Films Using Novel Close Space Sublimation Depositor** *D. Marrufo, John McClure, D. Zubia, UTEP*

PARALLEL TECHNICAL SESSIONS II

Session 2-A: **Energy Materials Technology II** Session Chair: Yirong Lin, UTEP	Room: Salon I Double Tree El Paso
10:30 am	**Structure and Residual Stress Analysis of Titanium Nitride PVD Coatings** *G. Martinez, C.V. Ramana, UTEP*
10:45 am	**Novel Control Technique for Cadmium Sulfide Chemical Bath Deposition Using Real Time Monitoring of Cadmium Ion Molarity** *F. Anwar, R. Ordonez, H. Prieto, D. Zubia, UTEP*
11:00 am	**Control Study of Hierarchical Structural Fiber for Electrochemical Energy Storage** *Md. Khan, M. Mendoza, M. Shuvo, M. Garcia, T. Wilson, Y. Lin, UTEP*
11:15 am	**Investigation of Thermal Conductivity and Mechanical Properties of Hafnia-Zirconia Based Thermal Barrier Coatings** *M. Noor-A-Alam, A.R. Choudhuri, C.V. Ramana, UTEP*
Session 2-B: **Novel Testing and Materials** Session Chair: C. V. Ramana, UTEP	Room: Salon II Double Tree El Paso
10:30 am	**Two-Dimensional Laser Specteroscopy to Study Ultrafast Dynamics in Materials** *C. Li, UTEP*
10:45 am	**Thermoelectric Properties of Carbon Nanotubes** *A. Chowdhury, O. Garcia, M. R. Khan, L. A. Cabrera, UTEP*
11:00 am	**Investigation of Thermoelectric Properties of SiC+ SWCNTs** *L. Babrera, O. Garcia, M. Khan, A.R. Chowdhury, UTEP*
11:15 am	**Synthesis and Characterization of Graphene Aerogel for High Performance Energy Storage Application** *M. Shuvo, M. Mendoza, M. Khan, M.A. Garcia, T. Wilson, Y. Lin, UTEP*
Session 2-C: **Modeling and Emerging Technologies II** Session Chair: Norman Love, UTEP	Room: Salon III Double Tree El Paso
10:30 am	**Central Finite-Volume Schemes in Global Atmospheric Models** *K. Katta, R. Nair, V. Kumar, UTEP*
10:45 am	**Model of a Pipe Flow Distributor for Single Tank Thermocline Thermal Storage System** *S. Afrin, V. Kumar, UTEP*
11:00 am	**Bacterially-Mediated Precipitation of Ferric Iron Minerals During the Leaching of Basaltic Rocks** *K. Schnittker, J. Navarrete, I. Cappelle, D.M. Borrok, UTEP*
11:15 am	**Fluent Simulations for Fluid Flow in Porous Media for Carbon Sequestration Application** *E. Cordero, J. Ortega, P. Delgado, V. Kumar, D. Crandall, G. Bromhal, UTEP*

PARALLEL TECHNICAL SESSIONS II

Session 2-D: **Heat Transfer and Sustainability** Session Chair: Evgeny Shafirovich, UTEP	Room: Discovery Double Tree El Paso
10:30 am	**Powering Large Manufacturing Facilities Using Renewable Energy: Assessment on Reliability and Cost** *J. Jimenez, T. Jin, S. Villarreal, M. Cabrera-Rios, TXST*
10:45 am	**Challenges on Bio-Fuels Distribution Network in the US** *G. Reyes, H. Sohn, NMSU*
11:00 am	**A Central Vs Distributed Micro-Storage Management Using Game Theory and Evolutionary Techniques** *N. Lopez, K. Gutierrez, J.F. Espiritu, UTEP*
11:15 am	**Sustainable Commodity Wood Plastic Composite Materials from Chile Fibers and Plastics** *H. Alodan, S. Hespeler, J. Soltero, B. Garcia, D.J. Valles-Rosales, NMSU*
Session 2-E: **Materials and Sensor Design** Session Chair: Ishrap Shabib, UTEP	Room: Voir Dire Double Tree El Paso
10:30 am	**Targeted Delivery of Drug Using Novel Photo Voltaic Devices** *M. Bhuyan, UTEP*
10:45 am	**Effects of Variation in the Material Behavior on Indentation Derived Elastic Modulus and Hardness** *H. Faisal, R. Tarefder, UNM*
11:00 am	**Dynamic Modulus Testing of New Mexico Asphalt Mixtures** *M. Weldegiorgis, R.A. Tarefder, UNM*
11:15 am	**Development of TiO_2 Nanowires on Carbon Fiber Substrate Utilizing Different Titanium Precursors** *M. Mendoza, A. Khan, M. Shuvo, M.A Garcia, T. Wilson, Y. Lin, UTEP*
Session 2-F: **Energy Enabling Technologies** Session Chair: Mujibur Khan, UTEP	Room: Justice Double Tree El Paso
10:30 am	**3-D Printing Nanolithography with DNA for Water Remediation Applications** *J. Sanchez, J. Aguirre, M. Perez, R.B. Wicker, J.C. Noveron,UTEP*
10:45 am	**Synthesis and Structure Evaluation of Yttria-Stabilized Hafnia Nano-Coatings** *A. Garcia, C. Barraza, M. Noor-A-Alam, C.V. Ramana, UTEP*
11:00 am	**Hafnium Oxide – Cobalt Ferrite Composite For Use in High Density Energy Capacitors** *S. Wells, C.V. Ramana, UTEP*
11:15 am	**Selective Growth of CDTE Thin Films on Micro and Nano Patterned CDS Substrates for Solar Cell Applications** *B. Aguirre, J.L. Cruz-Campa, R. Ordonez, F. Anwar, J.C. McClure, G. Nielson, D. Zubia, UTEP*

RESIDENTIAL PHOTOVOLTAIC APPLICATION IN EL PASO: DOES IT PROMOTE ELECTRICITY SUSTAINABILITY?

Michael Cole
Mechanical Engineering Department
The University of Texas at El Paso
El Paso, TX 79968, USA

Keywords*: Sustainability, Subsidy, Solar, Electricity, Grid*

ABSTRACT

Sustainable energy management is the top factor affecting the prosperity of our global community. All other resource management is governed by a society"s ability to best use energy sources.[1] This paper discusses electricity sustainability in El Paso, and several key factors that determine how this community pursues the migration from the 20th Century fossil and nuclear fuel driven centralized model to a 21st Century model that embraces distributed, renewable electricity sources. El Paso is a top solar intensity benefactor in the United States with access to the sun 84% of the time it is available, as measured by the 54 year study by the National Climatic Data Center.[2] It is then a prime test bed to understand the impact residential, distributed generation using photovoltaic (PV) technologies may have toward sustainable electricity solutions. The key finding is that distributed, grid tied residential PV is a sustainable solution for El Paso today, but that the limited installation and growth demonstrates that success of this technology requires significant community education, awareness, and financial commitment in combination with a supported, coordinated utility partnership to make distributed generation a viable, sustainable electricity option for the city.

1 Introduction

Centralized power generation is well suited to operate at steady state conditions. The large facilities are engineered to adapt to demand variability, but face lead and lag times that necessitate over-production and resultant loss due to storage limitation. Accordingly, peak demand during the day is a key concern for utility planners to coordinate generation across multiple facilities and complex transmission and distribution (T&D) systems to ensure reliable delivery to customers. El Paso Electric (EE) continuously measures and projects these fluctuations in terms of Low Load and Peak Load ranges and anticipated growth to plan capacity as illustrated in Figures 1 and 2. Most recently on June 28, 2011, EE issued a "Request for Proposals for Electric Peaking Power Supply and Load Management Resources" for supply and/or demand side delivery of 80-100 MW in 2014 and 2015, and 160-200 MW in 2016 to meet anticipated peak beginning by summer of 2014.[3]

Distributed solar generation is of interest toward this effort for several technical reasons. First, PV maximum generation occurs from 10 am to 5 pm in El Paso, which coincides with the peak demand curve. Second, line losses are reduced as residential PV is installed at the load for near direct feed to the home for greater efficiency and reduced grid stress. Finally, abundant free solar energy as fuel eliminates environmental impacts and makes operational cash flow predictable. However, high startup costs limit the utility and, more importantly, community willingness to adopt residential PV systems on a large scale in El Paso. At present, only approximately 140 residential systems operate with a nameplate capacity of less than 500kW. Even with solar insulation ranked among the highest in the Nation, that small

installed base only accounts for 19% of nameplate rating[4] or 95kW. At present, that level of participation only offsets a scant 0.024% of peak demand listed in EE‟s proposal request. Lack of community involvement would indicate that engagement only exists with Early Adopter segments, and not a sustainable solution.

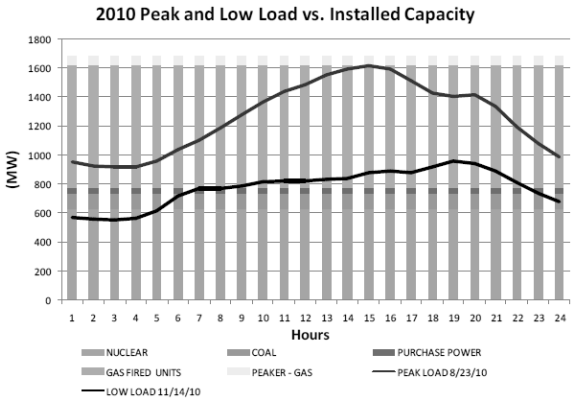

Figure 1: EE Daily Demand Curves[5]

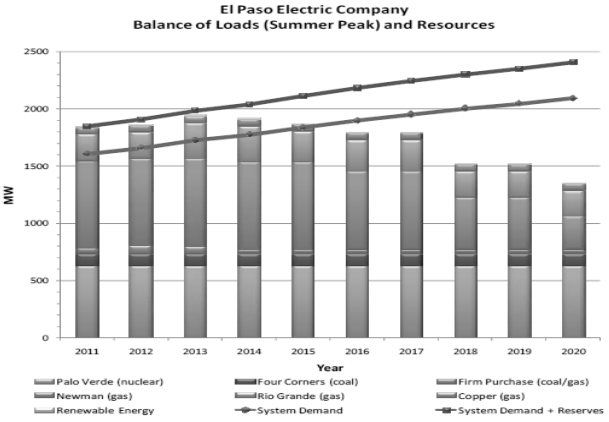

Figure 2: EE Demand and Generation Forecast[3]

2 Sustainability of Residential Solar PV Generation

Assessment of this topic is far reaching, as distributed solar PV generation affects many elements of a community. The broad effect is that future capital investment and operational expense is shifted from the fixed monopoly to the community for targeted elements of demand, and that large front end cost can be treated as an investment through monthly electric bill reduction or elimination. This review cannot assess peripheral benefits toward environmental quality, workforce creation, or efficiency benefits through education and awareness, but each of those factors are significant benefits to consider with residential PV deployments. Here, sustainability will only be considered in terms of current retail electricity cost and investment cash flows.

2.1 Model and Assumptions

Net Present Value assessment of cash flow is the study basis to understand if grid-tied, residential PV adoption offers financial benefit when compared to the traditional, centralized model. If more economically viable, it can be assumed to then be more sustainable to address peak demand. Base load will continue to be addressed with established infrastructure. Also, more complex benefits, as mentioned in section 2, would be in addition to these results. Key assumptions include a 4.7kW grid tied solar system, $4/W base price, useful life of 20 years, current kWh summer electricity pricing and connection fees as offered by EE, and annual rates of 3% inflation and 3.5% electricity pricing increase.[6]

2.2 Results

Under model assumptions and constraints, figure 3 plots net present value of various financial models with key decision points indicated:

A. Current model payback point: Citizen leverages currently available PV subsidy and invests in a solar system today and equals a net present value of centralized model participation - Payback ~4 years.

B. Full investment repaid: Subsidized citizen recovers all cost of initial investment, and begins generation of „Free“ electricity – Payback ~7 years.

C. Subsidized citizen matches $19k mutual fund investment at 1% – Payback ~14 years.

D. Subsidized citizen matches $19k bond fund investment at 5% – Payback ~18 years.

E. Unsubsidized citizen begins to benefit over centralized model.

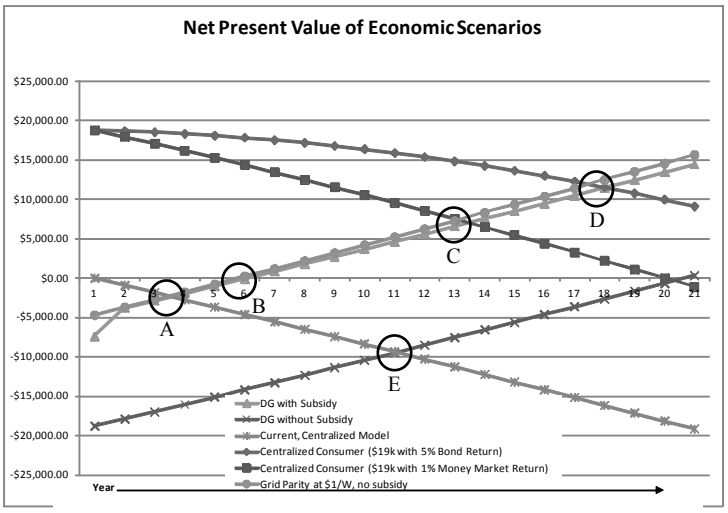

Figure 3: Net Present Value of Economic Scenarios

Note the inclusion of "Grid parity of $1/W, no subsidy" model – Financial performance is nearly aligned, and only slightly better than the current subsidy model at $4/W base cost and $2/W subsidy. It nearly mimics the DOE SunShot goal to make solar systems cost-competitive with other forms of unsubsidized energy: "The U.S. Department of Energy (DOE) is supporting efforts by private companies, academia, and national laboratories to drive down the cost of solar electricity to about $0.06 per kilowatt-hour. This in turn will enable solar-generated power to account for 15–18% of America's electricity generation by 2030."[7]

3 Conclusions and Future Work

This model demonstrates that distributed generation PV investment is a sustainable solution for El Paso based on financial benefit either with or without subsidy. However, current adoption is surprisingly low indicating (1) a gap in diffusion of education and awareness within our community, and/or (2) lack of disposable income for initial capital investment. Efforts in HB 1937, SB 981, and SB 1910 legislation combined with active ongoing development provide a platform for Texas communities to advance sustainable electricity options, but they remain relatively unapplied. Further study is required to unravel the hurdles preventing more wide scale adoption in El Paso and leverage benefits of peak demand offset, appropriate efficiency actions, and community capital investment rather than continue to foster distant, fixed monopoly owners requiring high return on investment. Accordingly, additional studies are planned to better understand motivational patterns and enablers across the El Paso demographic regarding adoption of distributed, grid-tied residential PV.

References

[1] Smalley, R. E. (2005, June). Future Global Energy Prosperity: The Terawatt Challenge. *Materials Research Society Bulletin* , 412-417.

[2] National Climatic Data Center, Ranking Of Cities Based On % Annual Possible Sunshine, http://www.ncdc.noaa.gov/oa/climate/online/ccd/pctposrank.txt, accessed 4/20/2011.

[3] El Paso Electric Company, Request For Proposals For Electric Peaking Power Supply And Load Management Resources, June 28, 2011, http://www.epelectric.com/files/html/RFPs/Amended_2011_Peaking_Unit_RFP_07-25-2011.pdf, accessed 3/1/2012.

[4] National Renewable Energy Laboratory, PVWatts V1, applied for El Paso, TX, 4.7 kW system, http://rredc.nrel.gov/solar/calculators/PVWATTS/version1/, accessed 3/4/2012.

[5] El Paso Electric Company, Conventional Capacity Addition And Generation Option Considerations, July 20, 2011, http://www.epelectric.com/files/html/IRP_2011/IRP_7-20-11_Final.pdf, accessed 3/1/2012.

[6] U.S. Energy Information Administration, Short-Term Energy Outlook, http://www.eia.doe.gov/steo/gifs/Fig23.gif, accessed 4/20/2011.

[7] US Department of Energy, SunShot Initiative, About SunShot, Cost Competitive Solar Energy, http://www1.eere.energy.gov/solar/sunshot/about.html, accessed 3/1/2012.

COMBUSTION OF LUNAR REGOLITH/MAGNESIUM MIXTURES IN DIFFERENT ENVIRONMENTS

A. Delgado, E. Shafirovich*
Department of Mechanical Engineering, The University of Texas at El Paso
500 W. University Ave., El Paso, TX 79968, USA
* Corresponding author (eshafirovich2@utep.edu)

Keywords: *in-situ resource utilization, combustion, lunar regolith*

ABSTRACT

Combustible mixtures of lunar regolith with magnesium could be used for the production of construction materials on the Moon. The present paper investigates the influence of environment on the combustion products of JSC-1A lunar regolith simulant mixed with magnesium.

1 Introduction

Self-propagating high-temperature synthesis (SHS) has been envisioned for the production of construction materials on the Moon. This technique involves self-sustained propagation of the combustion wave over the mixture due to exothermic reactions between the mixture components. SHS has been used for synthesis of numerous ceramic and other compounds. Prior research on SHS in the mixtures of JSC-1A lunar regolith simulant with aluminum and magnesium has been conducted [1, 2]. Thermodynamic calculations of the adiabatic flame temperatures and combustion products over a wide range of the mixture ratios have shown that magnesium provides the highest adiabatic temperatures. Experiments on the combustion of Mg/JSC-1A mixture pellets in argon environment determined the velocity of the combustion front propagation for different particle sizes of the regolith simulant. These experiments have shown, however, that the strength of the combustion products is not sufficiently high for using them as construction materials.

The goal of the present paper is to investigate the influence of heat transfer from the mixture to the surroundings during combustion and subsequent cooling on the mechanical properties of the obtained products and to determine the optimal conditions for the fabrication of strong products. Specifically, combustion of the pellets submerged in an inert powder (JSC-1A or silica) was investigated and compared with the combustion in argon environment.

2 Experimental Procedure

JSC-1A powder (Orbitec) was milled in a planetary ball mill as described elsewhere [2] and mixed with magnesium (-325 mesh, i.e. less than 44 μm, 99.8% pure, AlfaAesar). The powder mixtures (74%JSC-1A and 26% Mg) were compacted into pellets (diameter 25.4 mm) using a hydraulic press (19.6 kN). Pellets were wrapped with a 3 mm thick ceramic fiber insulator.

A thermocouple in a two-channel ceramic insulator was inserted into each pellet to measure the temperature during combustion and cooling. Two types of thermocouples were used: W/Re5% - WRe26% (type C, Omega Engineering) and Chromel-Alumel (type K). The thermocouples were connected to a portable USB-based data acquisition system.

For the experiments with submerged pellets, an aluminum can containing either JSC-1A or silica powder was used (Fig. 1). The pellets were placed in a steel chamber (diameter 30 cm, height 40 cm), connected to a compressed argon cylinder and a vacuum pump. During the experiment, the pellet was ignited at the top by a Nichrome wire connected to a DC power supply. The experiments were conducted in argon environment at atmospheric pressure.

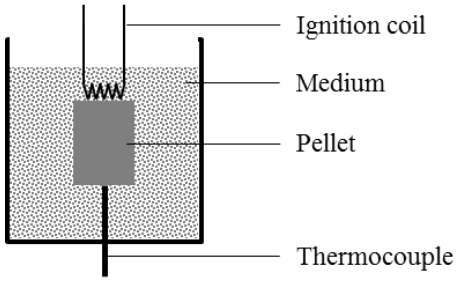

Fig.1. Schematic of the pellet location in the can.

3 Results and Discussion

The analysis of the obtained combustion products has shown that the use of silica resulted in the highest strength of the obtained materials. In contrast with the products obtained in argon environment, these materials could not be broken by hands. It was possible to cut them using a saw. Figure 2 shows a photograph of the combustion products obtained in silica environment.

Fig. 2. Combustion products obtained in silica environment.

Figure 3 shows the results of temperature measurements. The data was plotted by setting time equal to zero at time when the maximum temperature occurred. The maximum temperature was independent on the environment and was equal to 1350-1400°C. It is seen that the cooling rate significantly depends on the environment. For example, as compared with combustion in argon, the use of silica leads to a higher cooling rate immediately after the combustion, but the effect becomes the opposite at temperatures lower than 1000°C. Additional experiments and heat transfer analysis are required to explain these observations.

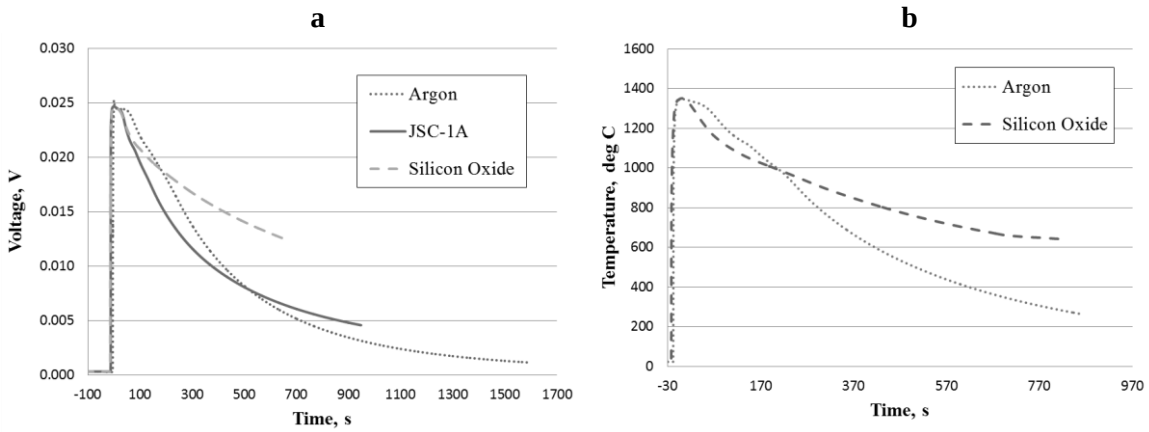

Fig.3. Temperature measurements for JSC-1A/Mg combustion obtained with a) C-type and b) K-type thermocouples.

4 Future Work

Ongoing research focuses on mechanical properties of the JSC-1A/Mg combustion products. Indentation and compression tests will determine the hardness and strength of the obtained materials.

5 Acknowledgement

This research was supported by the NASA Office of Education (Group 5 University Research Centers).

References

[1] C. White, F. Alvarez and E. Shafirovich "Combustible Mixtures of Lunar Regolith with Metals: Thermodynamic Analysis and Combustion Experiments". *Journal of Thermophysics and Heat Transfer*, Vol. 25, No. 4, pp. 620 - 625, 2011.

[2] Álvarez F., Delgado, A., Frias, F., Rubio, M., White, C., Narayana Swamy, A.K., and Shafirovich, E., "Microgravity Combustion of Thermite Mixtures for Welding in Space and for Production of Structural Materials from Lunar Regolith," 50th AIAA Aerospace Sciences Meeting, Nashville, TN, January 9-12, 2012, AIAA Paper 2012-1119.

HYDROGEN GENERATION FROM WATER USING ACTIVATED ALUMINUM

A.K. Narayana Swamy and E. Shafirovich*
Department of Mechanical Engineering, The University of Texas at El Paso
El Paso, TX 79968, USA
*Corresponding Author (eshafirovich2@utep.edu)

Keywords: *hydrogen production, hydrogen storage, aluminum, water*

ABSTRACT

The reaction of aluminum with water has the potential for on demand hydrogen generation. Conventional aluminum powders, however, do not react with water due to a protective oxide layer on the surface. To activate aluminum, various methods have been proposed, which involve harmful, corrosive, or expensive materials. Mechanical activation of aluminum powder using high-energy milling with sodium chloride has been reported recently, but aluminum powders are expensive. The present paper investigates the preparation of an activated aluminum powder from aluminum foil that is available as scrap. The obtained results demonstrate that a highly reactive, fine aluminum powder can be obtained from aluminum foil by high-energy ball milling with sodium chloride. The obtained powder can be used for hydrogen production from water.

1 Introduction

Chemical splitting of water through the reaction with aluminum could be used for on demand hydrogen generation in various applications, including stationary and portable fuel cell power systems. The reaction releases theoretically 1.5 moles of H_2 per 1 mole of Al. Aluminum, however, is usually coated with a protective oxide film that inhibits its reaction with water. The known methods for activation of Al involve corrosion in strong alkaline solutions, high-energy ball milling, alloying with bismuth and gallium, and use of elevated temperatures [1].

In this context, recent studies on high-energy ball milling of aluminum powder with water-soluble inorganic salts such as sodium chloride (NaCl) [2, 3] are of great interest. It is reported that this process produces an activated aluminum powder that readily reacts with hot water. Further, NaCl can be dissolved in cold water after the milling process and the remaining Al powder retains its high reactivity with hot water [3]. As compared to other methods for Al-based water splitting, the process offers a number of advantages such as relatively low reaction temperatures, low cost of sodium chloride (which can also be recycled), and no need for rare, corrosive, toxic or environmentally harmful compounds.

A relatively high cost of aluminum powder, however, is a major obstacle for large-scale application of this method. The energy consumption for production of Al powder and hence its

cost could be significantly reduced by usin g recycled alum inum scrap and waste where aluminum is contained in m etallic, non-oxidized fo rm. In the presen t paper, we inv estigate the feasibility o f direct, sin gle-step p roduction of the activated Al powder from aluminum foil through high-energy ball milling.

2 Experimental Procedure

Aluminum f oils (u ltra pure, VW R) of 15 µm , 23 µm , and 36 µm thicknesses and sodium chloride (>99.0% purity, Sigm a-Aldrich) were used as starting m aterials. The Al foil pieces (10 mm x 10 mm) and the NaCl powder were m illed simultaneously in a p lanetary ball mill (Fritsch Pulverisette 7 prem ium line) u sing zircon ia gr inding bowls and zirconia grinding balls in air atmosphere. The milling procedure included several cycles with the total milling time of 30 min. The powders were characterized using scanning electron m icroscopy, energy dispersive X-ray spectroscopy, and BET specific surface area analysis.

A 0.7-g sample of the resulting Al/NaCl m ixture was treated with an excess of 750 m L of distilled water at 65°C. The wa ter tem perature, m easured by a thermom eter, was m aintained constant using a hot plate. The volum e of rel eased gas was monitored u sing water displacement in an inverted gradu ated cyli nder. Based on the volum e, atmospheric pressure, and tem perature of water in the inverted cylinder, the amount of gas in moles per one mol of Al was calculated.

2 Results

The milling of Al foil with NaCl converted the Al foil pieces into a fine powder. Figure 1 shows SEM microphotographs of the powders obtained from 15-µm and 36-µm foils. It is seen that the average particle size is of the order of 1 µm in both cases.

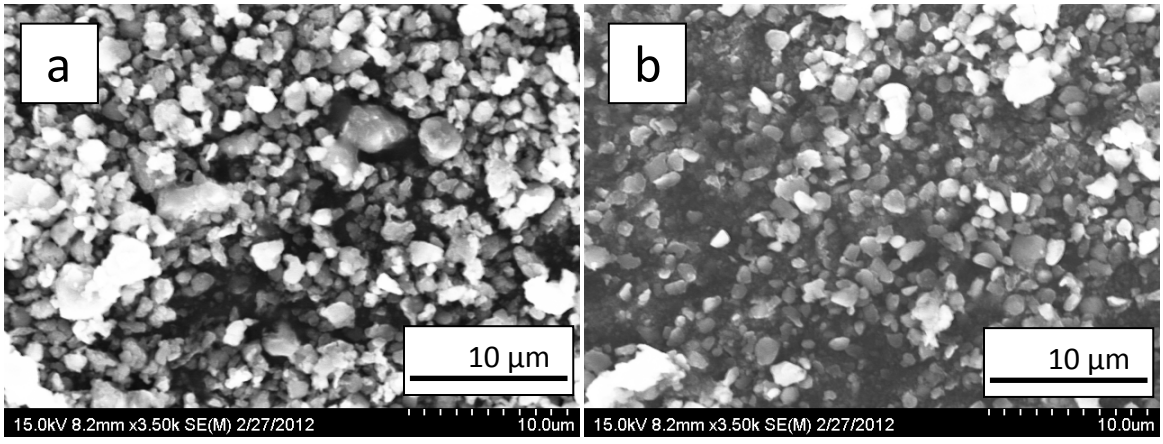

Fig. 1 Microphotgraphs of powders obtained by milling (a) 15-µm and (b) 36-µm Al foil with NaCl (1:1 mass ratio)

Figure 2 shows the extent of the reaction as a function of time for the three foil thicknesses. It is assumed that the evolved gas is 100% hydrogen and that the complete reaction would produce 1.5 mol H_2 per mol Al. It is seen that after a short induction period (no bubbling), fast reaction occurs. The reaction extent was 50 % after 5 min, 85% after 10 min, and more than 95% after 1 hour.

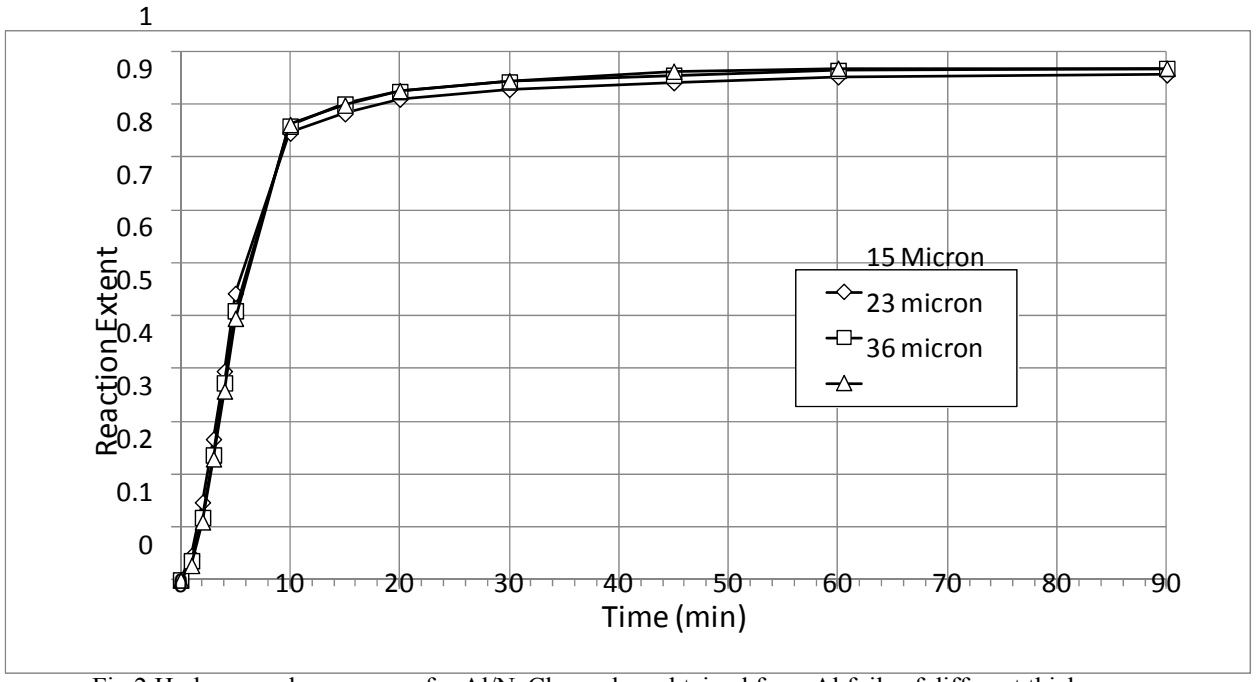

Fig.2 Hydrogen release curves for Al/NaCl powders obtained from Al foils of different thicknesses.

3 Conclusions

The obtained results demonstrate that a highly reactive, fine aluminum powder can be obtained from Al foil by high-energy ball milling with sodium chloride. The obtained powder readily reacts with hot (65°C) water. A major advantage of the proposed process is the feasibility of using secondary aluminum (foil scrap), which is less expensive than commercial Al powders.

3 References

[1] Wang HZ, Leung DYC, Leung MKH, Ni M. A review on hydrogen production using aluminum and aluminum alloys. Renewable and Sustainable Energy Reviews 2009; 13:845–853.

[2] Alinejad B, Mahmoodi K. A novel method for generating hydrogen by hydrolysis of highly activated aluminum nanoparticles in pure water. Int J Hydrogen Energy 2009; 34:7934-7938.

[3] Czech E, Troczynski T. Hydrogen generation through massive corrosion of deformed aluminum in water. Int J Hydrogen Energy 2010; 35:1029-1037.

MICROGRAVITY COMBUSTION OF THERMITE MIXTURES FOR WELDING IN SPACE

J. Frias, A. Delgado, E. Shafirovich*
Department of Mechanical Engineering, The University of Texas at El Paso
El Paso, TX 79968, USA
* Corresponding author (eshafirovich2@utep.edu)

Keywords: *Combustion, Thermites, Welding, Microgravity, Space Technologies*

ABSTRACT

Success of long-duration spaceflight and future space exploration missions will be highly dependent on maintenance and repair challenges. Because of mass and volume constraints to carry spare parts onboard spacecraft, an evaluation of new approaches for maintenance and repair is necessary. Exothermic welding is well known as a reliable, low-energy consuming method for connecting copper wires or cables. However, this method typically relies on Earth's gravity for moving the molten metal from the combustion zone to the welding zone as well as for separation of slag. This report presents the results and analysis of the experiments on exothermic welding conducted onboard reduced-gravity research aircraft at NASA Johnson Space Center in April 2011.

1 Introduction

Combustion of thermites (mixtures of metal powders with metal oxides that exhibit exothermic redox reactions) has various applications in pyrotechnics, munitions, welding, materials synthesis, etc. An important feature of this process is low energy consumption since the occurring exothermic reactions are self-sustained. Only a small amount of energy is required for ignition, while the combustion front propagates due to the release of chemical energy during the reaction. The low energy consumption is especially attractive in space applications, where energy is usually limited. This paper deals with applications of thermite combustion for space exploration, specifically, for welding in space.

Exothermic welding is a reliable, low-energy consuming method for connecting electrical conductors, such as copper wires or cables, particularly in field conditions (e.g., for grounding conductors). It involves a highly exothermic reaction between aluminum and copper oxide which, upon ignition, produces aluminum oxide and copper:

$$2Al + 3CuO \rightarrow Al_2O_3 + 3Cu \quad (1)$$

This method, however, utilizes Earth's gravity to move molten copper from the combustion zone to the area of the desired weld. Also, gravity helps separate alumina slag from copper through the buoyancy effect. The experiments presented in this paper tested special approaches developed for conducting the exothermic welding process in a reduced gravity environment.

2 Experimental Procedure

The testing apparatus included a set of industrial units for exothermal welding (CADWELD), modified for operation in microgravity. The unit consists of a one-time-use mold, made of ceramics or graphite, where two perpendicular rods are installed (Fig. 1). Typically, the vertical rod is made of steel and coated by copper, while the horizontal rod is a copper cable or wire. The mixture of Al and CuO powders is located in a tapered compartment above the weld cavity and supported by a thin steel disk. The mixture is ignited by an electric spark produced by a battery powered electric igniter. During combustion, the bottom disk melts allowing the molten material to flow into the weld cavity due to gravity.

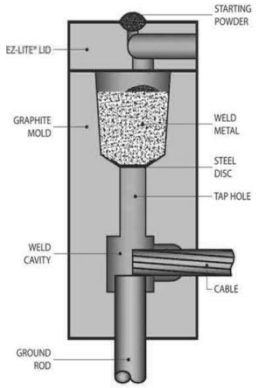

Fig. 1. Schematic of a CADWELD unit for exothermic welding.

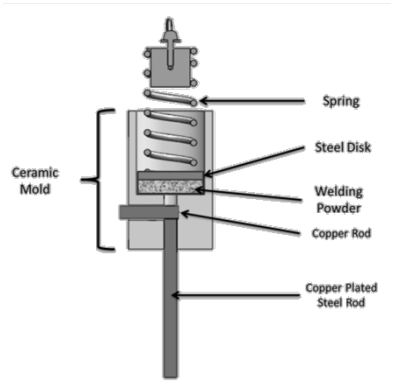

Fig. 2. Schematic and picture of a modified unit for exothermic welding, used in the microgravity experiments.

The modification involved the use of a spring that should replace the gravity and push the molten products to the weld cavity (Fig. 2). The spring and the Al/CuO mixture were separated by a thermally-insulated steel disk.

The experiments were conducted during two parabolic flights of modified Boeing 727 aircraft (ZERO-G Corporation). Welds were obtained in 17 tests conducted during reduced gravity periods. In addition, three welds were obtained during horizontal flight (normal gravity) and three during parabolic pull-up (acceleration of about 1.8 g). Also, 5 tests were conducted on the ground.

The welds obtained in normal and reduced gravity were analyzed using scanning electron microscopy and energy-dispersive X-ray spectroscopy (SEM-EDS, Hitachi S-4800). The goal of EDS elemental analysis was to detect copper and aluminum across the weld, which would help understand whether the separation of alumina from copper occurred in microgravity.

3 Results and Discussion

Figure 3 shows the weld obtained under normal gravity conditions during the flight. Note that the spring mechanism was used for this sample. Contrary to the weld obtained on the ground (without any spring), the sample obtained during the flight exhibited a loose weld. The horizontal copper rod did not weld properly with the welding mixture. Large pores are observed throughout the weld. Aluminum was found throughout the weld. For example, EDS analysis in area 1 showed mainly Cu, but in the area 2, located below area 1, aluminum prevails (Fig. 4). This indicates that upward movement of alumina slag was inhibited, which may explain the reduced strength of the weld.

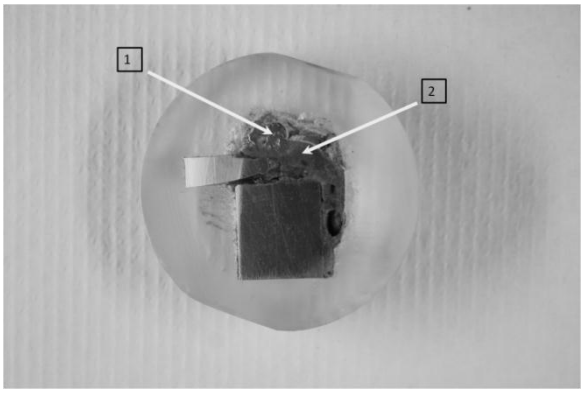

Fig. 3. Weld sample obtained at normal gravity during horizontal flight (with a spring).

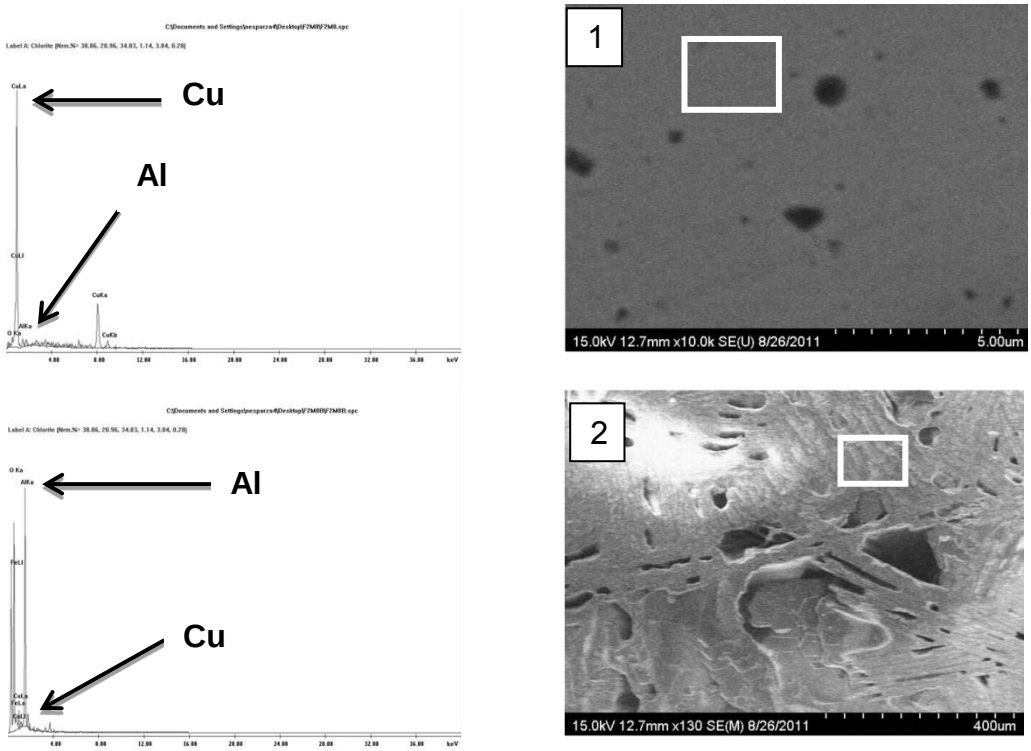

Fig. 4. Microphotographs and EDS spectra for areas 1 (top) and 2 (bottom) in Fig. 8. The rectangles on photographs show the areas where EDS was done.

4 Conclusions

The experimental results revealed that the tested spring mechanism was unable to fully replace the gravity in the exothermic welding process. In fact, the welds obtained at normal gravity with the spring were worse than those obtained at normal gravity without any spring. Detection of aluminum below copper indicates that the spring mechanism inhibited separation of alumina slag from copper, causing a weaker weld. Only increase in gravity up to 1.8 g allowed obtaining strong welds despite the presence of aluminum in several spots.

In microgravity, aluminum was detected in different places throughout the sample and copper did not spread over the vertical rod as occurred at normal and increased gravity. As a result, all the welds obtained in microgravity were weak.

EFFECT OF BIDISPERSE PARTICLES ON PRESSURE DROP IN A GAS-SOLID FLUIDIZED BED

Md Rashedul H Sarker[1], Raufur R. Chowdhury[1], Norman Love[1], Ahsan Chourhuri*
[1] Department of Mechanical Engineering, El Paso, TX 79968, USA;
* Corresponding author (ahsan@utep.edu)

ABSTRACT

An experimental study in a laboratory scale fluidized bed is presented to identify the effect of particle shape on a gas solid fluidized bed. A quartz tube having 12.4 cm inner diameter has been used as a fluidized bed. Borosilicate glass beads were used as the test particle with different geometries. 1.0mm spherical particles and three different ranges of non-spherical particles are used. For non-spherical particles 0.850-1.0 mm, 1.0 - 1.18 mm, and bidisperse 0.850-1.180 mm ranges are used whose mean diameters are 0.925 mm, 1.09 mm and 1.01 mm, respectively. It is seen from experimental measurements that the minimum fluidization state occurs earlier for non-spherical particles compared to spherical particles as they have higher void space and lower sphericity. It is also seen that bidisperse non-spherical particles had the lowest minimum fluidization velocity of all tested geometries.

1 Introduction

Nature has abundant fossil fuel. Coal is one of them. Combustion of coal to produce energy emits air pollutants. One effective and clean way to get energy and some other valuable products from coal is by coal gasification technology. By this technology it is possible to control some emissions without sacrificing performance. Gasification breaks down the feedstock into their molecular level which drives out all ash and impurities from feedstock and ensures a clean production of synthetic gas. The Department of Energy is focusing on enhanced efficient and reliable coal gasifiers[1]. From literature it has been found that most experimental results on fluidized beds are based on spherical particles but in real gasification process coal is expected to be non spherical. Minimum fluidization velocity is an important parameter to characterize the fluidized bed. Minimum fluidization can be affected by many factors like bed diameter, bed geometry, bed height, particle diameter, particle shape, or density of particles. Gunn et al.[2] found no significant effect on minimum fluidization for bed height with cylindrical shape fluidized bed. Geldart el al.[3] found a significant effect of bed height on minimum fluidization for rectangular shape fluidized bed. Hilal et al.[4] observed a decrease of minimum fluidization velocity with increase of bed diameter. Escudero et al.[5] determined that minimum fluidization velocity is insensitive to bed height and sensitive to particle density. Inspired by these issues we have conducted an experiment to identify the effect of particle shape on gas-solid fluidized bed dynamics. We have compared experimental measurement of spherical particle and non spherical particles with similar mean diameters and different bed heights.

2 Experimental Procedure and Setup

Figure 1 is a laboratory scale packed fluidized bed with its basic components. The bottom part of bed where it holds the particle is made of plexi glass tube with 12.7 cm outer diameter and 0.318 cm wall thickness. Quartz tube with 12 cm outer and 0.5 cm wall thickness inserted into plexiglass tube for better optical access.

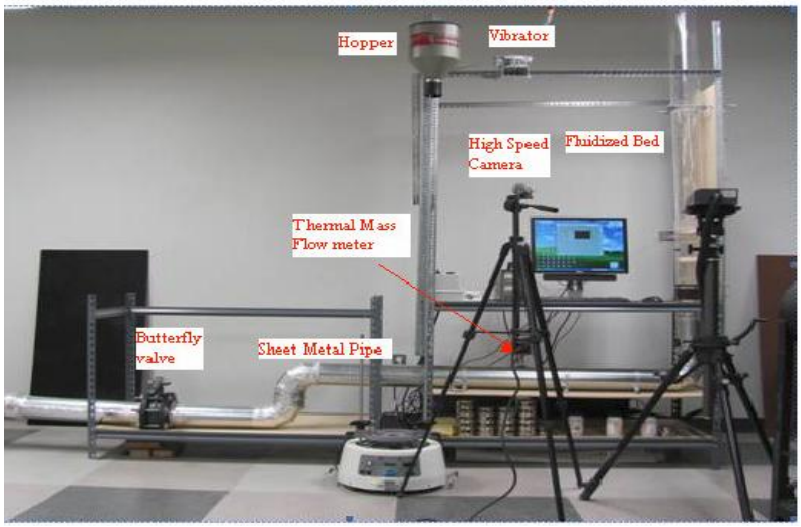

Fig1: Experimental setup of cylindrical fluidized bed

Air flow as a gasifying agent is introduced to fluidized bed through 12.7 cm diameter sheet metal pipe from a 3730 kW pressure blower with 34 m^3/min flow rate. Butterfly valve to control flow rate, thermal mass flow meter to measure volumetric flow rate, digital manometer capable of measuring 0-2 psi range were also used with this setup.

1 mm borosilicate glass beads used as spherical and 6 mm glass beads crushed by a hydraulic compressor and sieved to produce different range of non spherical particles. Among these ranges are 0.850-1.0 mm and 1.0-1.180 mm diameter particles which were selected for the current experiment. Another range of particles with 0.850-1.180 mm diameter was made by mixing the previous two ranges. Mean diameter of the three ranges of non-spherical particles were 0.925 mm, 1.09 mm and 1.01 which are very close to the mean diameter of spherical (1 mm) particle. Experimental measurements of non-spherical particles for different ranges compared with measurements of 1mm spherical particles were done to identify the effect of particle shape.

3 Results & Discussion:

Pressure drop across the fluidized bed with increasing superficial gas velocities was measured for both shape of particles and compared. The experimental results are presented below. Figure 2 shows the effect of particle shape at 5.5 cm bed height. Minimum fluidization state occurs earlier for non spherical particles because of larger void space, lower sphericity and wide range of particles than the spherical. Figure 3 shows the effect on minimum fluidization velocity for particle shape as well as particle size. It has found that minimum fluidization velocity for each particle size is independent with increasing or decreasing bed height.

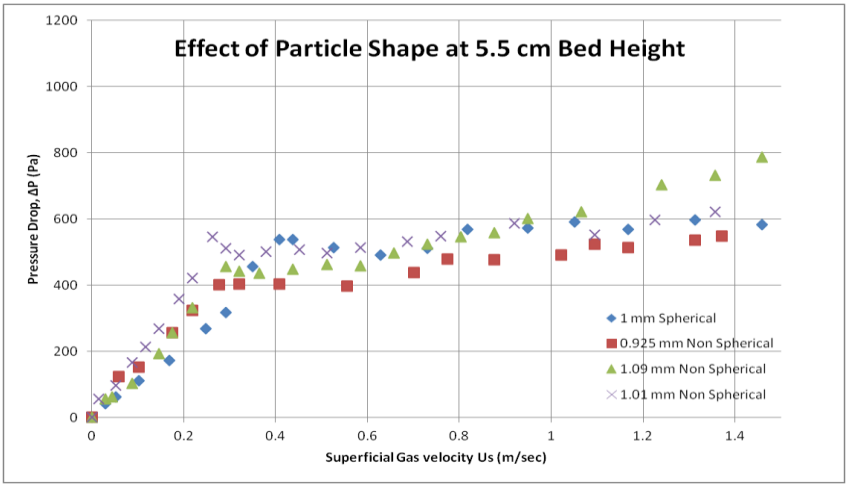

Fig 2: Effect of particle shape

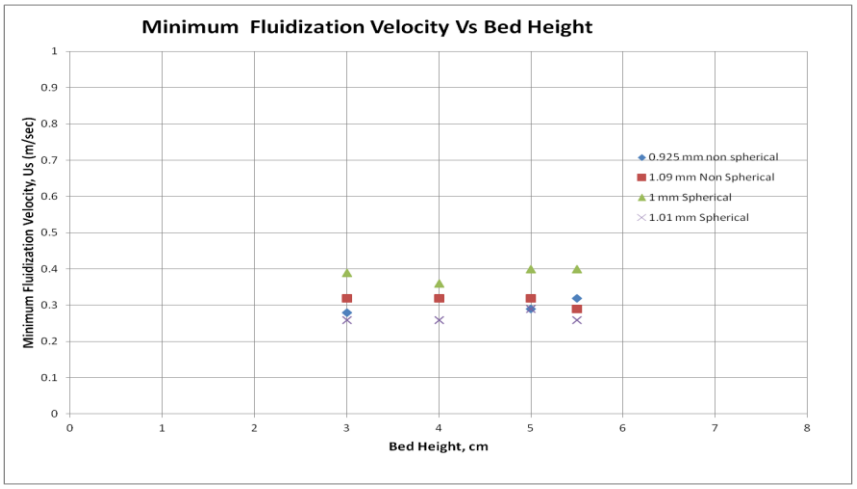

Fig 3: Minimum fluidization velocity at different bed heights

References:

[1] U.S. Department of Energy, Clean Coal Technologies-Coal Gasification R&D Website, URL: http://www.fossil.energy.gov/programs/powersystems/gasification/index.html

[2] Gunn D. J., Hilal N., "The Expansion of Gas-Fluidized Beds in Bubbling Fluidization", Chemical Engineering Science, Vol. 52, No. 16, 1997, pp. 2811-2822.

[3] Geldart D., Cranfield R. R., "The Gas Fluidization of Large Particles", Chemical Engineering Journal, Vol. 3, 1972, pp. 211-231.

[4] Hilal N., Ghannam M. T., Anabtawi M. Z., "Effect of Bed Diameter, Distributor and Inserts on Minimum Fluidization Velocity", Chemical Engineering Technology, Vol. 24, No. 2, 2001, pp. 161-165

[5] Escudero D., Heindel J., "Bed Height and Material Density Effects on Minimum Fluidization Velocity in a Cylindrical Fluidized Bed", 7th International Conference on Multiphase Flow, Paper No. 1674, Tampa, FL, 2010.

DEVELOPMENT OF AN OPTICALLY ACCESSIBLE HIGH PRESSURE TURBINE COMBUSTOR

S. Sarker[1], J. Nunez[1], C. Valdez[1], N. Love[1*], A. Choudhuri[1*]
[1] Center for Space Exploration Technology Research (cSETR)
The University of Texas at El Paso
El Paso, TX 79968, USA
* Corresponding author (ahsan@utep.edu)

Keywords: Combustion, Turbine, Syngas, Flashback, High-Pressure

ABSTRACT

Future generation gas turbine combustors for power production are expected to have the capability of operating on high hydrogen content (HHC). To ensure the implementation of HHC in power generation without negotiating operational or emission advantages, a study of the flame stability regime and behavior of HHC under gas turbine condition leads to the necessity of the development of an optically accessible high-pressure turbine combustor. The design is based on 500 kW power and 1.5MPa pressure which is the representative pressure of real gas turbine. Furthermore, it has the flexibility of operating with variable syngas compositions along with a variety of fuels to analyze the flame structure, flow field characterization using high speed particle image velocimetry (PIV), and flashback propensity for high hydrogen content fuels under realistic gas turbine conditions.

1 Introduction

Coal derived fuels, such as synthetic fuel, have been studied for use in gas turbines due to the potential operational gains and pollutant reducing characteristics. Future generation gas turbine combustors are expected to operate with fuel compositions ranging from natural gas to different syngas compositions. One of the main challenges is the concentration of hydrogen, which has shown to significantly affect the flame characteristics even when only 5% vol. hydrogen is present [1].

Some fundamental flame characteristics such as laminar flame speed, flame stability, and emissions characteristics have been investigated in some other studies. Although flame velocity and stoichiometry are generally reasons for flashback, the kinetics of the hydrogen can dominate flashback behaviors in syngas fuels [2]. To analyze the influence of the flow field and chemistry on flame flashback, a research group conducted experiments using a center-body swirl stabilized lab-scale gas turbine combustor with similar fuel compositions and found that the percentage of H_2 in the fuel mixture rather than increasing swirl number influenced flame flashback more [3].

The combustor is designed to operate up to 1.5 MPa and temperatures up to 2400 K. These pressures and temperatures were selected in order to accommodate high hydrogen/hydrogen fuel compositions as well as pressures representative of an actual gas turbine system. An analysis of the flame structure, flow field characterization using high speed PIV, and flashback propensity in

high hydrogen content fuel under realistic gas turbine conditions is to be performed using this design.

2 Experimental Procedure

The present combustion chamber is designed to accommodate multiple geometrical configurations including a non-swirl stabilized, swirl flow, and center-body stabilized flames that will test geometry influences on flame behavior and NOx emission. It is composed of two cylindrical chambers: an inner quartz chamber housed in a stainless steel chamber having three optically accessible windows and multiple instrumentation ports for a broad range of investigation techniques permitting analysis of combustion and ignition (Fig. 1). Two different cooling systems are included for the inner and outer chamber to reduce the thermal stress. The test chamber is also fitted with a variable area flow restrictor to control the pressure drop across combustion chamber. The outer test section is equipped with copper coiling using cooling water as a driving fluid (Fig. 2). The inner coolant system is designed to circulate nitrogen around the inner quartz tube. The use of a variable throat area restrictor, multiple cooling systems, as well removable modular sections and optical access will allow the combustor to be compatible to work in a wide range of operations.

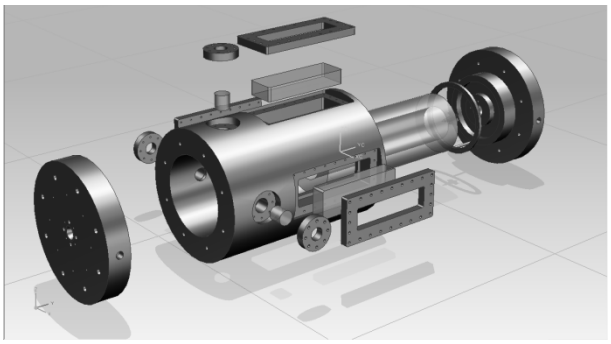

Fig. 1. Combustor parts

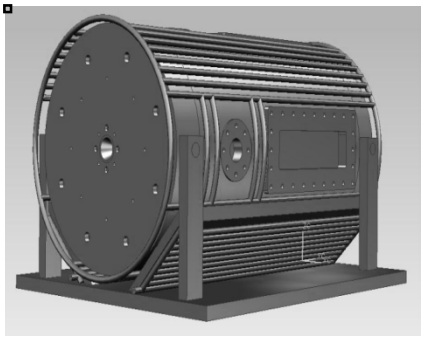

Fig. 2. Outer cooling of combustor with stand

2.1 Combustor Components

A. Inlet Manifold: The inlet manifold is composed of three modular sections. The first section acts as the fuel/air inlet mixture section. The second section is a removable static mixture section which is composed of a honeycomb located inside the chamber that removes irregularities and makes the flow uniform. This section is then attached to third section which connects the inlet manifold to the main combustor.

B. Front Cap of Combustor: The front cap is composed of one solid section acting as a connection between the main combustor section and the inlet manifold. The inner hole located in the center of the end cap will house the swirler and also allow the passage of the fuel and air mixture. The ignition system is also located through the front cap.

C. Ignition System: A coaxial pilot flame has been integrated into the combustor to be used as the igntition system. An extended spark plug electrode provides the electric discharge that is needed to ignite the fuel and provide a stable flame for the combustor. The coaxial pilot flame

also has a nitrogen inlet for safety purposes. This port can also be used as an inlet for air for a premixed flame.

D. Combustion Chamber: The combustor has an inner diameter of 27.94 cm with an 8.89 cm thickness. The total length of the combustor is 64.77 cm. Three window ports are located on the two sides and top of the combustor. Three circular ports allow for either instrumentation devices to be located or visualization at the end of the combustor. The window covers are needed to hold down the rectangular quartz windows.

E. End Cap: The end cap has removable modular sections that include the converging diverging nozzle (CD), and the outer main cap which connects the end cap to the main combustion chamber. The main purpose of the CD nozzle is to the control the throat to maintain the desired pressure inside the chamber. The main end cap acts as a sealant to the main combustion chamber. It is also the link between the combustion chamber and the exhaust.

2.2 Structural Analysis

Because of the rapid increase in temperature of the combustor wall, finite element analysis was conducted to determine the wall thicknesses of the combustor as well as the operational temperature which is needed to fix the coolant flow rate. The thermal load was set to 340 K for the chamber wall and 800 K for the quartz window, while the pressure was set to 1.5MPa. The obtained maximum stress was determined to be less than the yield strength of AISI stainless steel 410 and quartz using the wall thickness of 8.89 cm and window thickness of 5.08 cm.

The wall temperature was calculated using Eq. 1 where convection was considered to be the primary contributor to heat transfer inside the chamber.

$$\dot{Q} = \dot{m} C_p \frac{dT}{dx} = hA(T_{Ad} - T) \quad (1)$$

Several calculations were also performed in addition to this as design parameters, these will be included in the presentation of the final work.

3. Conclusion and Future Work

This paper presents the design and development of a high-pressure gas turbine combustor. This combustor will be used to investigate and develop flashback mitigation technologies of high hydrogen content fuel under gas turbine conditions.

4. References

[1] V. Ardha, B. Dam, N. Love, A. Choudhuri "*Effect of Local Flow Field Fluctuations on Characteristics of Turbulent Flames"*.9th International Energy Conversion Engineering Conference, Paper No. AIAA 2011-5595, 2011.
[2] D. Dayu, R. Franco, A. Choudhuri, R. Lewis *"Investigation of Flashback Propensity of Syngas Premixed Flames".* AIAA/ASME/SAE/ASEE Joint Propulsion Conference and Exhibit, Paper No. AIAA-2005-3585, 2005.
[3] B. Dam, G. Corona, M. Hayder, A. Choudhuri *"Effects of Syngas Composition on Combustion Induced Vortex Breakdown (CIVB) Flashback in a Swirl Stabilized Combustor".* Fuel, Vol. 90, No. 2, 3274-3284, 2011.

GODDARD LABORATORY
DATA ACQUISITION AND REMOTE CONTROL SYSTEM

J. Barragan[1], J. Flores[1]*
[1] Center for Space Exploration Technology Research, University of Texas at El Paso, El Paso, TX 79938, USA;
* Corresponding author (jmbarragan@miners.utep.edu)

Keywords: *Data acquisition, testing facilities.*

ABSTRACT

The University of Texas at El Paso has designed and built the Goddard Laboratory to allow team members to execute experiments pertaining to heat transfer, combustion characterization and ignition physics. Experimentation conducted in the remote Goddard bunker needs to be executed precisely and all data generated needs to be collected effectively. For these reasons, all systems need to be fully integrated for control and data collection. Using LabVIEW and a patch panel, these tasks can be accomplished remotely and in a safe manner from a control-room outside the bunker. The infrastructure of the Data Acquisition and Remote Control System (DARCS) is described in this paper, along with the integration of its components with current experiments.

1 Introduction

Methane is considered to be relatively inexpensive to produce, easy to handle and a non-toxic propellant [1]. For these reasons, research in this realm has recently increased and has become a main objective at the Center for Space Exploration Technology Research (cSETR). To better understand methane combustion and ignition physics, the cSETR developed a Multipurpose Optical Accessible Combustion Chamber (MOAC) and a Torch Igniter. The MOAC was designed to easily conduct experiments pertaining to ignition physics with different configurations, interchangeable propellant injectors and nozzle components [2]. Along side the MOAC, a Torch Ignition System was developed to serve as its main injector ignition source. Another system developed by the cSETR was the Cryogenic Delivery System, which is capable of producing Liquid Methane and delivering it along side Liquid Oxygen [2]. In order to execute the desired test, the described systems were fully integrated for control and data acquisition purposes. To accomplish this, a Data Acquisition and Remote Control System (DARCS) was developed to ensure all current and future experiments are executed safely and all data produced is collected reliably. The safe execution of both combustion and heat transfer test is achieved by conducting all experiments remotely in a projectile-proof bunker that is constantly monitored for ventilation and pressure relief requirements. The remote location is equipped with needed infrastructure instrumentation and equipment for control and data collection purposes.

2 Current Experimental Systems

2.1 Cryogenic Delivery System

The main purpose of this cryogenic system is to deliver cryogenic propellants by incorporating a pre-chill, purge and feed stage. The system uses eight actuated solenoid valves that are signaled to open by 120 V. Along side the valves, the systems' pressure is under constant supervision with the help of 2 cryogenic pressure transducers that ensure normal pressure conditions are not exceeded, avoiding any burst in the system. The pressure sensors require an excitation voltage of 10 V DC and output a signal in the range of 0 to 30 mV DC. For temperature readings, two silicon diode sensor are used in the system, which require an excitation signal of 10 μA and return a signal ranging from 0 to 1.5 V DC. Along side temperature and pressure, cryogenic flow measurements are accomplished with a turbine flow meter that outputs a current in the range of 0 to 20 mA.

2.2 Multipurpose Optical Accessible Combustor

The Multipurpose Optical Accessible Combustor was designed to characterize combustion of bi-propellant engines by allowing optical instrumentation to collect visual data produced when testing. Aside from visual instrumentation, the MOAC also requires constant temperature and pressure measurements for later analysis and to ensure operations are within design limitations. As part of the design, the MOAC utilizes a high temperature pressure transducer to sense chamber pressures. This instrument requires an excitation signal of 5 V dc and returns a signal in the range of 0 to 100 mV DC. For temperature readings, the MOAC was designed to house two thermocouples capable of operating at high chamber temperatures.

2.3 Torch Igniter

The Torch Ignition System designed to ignite the MOAC injector is comprised of three sub-systems: propellant delivery, spark generation and propellant injection. The propellant delivery system requires control and feedback accomplished with two flow meters and two solenoid valves. The flow meters require an excitation input signal of 12 V DC and output a signal ranging from 0 to 5 V DC. To initiate flow the solenoid valves are actuated when receiving a 24 V DC signal. For spark generation, the system uses a high-voltage DC-DC converter that supplies the spark electrodes with 25 kV at 0.16 mA. This converter requires 12 V DC for power and a 0 to 5 V signal for control.

3 Data Acquisition Remote Control System

The DARCS achieves control and data collection with hardware capable of controlling a minimum of 12 solenoid valves, processing a minimum of 14 mV signals, collecting a minimum of 2 mA signals and supplying different AC/DC voltages to a variety of instruments. The system employs an Advantech industrial computer running Windows XP Professional and is capable of housing 2 ISA and 10 PCI cards. For data collection and instrumentation control, National Instruments hardware interfaces with the computer through National Instruments LabVIEW software.

3.1 Valve System Integration

The different valves used in both, the Cryogenic Delivery System and the Torch Ignition System, require a constant voltage to open and initiate flow. In the Cryogenic Delivery System, all valves are activated with a constant signal of 120 V AC. In the Torch Ignition System, similar valves require a constant signal of 24 V DC delivered by an EXTECH power supply. On the Cryogenic Delivery System, valves are activated with

an APC AC UPS power supply that is capable of providing a voltage of 120 V DC. For control with LabVIEW, the valves are connected to PCI cards (NI PCI-6521) installed on the computer. This card allows the operator to control eight mechanical relay outputs that close and open to complete or break the valves electrical circuit. When activated, the valves receive the required voltage to open.

3.2 Sensors System Integration

Pressure sensors require an excitation voltage and return a mV signal proportional to pressures. An EXTECH power supply provides the sensors with 10 V DC and 5 V DC for both, the cryogenic transducers in the delivery system and the high temperature transducer in the MOAC, respectively. Data acquisition with LabVIEW is accomplished by collecting corresponding signals from both pressure sensors with a PCI Card (NI PCI-6220). This card is capable of collecting up to 16 analog inputs in the range of +/-10 V DC, suitable for both the cryogenic and high temperature sensor of ranges 0 to 30 mV Dc and 0 to 100 mV DC, respectively. The two Torch Igniter flow meters require excitation voltages of 12 V DC and are provided by an EXTECH power supply. The return output signals in the range of 0 to 5 V DC are captured by the PCI card (NI-PCI-6220) capable of reading inputs in the range of +/- 10 V DC. For the Cryogenic Delivery System, the flow measurements are recorded with the PCI card (PCI-6238) that is capable of reading input signals ranging from 0 to 20 mA, which are outputted by the flow meters microprocessor transmitter. The cryogenic diode temperature measurements are sampled with a 218S monitor from Lake Shore, capable of 8 input channels. Both temperature sensors inside the MOAC output a signal proportional to chamber temperature, which are then connected to a thermocouple module that is connected to the computer.

4 Conclusion

Currently, the three mentioned integrated systems are fully operational and ready for testing. The MOAC, Torch Igniter and Cryogenic Delivery System have generated data for analysis and future testing is under development. Aside from the discussed systems, team members have integrated different test setups with the Goddard bunker and DARCS. The DARCS modular design has been effective and has streamlined instrument integration for full control and feedback. Future DARCS development will increase instrumentation support and will use more efficient power distribution methods.

References

[1] Neill, T., Judd, D., Veith, E., & Rousar, D. (2009). Practical uses of liquid methane in rocket engine applications. Acta Astronautica 65, 696–705.

[2] Navarro, C. D., Betancourt-Roque, J., Sanchez, L. E., Robinson, N., & Choudhuri, A. (2011). Development of a Multi-Purpose Optically Accessible Rocket Combustor for Liquid Oxygen and Hydrocarbons. 47th AIAA/ASME/SAE/ASEE Joint Propulsion Conference & Exhibit. San Diego, CA: AIAA.

[3] Pineda, F., Flores, J. R., Garcia, C. P., Navarro, C. D., & Choudhuri, A. (2011). Cryogenic System Development for LOX/Hydrocarbon Propulsion Research. 47th AIAA/ASME/SAE/ASEE Joint Propulsion Conference & Exhibit. San Diego, CA: AIAA.

EFFECT OF DILUENTS ON FLAME RADIATION AND STRUCTURES OF OXY-FUEL FLAMES

M. DeLaTorre[1], B. Dam[*], V. Ardha[1], N. Love[1] and A. Choudhuri[1]
[1] Department of Mechanical Engineering, University of Texas at El Paso
El Paso, TX 79968, USA
* bkdam@miners.utep.edu

Keywords: Radiation heat release factor, Mass flow rate, Fuel energy input, Radiation output, Equivalence ratio

ABSTRACT

This paper presents experimental measurement of radiative heat release rates of oxy-fuel flames and the effects of recirculated CO_2 and H_2O in oxy-fuel combustion conditions. The radiative heat release rate of CH_4-O_2 flames diluted with CO_2 is increased as the percentage of CO_2 is increased in the oxidizer mixture even though the adiabatic flame temperature decreases. Once the equivalence ratio reached richer conditions (Φ >1) the radiative factor increased along with the equivalence ratio. It was observed that the emissivity of CH_4-O_2-CO_2 increased as the recirculation ratio of CO_2 in the oxidizer increased which is subjected to increase in the radiation heat transfer rate of oxy-fuel flames diluted with CO_2. The adiabatic flame temperature is measured for each case by using STANJAN software.

1 Introduction

Fossil fuels have been used for many years to generate power. Lately there has been a growing concern of the greenhouse gases being released into the atmosphere and efforts are being made to decrease the emissions of them. This poses a challenge to the energy production industry since they rely heavily on the use of fossil fuels for power production, which generates greenhouse gases and pollutants as a byproduct. With government agencies imposing strict regulations in order to keep greenhouse gases and pollutant emissions at a controlled level there have been developments in the energy industry to regulate emissions. There are different approaches to capture and store carbon dioxide: pre-combustion capture and post combustion capture. When combustion takes place with air, nitrous oxide is produced which it not only lowers the flame temperature and increases the volume of combustion products but also is considered a greenhouse gas. Oxy-fuel combustion is a pre-combustion technique that has received much attention due to its ability to eliminate the emissions of the greenhouse gases including nitrous oxide leaving only water in the form of vapor and carbon dioxide as the byproducts of combustion; this is achieved by reacting the fuel with pure oxygen. This allows for relatively easier separation, capture and storage of the carbon dioxide by condensing the water off the combustion products.

The U.S. Department of Energy has investigated the performance of CO_2 and H_2O diluted oxy-fuel combustion system in a high-pressure combustor [1]. Jupitar Oxygen Corporation also developed an oxy-fuel system that uses an untempered high temperature oxy-fuel flame, currently on the market for environmentally sound energy production [2-3]. The focus of this paper is to study the effects that the recirculation of carbon dioxide and steam have on the radiative heat release rate of methane combustion. The global radiation was measured using a

Mark IV series non-contact temperature sensor & radiometer with 150° view angle and 0.1 to 92 μm wavelength ranges. For the experiments the radiative heat release factor (F) is calculated using Eq. (1):

$$F = \frac{q_r}{q_{in}} \qquad (1)$$

Where q_r is the radiation output from the flame and q_{in} is the firing input of the combustion.

2 Technical Approach

Figure 1 shows the complete experimental setup used to acquire the oxy-fuel flame radiation measurements. Research grade fuel and oxidants were delivered to the burner from pressurized tanks. Manual precision metering valves in conjunction with low-torque-quarter-turn plug valves were used to control and meter fuel and oxidant flow rates. A bank of digital mass flow controllers was used to measure mass flow rates of fuels and oxidant to achieve the desired compositions. Prior to each experiment the mass flow meters were calibrated using a laser based mass flow meter calibrator.

3 Results and Discussion

Figures 2 and 3 show the radiative heat release rate of CH_4-O_2-CO_2 flames varying with recirculation ratio of CO_2 in the oxidizer at different equivalence ratio. It is interesting to note that the radiative heat release rate increases as the CO_2 diluents increase in the oxidizer mixture even though the adiabatic temperature decreases. Emissivity is plotted against recirculation ratio of CO_2 in Figure 4.

4 Conclusions

The preliminary sets of data have shown that flame radiation is primarily a function of emissivity of the flame. However emissivity is dictated by equivalence ratio and percentage of recirculation ratio.

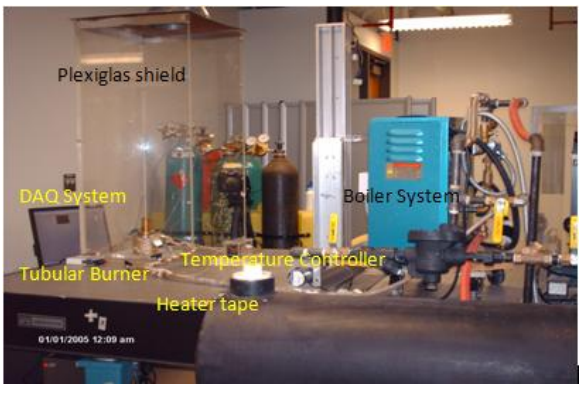

Fig. 1 Experimental setup for experiment

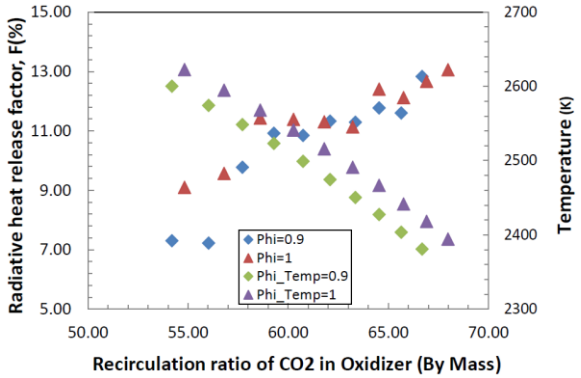

Figure 2 Radiation heat transfer of CH_4-O_2 flames at different equivalence ratio

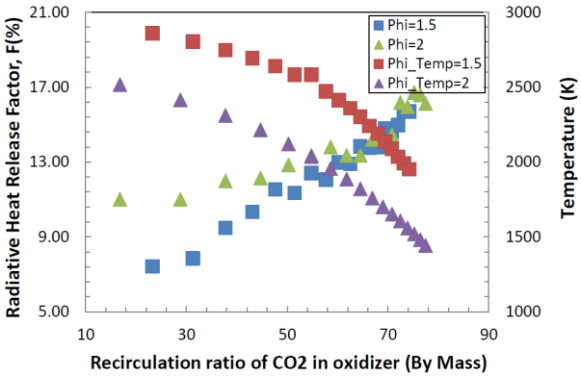

Figure 3 Radiation heat transfer of CH_4-O_2-CO_2 flames at fuel rich conditions

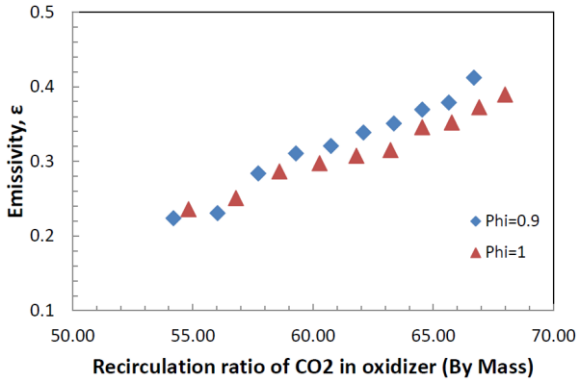

Figure 4 Emissivity of CH_4-O_2-CO_2 flames at different recirculation ratio of CO_2 in the oxidizer mixtures

References

[1] U.S Department of Energy, National Energy Technology Laboratory - Carbon sequestration Technologies Website, URL: http://www.netl.doe.gov/technologies/carbon_seq/ 2007Roadmap [Accessed on 2007].

[2] U.S Department of Energy, National Energy Technology Laboratory - Carbon sequestration Technologies Website, URL: http://www.netl.doe.gov/newsroom/labnotes/2011/03-2011.html#2.

[3]Ochs, T., Gross, A., Patrick, B., Oryshchyn, D., Summers, C., Turner, P., 2005, "The Next Generation of Oxy-Fuel Boiler Systems," Technical Report No. DOE/ARC-2005-058, Albany research center, Department of Energy.

MOLECULAR DYNAMICS SIMULATION OF STRAINED, NANOSCALE CDTE CRYSTAL GROWTH USING BOND-ORDER POTENTIALS

X. W. Zhou[2], D. K. Ward[3], J. L. Cruz-Campa[4], G. N. Nielson[4], D. Zubia[1], J. McClure[1], J.J. Chavez[1]*

[1] Department of Electrical and Computer Engineering, University of Texas at El Paso, El Paso, TX 79902, USA;

[2] Mechanics of Materials Department. Sandia National Laboratories, Livermore, CA 94550, USA;

[3]Radiation and Nuclear Detection Materials and Analysis Department, Sandia National Laboratories, Livermore, CA 94550, USA;

[4]MEMS Technologies Department, Sandia National Laboratories, Albuquerque, NM 87185, USA;

* J.J. Chavez (jjchavez5@miners.utep.edu)

ABSTRACT

The record solar cell efficiency of Cadmium Telluride (CdTe) / Cadmium Sulfide (CdS) modules is currently limited to a record ~17.3% out of a theoretical maximum of ~29%. This is caused by the large lattice mismatch of 10% between CdTe and CdS which results in a high density of charge trapping defects that reduce the device's performance. An approach to address this issue is to lower the lattice mismatch strain experienced by the two materials through nanoscale fabrication methods. By alloying CdTe with Zn and growing selectively on a nanopatterned CdS substrate, the strain in the $Cd_XZn_{1-X}Te$ /CdS heterostructure can be dramatically reduced since the lattice mismatch of ZnTe(111)-CdS(0001) is only 3%. The application of recently developed CdTe and $Cd_XZn_{1-X}Te$ bond-order potentials (BOP) in molecular dynamics (MD) simulations that offer unprecedented quantum mechanics accuracy allow the visualization of nanoscale defect formations not available in experimental procedures.

1. Background

The cost of $0.15/kWh for electrical energy generated using CdTe solar cells is the lowest of any other semiconductor technology[1]. The material's current energy-conversion efficiency record of 17.3% is significantly lower than the theoretical value of 29%[2,3]. If the energy efficiency is improved significantly, CdTe solar cells have the potential to profoundly impact the energy supply given that their cost drops below the $0.10/kWh retail price for conventional energy in the USA. The current under-achievement of the energy efficiency of CdTe solar cells is attributable to the charge-trapping defects[4-8]. Because CdTe solar cells are composed of multilayered films, a variety of nanoscale defects can be present due to the lattice-mismatch strains. Innovations in the material have been difficult because these defects cannot be visualized in experiments. Consequently, defect configurations, their effects, and their formation mechanisms have not been well understood. A recently developed CdTe bond-order potential (BOP)[9] has made it possible to use molecular dynamics (MD) simulations to study defects with an accuracy approaching that of quantum mechanics methods. The objective of the present work is to perform such BOP-based MD simulations to explore defect formation during growth of CdTe over layers. This can provide critical insight required to improve the energy efficiency of CdTe modules.

2. Bond-Order Potential: A Breakthrough in Semiconductor Modeling

MD simulations of semiconductor growth are extremely challenging because they sample a large number of metastable configurations not known a priori. These must ultimately be reconstructed into the equilibrium crystal for any analysis to be meaningful. An interatomic potential becomes predictive when it captures properties of a variety of pre-designed phases and correctly predicts crystalline growth while it samples random configurations at the growth surface. No previous semiconductor potential achieves this. A vast majority of previous MD simulations of crystalline growth of semiconductor vapor deposition[10-14] were achieved using Stillinger-Weber (SW)[15] potentials. It has been established[16] that while SW potentials can easily ensure the crystalline growth, they cannot satisfactorily capture the property trends of other configurations and hence they cannot accurately reveal defect formation. Tersoff potentials[17], on the other hand, can capture property trends more accurately. However, this also makes it more difficult to ensure the lowest energy for the equilibrium phase. As a result of parameterization problems, many literature Tersoff potentials[18-20] predict amorphous growth during vapor deposition simulations. Not surprisingly, we found[16] that none of the existing CdTe Stillinger-Weber[21] and Tersoff[18] types of potentials sufficiently address the defect issues. The CdTe BOP[9] represents a breakthrough since: (a) it is analytically derived from quantum mechanical theories and its quantum accuracy has been widely documented[22-26]; (b) captures properties of a large number of phases; and (c) its ability to predict crystalline growth has been demonstrated[9].

3. Experimental Validation

High-resolution transmission electron microscopy (HRTEM) experiments have been conducted to examine defects in the CdTe/GaAs multilayered films with a lattice mismatch of 12.78%[27]. We performed an MD simulation of CdTe over layer growth using the same lattice mismatch in order to directly compare with HRTEM results. The geometry of the computational cell is shown in Fig. 1(a). The system is periodic in the x- and z-directions containing respectively 100 (10-1) and 8 (101) planes. In order to introduce the lattice mismatch using CdTe BOP, a substrate containing 35 (040) planes in the y- (thickness) direction was first created with the x- dimension compressed by 12.78% to match the lattice constant of GaAs. To prevent the dimension from relaxing back to that of CdTe, the atomic positions of the bottom 35 (040) planes were fixed during constant volume MD simulation of vapor deposition. An adatom incident kinetic energy of 0.1 eV, an incident direction normal to the surface, a substrate temperature of 1000 K, a stoichiometric vapor ratio of Cd/Te = 1, and a deposition rate of around 0.96 nm/ns were used. MD simulations of vapor deposition must be performed at accelerated deposition rates due to a high computational cost. While this may lead to overestimates of kinetically-trapped defects such as vacancies, it conservatively reveals the formation of non-kinetically-trapped defects such as misfit dislocations. The configuration obtained after about 4 ns of deposition is shown in Fig. 1(a) in comparison with the HRTEM experimental image[27] reproduced in Fig. 1(b).

Fig. 1(a) indicates 7 misfit dislocations near the interface. Both dislocation configurations and average dislocation spacing are in remarkably good agreement with the experimental results shown in Fig. 1(b). Detailed analysis of simulated results indicated that the misfit edge dislocations lie in the [101] directions and have a Burgers vector of [10-1]a/2.

In conclusion, we demonstrate that the new BOP-based MD model enables new sciences of CdTe vapor deposition to be revealed with significant improvements over other methods on capturing properties of many structures; and that misfit dislocations in the CdTe/GaAs multilayers are predicted in good agreement with the HRTEM experiments.

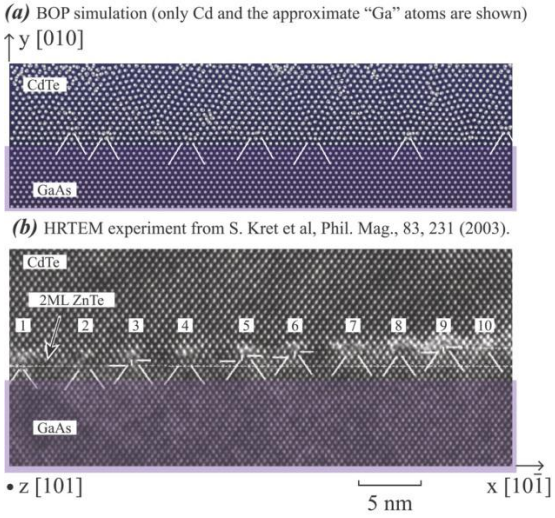

Fig. 1: BOP simulation and HRTEM image[27] of atomic structure of CdTe/GaAs multilayers.

References

[1] K. Zweibel, *Science 328*, 699 (2010).

[2] A. Shah, P. Torres, R. Tscharner, N. Wyrsch, and H. Keppner, *Science 285*, 692 (1999).

[3] K. D. Dobson, I. Visoly-Fisher, G. Hodes, and D. Cahen, "Solar Energy Mater." *Solar Cells 62*, 295 (2000).

[4] V. Babentsov, V. Boiko, G. A. Schepelskii, R. B. James, J. Franc, J. Prochhazka, and P. Hlidek, *Nucl. Instru. Meth. Phys. Res. Sec. A: Accel., Spectro., Detect. Assoc. Equip. 633*, S81 (2011).

[5] A. E. Bolotnikov, G. S. Camarda, G. A. Carini, Y. Cui, K. T. Kohman, L. Li, M. B. Salomon, and R. B. James, *IEEE Trans. Nucl. Sci. 54*, 821 (2007).

[6] E. Saucedo, P. Rudolph, and E. Dieguez, J. *Crystal Growth 310*, 2067 (2008).

[7] D. Zeng, W. Jie, T. Wang, G. Zha, and J. Zhang, Nucl. Instru. .Meth. Phys. Res. A 586, 439 (2008).

[8] T. E. Schlesinger, J. E. Toney, H. Yoon, E. Y. Lee, B. A. Brunett, L. Franks, and R. B. James, *Mater. Sci. Eng. 32*, 103 (2001).

[9] D. K. Ward, X. W. Zhou, B. M. Wong, F. P. Doty, J. A. Zimmerman, and D. G. Pettifor, *Phys. Rev. B* (2011).

[10] C. H. Grein, J. P. Faurie, V. Bousquet, E. Tournie, R. Benedek, and T. de la Rubia, J. *Crystal Growth 178*, 258 (1997).

[11] Y. H. Xie, G. H. Gilmer, C. Roland, P. J. Silverman, S. K. Buratto, J. Y. Cheng, E. A. Fitzgerald, A. R. Kortan, S. Schuppler, M. A. Marcus, et al., *Phys. Rev. Lett. 73*, 3006 (1994).

[12] G. H. Gilmer, H. Huang, and C. Roland, Comp. Mater. Sci. 12, 354 (1998).

[13] B. Strickland and C. Roland, *Phys. Rev. B 51*, 5061 (1995).

[14] H. W. Lu and J. Y. Feng, Modell. Simul. Mater. Sci. Eng. 8, 621 (2000).

[15] F. H. Stillinger and T. A. Weber, *Phys. Rev. B 31*, 5262 (1985).

[16] D. K. Ward, X. W. Zhou, B. M. Wong, F. P. Doty, and J. A. Zimmerman, J. *Chem. Phys. 134*, 244703 (2011).

[17] J. Tersoff, *Phys. Rev. B 39*, 5566 (1989).

[18] J. Oh and C. H. Grein, J. *Crystal Growth 193*, 241(1998).

[19] M. Nakamura, H. Fujioka, K. Ono, M. Takeuchi, T. Mitsui, and M. Oshima, J. *Crystal Growth 209*, 232 (2000).

[20] P. A. Ashu, J. H. Jefferson, A. G. Cullis, W. E. Hagston, and C. R. Whitehouse, J. *Crystal Growth 150*, 176 (1995).

[21] Z. Q. Wang, D. Stroud, and A. J. Markworth, *Phys. Rev. B 40*, 3129 (1989).

[22] D. G. Pettifor, M. W. Finnis, D. Nguyen-Manh, D. A. Murdick, X. W. Zhou, and H. N. G. Wadley, *Mater. Sci. Eng. A 365*, 2 (2004).

[23] D. G. Pettifor and I. I. Oleinik, *Phys. Rev. B 59*, 8487 (1999).

[24] D. G. Pettifor and I. I. Oleinik, *Phys. Rev. Lett*. 84, 4124 (2000).

[25] D. G. Pettifor and I. I. Oleinik, *Phys. Rev. B 65*, 172103 (2002).

[26] R. Drautz, D. A. Murdick, D. Nguyen-Manh, X. W. Zhou, H. N. G. Wadley, and D. G. Pettifor, *Phys. Rev. B 72*, 144105 (2005)

[27] S. Kret, P. Dluzewski, P. Dluzewski, and J.-Y. Laval, *Philo. Mag. 83*, 231 (2003).

A FINITE ELEMENT DAMAGE MODEL FOR COHESIVE FAILURE OF MATRIX IN ASPHALT MIX

M. Hossain [1], R. Tarefder [1]*
[1] Department of Civil Engineering, University of New Mexico, Albuquerque, NM 87131, USA;
* Corresponding author (tarefder@unm.edu)

Keywords: Cohesive damage, Finite element method, Matrix.

ABSTRACT

In this study the cohesive damages of matrix under both dry and wet conditions have investigated using Finite element methods (FEM). The compressive strength and shear strength of matrix are determined in laboratory under both dry and wet conditions. The FEM model consists of an aggregate surrounded by 0.02 " thick matrix. A uniformly distributed load is applied on matrix to simulate the tire pressure. Three different load patterns namely triangle, saw-tooth and rectangle are applied to simulate the traffic speed on the pavement. It has been observed that for triangle and saw-tooth load pattern matrix under dry condition shows more damages than wet condition. The damages initiates at the location where the load are placed and then progressed along the surface of matrix. For higher magnitude of deformation load and under wet conditions the damage progresses along the interface of aggregate and matrix. On the other hand under dry condition the damages progresses along surface of matrix and in between the surface and interface of aggregate and matrix.

Table 1. Mechanical properties of matrix under dry and wet conditions

	Test type	Maximum stress (psi)	Strain at maximum stress (in/in)	Elastic modulus (psi)
Dry	Compression	293	0.0448	27952
	Shear	81	0.0181	21413
Wet	Compression	379	0.0478	18773
	Shear	118	0.0186	20174

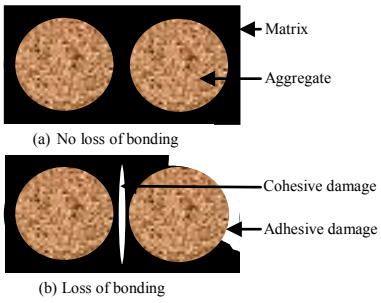

Fig. 1. Schematically adhesive and cohesive damages in aggregate and matrix

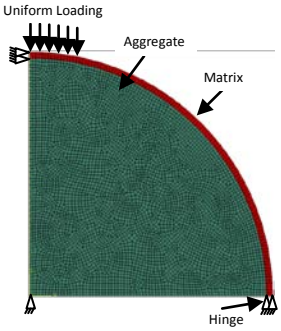

Fig. 2. A generalized FEM diagram of aggregate coated with matrix, boundary conditions and loading situation.

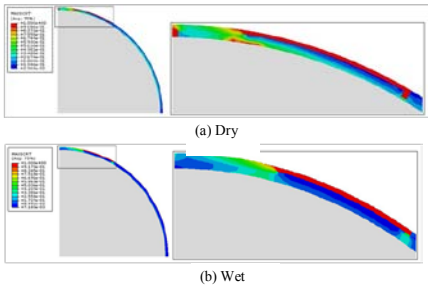

Fig. 3. Damage initiation criteria for rectangular pattern load under dry and wet conditions.

1. Introduction

Asphalt pavements are exposed to traffic and environment shows several types of distresses, damages and failure over time. The damages into the pavements mostly occur into material and interface of materials. Both asphalt and aggregate can be damaged due to traffic and exposed environmental conditions. Also the interface between the aggregate and asphalt can be damaged for the similar reasons. The damages within asphalt materials are called cohesive damage and the damages between the asphalt and aggregate interface are called adhesive damages. Cohesive and adhesive damages are two major reasons of pavement damages and leading to failure. A generalized phenomenon of adhesive and cohesive damage is shown in Fig. 1. In this study a FEM has been developed with aggregate coated by matrix. The matrix is defined as asphalt combined with aggregate greater than #200 sieve size but smaller than #4 sieve size. The damages within matrix have been evaluated using maximum nominal stress criteria.

2. Damage Laws

The elastic behavior is written in terms of an elastic constitutive matrix that relates the nominal stresses to the nominal stains of the material. The elastic behavior can then be written as,

$$t = \begin{Bmatrix} t_n \\ t_s \\ t_t \end{Bmatrix} = \begin{bmatrix} K_{nn} & K_{ns} & K_{nt} \\ K_{ns} & K_{ss} & K_{st} \\ K_{nt} & K_{st} & K_{tt} \end{bmatrix} \begin{Bmatrix} \varepsilon_n \\ \varepsilon_s \\ \varepsilon_t \end{Bmatrix} = K\varepsilon \qquad (1)$$

Damage is assumed to initiate when the maximum nominal stress ratio reaches a value of one. This criterion can be represented as,

$$max\left\{\frac{t_n}{t_n^0}, \frac{t_s}{t_s^0}, \frac{t_t}{t_t^0}\right\} = 1 \quad (2)$$

t_n^0, t_s^0 and t_t^0 are normal and shear strength of matrix. The strength of matrix is given in Table 1.

3. Finite element model development

The finite element model was developed by using ABAQUS/CAE 6.9 -EF1[1]. The model consists of a one quarter of aggregate coated with matrix. A generalized shape of aggregate with coated matrix and the FEM model is shown in Fig. 2. The aggregate is assumed as circular shape with a radius of 0.75". The thickness of the matrix is assumed as 0.02". The elastic modulus of the aggregate is selected as 30,000 psi and the Poisson's ratio is 0.30. The density of aggregate is selected as 0.06 pci. The mechanical properties of the aggregate are common for gravel. The elastic modulus of matrix under dry and wet condition is given in Table 1. The model is developed as an axi-symmetric since the loading and the shape of the model is symmetric to the vertical axis. The restraining condition on the left side of the model is axi-symmetric. The bottom side of the model is hinged supported. Four nodded d linear quadrilateral cohesive elements are used to characterize matrix. Three and four nodded linear quadrilateral plane stress elements are used to model aggregate. Maximum stress criteria require maximum stress in vertical and shear directions. Since the model is two dimensional, only the one shear direction data is required.

Real pavement experiences cyclic pressure load which comes from traffic. For this reason the FEM is simulated with three different pattern loads. The loading cycle resembles one passes of wheel over the pavement. Several studies were done with cyclic loading on asphalt concrete pavements (Saad et al. 2005[2]).

A uniformly distributed load (UDL) is used instead of single point load. The total length of the UDL is considered as 0.8". A deformation magnitude of 0.0285" and 0.057" are used to simulate tire pressure on pavements.

4. Results and discussions

It has been observed that damage initiates away from the support and at the end of loading zone. The progression of damage under both dry and wet conditions for 0.0285" deformation loading are shown in Fig. 3. It has been seen that under both dry and wet conditions the damage initiates at surface of matrix and progress to the surface of matrix. Also under dry condition and for 0.057" load magnitude the damage progresses in between the surface and interface locations. On the other hand under wet condition with 0.057" magnitude load the damage progresses at surface of matrix and the interface of matrix and aggregate.

5. References

[1] ABAQUS/CAE User's manual, Dassault Systems, Version 6.9-EF1, 2009.

[2] B. Saad, H. Mitri, and H. Poorooshasb "Three-dimensional dynamic analysis of flexible conventional pavement foundation." *Jnl. of Trans. Engg*, ASCE. Vol. 131, No. 6, pp. 460-469, 2005.

APPLICATION OF SYSTEM DYNAMICS TO SELECT THE MOST OPTIMUM AIRPORT PAVEMENT MAINTENANCE

M. Rahman[1]*, R. Tarefder[2]
[1] Department of Civil Engineering, Graduate Research Assistant, Albuquerque, NM 87131, USA;
[1] Department of Civil Engineering, Associate Professor, Albuquerque, NM 87131, USA;
* Corresponding author (mrahman@unm.edu)

Keywords: *pavement maintenance, pavement condition index, pavement life cycle cost, benefit cost analysis, system dynamic modeling*

ABSTRACT

New Mexico has about 50 general aviation airports with pavement condition varying from serious to good. The current need is to determine the most optimum pavement maintenance strategy for four New Mexico airports. In this study, the results of a number of crack treatments (crack sealing, patching) as well as surface treatments (slurry seal, overlay) are compared in terms of Pavement Condition Index (PCI) improvement, life cycle treatment cost, emission cost and accident cost. Three different modules have been developed using system dynamic software named Powersim. PCI module is capable of determining PCI of future years after application of different maintenance treatments. Benefit module can show the functional benefit due to maintenance work in monetary term which uses the average PCI after maintenance from PCI module and budget required to maintain a certain PCI throughout the design period from MicroPAVER analysis. LCC module is capable of performing life cycle cost analysis and helps to determine the life cycle treatment cost. Emission cost and accident cost due to various maintenance treatments are determined using resulting International Roughness Index in MEPDG and PaLATE (Pavement Life Cycle Assessment Tool for Environmental and Economic Effects) respectively. The analysis shows that slurry seal has the most benefit to cost ratio among all maintenance treatments and PCI at the time of first application of a maintenance work plays an important role in benefit to cost ratio.

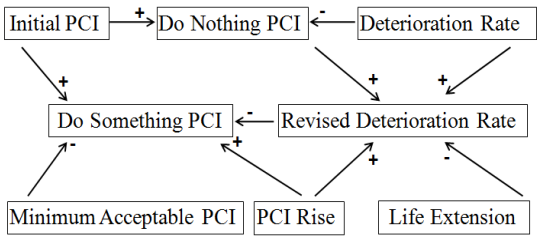

Fig.1. PCI causal loop diagram.

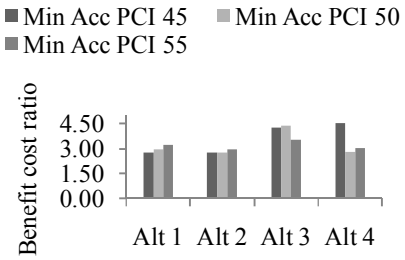

Fig.2. Benefit cost ratio of different alternatives for Fort Sumner airport.

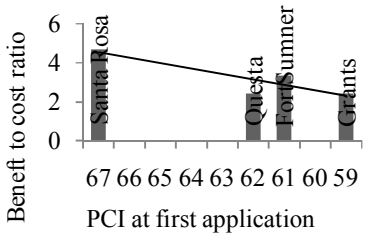

Fig.3. Average benefit cost ratio at airports of different pavement condition.

1 Study approach

A system dynamic model has been developed using Powersim to estimate the average PCI of different maintenance practices over the analysis period of 20 years. The do nothing PCI trend and the predicted rate of deterioration are determined using MicroPAVER. If a certain PCI is maintained throughout the analysis period of 20 years by applying different types of preventive and major repair in every year of the design life, then the money required to maintain that fixed PCI is estimated using the same tool. In estimating functional benefit it has been assumed that, if a maintenance work in system dynamic model shows a average PCI equal to the PCI maintained by MicroPAVER throughout the life, then it will also give functional benefit equal to the money estimated by MicroPAVER to maintain that certain PCI in 20 years design period. As minimum acceptable PCI, 45, 50 and 55 are used for every alternative in the system dynamic model. Traditionally, the relative difference in benefit due to a rehabilitation is determined by comparing the area under the treatment curve and area under the do nothing curve [1]. Data regarding the life extension of the pavement due to various treatments and their unit costs have been obtained from Airport Cooperative Research Program Synthesis 22: Common Airport Pavement Maintenance Practices [2]. The causal loop diagram of PCI module is shown in Fig 1. Life cycle cost analysis of different alternatives is performed using another system dynamic model. To estimate the environmental damage cost, life cycle gas emission due to different maintenance is calculated using software named PaLATE. It is developed by University of California, Berkley; and capable of calculating air pollution due to application of various alternatives [3]. Using the volume of the asphalt material needed for different treatments, the vehicular emissions due to transportation and the air pollution due to asphalt production and application processes are obtained. Monetary value or disbenefit of a treatment is used from AEA Technology [4]. Accident costs are calculated using the resulting IRI for different alternatives using MEPDG tool [5]. The most optimum maintenance treatment is determined by benefit to cost methodology.

2 Results of the analysis

Benefit cost analysis has been performed using equation 1 to obtain the most optimum maintenance treatment:

$$Cost\ Benefit\ Ratio = \frac{Functional\ Benefit}{Life\ Cycle\ Treatment\ Cost + Emission\ Cost + Accident\ Cost} \quad (1)$$

Fig.1 shows benefit cost ratio for various maintenance treatments applied at Fort Sumner airport when maintaining different minimum acceptable PCI. Alternative 3 (slurry seal) has given the maximum B/C ratio among all alternatives. Only for minimum acceptable PCI 45, thin overlay (Alternative 4) has shown better B/C ratio than slurry seal (Alternative 3). Other airports have shown similar results. If only the crack treatment is considered, then crack sealing has given better result than patching for all airports except Santa Rosa. For Santa Rosa, patching has more B/C ratio than crack sealing, and hence is more effective crack treatment in that airport. Treatments are only applied in the current year and the year when PCI goes below minimum acceptable limit and this is why it is very important to assign the minimum acceptable PCI in life cycle cost analysis for the current study. For Fort Sumner, if minimum acceptable PCI value is taken as 45, then Alternative 4 (thin overlay) shows the best result. But if 50 is taken as the minimum acceptable PCI, then Alternative 3 (slurry seal) shows the highest B/C ratio.

B/C ratio also depends on the condition of the pavement at the time of first maintenance application. The average B/C ratio of all alternatives considering all three minimum acceptable PCI at different pavement condition is shown in Fig.2. Among the four airports, Santa Rosa has the highest current PCI value of 67 and therefore has shown the highest average benefit to cost ratio. Grants has the lowest current PCI and the lowest B/C ratio as well. Fig.2 represents that, it is better to apply a preventive work when the pavement will be in relatively good condition.

3 Conclusions

- Among the four alternatives, slurry seal has the maximum benefit to cost ratio, hence it is the most optimum pavement maintenance strategy for this current study.
- Minimum acceptable PCI selection plays an important role in determining a cost effective treatment as well as aiming target level of service.
- It is more effective to apply a preventive maintenance work in an airfield before it goes close to the lower limit of critical PCI value.

References

[1] R. Hass, W. Hudson and J. Zaniewski "*Modern pavement management*". 1st edition, Krieger publication company Florida, 1994.

[2] J. Hajek, J. Hall and D. Hein "Common airport pavement maintenance practice". *Airport cooperative research program*, Synthesis 22, 2011.

[3] S. Chan, B. Lanen and T. Kazimierowski "Pavement preservation-A solution for sustainability". *Transportation Research Record*, No. 2235, pp 36-42, 2011.

[4] AEA Technology "Damages per tonne emission of PM2.5, NH3, SO2, NOx and VOCs from each EU25 member state". *Clean Air for Europe Programme*, European Commission, 2005. < http://bca.transportationeconomics.org/benefits/emissions >

[5] A. Ihs "The influence of road surface condition on traffic safety and ride comfort". *6th International Conference on Managing Pavement*, 2004.

COMPARISON OF TWO MAINTENANCE STRATEGIES OF AIRFIELDS USING LCCA

M. Ahmed[1]*, R. Tarefder[2]
[1] Civil Engineering, Graduate Research Assistant, UNM, New Mexico, NM 87106, USA;
[2] Civil Engineering, Associate Professor, UNM, New Mexico, NM 87106, USA;
* M. Ahmed (mahmed@unm.edu)

Keywords*: LCCA, ELMOD, FAARFIELD, Airfield Maintenance*

ABSTRACT

Airfields of different airports all over New Mexico have been evaluated since 2008 to determine functional and structural condition. Based on this condition evaluation, maintenance strategies have been developed using two software, namely ELMOD and FAARFIELD. In this study, each maintenance strategy has included maintenance alternatives to maintain the airfields of Cavern City Air Terminal over 35 years. Goal of this study is to determine the most economical maintenance strategy that can ensure better functional and structural condition. Life Cycle Cost Analysis (LCCA) has been performed to estimate the total cost required to implement these maintenance strategies over 5, 10 and 35 years. Estimated costs for both ELMOD and FAARFIELD based maintenance strategies have been compared. It has been observed that ELMOD based maintenance is better economical than FAARFIELD based maintenance.

Table 1: Maintenance stream diagram from ELMOD analysis

Cavern City Air Terminal

	RW 14L-32R		RW 8-26		RW 14R-32L		RW 3-21	
	Alt. 1	Alt. 2	Alt. 1	Alt. 2	Alt. 1	Alt. 2	Alt. 1	Alt. 2
0	Overlay	Overlay	Overlay	Overlay				
3		Fog				Fog		Fog
4			Fog					
5	Fog			Fog				
6					Slurry		Slurry	
8			Overlay			Fog		Fog
9		Fog						
10	Overlay			Overlay				
12		Overlay	Fog		Slurry	Fog	Slurry	Fog
15	Fog	Fog		Fog	Overlay	Overlay	Overlay	Overlay
16			Overlay					
18					Slurry		Slurry	
19						Fog		Fog
20	Overlay		Fog	Overlay				
21		Fog						
23						Fog		Fog
24		Overlay	Overlay		Slurry		Slurry	
25	Fog			Fog				
27		Fog				Fog		Fog
28			Fog					
30	Overlay			Overlay	Overlay	Overlay	Overlay	Overlay
32			Overlay					
33		Fog						
34						Fog		Fog
35	Fog			Fog	Slurry		Slurry	

Table 2: Maintenance stream diagram from FAARFIELD analysis

Year	Cavern City Air Terminal							
	RW 14L-32R		RW 8-26		RW 14R-32L		RW 3-21	
	Alt. 1	Alt. 2	Alt. 1	Alt. 2	Alt. 1	Alt. 2	Alt. 1	Alt. 2
0	Overlay	Overlay			Overlay	Overlay		
4		Fog	Fog	Slurry		Fog	Fog	Fog
5	Slurry				Slurry			
8		Overlay				Overlay		
9			Overlay	Overlay			Overlay	Overlay
10	Overlay				Overlay			
12		Fog				Fog		
13			Fog				Fog	
14				Slurry				Fog
15	Slurry				Slurry			
16		Overlay				Overlay		
17			Overlay				Overlay	
18								
19				Overlay				Overlay
20	Overlay	Fog			Overlay	Fog		
21			Fog				Fog	
24		Overlay		Slurry		Overlay		Fog
25	Slurry		Overlay		Slurry		Overlay	
28		Fog				Fog		
29			Fog	Overlay			Fog	Overlay
30	Overlay				Overlay			
32		Overlay				Overlay		
33			Overlay	Slurry			Overlay	Fog
35	Slurry				Slurry			

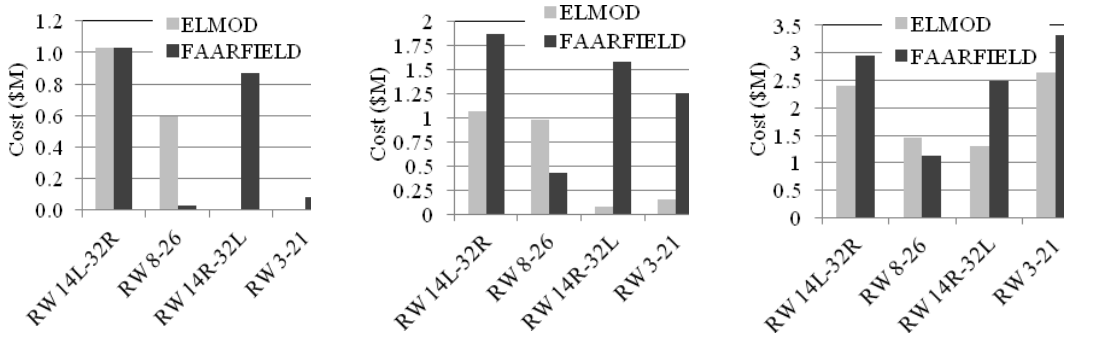

(a) 5 year maintenance (b) 10 year maintenance (c) 35 year maintenance

Figure 1: Cost comparisons between ELMOD and FAARFIELD based maintenance

1 Introduction

An airfield pavement evaluation program has been carried out since 2008 by Aviation Division of NMDOT [1]. Based on the condition during pavement condition evaluation and future deterioration, need for rehabilitation and maintenance has to be determined. To ensure the best suited application method and better economical investment, competing options or strategies need to be compared to each other.

Main objective of this study is to compare two different methodologies to determine maintenance cost. First methodology has been developed based on ELMOD analysis and the

second one is developed based on FAARFIED analysis. Both of these methodologies generate maintenance strategies for the maintenance program for 35 years. Finally, LCCA has been performed to estimate maintenance costs. Maintenance strategies have been developed to maintain the runways of Cavern City Air Terminal, Carlsbad, New Mexico. Runways in this airport are: RW 32L-14R, RW 8-26, RW 14R-32L and RW 3-21.

2 Development of Maintenance Strategies

Maintenance program has been developed with different maintenance strategies. Each strategy comprises different maintenance alternatives. These treatments have been scheduled at different time to serve the specific purpose, i.e. functional or structural requirement [2]. Time for this maintenance has been determined based on the pavement remaining life, overlay thickness requirement, and functional parameter deterioration.

Both ELMOD and FAARFIELD perform the analysis to determine required overlay thickness and remaining life. Table 1 shows the stream diagram of maintenance alternatives for ELMOD analysis. In addition, Table 2 shows the stream diagram of maintenance alternatives as developed based on FAARFIELD calculation. For each of the runway maintenance program analysis, two different strategies have been developed. These strategies are not identical due to the difference in analysis from two mentioned software.

3 Cost Comparison of Maintenance Strategies

Maintenance treatments that have been considered to apply for pavement maintenance program are: overlay, i.e., milling and filling, fog seal and slurry seal. LCCA has been performed on four different runways of Cavern City Air Terminal based on the unit price of material. Maintenance costs for ELMOD and FAARFIELD analysis over 5, 10, and 35 years, respectively, have been shown in Figure 1(a) through (c). It has been observed that ELMOD based maintenance is more expensive than FAARFIELD based maintenance in RW 8-26 (5-year maintenance cost). It continues for both 10 and 35 year maintenance. However, ELMOD is the most economical in all other cases.

4 Conclusion

The above cost analyses show that maintenance cost resulting from ELMOD analysis is less expensive than that from FAARFIELD. In some maintenance alternatives, it has been observed that cost resulting either from ELMOD or FAARFILED is negligible. This is due to the absence of maintenance treatment at that particular time. In overall, ELMOD based maintenance methodology is the most cost saving for the airfields.

References

[1] M. Ahmed, R. Bisht and R. Tarefder "Analysis of FWD data and Characterization of Airfield Pavements in New Mexico". *Proceedings of the 8th International Conference on the Bearing Capacity of Roads, Railways and Airfields*, Champaign, Illinois, Vol. 1, pp 669-678, 2009.

[2] R. Haas, W. Hudson and J. Zaniewski "*Modern Pavement Management*". 1st edition, Krieger Publishing Company, 1994.

OPTIMAL SITING OF WIND TURBINES USING VIRAL SYSTEMS ALGORITHM

Carlos Ituarte-Villarreal, Claudia S. Valles and Jose F. Espiritu
Department of Industrial, Manufacturing & Systems Engineering, The University of Texas at El Paso. 500 W. University Avenue, El Paso, TX 79968, USA;

Keywords: *Wind-farm, Viral Systems, Reliability, Metaheuristics*

ABSTRACT

In this paper, a viral systems optimization algorithm is developed to optimize wind turbine layout in a wind farm. The main objective of this research is to find the best layout configuration of wind turbines in a fixed area which minimizes the cost per unit produced. The optimization problem is formulated as the minimization of energy cost per unit produced which is form by the estimated total cost and total power produced. The viral system algorithm developed in this paper is used to solve a specific problem which takes into consideration three wind speeds and thirty-six wind directions, furthermore in the present paper, different types of wind turbines with different reliabilities, efficiencies and costs are considered. As a solution to this problem the layout of a wind-farm in which the electricity is produced at the minimum cost is obtained.

1 Introduction

Electricity is a basic need in our society; without it lighting, communications, telephone, radio, would not exist and people would have to renounce to devices that are an integral part of their homes. Among the different ways of producing electricity, wind turbines utilize the movement of an air mass moving the blades of the turbine and thereby generating electric power. During the production of electricity the wind leaving the wind turbine loses an amount of energy which is converted into kinetic energy in the turbine rotor, so that the wind has passed through the apparatus is reduced in speed, this turbulent wind is known as wake. The wake normally has an impact on downstream turbines, reducing wind speed and therefore also reducing the energy produced by them. This paper aims to find the layout that maximizes energy production within a wind farm while the total cost is minimized. To find configuration a viral systems algorithm is used.

2 Model Description

The models used in this research to evaluate wake effect are very similar to the one developed by Jensen in 1983 [1]. Jensen's model is based on the conservation of momentum inside the wake and on the assumption that the wake increase will be linear. The cost and objective functions are comparable to the one presented in Mosetti et al. [2] and Grady et al. [3]. In this study a wind farm of 2km by 2km which was partitioned into 100 possible turbine locations.

Based on the statement of momentum balance and Betz theory, the wind speed behind the turbine rotor can be calculated by equation (1):

$$\frac{\quad}{\quad} \tag{1}$$

where U_0 is the initial wind speed, a represents the axial induction factor, x is defined as the distance downstream and r_1 is the downstream wake radius. Entrainment constant α is empirically calculated by equation (2), where z is the height of the wind turbine rotor and z_0 the surface roughness, readers can refer to [1] for details.

$$\frac{\quad}{\quad}, \tag{2}$$

3 Objective Function

The investment cost considers only the number of turbines purchased; this cost relation was presented first by Mosetti et al. [2], and assumes a non-dimensional cost per year of a single turbine and it depends on the supplier of this turbine also a maximum cost reduction of 1/3 for each additional wind turbine purchased. Equation (3) describes the total cost per year for a wind farm:

$$- \quad - \qquad , \tag{3}$$

where N represents the total number of turbines purchased. The total power production is calculated base on the wind speeds of each turbine U_i and is given by equation (4):

$$. \tag{4}$$

As stated before, the objective function considered by this research is formed by the cost of producing the energy and total power produced. This objective function is given by the equation (5):

$$\frac{\quad}{\quad}, \tag{5}$$

4 Optimization method

Virals systems algorithm mimics how bacteriophage viruses reproduce. Cortés et al.[4] developed the use of a viral system algorithm to solve combinatorial problems by using a selective method on how the virus seeks out the weakest cells and attempts to infect them. Like real viruses, this methodology seeks the optimum solution by seeking the best solutions in a group, which correspond to weakest cells. In addition, cells may defend themselves from attack with antibodies. Readers can refer to [4] for details.

5 Numerical Example

The wind speeds for this numerical example are based on probabilistic data and are showed in Figure 1. Therefore, it is necessary to note this when replicating results. All turbines considered have a rotor diameter of 40 m, ground roughness of 0.3, trust coefficient of 0.88 and a height of 60m. Three wind speeds are considered for this numerical example case, 8, 12 and 17 m/s.

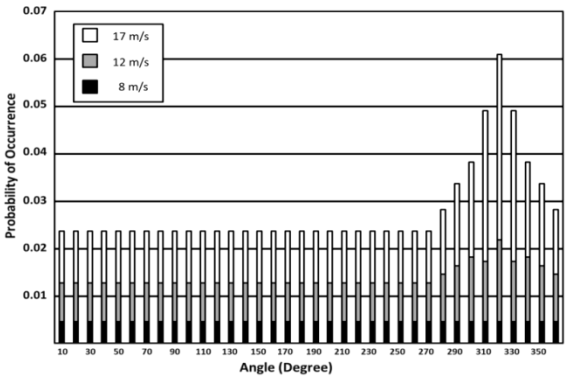

Fig.1. Wind speeds and directions.

After running the program, the best layout found by the viral systems algorithm is show in figure 2, with a total cost of 21.05, 28 turbines placed and a cost per unit of power produced of 0.0008872.

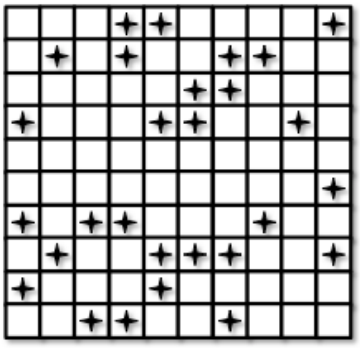

Fig.2. Optimal configuration

References

[1] N. O. Jensen, " A note on Wind Generator Interaction". Risø National Laboratory, Roskilde, Denmark. Risø-M-2411, 1983

[2] G. Mosetti,, C. Poloni, and B. Diviacco. "Optimization of wind turbine positioning in large windfarms by means of a genetic algorithm". *Journal of Wind Engineering and Industrial Aerodynamics*, Issue 51, pp 105-116, 1994

[3] S. A. Grady, M. Y. Hussain. and M. M. Abdullah, (2005). "Placement of wind turbines using genetic algorithms". *Renewable Energy*, Issue pp 30, 259, 2005

[4] P. Cortés, J. García, J. Muñuzuri, and L. Onieva, "Viral systems: A new bio-inspired optimization approach ", *Computers and Operations Research*, 35, 9, pp2840-2860, 2008.

USING GENETIC ALGORITHMS TO SOLVE COMPONENT REPLACEMENT PROBLEMS IN POWER INDUSTRY

Anuar Aguirre and Jose F. Espiritu
Industrial, Manufacturing and Systems Engineering
El Paso, TX 79968-0521, USA

Keywords Power Industry; Component Replacement; Genetic Algorithms; Cost analysis

ABSTRACT

A new component replacement analysis method to solve component replacement problems for complex electricity distribution systems using Genetic Algorithms is developed. There are two different types of potential decisions to be made at the beginning of each planning period, either to keep the component in the system for one more planning period or to replace it with a new component. The main objective is to obtain an optimal replacement schedule over a finite time horizon subject to annual budget constraints, with the objective of minimizing the total Net Present Value of unmet demand, maintenance and purchase costs. The Method is applied to a radial system configuration; extensions to apply the model to complex configurations will be presented.

1. Introduction

The distribution system is the part of the electric power system, which has most of the impact on the level of reliability experienced by the costumer [1]. The distribution system connects the electric power to the customers that require it (houses or industry) at voltages below than in the transmission or sub-transmission systems. The transmission system sends the electric power directly to the distribution substation and then it converts the electricity to a lower voltage in order to be used on a primary distribution feeder. Most of the distribution systems are operated in radial networks, but sometimes the configuration is changed during operation [2]. Radial networks have some advantages over other network configurations. For example radial networks have lower short circuit currents and simpler switching and protecting equipment. Most of the equipment is approaching to be 50 years old [3]. That means that the infrastructure is becoming very old and then the cost to operate and maintain are increasing and more important the infrastructure is less reliable. The components became old the electricity outages increase leading to increased operating costs [4]. Hence there is a need to develop methods, which would address this problem of the aging infrastructure and thus help us develop a reliable electricity transmission and distribution networks.

2. Genetic Algorithms

Genetic algorithms (GA's) are inspired in the natural selection process of individuals and the evolution of species. GA's use the reproduction mechanisms and the genetic transmission characteristics. GA's start with a population of random individuals, called chromosomes, which are revised over successive generations. The crossover and mutation operators are used to introduce new prospective design solutions at each

generation. During each successive generation, each individual is evaluated according to a fitness function. Individuals with high-fitness values rank at the top, while individuals with low-fitness function values are ranked lower and they are likely to disappear from the population. The algorithm continues for a pre-determined maximum number of generations or until no additional improvement is observed..Figure 1 shows a flowchart with the main GA steps.

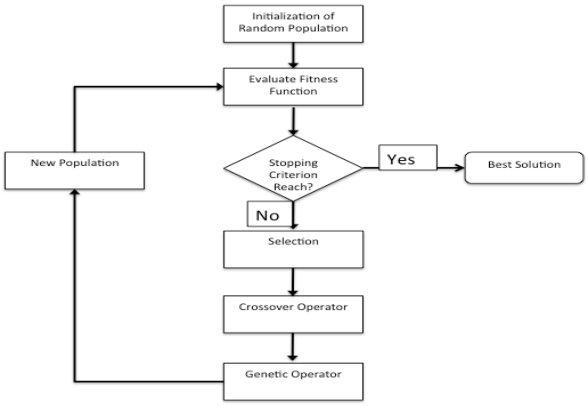

Fig.1. Genetic Algorithm Flow chart

3. Component aging and system unavailability

To evaluate the current age of the component in the power grid I will be using N.H.P.P (Non-Homogeneous Poisson Process), where events occur randomly over time at an average rate of λ events per unit time.

The failure intensity function for each component *l* in the system is given by,

(1)

(2)

The expected number of failures by age τ on any one-year time interval of the component is calculated by:

(3)

The maintenance cost of the component is calculated by using the following equation:

(4)

The unavailability cost of the component is calculated by using the following equation:

(5)

The objective function with an N number of components and planning horizon K is formulated as following:

Subject To, Budget Constraints.

4. Example

The main objective is to find the best replacement schedule for the components of the radial configuration network. In the present example, the components considered are shown in Table 1.

Component	Initial Age	Outages/year		Hours/Outage	$/Outage	$
1) Line 13.8kV	20	1.9560	1.25	1.32	1500	45,000
2) Breaker 13k	10	0.0036	1.60	83.12	1000	35,000
3) Line 600 ft	40	0.0055	1.80	26.51	1900	33,300
4) Switch	35	0.0061	1.85	5.60	700	10,000

Table 1. Component Data

The algorithm is run for 50 generations and the lowest total cost obtained at the end of 50th generation is $307,070.

5. Conclusions

The electric energy is basic for our daily normal life. Most of the electric power components are becoming old and they need to be replaced or maintained in an optimal way, because a failure in the system can cause a blackout. Most of the actual problems in the energy supply occur in the distribution part of the power grid. One most simple configuration for the distribution network is the radial configuration, Even though a radial configuration is a simple and cheap way to provide electricity, it has a very low reliability. For that reason a method for determining the replacement schedules for components in the power distribution systems subject to annual budget constraints was developed and presented in this paper. The component replacement schedules was obtained and the total cost lies well within the allocated budget amount. The best solution has a cost of $307,070.

References

[1] R. Billinton and W. Li (1994). "*Reliability Assessment of Electric Power Systems using Monte Carlo methods*". Plenum press, New York, 1994.

[2] M.E. Baran,. F.F. Wu, (1989). "Network reconfiguration in distribution systems for loss reduction and load balancing". *IEEE Transactions on Power Delivery.* Vol.4, Issue 2, pp 1401-1407.

[3] R.E. Brown and H.L. Willis (2006). "The economics od aging components". *IEEE Power and Energy Magazine.* Volume 4, Issue 3, pp 36-43.

[4] Espiritu J. F., and Coit D. W. (2007). "A Component Replacement Model for Electricity Distribution Systems". *International Journal of Performability Engineering.*

SHORT-TERM PREDICTION OF WIND FARM POWER OUTPUT USING A HYBRID INTELLIGENT ALGORITHM BASED ON METEOROLOGICAL INFORMATION

A. Haque[1], P. Mandal[2]*, and B. Tseng[2]
[1]Department of Electrical and Computer Engineering
University of New Brunswick, Fredericton, NB, E3B 5A3, Canada
[2]Department of Industrial, Manufacturing and Systems Engineering
University of Texas at El Paso, El Paso, TX 79968, USA
* Corresponding author (pmandal@utep.edu)

ABSTRACT

A hybrid intelligent algorithm based on the wavelet transform (WT) and fuzzy ARTMAP (FA) network is proposed in this paper for predicting the power output of a wind farm utilizing meteorological information such as wind speed, wind direction, and temperature. The test results show a significant improvement in forecasting error through the application of a proposed hybrid WT+FA model over a benchmark persistence method, other soft computing models (SCMs) and hybrid models as well. The proposed hybrid wind power forecasting strategy is applied to real life data from Kent Hill wind farm located in New Brunswick, Canada.

1 Introduction

It is well known that wind power produced by wind turbines is intermittent in nature and this unpredictability poses a fundamental problem for power system operators. Accurate wind power forecasting is beneficial for wind plant operators, utility operators as well as utility customers. For meeting up the customers' demand, wind power forecasting facilitates scheduling the connectivity of wind turbines or conventional generators, thus improve the reliability of wind generated electricity [1], [2].

Several methods are reported in literature for short-term wind power forecasting such as the persistence method, physical modeling approach, statistical models, and soft computing models (SCMs). The persistence method, also known as a 'Naive Predictor', is used as a benchmark for comparing other tools for short-term wind forecasting. This method simply uses the past hour wind power value as the forecast for the next hour. Any developed forecast method is first tested against the persistence method in order to baseline its performance [3], [4]. Forecasting tools based on soft computing methods are gaining significant attention. Soft computing is an emerging field that consists of neural networks (NNs), fuzzy logic, evolutionary computation, machine learning, and probabilistic reasoning. The advantage of the SCM is that it has ability to handle non-linearity more effectively and to extract patterns and detect trends that are too complex to be noticed by either humans or other computer techniques. Among SCMs, NNs have been widely used in forecasting purposes. Different types of NNs are backpropagation NN (BPNN), probabilistic NN, radial basis function NN (RBFNN), self-organizing feature maps (SOFM), cascade correlation NN, extended Kalman

filter (EKF)-based NN, adaptive resonance theory NN, fuzzy ARTMAP (FA), support vector machines (SVMs).

This paper proposes a novel hybrid intelligent algorithm for predicting wind farm power output. The innovative aspect of this paper lies on developing an accurate, efficient, and robust wind power forecast model using a hybrid approach based on wavelet transform (WT) and a SCM based on FA, i.e., WT+FA, which considers the interaction of wind power with wind speed, wind direction, and temperature in the forecast process.

2 Proposed Hybrid Method for Wind Power Forecasting

Fig. 1 shows the schematic diagram of the proposed hybrid method for hour-ahead wind power forecasting based on the FA network combined with the WT. The forecasting procedure is explained as follows:

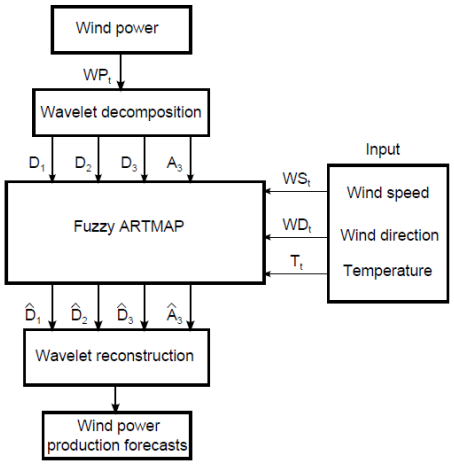

Fig. 1. Schematic diagram of the proposed hybrid WT+FA model for wind power forecasting.

Step-1: Hourly input data of wind power (WP), wind speed (WS), wind direction (WD), and temperature (T) are first decomposed using WT.
Step-2: The individual decomposed wind power signals (A3, D1, D2, and D3) along with WS, WD, and T data are then fed into FA network.
Step-3: The output components of the FA network are the individual forecast of decomposed approximation ($\hat{A}3$) and detail signals ($\hat{D}1$, $\hat{D}2$, and $\hat{D}3$), which follow the process of wavelet reconstruction as shown in Fig. 1 in order to produce the final wind power forecasts.

3 Numerical Results and Discussions

To evaluate the effectiveness and forecasting performance of the proposed WT+FA model, the results are compared with other SCMs such as BPNN, RBFNN, ANFIS and FA, and also with the combination of wavelet and these SCMs. The principal statistics used to evaluate the performance of the proposed model is mainly measured by using mean absolute percentage error (MAPE) defined as:

$$MAPE = \frac{1}{N}\sum_{t=1}^{N}\frac{|WP_t^{true} - WP_t^{forecast}|}{\overline{WP_t}^{true,N}} \times 100\%. \quad (1)$$

where N=24 for daily wind power forecasts, N=168 for the weekly wind power forecasts, WP_t^{true} is the actual wind power in hour *t*, $WP_t^{forecast}$ is the predicted wind power for that hour.

TABLE I

MAPE COMPARISON FOR DAILY WIND POWER FORECASTS

Model	Season				Average
	Winter	Spring	Summer	Fall	
Persistence	30.48	26.37	36.79	21.74	28.85
BPNN	27.64	19.64	24.55	18.21	22.51
RBFNN	26.39	18.14	27.78	23.05	23.84
ANFIS	31.08	19.27	22.71	22.31	23.84
FA	19.11	14.46	19.16	13.52	16.56
WT+BPNN	23.51	15.97	22.44	17.80	19.93
WT+RBFNN	22.43	15.30	23.97	19.39	20.27
WT+ANFIS	22.34	14.65	19.64	18.55	18.80
WT+FA	**12.84**	**11.75**	**16.11**	**10.22**	**12.73**

TABLE II

MAPE COMPARISON FOR WEEKLY WIND POWER FORECASTS

Model	Season				Average
	Winter	Spring	Summer	Fall	
Persistence	26.52	24.92	23.24	15.84	22.63
BPNN	28.17	22.34	27.92	19.47	24.48
RBFNN	25.77	23.19	25.66	18.24	23.22
ANFIS	24.39	20.28	21.72	16.32	20.68
FA	18.46	18.66	19.31	13.25	17.42
WT+BPNN	25.00	20.45	22.33	16.38	21.04
WT+RBFNN	23.81	21.43	21.52	15.20	20.49
WT+ANFIS	20.63	18.26	19.26	12.25	17.60
WT+FA	**14.89**	**17.37**	**18.05**	**12.93**	**15.81**

The daily and weekly MAPEs demonstrate the superior predicting performance of the proposed hybrid WT+FA model over the persistence method, individual SCMs, and WT+SCMs. Forecasting short-term wind power with a higher rate of accuracy is extremely important for the power system operators as they face challenges associated with fluctuating wind power production with the increasing installed wind power capacity. Based on the presented simulation results, the proposed forecasting framework demonstrates a significant improvement over other tested alternatives.

4 Conclusions

The presented work contributed to alleviate an important problem of wind power production forecasting as the test results obtained through the simulation demonstrate that the proposed hybrid intelligent algorithm is significantly accurate, efficient, robust and performs well in multiple seasons. The future work would be interesting to carry out uncertainty associated with wind power forecasting.

References

[1] M. Negnevitsky, P. Johnson, and S. Santoso, “Short term wind power forecasting using hybrid intelligent systems,” in Power Engineering Society General Meeting, 2007. IEEE, June 2007, pp. 1–4.

[2] A. Kusiak, H. Zheng, and Z. Song, “Short-term prediction of wind farm power: A data mining approach,” Energy Conversion, IEEE Transactions on, vol. 24, no. 1, pp. 125–136, March 2009.

[3] S. Soman, H. Zareipour, O. Malik, and P. Mandal, “A review of wind power and wind speed forecasting methods with different time horizons,” in North American Power Symposium (NAPS), Sept. 2010, pp. 1–8.

[4] J. Catalao, H. Pousinho, and V. Mendes, “Hybrid wavelet-PSO-ANFIS approach for short-term wind power forecasting in Portugal,” IEEE Transactions on Sustainable Energy, vol. 2, no. 1, pp. 50–59, Jan. 2011.

WIND SPEED PREDICTION USING A COMBINED INTELLIGENT APPROACH

A. Haque[1], P. Mandal[2]*, and B. Tseng[2]
[1] Department of Electrical and Computer Engineering
University of New Brunswick, NB E3B 5A3, Canada
[2] Department of Industrial, Manufacturing, and Systems Engineering
University of Texas at El Paso, TX 79968, USA
*Corresponding author (pmandal@utep.edu)

ABSTRACT

This paper presents a short-term wind speed prediction techniques based on combination of adaptive neuro-fuzzy inference system (ANFIS) and similar days (SD) method, which considers similar historical weather information corresponding to the forecasting day in order to evaluate similar wind speed days. The prediction capability of the proposed hybrid SD+ANFIS model is demonstrated by an comparison with a benchmark persistence method, other soft computing models (SCMs) and hybrid models as well. The test results demonstrate that the proposed SD+ANFIS model provides a considerable improvement of the forecasting accuracy compared to other models especially it shows an improvement in the forecasting error of an individual ANFIS model by up to 48% through the application of the SD method.

1 Introduction

Wind represents a clean and sustainable source of energy and is in abundant supply. However, the increase in wind power penetration requires a number of issues to be addressed including wind forecasting and power output, market integration, power system stability and reliability, etc.[1]. Accurate wind speed forecasting is beneficial for wind plant operators, utility operators as well as utility customers. Several methods are reported in literature for short-term wind speed forecasting, which are found in [2],[3].

This paper describes short-term wind speed forecasting approaches by considering various SCMs individually, and the combined approach of a SCM and similar days (SD) method. The SCMs considered in this paper are backpropagation neural network (BPNN), radial basis function neural network (RBFNN), and ANFIS, and the combined approaches are termed as SD+BPNN, SD+RBFNN, and SD+ANFIS. It is emphasized that though the performance of seven different forecasting models are explored in the paper, this paper introduces SD+ANFIS as the main proposed short-term wind speed forecasting model.

2 Description of Similar Days and ANFIS

2.1 Similar Days Method for Wind Speed Forecasting

The basic principle of the SD method is to match historical with similar properties to that of the forecast day [4]. Fig. 1 shows the flowchart of forecast process based on SD. In the context of wind speed similarity, minimum-distance Euclidean criterion (||EN||) is adopted in this paper in order to evaluate the similar wind speed days corresponding to the forecast day [4], where wind speed, wind direction are taken into consideration during the SD selection process.

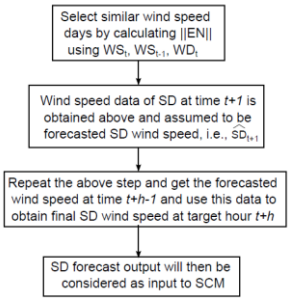

Fig.1. Forecasting process based on SD method.

2.2 Adaptive Neuro-Fuzzy Inference System

ANFIS is a class of adaptive multilayer feedforward networks, which are applied to nonlinear forecasting models. ANFIS incorporates the self-learning ability of neural network with the linguistic expression function of fuzzy inference[5]. The five-layered ANFIS model is as shown in Fig. 2. Note that the SD method is combined with ANFIS model making an integrated forecasting model as SD+ANFIS. Among different individual and integrated SCMs implemented in the paper, this paper focuses on the SD+ANFIS technique as the proposed wind speed forecasting model.

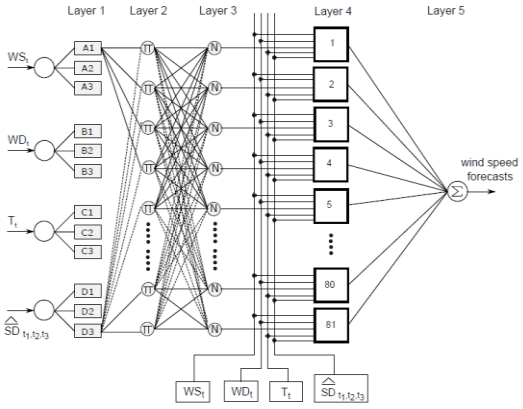

Fig.2. Architecture of the ANFIS model.

2.3 Numerical Results and Discussions

The forecasting approaches were tested using the real data of North Cape wind farm located in the PEI, Canada. Table I presents results obtained from all the chosen forecasting models and the results are compared with the persistence method, which is used as a benchmark for comparing other methods for short-term wind speed forecasting. With the application of SD+SCM, the errors are greatly improved as it can be observed in Table I that when SD is combined with ANFIS, the MAPE value is found to be lower (7.65%) than that of single use of SD (14.82%) and ANFIS (12.85%) in winter. So, with an introduction of SD into ANFIS model, the SD+ANFIS output resulted into an improvement in error by 40.46% over the ANFIS model. The MAPE values obtained from the SD+ANFIS demonstrate that there is a large improvement in error approximately in the range of 40%−48% in all the seasons over the direct use of ANFIS model only. In order to demonstrate the prediction capabilities of the

Table I

COMPARISON OF 1-HOUR-AHEAD FORECASTING PERFORMANCE OF THE CHOSEN MODELS WHEN FORECASTING LOOK-AHEAD TIME IS 24 HOURS

Season	Error	Persis	SD	BPNN	RBFNN	ANFIS	f_5	f_6	f_7^*
Winter	MAPE	13.23	14.82	13.88	13.67	12.85	8.89	8.67	7.65
	MAE	1.11	1.32	1.21	1.19	1.15	0.77	0.68	0.58
	RMSE	1.38	1.74	1.36	1.43	1.34	0.98	1.02	0.73
Spring	MAPE	18.69	13.72	15.82	14.11	13.88	10.88	9.23	8.02
	MAE	0.93	0.52	0.62	0.50	0.56	0.45	0.34	0.35
	RMSE	1.21	0.66	0.74	0.71	0.79	0.54	0.59	0.58
Summer	MAPE	16.91	9.52	14.37	13.92	14.13	9.45	9.65	7.27
	MAE	1.01	0.84	1.28	1.13	1.19	0.99	0.97	0.68
	RMSE	1.34	1.16	1.58	1.45	1.38	1.25	1.28	0.97
Fall	MAPE	6.75	8.72	11.75	10.36	11.06	6.85	7.46	6.17
	MAE	0.92	0.82	1.02	0.98	0.91	0.87	0.89	0.65
	RMSE	1.17	1.22	1.4	1.25	1.32	1.2	1.35	0.94

Persis: persistence method; f_5: SD+BPNN; f_6: SD+RBFNN; f_7^*: proposed SD+ANFIS model

considered models, Table I also presents MAE and RMSE values for all the test cases. It is observed that the MAE and RMSE errors of low values are obtained from the SD+SCM models. In all the test cases, through the application of SD method into SCM, SD+SCMs outperform the direct use of a single SCM and compare favorably well over the persistence method. The reason of using 24-hour prediction by repeating 1-hour predictions is to deliver 1-hour-ahead forecast with the look-ahead time of 24 hours. Power system operator requires different length of forecasting horizon for operation of interconnected power systems.

Forecasting short-term wind speed with a higher rate of accuracy is always a major concern for the power system operator. This paper contributes to alleviate the major problem of short-term wind speed forecasting in which the proposed prediction model based on ANFIS combined with SD method is applied to forecast 1-hour-ahead wind speed output of a wind farm.

3.3 Conclusions

This paper presented soft computing approaches for predicting short-term wind speed. The performance of the BPNN, RBFNN and ANFIS models were explored with and without integration of similar days method. The interaction between wind speed and other weather parameters such as wind direction and temperature were taken into consideration in the wind speed forecast process. The test results obtained for 1-hour-ahead forecasts confirm that the proposed wind speed forecasting algorithm based on ANFIS combined with the similar days method is capable of transforming the historical numerical weather data into wind speed predictions of higher accuracy.

References

[1] S. Singh and I. Erlich, “Strategies for wind power trading in competitive electricity markets,” IEEE Transactions on Energy Conversion, vol. 23, no. 1, pp. 249 –256, March 2008.

[2] S. Soman, H. Zareipour, O. Malik, and P. Mandal, “A review of wind power and wind speed forecasting methods with different time horizons,” in North American Power Symposium (NAPS), Sept. 2010, pp. 1–8.

[3] J. Catalao, H. Pousinho, and V. Mendes, “Hybrid wavelet-PSO-ANFIS approach for short-term wind power forecasting in Portugal,” IEEE Transactions on Sustainable Energy, vol. 2, no. 1, pp. 50–59,Jan. 2011.

[4] P. Mandal, T. Senjyu, N. Urasaki, T. Funabashi, and A. Srivastava, “A novel approach to forecast electricity price for PJM using neural network and similar days method,” Power Systems, IEEE Transactions on, vol. 22, no. 4, pp. 2058 –2065, Nov. 2007.

Delgado, P.[1], Kumar, V.[1]

[1]University of Texas El Paso

Abstract:

The challenge of modeling multiphase flow phenomena in geological formations such as oil and natural gas reservoirs is often hindered by a lack of critical information at the microscopic level. The **Heterogenous Multiscale Method (HMM)** provides a promising way of incorporating microscale physical models in a macroscale continuum fluid model with minimal computational cost. The current study develops a framework for realizing large-scale parallel implementation of a stochastic simulation of single phase flow in a porous media coupling microscopic network models with a continuum finite volume model for single phase flow. Results indicate that the iterative coupling algorithm may benefit from a data decomposition strategy that incorporates parallel linear solvers.

1. Introduction

The immediate and paramount need to understand the long term safety of carbon sequestration drives the development of high resolution simulations of carbon storage in the various geological formations. The Heterogeneous Multiscale Method developed by Chu et al (2011a, 2011b) is a promising framework to realize stochastic multiscale simulations. In their work, they discretized the continuum scale mass conservation equations for single phase flow using the finite volume method as shown in Fig 1, with fluxes obtained by solving a microscale network model. The iterative coupling between the microscale and macroscale models results in the solution of the coupled equations

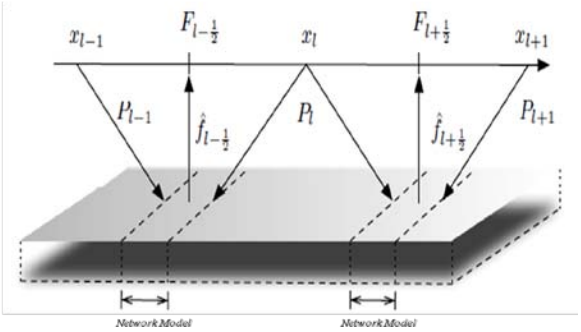

Fig 1: Iterative coupling between the microscopic & macroscopic models

$$\text{Microscale} \quad \begin{cases} q_{ij} = g_{ij} \nabla P_{ij} \\ \sum_{j \in K_i} q_{ij} = 0 \end{cases}, \quad g = \frac{\pi \cdot r^4}{8 \mu L} \qquad \textbf{Eq. 1}$$

$$\text{Macroscale} \quad \begin{cases} D^- \left(\frac{f\left(P_i^{(n)}, P_{i+1}^{(n)}\right)}{D^+\left[P_i^{(n)}\right]} D^+\left[P_i^{(n+1)}\right] \right) = S_i \\ F\left(x_{l+\frac{1}{2}}, P_{l+\frac{1}{2}}^{(n)}, D^+(P_l^{(n)})\right) = \hat{f}_{l+\frac{1}{2}}\left(P_l^{(n)}, P_{l+1}^{(n)}\right) \end{cases} \qquad \textbf{Eq. 2}$$

which reduces the problem to that of solving multiple linear systems of equations at the microscopic level (Eq. 1), and using their derived flux values to assemble and solve the macroscopic pressure equation (Eq. 2) in an iterative manner to obtain successive approximations of the macroscopic pressure.

The inherent randomness of statistical data to generate microscale models render individual deterministic models to be of very limited use for risk assessment. We extended this multiscale model to stochastic framework to assess probable outcomes. We replaced he coupled equations Eq.1 & Eq. 2 by a sequence of random simulations with randomly generated conductance matrix systems at the microscale. The heavy computational cost of a single multiscale simulation in the stochastic framework required an efficient parallelization of the multiscale algorithm which avoids communication when solving the microscale network models.

2. Experimentation:

We hypothesized that the macroscopic pressure distribution would also result in linear distributions. To test this hypothesis, we ran 10 stochastic simulations, each with 100 deterministic simulations on a porous media system with no source terms and linear conductance models on a 20x20 2D rectangular lattice. Spatial histogram bins for the stochastic solution were chosen on the same order of the spatial discretization. We also examined the scalability of the parallel algorithm by testing its performance 100 times on a shared memory system with eight cores. We predicted that linear speedup should be achievable up to the number of cores on the machine.

3. Results

Figure 2 illustrates the apparent constant pressure gradient at the macroscale resulting from an assumed linear conductance model at the microscale. This linear gradient is independent of the chosen throat radii distributions at each spatial location. As predicted, there is little deviation from the Darcy model at the macroscopic level.

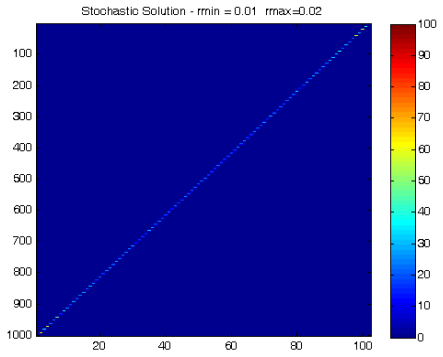

Figure 5: Stochastic solutions of macroscopic pressure. Colors show the probability of macroscopic pressure

Figure 3 shows the results of parallel implementation of the multiscale simulation without parallel linear solving. The results indicate that despite After testing 100 implementations of the

parallel multiscale algorithm, it is evident that linear scalability was not achieved. Further testing is necessary to determine the exact cause of the slow down in the algorithm.

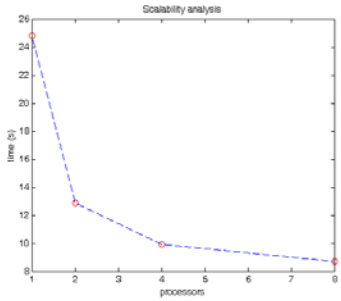

Figure 6 – Parallelization of the multiscale algorithm does not result in perfectly linear speedup.

4. Conclusions

Stochastic simulations of the multiscale algorithm with linear conductance at the microscale resulted in a nearly linear pressure gradient at the macroscopic level, independently of the throat radii distributions at the microscopic level. Furthermore, the stochastic framework appears to be a good visualization technique for analyzing the results of multiple random simulations.

Parallel implementation of the stochastic algorithm that avoids parallel linear solves does not result in the expected linear speedup. Possible sources of deficiencies include parallel IO operations in the microscale stiffness matrix assembly process, and CPU occupancy by other processes running on the same machine.

The simulations above have demonstrated the usefulness of stochastic simulations of multiscale single phase steady state flow through porous media. Chu et al (2011b) developed a method to incorporate stable two phase displacement using network models. We propose the use of microscale models to simulate viscous and capillary fingering in a network model and incorporate it in a multiscale simulation.

References

Chu, J., Engquist, B., Prodanovic, M. & Tsai, R. (2011a) A multiscale method coupling network and continuum models in a porous media I – single phase flow. ICES Report 11-15

Chu, J., Engquist, B., Prodanovic, M. & Tsai, R. (2011b) A multiscale method coupling network and continuum models in a porous media I – single and two phase flow. ICES Report 11-42

STUDYING HEURISTICS TO REDUCE POWER CONSUMPTION IN PEER-TO-PEER NETWORKS

G. Perera[1]
[1] Computer Science Department, UTEP
El Paso, TX 79968
gcperera@utep.edu)

Keywords: *IT; power consumption; P2P Networks; heuristics.*

ABSTRACT

Reduction of energy consumption in the Information and Communication Technology (ICT) area has attracted the attention of the research community. It is important to study heuristics that can be used in energy-efficient protocols and applications. In this paper, the problem of reducing power consumption for P2P networks is studied as an application of the well-known Minimum Set Cover problem for which a new minimum set cover heuristic, called Random Map Out (RMO) is implemented, evaluated, and compared against the popular Greedy heuristic. Our hypothesis is that P2P file sharing networks have redundant files. Therefore, redundant files shared by P2P nodes can be powered down to save energy. Our challenge is to identify the nodes that are redundant and powered down these nodes without disrupting file availability. Experimental evaluation showed that RMO has more nodes available and significantly less amount of processing (i.e., number of file comparisons) than the Greedy heuristic for distributed case.

1 Introduction

Reduction of energy consumption in the Information and Communication Technology (ICT) area has attracted the attention of the research community. Because power consumption from ICT can be attributed to computers and data centers it is important to study heuristics that can be used in energy-efficient protocols and applications. In particular, it is interesting to understand how future application architectures such as P2P networks can provide energy-efficient heuristics that allow the resources (i.e., files) provided by their nodes to be available but still maintain reduce network power consumption [1][3][7].

Figure 1 shows an example P2P network showing redundant P2P nodes. The five nodes shown in Figure 1 are sharing files identified with letters. For example, node 4 is sharing the three files named u, v, and w. The files shared by node 3 are shared by node 2, and the files shared by node 5 are shared by nodes 2 and 4. Thus, nodes 3 and 5 are redundant [8][9]. The contributions of this investigation are twofold. The first one is a novel study on how to enable power management in P2P file sharing nodes viewing power management as a Minimum Set Cover problem. The second one is a new heuristic for the Minimum Set Cover problem called Random Map Out (RMO). RMO was developed and evaluated experimentally showing a comparable Minimum Set Cover size as the Greedy well known heuristic. Additionally, when compared to the Greedy heuristic, RMO can be more easily distributed among the nodes of a P2P network.

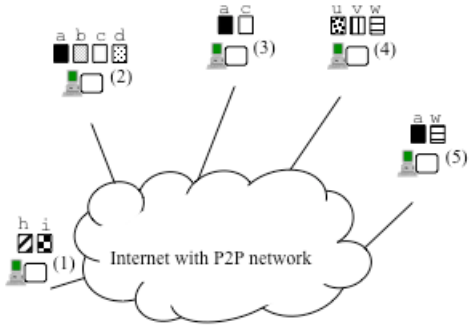

Figure 1 Example P2P network showing redundant servers

2 A Model for P2P Power Management

The Minimum Set Cover problem is defined as the *minimum number of sets (called a cover) from a collection of input sets*. The union of the sets that belong to the cover must contain all the elements of the universe and the input sets are subsets of the universe [2][4][5][6].
The Minimum Set Cover problem can be a mapping to P2P power management. Given universe *U* and a collection *S* of subsets of *U*, a set cover is the sub-collection *C* contained in *S* whose union is *U*. The Minimum Set Cover is the *C* with the fewest number of subsets. Using this model for P2P power management we have:

- Subsets of *S* are the P2P nodes.
- Shared files are the elements of *U*, thus a file is an element of *U*.

Therefore, the Minimum Set Cover, *C*, is the subset of P2P nodes that must be powered-on so that at least one instance of each file (each element in the universe *U*) is shared or available.

The Greedy heuristics is well-known solution for the Minimum Set Cover problem [2][10][13]. We compared Greedy to a new heuristic for set cover that can be distributed and used in networks with a reduction in processing is proposed as the new Random Map Out (RMO). The most important step of the RMO heuristic is to determine if a given set from th input belongs to the set cover or solution. In the RMO heuristic all sets are initially assigned to the set cover. Therefore, when the RMO heuristic determines that a set does not belong to the solution, it will remove it. The sets in the output are a minimal cover. Each node independently and randomly executes the distributed RMO heuristic.

3 Performance Evaluation

The performance evaluations of the RMO and Greedy heuristics require the definition of metrics. There are two performance metrics of interest for Minimum Set Cover heuristic:

1. The size or cardinality of the resulting minimal Minimum Set Cover.
2. The computational complexity (i.e., the running time or processing time for the minimum set cover).

The set cover size corresponds to the number of nodes that should remain powered-on so file availability is not affected and the computational complexity corresponds to the number of element comparisons required to achieve a minimal set cover [11][12].

Overall, a set cover heuristic is better, if it has significantly fewer comparisons (i.e., at least 50% fewer comparisons), and roughly the same set cover size. The observations of the results from all experiments are as follows.

- RMO is better as the ratio of elements per set ( ) increases.

• RMO is better for networks with uniform or slightly peaked file distribution.

• RMO has M times fewer comparisons with M processors and Greedy does not have a reduction in comparisons.

• Greedy is better for networks with highly peaked file distribution and the ratio of elements per set decreases.

4 Conclusions

P2P power management was investigated as a set cover problem. It was experimentally shown that the RMO with respect to M (total number of sets) has more sets in the cover a cover and significantly less number of comparisons. The set cover approach to P2P networks is a promising direction for power management and can result in significant energy savings by enabling redundant nodes to power down.

References

[1] K. Christensen and B. Nordman, "Improving the Energy Efficiency of Networks: A Focus on Ethernet and End Devices," presentation to Cisco, October 2006.

[2] T. H. Cormen, C. E. Leiserson, and R. L. Rivest, "Introduction to Algorithms, 2nd ed., Cambridge Mass., MIT Press, 2001.

[3] Energy Information Administration (EIA), Average Retail Price of Electricity to Average Retail Price of Electricity to Ultimate Customers, September 2006. Avalaible at: http://www.eia.doe.gov/cneaf/electricity/epm/table5_3.html.

[4] M. R. Garey and D.S. Johnson, "Computers and Intractability: A Guide to the Theory of NP-Completeness," W.H. Freeman, New York, 1979.

[5] F. Hadlock, D. Balasubramanian, J. Bittinger, C. Davis, S. Kesiraju , J. Kolpack J. Northcutt, S. Sudireddy, M. Tyler, J. Williams, and J.Wyatt, "An Internet Based Algorithm Visualization System," Journal of Computing Sciences in Colleges, Vol. 20, No. 2, December 2004, pp. 304-310.

[6] R. Hassin and A. Levin, "A Better-than-Greedy Approximation Algorithm for the Minimum Set Cover Problem," in Proceedings of SIAM Journal on Computing, April 2005, Vol. 35, No. 2, pp. 189-200.

[7] IPOQUE, Internet Study 2007, Leipzig, Germany, (2007).

[8] T. Klingberg and R. Manfredi, "Gnutella draft specification v0.6," June 2002. URL: http://rfc-gnutella.sourceforge.net/src/rfc-0_6-draft.html.

[9] F. Oberholzer and K. Strumpf, "The Effect Of File Sharing On Record Sales An Empirical Analysis," School of Business,University of Kansas, June 2005.

[10] M. Ohlsson, C. Peterson, and B. Söderberg, "An Efficient Mean Field Approach to the Set Covering Problem," Complex Systems Division, Department of Theoretical Physics, University of Lund, Technical Report, February 1999.

[11] G. Perera and K. Christensen, "Targeted Search: Reducing the Time and Cost for Searching for Objects in Multiple-Server Networks," in Proceedings of the International Performance Computing and Communications Conference, April 2005, pp. 143-149.

[12] S. Saroiu, P. Gummadi, and S. Gribble, "A Measurement Study of Peer-to-Peer File Sharing Systems," in Proceedings of SPIE Multimedia Computing and Networking, Vol. 4673, December 2001, pp. 156-170.

[13] P. Slavìk, "A Tight Analysis of the Greedy Algorithm for Set Cover," Journal of Algorithms, Vol. 25, November 1997, pp. 237-254.

Energy Efficiency and Conservation: A Case Study at the University of Texas at El Paso

O. Moreno[1], H. Taboada[1], and J. Villalobos[2]
[1]Industrial, Manufacturing and Systems Engineering, Graduate Research Assistant, El Paso, TX 79968-0521, USA; ocmoreno@miners.utep.edu, hataboada@utep.edu
[2]Jorge A. Villalobos, Director, Facilities Services javillalobos@utep.edu

Keywords: *HVAC, Building Automated System, Chill Water Consumption*

ABSTRACT

The motivation to design energy efficient buildings is increasingly leading to complex and finely optimized ventilation and heating/cooling systems in buildings. While it is well known that commissioning is one of the most cost-effective means of improving energy efficiency in commercial buildings, the Building Automated System (BAS) can be utilized further to optimize thermal performance and generate energy savings. The Environmental Defense Fund (EDF) and University of Texas at El Paso (UTEP) partnered together to place a Climate Corps fellow to work with the Facilities Services Department at UTEP to identify energy consumption patterns and generate cost effective energy savings. The Environmental Defense Fund (EDF) Climate Corps Fellowship program is designed to train business, environmental management and engineering graduate students and place them in businesses and universities across the country to identify cost effective energy savings. This paper presents the EDF Climate Corps Public Sector fellow's recommended energy efficiency projects that identified a total of $361,037 in annual energy cost savings at UTEP. This represented an approximate 18% annual reduction in energy costs for the university. In addition, the projected 632,087kWh saved annually is equivalent to powering 54 residential homes and the 436 tons of carbon emissions saved is equivalent to taking 86 SUVs off of the road each year.

1 Recommended Energy Efficiency Projects

Heating, Ventilating and Air Conditioning (HVAC) systems account for more than half of the energy consumption of a university and lighting consumes another twenty percent [1]. While the facilities' team at UTEP is working on the installation of an energy dashboard with smart meters, a Building Automated System is currently being utilized to monitor the energy consumption across the campus. There were three distinct projects that analyzed the current status and further recommendations were proposed to reduce energy consumption.

1.1 Lighting Upgrades

Initially, UTEP has several buildings in which upgrades to the lighting systems can pay off in operational costs over a short time period. These facilities utilize high-energy light bulbs which if converted to lower wattage consuming devices, can save 557,450 of kW per year at an annual savings of $36,234/year. With a cost of $179,700 to replace the lighting fixtures, it is estimated that the average payoff on this investment is 5 years.

The following lighting projects as shown in Figure 1 were studied to determine the impact of replacing the existing fixtures with high efficiency LED lighting. Respectively, the approximate installation costs and payback periods are illustrated.

	Title	Details	Category	Cost	Saved kwh/Yr.	Saved Electric Cost/Yr @ $0.06/kwh	years payoff
1	Parking Garage Stairwell lighting	Add motion sensors to 125 stairwell lights in the Parking Garage	Cost Savings	$ 7,000	88,000	$ 5,720	1.2
2	Library Stairwell Lighting	Add motion sensors to 80 stairwell lights in the Library	Cost Savings	$ 4,000	42,600	$ 2,769	1.4
3	DHC Concourse Lighting	Retrofit 350 (300w) incandescent fixtures to 40 w LED on the DHC Concourse	Cost Savings	$ 77,000	330,000	$ 21,450	3.6
4	Parking Garage Lighting	Change 50 fixtures from 175w mh to 80w induction fixtures	Cost Savings	$ 15,000	32,850	$ 2,135	7.0
5	Admin Stairwell Lighting	Change 15 stairwell fixtures at Administration to bi-level motion sensing fixture	Cost Savings	$ 4,500	7,900	$ 514	8.8
6	Bookstore Inside Lighting	Change 125 fixtures from fluorescent and incandescent to LED	Cost Savings	$ 12,500	21,000	$ 1,365	9.2
7	Geo Stairwell lighting	Change 20 stairwell fixtures at Geo Science to bi-level motion sensing fixture	Cost Savings	$ 5,000	8,000	$ 520	9.6
8	Phys Plant Outside Lighting	Change 6 pole fixtures from 400w mh to 200w LED in Phys. Plant yard	Cost Savings	$ 9,500	5,500	$ 358	26.6
9	Phys. Plant Outside Lighting	Change 22 wall pack fixtures from 175watt high pressure sodium to 90 watt LED in Phy. Plant	Cost Savings	$ 21,000	10,000	$ 650	32.3
10	Rim/Wiggins Stair Lighting	Lighting at the corner of RIM and Wiggins to illuminate the stair case towards parking lot P4	Safety	$ 5,000	0	$ -	0.0
11	University Street Lighting	Change 5 pole fixtures from 400w metal halide to 200w LED fixtures on University street (light up	Safety	$ 8,000	5,000	$ 325	24.6
12	DHC Outside Lighting	Change 5 pole fixtures from 400w mh to 200w LED fixtures on Sun Bowl Dr. and DHC	Safety	$ 8,000	5,000	$ 325	24.6
13	Street Lighting	Change 2 pole fixtures from 400w MH to 94w LED fixtures on Sun Bowl Dr. and Kelly	Safety	$ 3,200	1,600	$ 104	30.8
14	Totals			$ 179,700	$ 557,450	$ 36,234	5.0

Fig.1. Proposed lighting upgrades

If all of the lighting upgrades are completed, the total savings can generate 557,450 kWh per year in energy savings and $36,000 per year in potential savings. The investment costs are relatively high for this project, $179,700, but the average payoff is in five years.

1.2: Pre-cooling and Bottling Up Experiment

In terms of energy use, faulty or improperly commissioned controls or sensors can result in heating and cooling systems running simultaneously or when not needed at all, which greatly increases energy consumption and costs [2, 3]. A study by Grigg and S later [4] found that proper installation and commissioning of building control systems can reduce the energy consumption by 15–20%, and a study by Mills et al. [5] identified commissioning (including retro-commissioning for older buildings) as one of the most cost-effective ways of improving energy efficiency in commercial buildings, with savings of $18 billion/year across the United States. There was a strong interest by the facilities team to determine if there was a low to no-cost solution to manage the costs of the additional loads on the energy demand with the expansion of the campus. The issue that was being addressed was whether by pre-cooling a building on the off-peak hours, the building temperature and consequently the chill-water consumption would drop enough during the peak hours to create a savings in chill-water utilization.

Figure 2 is a graph of the chill water use in the Foster-Steven's basketball complex. The Baseline curve is the average ton-hr. utilization on the BAS of the building for the week prior to the experiment. The day 1 and day 2 curves reflect the two different experiments days that were performed.

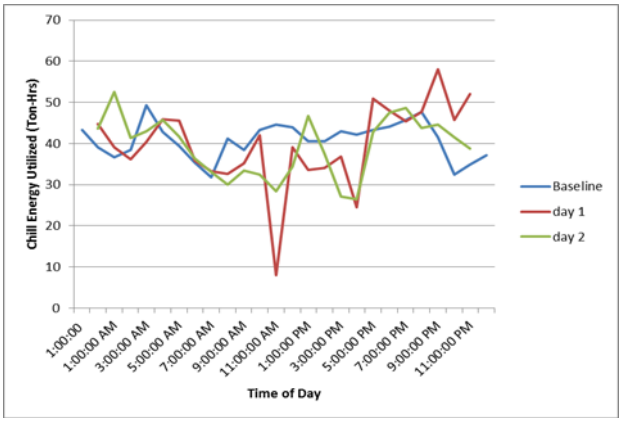

Fig.2. Ton-Hr. Utilization of the Foster-Stevens Building

If a rough estimate is utilized on a campus wide scale, and it is assumed based on these experiments, between 5 -10% reductions in chill water utilization is feasible with the modification of the building automation systems. This project would generate instant savings since no upfront costs are required and it could generate at least $188,000 in savings campus wide.

1.3 Project 3: Evaporative Pre-cooling Units Installation

In the third experiment, the objective was to determine the impact of not having an evaporative pre-cooler upstream of the cold deck. Figure 3 below illustrates the baseline in the College of Health Sciences with evaporative pre-cooling units installed and the experimental day they were turned off to generate the savings. It is believed that if this type of system is placed in strategic, large buildings like UGLC, Library, Engineering, Biology, there is a potential for lowering the chill water consumption by at least 8% per building.

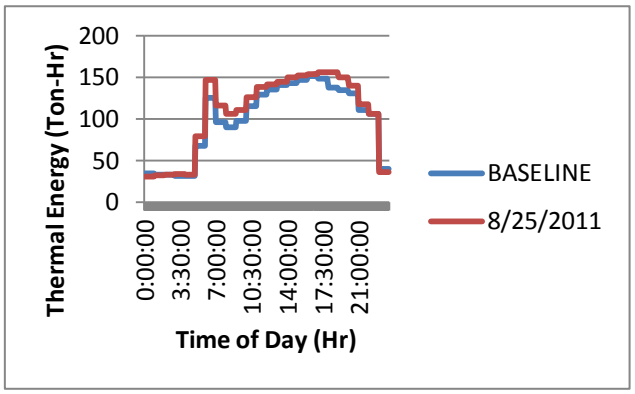

Fig.3.Evaporative Unit Test in the College of Health Science

Conclusions

The Climate Corps Public Sector fellow identified a total of $361,037 in annual energy cost savings at UTEP. In addition, the projected 632,087kWh saved annually is enough to power 54 residential homes and the 436 tons of carbon emissions saved is equivalent to taking 86 SUVs off of the road each year. Through the implementation of the recommended, quantified energy efficiency projects, UTEP could see an estimated 18% reduction in their annual energy costs.

References

[1] K. J. Moss "*Energy Management in Buildings*". 2nd edition, Taylor and Francis, 2006.

[2] M.G. Apte "A review of demand controlled ventilation". *Proceedings of Healthy Buildings*, Portugal, Spain, Vol. 4, pp 371-376, 2006.

[3] N. Brown, A.J. Wright, A. Shukla, G. Stuart, "Longitudinal analysis of energy metering data from non-domestic buildings". *Building Research & Information*, Vol. 38, No. 1, pp 80-91, 2010.

[4] P. Grigg, A. Slater, *Assessment of energy efficiency impact of building regulations compliance report*, Energy Efficiency Partnership for Homes, Research report, 2004.

[5] E. Mills, H. Friedman, T. Powell, N. Bourassa, D. Claridge, T. Haasl, M.A. Piette, *The Cost-Effectiveness of Commercial-Buildings Commissioning: A Meta-Analysis of Energy and Non-Energy Impacts in Existing Buildings and New Construction in the United States*, Lawrence Berkeley National Laboratory Report No. 56637, 2004.

STRESS-STRAIN RESPONSES OF AN I-40 PAVEMENT SECTION IN NEW MEXICO

M. R. Islam[1]*, R. A. Tarefder[2]
[1]PhD Student, Department of Civil Engineering, UNM, Albuquerque, NM 87131, USA;
[2]Associate Professor, Department of Civil Engineering, UNM, Albuquerque, NM 87131, USA;

* Corresponding author (mdislam@unm.edu)

Keywords: *Stress, Strain, Validation, Instrumentation*

ABSTRACT

Recently, New Mexico Department of Transportation (NMDOT) has designed a pavement section on I-40 (MP 141) using Mechanistic-Empirical Pavement Design Guide (MEPDG).This section is going to be instrumented during Spring 2012. The purpose of the instrumentation is to find out stress-strain at different layers and depths of the pavement under real traffic. To this end, this study determines the stress and strain behavior of the instrumented pavement section under traffic loading using commercial finite element software ABAQUS.

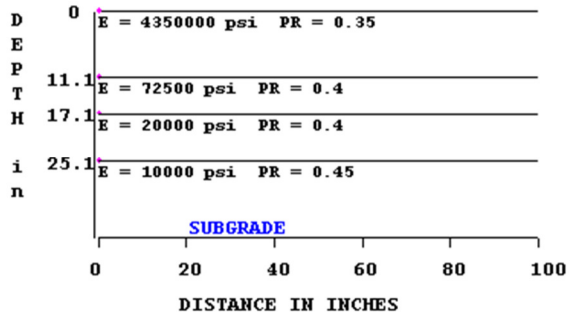

Fig. 1. The profile of the I-40 EB

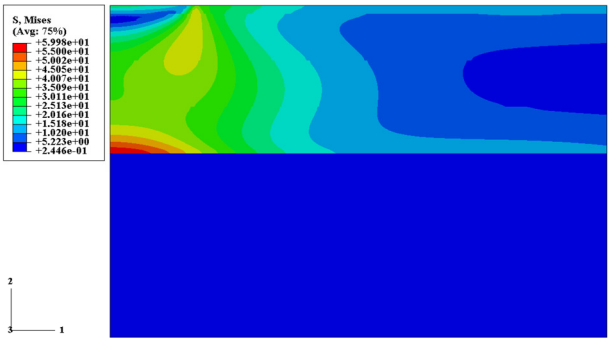

Fig. 2. Von-Mises Stress

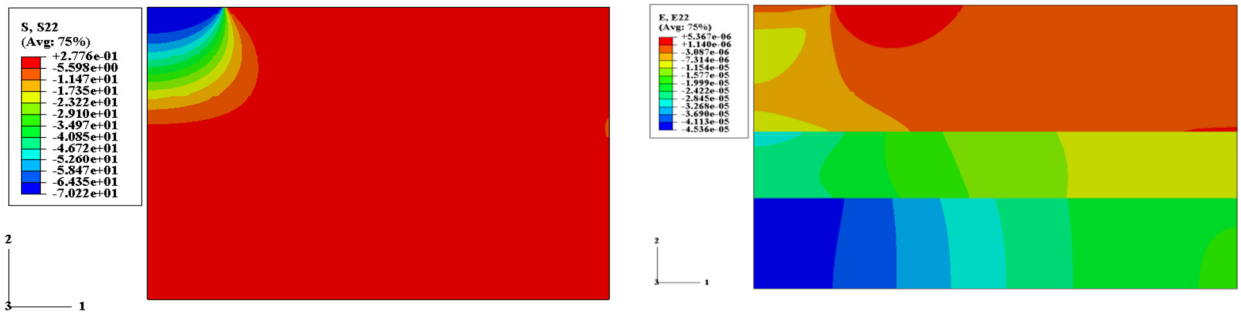

Fig. 3. Vertical stress (Left) and vertical strain (Right)

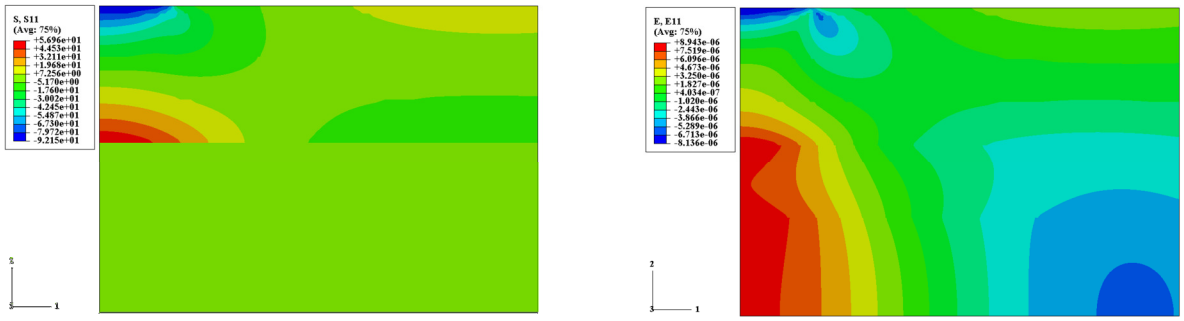

Fig.4. Horizontal stress (Left) and strain (Right)

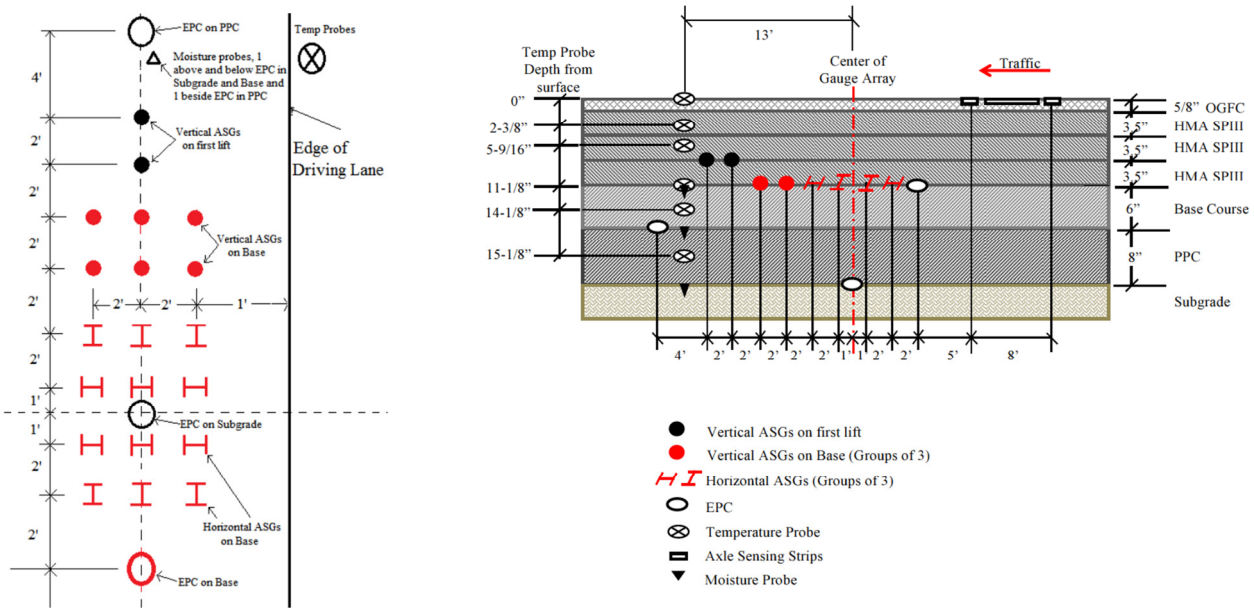

Fig. 5. a) Instrumentation plan view b) Instrumentation profile

1 Introduction

The section in Fig. 1 has four layers. The top layer is Asphalt Concrete (AC) of thickness 11.125 in. Then there is 6 in. crushed stone base layer. The Process Place Compact (PPC) is an 8 in. thick layer placed on the top of the natural soil. The modulus and the Poisson's ratio are taken from the available literature[1],[2]. These values are typical for these types of materials. The modulus of the AC layer is 4350 ksi, of the base 72.5 ksi, of the PPC 20 ksi and of the natural soil is 10 ksi. The Poisson's ratios are 0.35, 0.4, 0.4 and 0.45 respectively.

2 Numerical Analysis

Numerical analysis is conducted to get the best geometry of the instrumentation plan. The pavement is modeled with finite element software ABAQUS. The asphalt concrete (AC), the crushed stone base and the process place compact (PPC) are modeled as linear elastic media. The tire-pavement system is modeled using 2D axis-symmetric mesh. No lateral displacement at the

edges of the pavement, no vertical displacement at the foundation and no slip between layers is assigned as boundary conditions. The profile is shown in Fig. 1. The von-Mises stress is shown in Fig. 2. It shows the failure potential zones. Three zones are identified, the bottom of the AC layer, loading zone and adjacent to the wheel. Fig. 3 is the contour plot of the vertical stress and strain. The vertical stress is compressive just below the wheel. Far from the wheel it is tensile. This indicates the compressive stress is very low below the AC layer. The vertical strain is very close to the wheel. It has physical sense that the top down crack start from the adjacent of the wheel. Fig. 4 shows the horizontal stress and strain. It is same for both longitudinal and transverse directions. The horizontal tensile stress is the maximum at the bottom of the AC layer (Fig. 4). The repeating traffic loads cause fatigue failure at this point. Just below the tire the stress is compressive and the highest in magnitude. The horizontal elongation starts at the bottom of the AC layer and propagate beneath the layer.

3 Instrumentation Plan Based on ABAQUS Results

The detailed instrumentation design is shown in Fig. 5. As the horizontal strain is the highest at the bottom of the asphalt layer as in shown Fig. 4. we put 12 Horizontal Asphalt Strain Gages (ASG), 6 in transverse direction and 6 in longitudinal direction. This horizontal strain is a critical parameter to characterize fatigue performance. To get the deflection in AC layer 8 Vertical ASGs are used. Three Earth Pressure Cells (EPC) are supposed to reflect the vertical pressure on top of subgrade, top of PPC, and top of base. These pressure values are linked to the rutting prediction. Fig. 3 shows the vertical stress become constant below the AC layer. So, the three EPCs should give almost same result. Environmental variation like moisture and temperature variation is to be monitored. How the responses vary with moisture and temperature is to be correlated. Axle sensing strip is used just before the instruments to get the wheel wander. The Weigh-in-Motion is installed after the instruments to get the traffic configurations.

4 Conclusions

The critical locations of stress and strain follow previous study and expected locations. The maximum horizontal tensile stress is 56.9 psi which occurs at the bottom of the AC layer. The corresponding horizontal strain is 8.9με. These values are same both longitudinal and transverse direction. The vertical stress is 70 psi at the top of the AC layer, 11.5 psi at the top of base and 10.5 psi at the top of PPC layer and 2.3 psi at the bottom of the base. The vertical strain at the bottom of the AC is 9.8 με and at the bottom of the base is 45 με and at the bottom of the PPC is 43 με. The instrumented section is designed to verify all these responses.

References

[1] M. Kim "*Three-dimensional Finite Element Analysis of Flexible Pavements Considering Nonlinear Pavement Foundation Behavior''*. PhD Thesis, Department of Civil Engineering, University of Illinois at Urbana-Champaign, 2007.

[2] S. Mun "*Nonlinear Finite Element Analysis of Pavements and its Application to Performance Evaluation",* PhD Thesis, Department of Civil Engineering, North Carolina State University, 2003.

SAMPLE SIZE EFFECT ON HMA PERMEABILITY AND DETERMINATION OF 3D PERMEABILITY

M. Ahmad[1]*, R. Tarefder[1],
[1] Department of Civil Engineering, University of New Mexico, Albuquerque, NM-87106, USA;
* Corresponding author (mahmad@unm.edu)

ABSTRACT

Currently, Hot Mix Asphalt (HMA) concrete permeability is determined in the laboratory using cylindrical samples of 4 in. and 6 in. diameters. Permeability is calculated based on the assumption that the flow paths are vertical by restricting any water flow laterally. But the number of vertical flow path depends on the sample size or diameter. To this end, this study develops a procedure to find the sample size effect on the laboratory permeability value. In the analysis, distributions of voids on vertical and horizontal surfaces are assumed to be uniform. As a first step, an equation relating effective and total air void is established with few coefficients. In the second step, a method is developed to determine those coefficients and use them to determine 3D permeability.

Introduction

The voids in HMA can be divided in three categories: continuous, discontinuous and isolated [1]. Permeability occurs due the continuous voids only. Water flows through all permeable voids in a 3D field case. In general, field permeability differs from laboratory measurement of permeability. This is because, during laboratory testing, water flows in vertical direction only as sides of the sample are confined. Many researchers tried to correlate these two measurements depending on the experiments [2]. In this paper, we tried to find theoretical relations between 3D permeability and permeability measured in the laboratory. The flow lines are considered cylindrical with uniform cross section in permeability calculation.

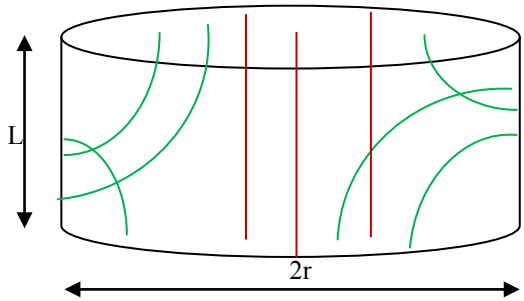

Fig.1. Active (red) and inactive (green)air void

Theory

If y% of the side area are voids among which x% do not continued from top to bottom face, then amount of inactive voids (green lines in Fig. 1) can be calculated by,

$$inactive\ voids = \frac{2\pi rLxy}{10000} \ldots\ldots\ldots\ldots\ldots\ldots\ldots\ldots\ldots\ldots (1)$$

If the top surface has V_a % air voids, then effective voids (red lines in Fig. 1) can be expressed as,

$$A_{eff} = \frac{\pi r^2 Va}{100} - \frac{2\pi rLxy}{10000} \ldots\ldots\ldots\ldots\ldots\ldots\ldots\ldots\ldots\ldots\ldots (2)$$

Then the distribution of effective voids over the circular area in percent is,

$$n_{eff} = \frac{A_{eff}}{A} = Va - \frac{2Lxy}{100r} \ldots\ldots\ldots\ldots\ldots\ldots\ldots\ldots\ldots (3)$$

Or,

$$\frac{dn_{eff}}{dr} = \frac{Lxy}{50r^2} = \frac{c}{r^2} \ldots\ldots\ldots\ldots\ldots\ldots\ldots\ldots\ldots\ldots\ldots\ldots (4)$$

A plot of Eq. (4) is shown in Fig.2 (assuming c=1) Eq. (4) shows an inverse change in effective void distribution with radius of the sample. This indicates that change in effective voids distribution decreases with radius. For smaller radius, the change is significant, but the change is negligible for higher radius. It indicate that the larger the radius of the laboratory sample, the smaller the difference between the laboratory permeability and the field permeability. When radius tends to infinity, it represents completely the field sample and the change in effective void distribution is zero.

For a specific asphalt mix, c should have a constant value. In next sections, proposed method for determining n_{eff} as well as c is described.

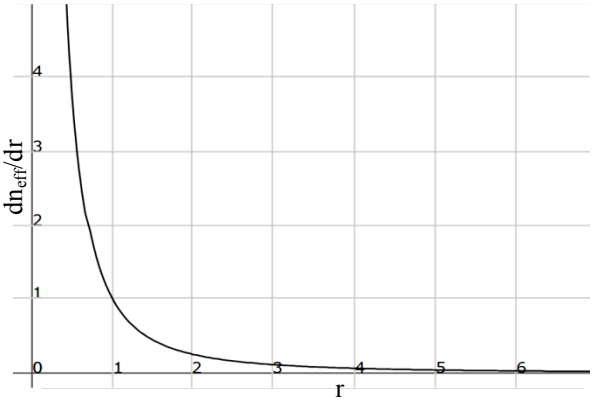

Fig-2. Change of Effective void distribution with radius

Method

Instrumentation

Fig.3 shows a schematic view of the instrument.

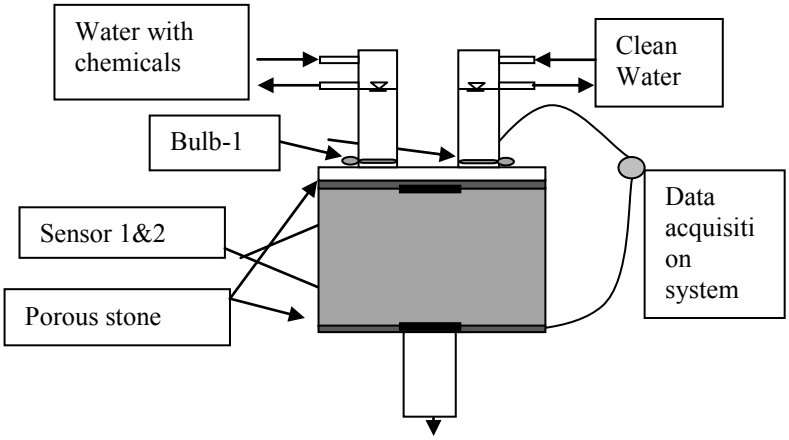

Fig.3. New device to measure effective air voids in HMA

Procedure

Step-1: All bulbs are closed. Clean water bulb-2 is opened for about 30 minutes for saturation. Bulb-2 is closed. Data acquisition system is switched on. Bulb-1 is opened. Water with chemicals will enter in the sample. Sensor-1 will send signal to data acquisition system and a stopwatch at data acquisition system will start automatically. When this water will reach at exit, sensor-2 will send signal to data acquisition system and the stop watch will stop automatically and the time is recorded. More sensors at the exit and taking time average with give more accurate results.

Step-2: Discharge Q_{real} (cm3/s) is measured, using constant head method.

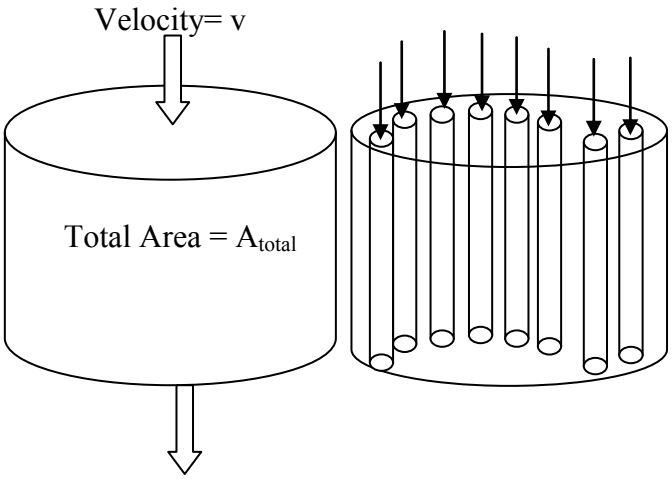

Fig.4. a) Whole section is permeable, b) actual sample

Calculation

Real velocity of the water inside the sample is,

$v = \frac{L}{t}$ ……………………(5)

Here,

L= length of the sample.

t= time from the data acquisition system.

If the total cross section area of the sample is free for water flow, then discharge will be,

$Q = A_{total} v = Av$ ………………………(6)

But in practical, most of the area in the section is occupied by solids and we have a small area free for water flow. Let the actual area occupied by permeable pores is A_{eff}.

Then actual discharge will be

$Q_{real} = A_{eff} \times v = vAn_{eff} = Ak \times pi = Ak_{tested} i$……………………(7)

=> $\frac{Q}{Q_{real}} = \frac{A}{A_{eff}} = \frac{A \times h}{A_{eff} \times h} = \frac{V_T}{V_{eff}} = \frac{1}{n_{eff}}$

Or, $effective\ porosity, n_{eff} = \frac{Q_{real}}{Q}$………………………..(8)

Here, Q_{real} is measured in step-2 and Q is calculated from equation (6). Hence effective void distribution can be determined. Here, i = hydraulic gradient for each capillary tube and p and q are number of tube corresponding to laboratory and field testing respectively.

6″ sample is tested first for n_{eff} then a 4″ core cut from the 6″ is tested. The constants V_a and xy can be determined solving two equations obtained from equation (3) for two n_{eff} values. In field, assuming all capillary tube has same discharge and head loss,

$$Q_{field} = \sum av = vAV_a = Akqi = Ak_{field} i \dots\dots\dots\dots\dots\dots\dots\dots\dots.\dots\dots\dots\dots\dots\dots (9)$$

From equation (7) and (9)

$$k_{actual} = k_{tested} \times \frac{V_a}{n_{eff}} \dots\dots\dots\dots\dots\dots\dots\dots\dots\dots\dots\dots\dots\dots\dots\dots (9)$$

Summery

Effective void ratio changes with radius, and can be determined using the test method described. Using equation-3, total permeable void ratio can be determined. Then actual permeability can be obtained using equaton-9.No laboratory test was performed to validate the theory. So, experiments and numerical simulations can be done in future to determine the actual field permeability.

References

[1] R.A. Tarefder, L. White and M. M. Zaman"Neural Network Model for Asphalt Concrete Permeability". *Journal of Materials in Civil Engineering*, ASCE, Vol. 17, No. 1, pp 19-27, 2005.

[2] K. Kanitpong, H. Bahia, J. Russel, and R. Schmitt "Predicting Field Permeability from Testing Hot-Mix Asphalt Specimen Produced by Superpave Gyratory Compactor". *Transportation Research Record,* Volume 1929, pp. 52-58, 2005.

DEVELOPMENT OF WIRELESS THERMOELECTRIC TEMPERATURE SENSORS

Jennifer J. Kuchle[1], Kazi Hassan[1], Norman Love[1] and Ahsan Choudhuri[1]
[1]*Center for Space Exploration and Technology Research (cSETR)*
University of Texas at El Paso, El Paso, Texas 79968

φ	=	Magnetic Flux
N_i	=	Number of Turns
A	=	Area of Wire
l	=	Length

ABSTRACT

The thermoelectric effect is the conversion of temperature differences to electric voltage and current, and vice-versa (Peltier-Seebeck effect)[1]. With the development of new technologies in the area of thermoelectrics, a great part of the wasted thermal energy in power plants is being converted to electricity under this principle.

Many efforts have been made on the research of the thermoelectric effect for power generation. For instance, Love et al. [2] tested several thermoelectric devices on a bench-scale thermoelectric heat recovery system that simulated automotive exhaust. Overall, thermoelectric efficiencies remain well below 10% prompting the use of thermoelectrics for other means such as sensor devices.

By characterizing and testing wireless thermoelectric sensors, the temperature on the surface of a gas turbine blade can be determined, and consequently, a better control of the temperature inside a gas turbine can be achieved. Knowing the temperature at several locations inside a gas turbine, the mechanical design and selection of the materials used can be improved and the overall efficiency of the system can be significantly increased. This paper presents the wireless transmission applicability of a linear Hall sensor for this application. The results obtained in this study will serve as the basis of further experiments with thermoelectric devices and thermoelectric-coated turbine blades.

1. Experimental Methodology

Thermoelectrics, capable of inducing a continuous current through a ring loop, create a magnetic flux in a direction perpendicular to the current. This magnetic flux can be computed analytically using the Eq. (1):

$$\varphi = \mu_0 N_i A/l \tag{1}$$

Magnetic flux is proportional to the temperature on the surface of the substrate. With this information, the thermoelectric coating can be used as the signal transmitter and a wireless receiver can be developed. In order to establish the relationship between magnetic field, output voltage and current, the principle of the Hall-effect was considered. In general, the Hall-based sensing device produces an electric signal when exposed to a magnetic field. The linear current sensor monitors the magnetic field created by a current flow [3]. In this study, a 5 mV/Gauss

ratiometric linear analog Hall effect sensor [4] for high temperature operation (~150 °C) was used. The ratiometric output voltage of this type of sensor is set by the supply voltage (5 Volts) and varies in proportion to the strength of the magnetic field. In this case, at initial conditions (when no external magnetic field was present), the output voltage was equal to one half of the supply (2.5 V).

In order to prove the practicality of the hall-effect sensor in this application, the magnetic field of a moving electromagnet was tested. For this experiment, a 22-gauge magnet wire was wrapped around a plastic core and the output voltage was recorded. A continuous current of 4.3 Amperes was supplied to the electromagnet attached to a moving pendulum (see Figure 1). The hall-effect sensor (signal receiver) was placed 1.3 cm away from the electromagnet. The output voltage values were obtained and recorded using LabVIEW and the resulting graphs were plotted.

The noise of the analog signal was obtained through LabVIEW and was filtered. A Discrete Fourier Transform (DFT) function was used in order to convert the signal from the time domain to the frequency domain. Evaluating 1,630 samples the DFT algorithm allowed the discretization of the original signal into the spectrum where the full range of frequencies of the input signal was revealed. The cutoff frequency and bandwidth were determined by the lowest allowable frequency (frequency of the pendulum) and the third highest frequency obtained. These values were 1.7 Hz and 20 Hz, respectively. Using this function, 60% of the noise was filtered and the signal was converted back into the time domain to get the filtered original signal, without compromising fidelity.

2. Results

The results obtained from the study are shown in Figure 2. The graph shows the relative output voltage recorded in the first fifteen seconds as the pendulum was activated. The moving coil showed a periodic pattern. The maximum and minimum V_{out} values obtained were 2.57 and 2.49 V, respectively.

Figure 3 shows the filtered signal obtained using the Discrete Fourier Transform function. The spectrum of the frequencies showed its first peak at ~2 Hz, the same value as the pendulum's frequency. Each peak in the graph displays a similar pattern except for small disturbances caused by vibrations and external noise. Further investigation is required with the addition of temperature as a new parameter. Adding heat to the system, the amount of the output voltage generated will be then correlated with the temperature gradient. From this information, the final temperature obtained at the surface will be computed due to the proportional relation of the electromagnetic field produced and temperature.

3. References

[1] Kasap, S. *Thermoelectric effect in metals: thermocouples*. E-Booklet. 1997.

[2] Love, N., Szybist, J., and Sluder, C. *Effect of heat exchanger material and fouling on thermoelectric exhaust heat recovery.* Applied Energy. Vol. 89. 2012. pp. 322-328.

[3] Nemir, D., and Beck, J. *On the significance of the thermoelectric figure-of-merit Z.* Journal of Electronic Materials. Vol. 39 (9). 2010. pp. 1897- 1901.

[4] Allegro Micro Systems. *Ratiometric linear hall effect sensor for high-temperature operation*. Accessed by Web December 12, 2011. <http://www.datasheetcatalog.org/datasheet/allegromicrosystems/1321.pdf>.

4. Appendix

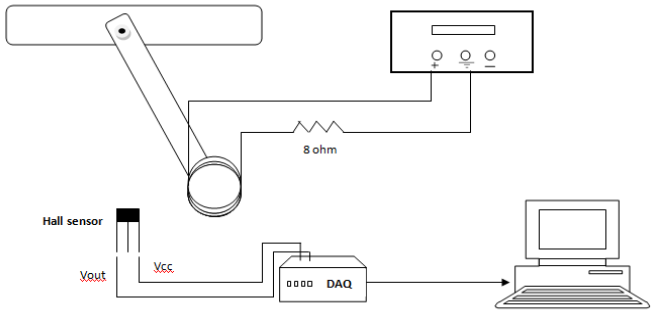

Fig. 1. Schematic diagram of experimental setup

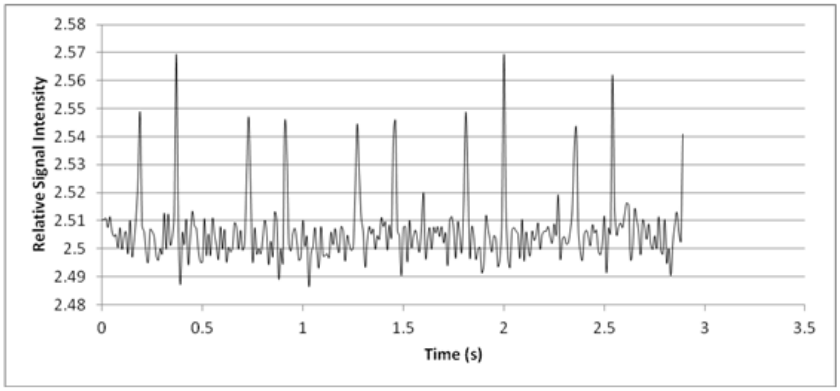

Fig. 2. Relative signal intensity vs time

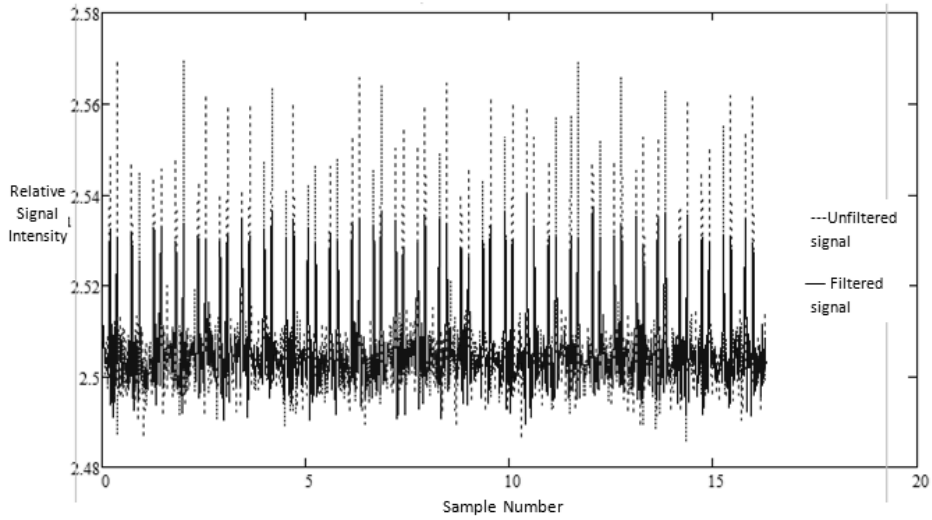

Fig. 3. Comparison of filtered and non-filtered signals

PREPARATION AND CHARACTERIZATION OF GA_2O_3

S. Sampath, K. Abhilash and Dr. Ramana*
Department of Mechanical Engineering
University of Texas at El Paso, El Paso, Texas 79968, USA

Keywords: *Ga_2O_3, Thin-films, Sputtering deposition, XRD, SEM, Structural properties*

ABSTRACT

The stable oxide of gallium, β-Ga_2O_3, is a wide band gap material. The Gallium Oxide (Ga_2O_3) thin film was deposited on Si and quartz substrate. The Gallium Oxide, which was made from a sintered powdered target by a RF sputtering magnetron system, was sputtered using Ar^+ as the sputtering gas. The deposition was done by varying the temperature from Room temperature C. The characteristic analysis of the samples was done by using X-ray Diffraction (XRD) and Scanning Electron Microscope (SEM). X-ray Diffraction on C has been performed since the samples at lower temperature did not give any peaks. SEM analysis was also performed on all sample C. The Optical characterization was done on the quartz substrates like absorption and transmittance parameters.

1 Introduction

The development of new and more efficient materials for gas sensing is a challenge as the demand for these devices continues to grow. Metal Oxides such as TiO_2, Ga_2O_3 have gained a great deal of interest in the science and technology communities. The current applications of Ga_2O_3 include luminescent phosphors, gas sensors and deep – ultraviolet transparent conductive oxides (deep – UV TCO). It also has application in solar cells. Oxygen sensors are used in monitoring and controlling systems of waste gases like - nitrogen oxides, carbon mono-oxide, combustion engines and chemical processes, etc. Pure Ga_2O_3 C so sensors with higher responses and lower operating temperatures can be obtained. We can also detect other gases by controlling the operating temperature.

2 Experimental

2.1 Characterization of the deposited film

The gallium oxide thin films were prepared by depositing gallium oxide on Si substrates by RF-magnetron sputtering. The gallium oxide target was prepared by sintering gallium oxide powder. Thin films of about 1.5μm thickness were deposited with gallium oxide using Ar as the sputtering gas at an RF power of 100W at a sputtering pressure of $1.9x10^{-2}$ C by keeping the sputtering time constant for 30min. Composition and crystallinity of the deposited films were analyzed by XRD and SEM.

2.2 Results and Discussion

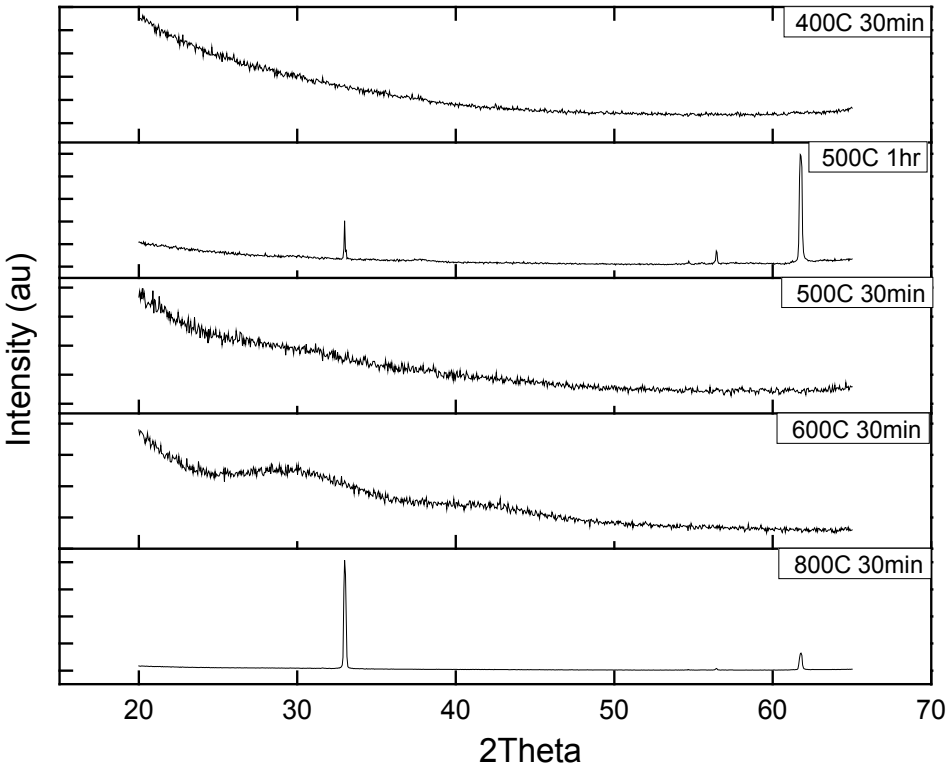

C for a time of 30min.

C shows a peak.

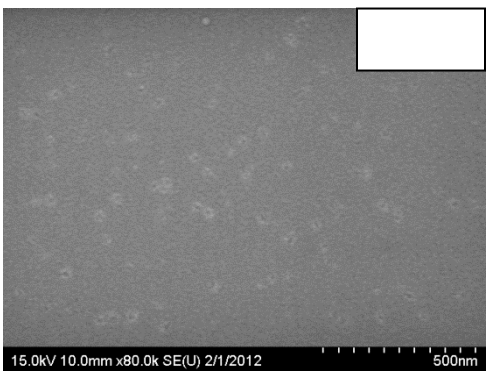

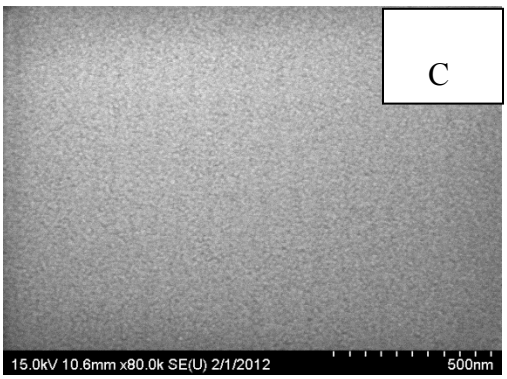

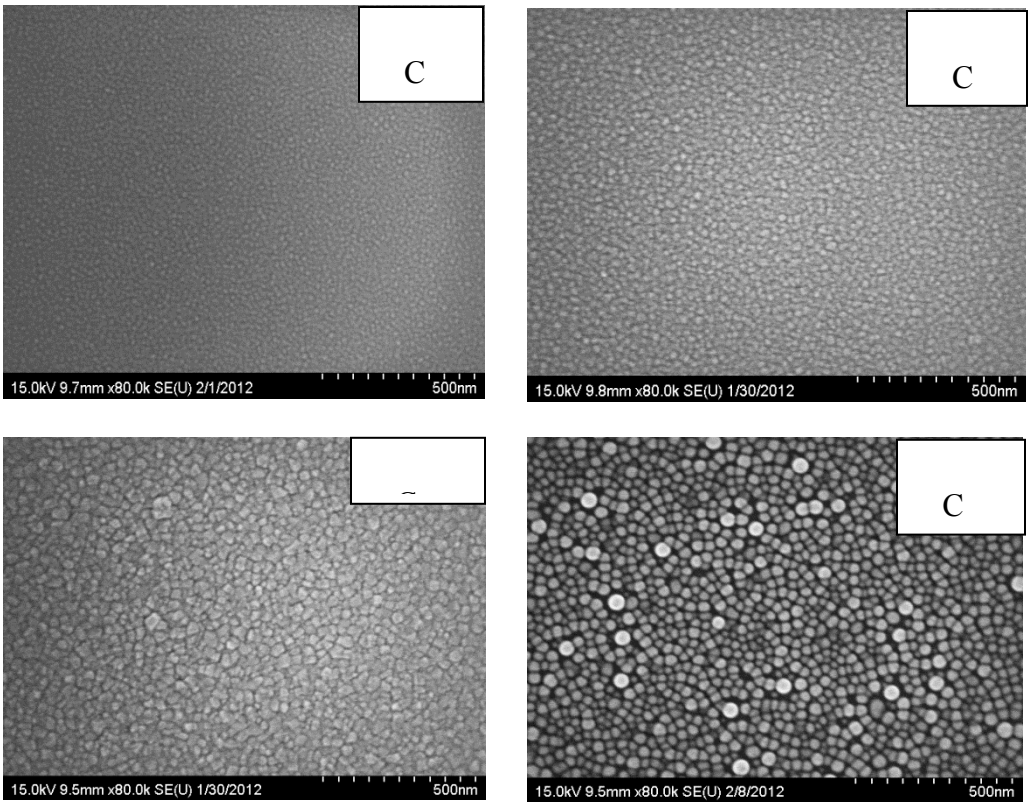

C for a time of 30min.

C.

3 Results and Conclusion

Ga_2O_3 was fabricated using sputter deposition at various temperatures from room tempera

C. The structural and optical properties of the materials have been studies using XRD and SEM. The results show that Ga_2O_3 is a good material for oxygen sensing at higher temperatures.

4 References

1. M. Ogita, K. Kobayashi, Y Yamada, Y. Nakanashi, Y.Hatanaka. "*Properties of Gallium oxide thin film sputtering from powder target for high temperature oxygen sensors*"Indust. J. Appl. Phys., vol. 1**,** 2001, pp 137-140.
2. Zhenguo Ji *, Juan Du, Jia Fan, Wei Wang. "*Gallium oxide films for filter and solar-blind UV detector*".
3. M. Fleischer, and **H.** Meixner, "*Selectivity in high-temperature operated semiconductor gas-sensors,*"*Sensors Actuators* B**,** vol. 52, pp. 179-187, 1998.
4. M. Rebien, W. Henrion, M. Hong, J. P. Mannaerts, and M. Fleischer, "Optical properties of gallium oxide thin films," *Appl. Phys. Lett.*, vol.81, pp. 250–250, 2002.
5. ***S* .** Geller, "*Crystal Structure of P-Ga203, "J. **Chem.** Phys.*,vol. 33, pp. 676-684, 1960.

THERMAL BARRIER COATINGS (TBC's) FOR HIGH HEAT FLUX THRUST CHAMBERS

C. BRADLEY, C.V. RAMANA and A. CHOUDHURI
Center of Space Exploration Technology Research
University of Texas at El Paso
El Paso, TX 79968
(915) 920-6047
cbradley2@miners.utep.edu

ABSTRACT

Thermal barrier coatings (TBC's) are ceramic coatings that are used extensively on turbine components to protect the components from the harsh service environments. Current TBC's that are used in industry are comprised of 8% yttria-stabilized zirconia (YSZ). Advanced turbine technology is pushing for higher temperatures to increase efficiency and the current TBC technology also needs to be modified. Yttria-stabilized hafnia (YSH) is being researched to compensate for the increase in high temperatures while being able to provide the same protection as current TBCs. In current thrust chambers there is no protective coating that insulates the inner lining of the chamber. Thrust chambers are being researched as potential candidates for TBC's in order to increase efficiency, increase heat transfer properties and to increase service life and burn times. Industrial grade YSZ be deposited using magnetron sputtering and thermal spray processes. These sputtering deposition processes were performed at 500°C to determine the best microstructure and bond between the substrate and TBC. TBC's deposited on copper, silver, and Haynes 230 (nickel-based superalloy) substrates are analyzed using scanning electron microscopy (SEM) and x-ray diffraction (XRD) to characterize the microstructure, coating thickness and TBC/substrate bond, and crystal structure. The results are presented and discussed.

I. Introduction

The last 30 years materials engineers have been under continual pressure to develop materials with a greater temperature potential or to produce configurations that can be effectively cooled or otherwise protected at elevated temperature conditions. Engineers are pressured to increase the efficiencies of current technologies due to the energy crisis that the world is facing. While the key tasks for the future of gas turbines are to increase overall efficiencies to meet energy demands of a growing world population and reduce the harmful emissions to protect the environment, space transportation is looking to lower costs while increasing operational efficiency and reliability of our space launchers. The important factor to take into consideration is the rocket nozzle design. High heat flux thrust chambers are exposed to more severe operating conditions when compared to gas turbines such external loads, heat transfer, transients, and the fluid dynamics of expanded hot gases[1]. In order to push for higher temperatures, engineers need to come up with a way to compensate for increased temperatures because material systems that are being used are either at or near their useful properties limit. The current work is focused on nanostructured yttria stabilized zirconia coatings for high temperature protective coating application in high heat flux thrust chambers.

II. Experimental

An 8%YSZ target of 2″ diameter and 0.125″ thickness was used to fabricate the TBC's onto copper, silver, 403 stainless steel and Inconel 738 substrates. Materials were mixed by solid state reaction using mixed proportions of ZrO_2 stabilized by Y_2O_3. Coatings were then grown using RF magnetron sputtering technique using previously optimized operating parameters, but changed the deposition temperature conditions to 500 °C.

III. Results

Figure 1 below represents the XRD analysis of thermally sprayed YSZ coating on copper which has a tetragonal structure. Sputter coated YSZ coatings are nanocrystalline in nature and have the face-centered cubic structure. The structure of both thermal spray and sputter coated YSZ can be observed in the SEM surface analysis in Figure 2.

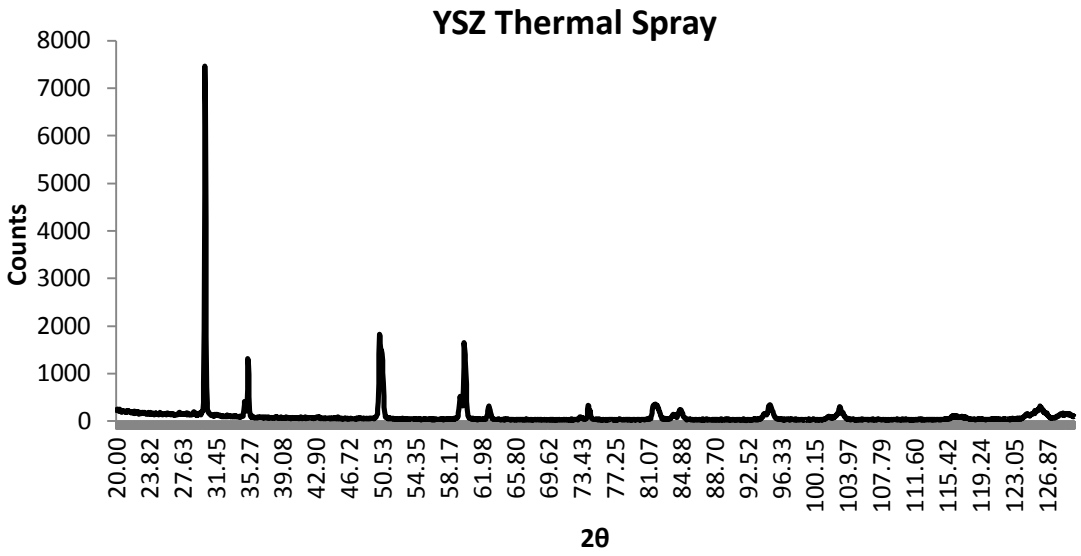

Figure 1. X-ray diffraction analysis of YSZ thermal spray coating on copper substrate.

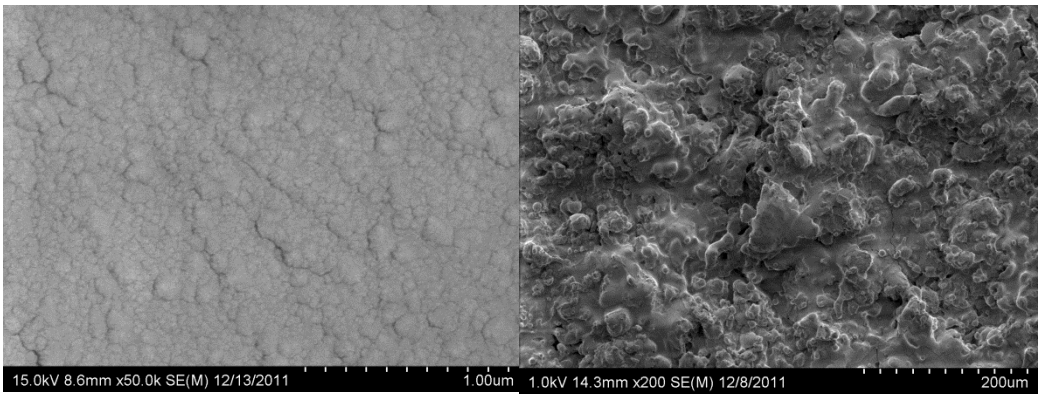

Figure 2. Surface characterization using SEM analysis of YSZ thermal spray coating on copper. The image on the left represents sputter coated YSZ and the right image is representative of YSZ applied using thermal spray.

Metallographic representation of the cross section is also observed in Figure 3. Both copper and Inconel 738 were used for the application of the thermally sprayed YSZ top coat. Inconel 738 had a MCrAlY bond coat applied before the application of the top coat whereas the copper was just coated with YSZ.

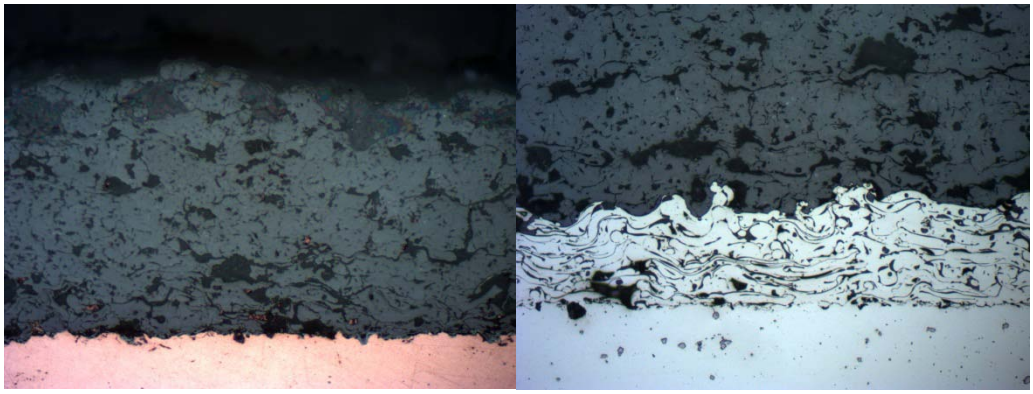

Figure 3. Metallographic examination of the cross-section for both copper (left) and IN-738 (right) of thermally sprayed YSZ. Notice the contrast differences between the top coat, bondcoat and substrates. Both images were taken at 200X magnification.

Once deposition processes are optimized then deposition will then be performed on actual small scale thrusters in a combustion chamber. Thermal mechanical analysis will be performed using a thermal cycling furnace to observe microstructural and mechanical behavior of the TBC's on the substrates. This research should aid in engineering decisions involving the use of YSZ for TBC's on thrust chambers to increase efficiency, improve regenerative cooling mechanisms and increase service life.

IV. Conclusions

It is obvious that the application technique changes the crystallographic structure as discovered through XRD analysis. SEM analysis shows the very different surface finish in both cases of thermally sprayed and sputter coated YSZ. For all cases of thermally sprayed YSZ, neither structure nor the surface finish changed with different substrates (Cu, 403 SS, IN-738). Further metallographic analysis and residual stress analysis are currently in progress.

References

1. Huzel, D. K., Huang, D. H., and Arbit, H., "Modern Engineering for Design of Liquid-Propellant Rocket Engines", American Institute of Aeronautics and Astronautics (AIAA), (1992).

This material is based upon work supported by National Aeronautics and Space Administration (NASA) under award number NNX09AV09A

THRUST MEASUREMENT AND PROPELLANT FEED SYSTEMS DEVELOPMENT FOR TESTING LOX/METHANE REACTION CONTROL THRUSTERS

Daniel H. Hernandez, Gustavo Martinez, Arturo Acosta-Zamora, Ahsan Choudhuri, PhD
NASA Center for Space Exploration Technology Research (cSETR)
Department of Mechanical Engineering
University of Texas at El Paso
El Paso, Texas, 79968-0521
E-mail:csetr@utep.edu

ABSTRACT

The paper describes the development of thrust measurement and propellant feed systems to test the performance of 2 to 8 lb_f LOX/Methane reaction control thrusters. The development of a cryogenic liquid propellant delivery system as well as thrust measurement device is necessary for accurate and repeatable testing of thruster performance. The propellant feed system includes three subsystems: (i) Liquid methane production and delivery subsystem, (ii) LOX delivery subsystem, and (iii) Propellants flow control and monitoring subsystem. Liquid oxygen is supplied via a previously designed system, which contains a self-pressurizing tank, a series of valves and other components, and is terminated at a manifold, allowing for the supply of the oxidizer to the thruster. A cart-based mobile liquid methane delivery system was designed in order to provide metered quantities of fuel to meet combustion requirements. A liquid methane production unit was also integrated within this system. Liquid methane production is accomplished with a condenser, utilizing liquid nitrogen as a chiller. A coil, using 316 stainless steel, was designed and installed in a double-ended sample cylinder where liquid nitrogen is routed through the coil, while gaseous methane surrounds it. This results in the gradual cooling of the methane, thus allowing for the production of liquid methane to be accomplished within the mobile unit itself. Flow control and monitoring of the system is done remotely from a control room through a LabVIEW program interface and a DAQ system; such program allows not only the manipulation of the components following an experimental procedure and timing, but also real-time data acquisition from the various components for flow, temperature, pressure, and thrust measurements within the system. The Thrust Measurement system uses a torsional thrust balance fitted with a laser-positioning sensor. The thrust balance utilizes torsional pivots to provide a consistent and measureable resistance to thrust.

1 Requirement Overview

1.1 Requirements

The design and development of the liquid methane propellant system and torsional thrust balance was centered on meeting the requirements detailed in Table 1. These parameters served as the basis for the determination of total propellant mass and volumetric flow required at each thrust level, thus providing a sizing parameter for the systems. The propellant system was designed to produce a total of 2L of liquid methane in a double-ended stainless steel cylinder and a maximum operating pressure of 300 psi. The thrust measurement system has a stiffness of 28.2, natural frequency of 7.5 Hz, and damping coefficient of 0.02 under operation.

THRUST MEASUREMENT AND PROPELLANT FEED SYSTEMS DEVELOPMENT FOR TESTING LOX/METHANE REACTION CONTROL THRUSTERS

Thrust	2 lbf to 8 lbf
ISP	>150s
Mixture Ratio	10
Propellant State	Gas, two-phase, and liquid
Run time	2 to 3 min at 50% duty cycle
Altitude 1	1st phase at ambient
Altitude 2	2nd phase at 11.3 psi

Table 1. Requirements for the propellant delivery system and torsional thrust balance

2 Propellant Delivery System

2.1 Description

The Center for Space Exploration and Technology Research has carried extensive research on the development of liquid propellant systems capable of producing and delivering the propellants while maintaining them in their liquid form. The propellant feed system for this project includes three subsystems: (i) Liquid methane production and delivery subsystem; (ii) LOX delivery subsystem; (iii) Propellants flow control and monitoring subsystem.

There are three main components of the system: 1) liquid nitrogen manifold 2) the liquid methane production tank and 3) the run tank. The liquid nitrogen manifold present in the system allows the user to connect a liquid nitrogen container to the system with a flexible hose, giving the system capability of being placed in different positions for convenience. Two identical double ended stainless steel cylinders were utilized in the system, one to serve as a condenser for liquid methane production, while the other serves as a container which may be pressurized up to 1800 psi for propellant delivery.

2.2 Torsional Thrust Measurement Balance

A thrust stand was developed such that thrust levels in the range of 2 to 15 lb_f could be measured with appropriate accuracy. A torsional thrust balance design was chosen due to its design being highly suitable for low thrust applications. Thrust balances operate by using the thruster to generate a moment; the thruster is placed at a known distance from the pivot axis, which offers a known resistance; therefore, the moment generated during operation induces a displacement of the moment arm. In turn, this displacement can be measured in various ways; most commonly, and arguably most simply, by an optical laser. Subsequently, this displacement can be correlated to a thrust value.

The assembly is constructed of stainless steel type 304. This material was chosen over aluminum due to the TTB being in service with liquid oxygen. Figure 2 shows the torsional thrust balance being utilized in thruster testing. An optical laser collects readings near the end of the arm for maximum resolution.

2.3 Propellant System and Thrust Measurement Interface

The propellant delivery and thrust measurement systems are integrated via the use of LabVIEW software. A program interface was developed to allow the control of system components as well as real-time data acquisition of mass flow, pressure, temperature, and thrust. Figure 2 shows the developed interface utilized during testing procedures.

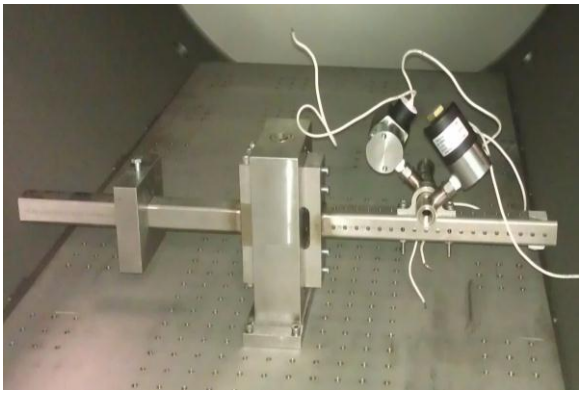

Fig. 1 Thrust Stand Assembly

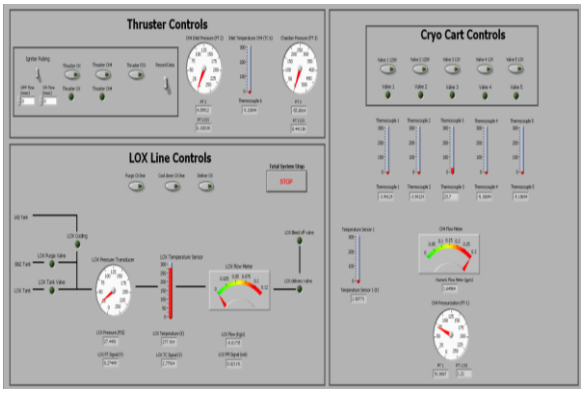

Fig. 2 LabVIEW program interface

Conclusions

The design and development phases of the thrust measurement and propellant delivery systems have been completed. Both systems are currently under use for testing of an 8 lb_f thruster. Steady state response as well as pulsing response is being analyzed. A natural frequency of 7.5 Hz and a damping coefficient of 0.02 were determined during actual testing operation.

3.3 References

[1] Brown, Charles D. *Spacecraft Propulsion.* American Insttue of Aeronautics and Astronautics, Inc. Washington, DC.

[2] Riverhawk Company. (2011). *Cantilevered pivot bearings*. Retrieved from http://www.flexpivots.com/cantileveredpivotbearings

[3] Rao, S. S. (2010). *Mechanical vibrations (5th edition)*. (5th ed.). New York: Addison-Wesley

[4] Sutton, G. P. (2010). *Rocket propulsion elements and engineering mechanics: Statics* . (8th ed.). New York: John Wiley & Sons, Inc.

[5] Zehe, M. (2010). Chemical equilibrium with applications. In *Chemical Equilibrium with Applications* Maryland: N.A.S.A. Retrieved from http://www.grc.nasa.gov/WWW/CEAWeb/

[6] Reaction Design. (n.d.). Chemkin. In *CHEMKIN* San Diego: Reaction Design. Retrieved from http://www.reactiondesign.com/products/open/chemkin.html

TEST AND DEVELOPMENT OF A CARBO-THERMAL RIG TO STUDY LIQUID METHANE HEAT TRANSFER CHARACTERISTICS

M. Galvan[1], A. Trujillo[2], C. P. Garcia[*], A. Choudhuri
[1] Mechanical Engineering, cSETR, El Paso, TX 79968, USA;
* Corresponding author (cpgarcia1@miners.utep.edu)

Keywords*: methane, heat transfer, carbo-thermal*
Are you planning on attend the student paper poster: (Yes)

ABSTRACT

This paper discusses the utilization of a high heat transfer test facility built at the Center for Space Exploration Technology Exploration Technology Research (cSETR) at the University of Texas at El Paso (UTEP) for the purpose of testing liquid methane ((L) CH_4) and regenerative cooling applications for liquid engine combustion chambers. In addition, experimentation is performed under vacuum conditions. Various measurement devices are used to obtain the relationship between the heat transfer and fluid flow behavior.

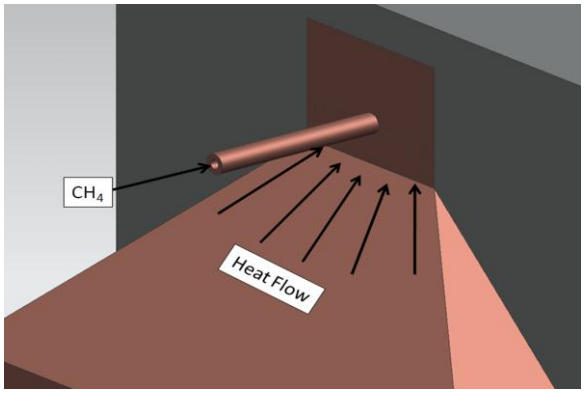

Fig. 1. Heat flow from tapered copper block to test section.

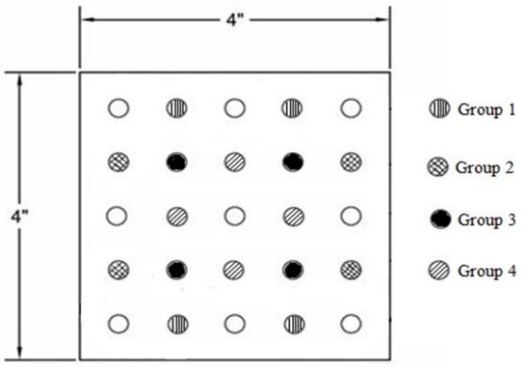

Fig. 2. Symmetric cartridge heater placement for even temperature distribution.

1 Introduction

The heat transfer characteristics of methane are currently being studied at the Center for Space Exploration Technology Research (cSETR) with the use of a carbo-thermal heating rig. Carbo-thermal is a term used to describe the study of a carbon-containing compound at elevated temperatures. The carbo-thermal rig concentrates heat onto an area to be able to study conductive heat transfer characteristics. While there are several heating methods to study heat transfer characteristics of fluids, a carbo-thermal rig was chosen because of its relevance to propulsion applications. A similar system was designed by the Air Force Research Laboratory in 2004 [1]. The cSETR heat rig was designed to incorporate key features of the AFRL design while omitting complex components such as a mobile heating block and spring loaded thermocouples [2]. The cSETR rig employs operation in a vacuum chamber, and a conductively heated modular test section. The modularity of the test section allows for various channel geometries to be considered in addition to type of fuel tested.

2 Condensing Operation and Testing

The carbo-thermal rig is supplied liquid methane by a methane condensing system. The condensing system was designed and built by cSETR due to the fact that liquid methane quantities available for purchase and industrial applications are too large for laboratory use. The condenser used to provide liquid methane for the heat rig consists of a 2.25 L stainless steel tank with a 10 foot long, 1/8 inch diameter stainless steel coil placed inside. Insulation for cryogenic application is achieved by wrapping the outer portion of the tanks with 25 feet of 1/4 inch diameter copper line and three layers of Aerogel^{TM} insulation. The condenser liquefies gaseous methane by allowing liquid nitrogen to flow through the inner and outer coils. By controlling liquid nitrogen flow rates through the individual coils the condensing tank temperature is maintained. Five E-type thermocouples inside the condenser tank allow the level of liquid methane inside to be monitored. The condenser fills with approximately 2 liters of liquid methane after 1 hour of operation.

3 Rig Operation and Testing

3.1 Rig System

The heat rig's current objective is to ultimately simulate a regenerative cooling channel on a bi propellant rocket engine. To simulate the conditions present in the engine, the heat rig incorporates a copper heating block fitted with cartridge heaters. The block has a tapered top to direct heat to a 1 x 2 x 0.85 inch copper test section, which rests on top of the heating block's smaller 1 x 2 inch area [4]. In addition, a cooling channel runs through the center of the test section. The current block design allows for a capacity of up to 25 cartridge heaters to be installed at any one time. A switch connected to the cartridge heaters allows for manual temperature control of the block. Moreover, liquid methane is flowed through the cooling channel, where it is heated by the test section, as shown in Fig. 1. Also, a stainless steel stand is used to support the heating block in the vacuum chamber, and an aluminum cradle maintains proper contact between the test section and heating block, promoting heat transfer. The experiment is conducted in vacuum conditions to reduce convective heat transfer losses and prevent oxidation of the heating block and test section inside the vacuum chamber. To obtain the temperature profile of the cooling channel, six sheathed K-type thermocouples are inserted into holes machined along the axis of the test section to record channel temperature. Furthermore, the heating block temperature is monitored with four K-type thermocouples placed along the tapered surface between the copper block and the aluminum cradle, as shown in Fig. 1.

Currently, the copper block is heated by sixteen 400 W cartridge heaters. Four groups of four cartridge heaters are utilized to heat the block evenly. The heating cartridges are arranged symmetrically throughout the block to prevent uneven temperature distribution. Fig. 2 shows a group of four heating cartridges placed in a diamond formation around the center cartridge hole, while twelve other heaters are placed symmetrically around the center of the block layout used to prevent uneven heating. Normal operation of the block allows channel wall temperatures of up to 650 °C.

Other equipment used in the heat rig includes inline E-type thermocouples installed in the methane line before and after the test section. Cryogenic pressure transducers were placed outside of the vacuum chamber to measure inlet and outlet pressures of the methane flow. A recent upgrade to the system includes the installation of a turbine flow meter upstream of the vacuum chamber inlet.

3.2 Operation and Testing

Before performing the experiment, a procedure checklist is followed to ensure that proper conditions are achieved. The system is checked for leaks at line connections, valves, and vacuum feedthroughs. Components are checked to ensure that they are suitable for testing. The thermocouples on the test section are checked to ensure that they are touching the channel surface with a continuity check. Before liquid methane flows through the system, it is necessary to chill the line with liquid nitrogen. Chilling ensures methane remains a cryogenic liquid as it flows into the test section. Once the line has been chilled the run tank is pressurized with helium and the run tank valve is then opened. As liquid methane flows through the test section, temperature and pressure data are recorded using a DAQ.

4 Discussion

While the condenser has successfully condensed the full capacity of the tank, there have been some issues while transferring the liquid methane from the condenser to the run tank. While transferring the liquid methane, only a small amount of liquid is actually transferred to the run tank before the liquid flow was interrupted. The problem is likely caused by vapor lock. An attempt was made to alleviate the vapor lock by adding vent valves on top of the condenser and in between the condenser and run tank. Because only a small volume of liquid methane was transferred, only cold methane gas data was obtained.

5 Conclusions and Future Work

From the performed experiments, it was determined that the current amount of liquid methane was only sufficient to perform a 30 second test, but it is desired to run longer tests to properly characterize the heat transfer properties. From the data obtained from the carbo-thermal rig, it was determined that the inlet conditions of methane were not within planned testing conditions.

To ensure that liquid methane is flowing through the cooling channel when obtaining the temperature profile, it is planned to upgrade the current condenser setup and implement a single 12 liter tank to avoid the issues associated with transferring the liquid methane from the condensing tank to the run tank. Once the temperature profile of the cooling channel is obtained, dimensionless properties such as Reynolds number, Nusselt number, and Prandtl number will be calculated so that the thermal conductivity and heat transfer aspects of liquid methane can be determined [3].

References

[1] Auyeung, T. P., Bates, R. W., Irvine, S. A., Maas, E. D. *Design of a High Heat Flux* "Facility for Thermal Stability Testing of Advanced Hydrocarbon Fuels", Air Force Research Laboratory Propulsion Directorate Edwards AFB, CA 93524, (Apr 2004)

[2] Bates, R.W., Billingsley, M.C., and Lyu, H.Y. "Experimental and Numerical Investigation of RP-2 Under High heat Fluxes", Air Force Research Laboratory, Propulsion Directorate Edwards AFB, CA 93524, Denver, CO (May 2007)

[3] Setzmann U., Wagner. W "A New Equation of State and Tables of Thermodynamic Properties of Methane Covering the Range from the Melting Line to 625 K at Pressures up to 1000MPa," *Institut fur Thermo-und Fluiddynamik, Ruhr-Universitat Bochum*. May 29, 1991

[4] De Witt, David P., F.P. *Incropera, Fundamentals of Heat and Mass Transfer. Fifth Edition*. Hoboken, NJ: John Wiley & Sons, Inc., 2002.

PRODUCTION OF COLD GAS METHANE FOR USE IN IGNITION PHYSICS RESEARCH

R. Ellis[1], J. Flores[1]*
[1] Center for Space Exploration Technology Research, University of Texas at El Paso, El Paso, TX 79938, USA;
* Corresponding author (jrflores2@miners.utep.edu)

Keywords: *Liquid Methane, Nitrogen, Heat Exchanger*
Are you planning on attending the student paper poster: No

ABSTRACT

In recent years, LOX-methane rocket propulsion has jumped to the attention of researchers as a viable propellant combination due to its many benefits. Some of which include high specific impulse due to its high energetic content, and the ability to incorporate the main propulsion to the reaction control system. To address the knowledge gap in ignition physics, cooling characteristics, and injector design in LOX-methane propulsion the Center for Space Exploration Technology Research has developed the Goddard Laboratory. The purpose of this paper is to detail the process which will be used to condense methane for use in combustion testing, as well as briefly detail the overall scope and hardware of the system for which it is being used.

Fig. 1. Coil heat exchanger

Fig. 2. Tank heat exchanger.

1 Introduction

Over the last few decades most research in the field of rocket propellants has centered on only a select few of widely used fuels and oxidizers. Recently however, more studies are being conducted in order to establish possible uses and benefits of several different propellant types. Liquid methane is among these new fuels that has very promising characteristics. Robinson et al. has identified the potential for greatly reducing the mass of future spacecraft by reducing the complexity of the propulsion system.[1] One of the greatest benefits of using liquid methane is the ability to incorporate the main propulsion system and the auxiliary reaction control system into one. Liquid methane also has many other advantages over contemporary fuels. Among these advantages a cryogenic LOX/LCH_4 propulsion system has the ability to keep both storage tanks at a similar temperature reducing the complexity of the cooling system. Liquid methane is also considered to be a non-toxic and inexpensive fuel.[2] However, liquid methane has not been tested as extensively as other fuels, therefore many characteristics of its combustion are still

unknown. The purpose of this setup is to produce liquid methane for use in a Multipurpose Optically Accessible Combustor (MOAC) in order to observe and record the characteristics of LOX/LCH_4 combustion, as well as for use in future combustion tests.

2 Hardware

The hardware used in the production of liquid methane consists of two main parts: two physical heat exchanging devices which use liquid nitrogen to chill the methane below its boiling point, and the Data Acquisition and Remote Control System (DARCS)[3] which records data and controls the entire process in a safe, metered and remote manner. Both heat exchangers are shown in figures 1 and 2 and detailed later in this paper. The DARCS incorporates a Graphical User Interface (GUI) through the use of National Instruments LabView program. The automation hardware consists of four PCI cards which control the output signals for solenoid valves as well as receive signals from thermocouples, pressure transducers, mass flow meters, and a Pirani vacuum gauge. This setup will be used to conduct experiments aimed at understanding the ignition physics and combustion characteristics of liquid methane.

2.1 Coil Heat Exchanger

There are currently two heat exchangers designs which will be tested for effectiveness. The first is a simple coil of pipe submerged in a liquid nitrogen bath and the second is a large insulated cylinder with a coil wrapped around it.
The first heat exchanger, shown in Fig. 1, was constructed using a 1 foot long coil of stainless steel with an outside diameter of 1/8” and a wall thickness of 0.028”. This coil is then filled with helium and submerged into a bath of liquid nitrogen at 77 K. The coil is then allowed to cool until it is very nearly the temperature of the liquid nitrogen. Once it has cooled methane at 300 K is run through coil in order to chill it to liquid.

2.2 Tank Heat Exchanger

The second heat exchanger is shown in Fig. 2 and is made of stainless steel with a thickness of 1”. It consists of small inlet inside diameter of 1/2” expanding to a diameter of 3.5” and then contracting to the original size. The larger diameter portion is 10.9” long and is wrapped in a 6’ coil of stainless steel pipe that is 1/4” diameter with a 0.018” thickness. The entire setup is wrapped in high quality Aerogel insulation so the heat loss is assumed to be negligible. The setup is then allowed to cool by running liquid nitrogen through the coil until the setup is approximately the temperature of the flowing liquid nitrogen. Once it has cooled, methane at 300 K is fed into the system in order to chill it to liquid.

3 Calculations

Calculations have been done on both heat exchangers with similar assumptions made as follows:

1. Each heat exchanger is cooled using liquid nitrogen before operation.
2. It is assumed that the inner surface temperature which is contact with the cooling methane is at the temperature of the liquid nitrogen 77 K.
3. The wall temperature remains constant during operation.
4. Steady State is achieved.

A spreadsheet was programmed in order to calculate the exit temperature of methane given a set of initial conditions which are defined by user inputs. The properties of methane at various temperatures were obtained by plotting the properties versus temperature and obtaining an equation which fits the data for that temperature range.
First the initial conditions must be specified. The conditions that are required are: the inlet temperature of the methane and nitrogen, the flow rates, the dimensions of the heat exchanger, and the material properties. There is also an initial condition for the estimated exit temperature of the methane. This is because of the iterative process that needs to be done in order to find the actual exit temperature. First a temperature is assumed and the calculations are completed and return a calculated exit temperature. The estimated temperature is then changed to this new calculated temperature and the process is repeated until they match.
The largest assumption made in this process is the assumption of constant wall temperature. With this assumption the following equation can be used for both heat exchanger designs:

$$T_e = T_s - (T_s - T_i)\exp(-hA_s/\dot{m}c_p) \quad (1)$$

Using equation 1, the exit temperatures were calculated for both the coil and tank heat exchangers, and were found to be 108 K and 140 K respectively. This indicates that for the coil heat exchanger liquid methane is produced, and chilled gaseous methane is created for the tank heat exchanger.

4 Preliminary Test

An experiment was conducted on the coil heat exchanger using a flow rate of 40 L/min, however, no data was recorded only the observation that with gaseous methane entering at room temperature, liquid methane was created. This seemingly confirms the calculations done previously but more experimentation is needed. An additional test was conducted on the tank heat exchanger using a flow rate of 1 L/min. In this test the tank was used to supply liquid methane to a small thruster, however, only chilled gaseous methane was produced. The likely cause of this is the flow rate being too low. This also agrees with the previous calculations.

5 Conclusion

In conclusion, the preliminary test results appear promising. The heat exchanger designs may need to be optimized but the goal of creating liquid methane has been achieved. Having the ability to create liquid methane in house is extremely important in order to begin studying its properties. This is a promising first step toward the eventual goal of understanding liquid methane combustion characteristics.

References

[1] P. Robinson, E. Veith, E. Hurlbert, R. Jimenez, T. Smith “445N LO2/LCH4 reaction control engine technology development for future space vehicles”. *Acta Astronautica*, 836-843

[2] T. Neill, D. Judd, E. Veith, D. Rousar “Practical uses of liquid methane in rocket engine applications”. *Acta Astronautica,* 65, pp 696-705.

[3] Navarro, C. D., Betancourt-Roque, J., Sanchez, L. E., Robinson, N., & Choudhuri, A. (2011). Development of a Multi-Purpose Optically Accessible Rocket Combustor for Liquid Oxygen and Hydrocarbons. 47th AIAA/ASME/SAE/ASEE Joint Propulsion Conference & Exhibit. San Diego, CA: AIAA.

THE DEVELOPMENT OF METHANE AND OXYGEN BI-PROPELLANT 1 TO 5 NEWTON CLASS THRUSTERS

Alejandra Vargas,[1] Marjorie A. Ingle,[2] Arturo Acosta,[3] Daniel H. Hernandez,[4] Ahsan Choudhuri, PhD[5]
NASA Center for Space Exploration Technology Research (cSETR)
Department of Mechanical Engineering
University of Texas at El Paso
El Paso, Texas, 79968-0521
E-mail: aavargas3@miners.utep.edu

Keywords: Bi-Propellant Thruster, Methane, Oxygen

Are you planning on attend the student paper poster: (Yes)

ABSTRACT

Current advancement of technology and manufacturing methods, have given considerable attention to micro thrusters for spacecraft applications. Micro propulsion systems are being considered for Miniature Kill Vehicles (MKV) and Micro Satellite Systems (MSS) with an emphasis in increasing performance while reducing weight and cost. Reducing the weight seems practical when reducing the size of the propulsion system, but problems are encountered with this process. Propulsion is strongly influenced by propellant selection and mixed ratio. A thorough understanding of stabilizing thrust levels and the ability to control the propulsion system is important in order to meet the requirements of the specific propulsion application. Certain applications might require long thrust durations, while others require small thrust pulses. Choice in propellant can influence hardware selection needed to achieve reliable thrust levels. This paper investigates the development of flight ready hardware (thruster) for cube sets atellites. The thruster was designed from a previous iteration, to have its own pressure and valve control system in order to control thrust levels and pulse lengths. The propellants to be tested will be gaseous Methane and Oxygen.

1 Requirement Overview

1.1 Requirements

The design and development of the bi-propellant thruster (Vernier Thruster) was centered on meeting the requirements detailed in Table 1. These parameters served as the basis for the determination of optimum thrust and mixture ratio levels for pulsing conditions.

Thrust	1 N to 5 N
ISP	110
Mixture Ratio	3.5
Propellant State	Gas
Run time	250 ms, 500 ms, 750 ms, 1000 ms
Altitude 1	1st phase at ambient

Table 1. Requirements for the bi-propellant thruster

2 Design

2.1 Injector

The design of the injector had gone through several iterations in order to find the best configuration for a co-axial swirl injector. A fundamental part of the design was to insure easy manufacturability while keeping the injector modular for different propellants. The injector used for these experiments is shown in Figure 1. The injector allows fuel to be injected into the rear of the thruster, where the flow is introduced tangent to the oxidizer flow at the core of the center of the body. The total mixing length in the injector body was ¼ in which led directly to the combustion chamber of the thruster. The single oxidizer inlet diameter was machined at 3/16 in. The inlet of the oxidizer and fuel were threaded for a 1/8 in NPT adapters. The propellant feed system was directly connected to these adapters.

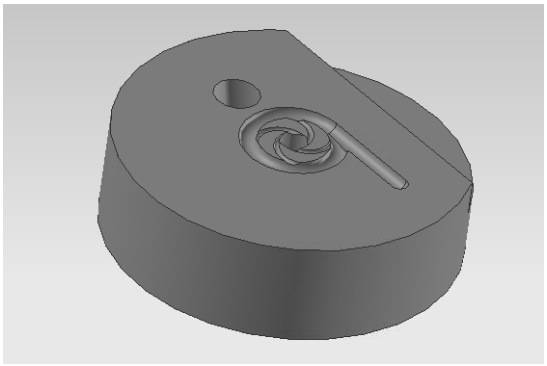

Figure 1. Injector Front

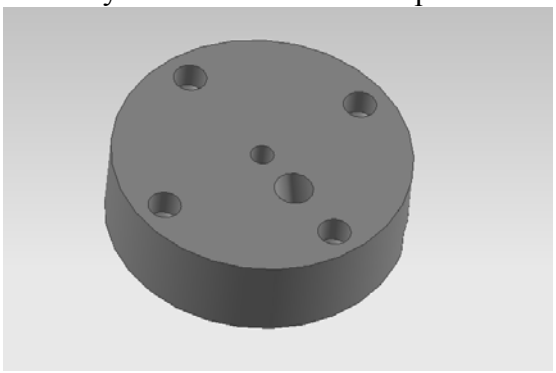

Figure 2. Injector Rear

2.2 Igniter

The igniter was made out of a steel tube with a .125 in outer diameter and a .085 in inner diameter. An alumina tube was inserted inside which insulated a single platinum wire. The platinum wire was bonded on to the alumina tube using Resbond 919, a high resistance ceramic compound with a high dielectric strength. The platinum wire protruded .01 in at one end of the igniter. This perturbation was necessary in order to create a high voltage arc within the wall of the injector. A voltage adapter was incased at the other end of the igniter to connect the high voltage transformer. The steel body of the igniter was threaded in order to seal the injector body from any leaks due to spikes in chamber pressure.

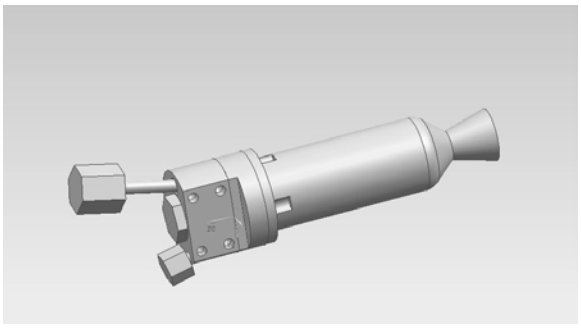

Figure 3. Thruster with Igniter

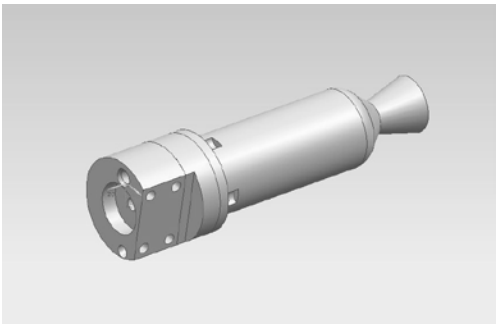

Figure 4. Thruster with Igniter ports

2.3 Nozzle

The nozzles are currently being designed with throat diameters of 0.118 in. for L^* values of 25, 40, and 50. The nozzles will be constructed from 304 stainless steel. Since all the testing was at altitude pressure, the area ratio of the nozzle was designed to be 3 in order for the exit plane pressure to match the ambient pressure of 14.7 psi.

3 Conclusion

The design of the new thruster has successfully incorporated the swirl injector, igniter, and nozzle has been successfully completed. The design is currently being manufactured in order to incorporate a new igniter that uses a different material similar to the properties of the platinum. The thruster is to be tested with the setup previously used and a new LabVIEW program that includes pulsing.

4 References

[1] Brown, C harles D . *Spacecraft Propulsion.* American I nsttue of A eronautics a nd Astronautics, Inc. Washington, DC.

[2] Yetter, V.Yang, Z.Wang, Y.Wang. “Development of meso scale liquid propellant thrusters”. 41th Aerospace Sciences and Meeting and Exhibit. Reno, Navada, January 2003. AIAA 2003-676

GROWTH OF THIN FILM CADMIUM TELLURIDE AND ZINC TELLURIDE FILMS USING NOVEL CLOSE SPACE SUBLIMATION DEPOSITOR

D. Marrufo[1]*, John McClure[2], and D. Zubia[1]
[1]Department of Electrical and Computer Engineering
[2]Department of Materials and Metallurgical Engineering
The University of Texas at El Paso
El Paso, TX 79968, USA;
* Corresponding Author (dmarrufo@miners.utep.edu)

ABSTRACT

Thin films of ZnTe and CdTe have been grown on CdS in a variety of methods for the use in photovoltaic systems. Limits to cell efficiency of these cells have been attributed to defects in the lattice that occur between the interface of CdS and CdTe for which ZnTe has been introduced to become a transition layer. During these film growths it was necessary to remove the sample and switch the source of the material being deposited to achieve different compositions in the film. It will be shown that a novel close space sublimation reactor has been developed in which the composition of the film being grown can be modified during the deposition process.

1 Introduction

Photovoltaics (PVs) which were originally thought of simply as an alternative for off-grid sites have in the last decade become recognized as a viable source for energy. The International Energy Agency estimates that from 2000 to 2010 the total annual power produced by installed photovoltaics increased from 207 MW to 14,195 MW in surveyed countries [1]. Unfortunately in the same report it is possible to see that the United States is lagging in the implementation of this technology both in annual installed photovoltaic power to Germany and the actual yearly production of PV modules in which China dominates with production of crystalline silicon based solar cells.

In this paper we will introduce the design and application of a novel close-space sublimation reactor (CSS4) whose intent is to manufacture $Zn_xCd_{(1-x)}Te$-based solar cells. Thin film CdTe-based PVs which have a theoretical efficiency of 29% are a perfect candidate due to the low cost of the raw materials required for the system, and because the efficiency of experimental and production PVs is still far away from optimal. The record CdTe PV had plateaued at 16.5% efficiency in 2001[2] and has just recently increased to 17.3% in the last year.

It is accepted that the low efficiency is due to a high defect density in the CdS-CdTe interface which leads to carrier recombination. This high defect density is built into the device when the CdTe layer is deposited onto the CdS due to the lattice mismatch of the two materials (~10%) [3]. It will be demonstrated that the CSS4 can be used to grow a buffer layer of ZnTe as well as the CdTe to reduce the lattice mismatch to CdS by controlling temperature of source and substrate, pressure and distance from source to substrate, all of which are parameters that affect growth rate and film quality during close-space sublimation. [4]

2 Depositor Design

The novel CSS4 shown in Figure 1(a) is able to control of principal parameters that affect deposition rates during close-space sublimation. The depositor can be completely automated using a computer interface. Three different material sources can be held within the chamber

in graphite crucibles. The crucibles are individually heated via cartridge heaters that can reach 1200˚C. The substrate is held within a graphite enclosure that also houses halogen lamps that provide radiation heat. Detailed view of both the cartridge heater and the substrate holder assemblies can be seen in Figure 1(b). Pressure can also be varied via a set of mass flow controllers which provide helium, oxygen or nitrogen flow and a vacuum pump providing sufficient vacuum to control the pressure down to 0.05 Torr. Finally movement is provided via two motors that are able change the distance between the source and substrate and also rotate the housing to switch between sources. [5]

3 Initial CdTe and ZnTe thin film characterization

Initial depositions show versatility of the CSS4 to create CdTe, ZnTe, CdTe/ZnTe and $Zn_xCd_{(1-x)}Te$ layers. An initial deposition using the CSS4 was developed to consistently deposit a 100nm thick film of ZnTe on a CdS/ITO/glass substrate as shown in the inset of Figure 2(a). A series of CdTe films were then grown following a ZnTe deposition by rotating the substrate holder to align with the CdTe source to finally create a CdTe/ZnTe/CdS/ITO/glass structures shown in the inset of Figure 2(b). Depositions for the growth of the CdTe films where initially performed by varying the source temp while maintaining a substrate temperature of 380˚C during 30 minutes. Afterwards, a second set of depositions were performed varying the substrate temperature while maintaining a source temperature of 425˚C. The grain structure of one of these films is shown in Figure 2(b). Source and substrate temperature greatly affects the film growth rate as shown in Figure 3(a) and (b). The grain size in comparison does not show such a simple trend over the temperature range chosen.

4 Conclusion and Future Work

The CSS4 reactor is capable of depositing different layers of CdTe and ZnTe during the same deposition run. It was also demonstrated that close space sublimation parameters of substrate and source temperature, distance between substrate and source, and pressure can be controlled via computer control. This proves that the CSS4 is capable of performing research level experiments with a high level of repeatability. The deposition parameters will be modified to grow a $Zn_xCd_{1-x}Te$ transition layer that provides better lattice match along the depth of deposition. These layers will then be characterized using Secondary Ion Mass Spectrometry **(**SIMS) which will allow us to plot the concentration of Zn, Cd and Te as a function of depth.

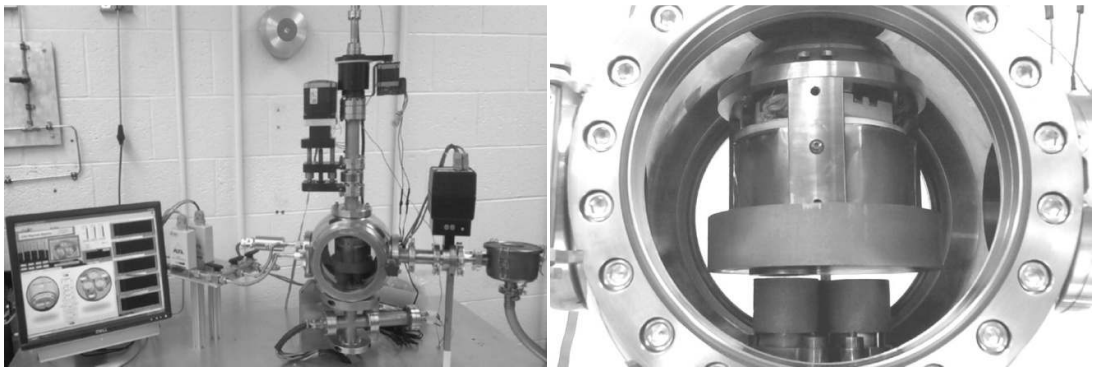

Fig.1. a) CSS4 close space sublimation reactor and computer interface left. b) Detailed view of CSS4 chamber showing substrate holder and source heaters.

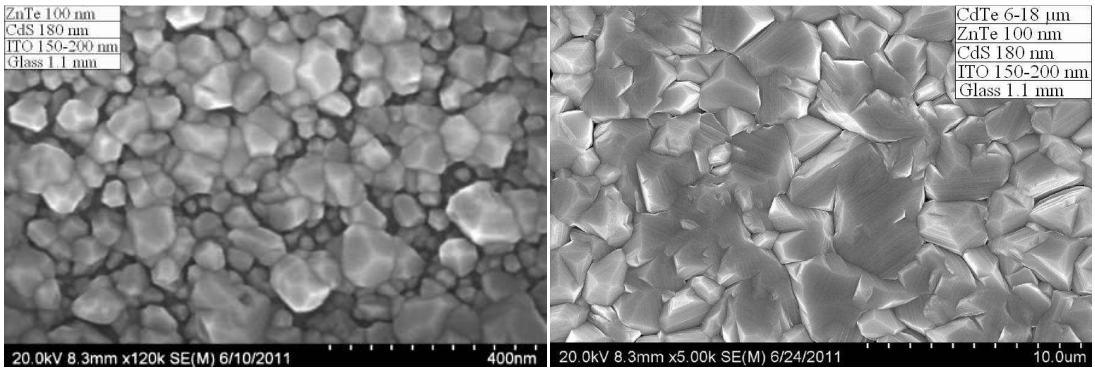

Fig.2. a) SEM image of 100nm ZnTe film deposited on CdS/ITO/glass substrate. b) SEM image of CdTe deposited on ZnTe/CdS/ITO/glass at 350-425˚C substrate-source temperature.

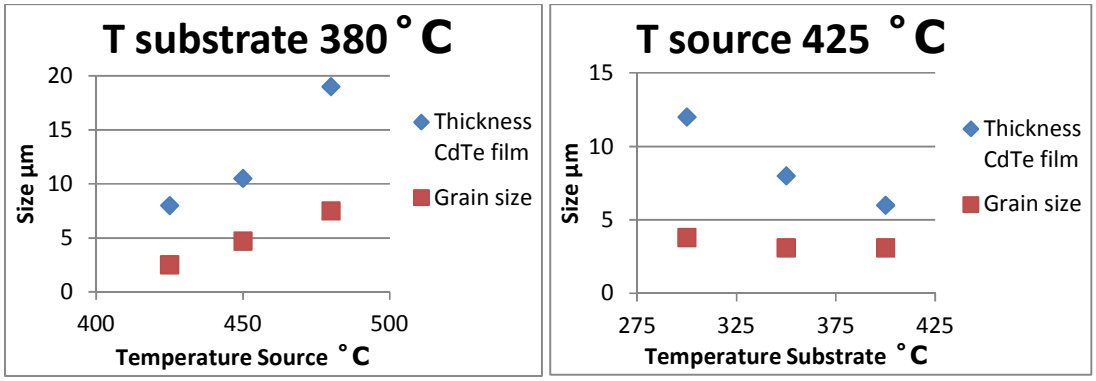

Fig.3. a) CdTe deposition results when maintaining constant substrate temperature at 380˚C and varying source. b) Results when maintaining constant source temperature at 425˚C

References

[1] IEA, "TRENDS IN PHOTOVOLTAIC APPLICATIONS Survey report of selected IEA countries between 1992 and 2010".Report IEA-PVPS T1-20:2011, International Energy Agency, 2011.

[2] X. Wu, J.C. Keane, R.G. Dhere, C. DeHart, D.S. Albin, A. Duda, T.A. Gessert, S. Asher, D.H. Levi, P. Sheldon "16.5%-efficient CdS/CdTe polycrystalline thin-film solar cells". *Proceedings of the 17th European PVSEC*, pp 995-1000, 2001.

[3] D. Zubia, C. Lopez, M. Rodriguez, A. Escobedo, S. Oyer, L. Romo, S. Rogers, S. Quiñonez, J. McClure "Ordered CdTe/CdS Arrays for High-Performance Solar Cells". *Journal of Electronic Materials*, Vol. 36, No 12, pp 1599-2007.

[4] J. Cruz-Campa, D. Zubia "CdTe thin film growth model under CSS conditions". *Solar Energy Materials & Solar Cells*, Vol. 93, pp 15-18, 2009.

[5] L. Rascon "Novel elemental CSS reactor: design and application to ZnCdTe depositions", *M.S. dissertation*, The University of Texas at El Paso, United States, 2008.

Structure and Residual Stress Analysis of Titanium Nitride PVD Coatings

Gustavo Martinez and C.V. Ramana
Department of Mechanical Engineering, The University of Texas at El Paso, El Paso, TX, 79968
Gustavo Martinez (gmartinez16@miners.utep.edu)

Attending Student Paper Poster (P. Presentation)

Keywords: *Titanium nitride, Thin Films, PVD coatings*

ABSTRACT

Titanium nitride (TiN) coatings are subject of numerous investigations because of its unique physical and mechanical properties such as hardness, chemical stability, wear resistance and diffusion barrier properties among others in many different applications. Such characteristics are dependant on many factors during physical vapor deposition (PVD) of the coatings including temperature, power, thickness and time of deposition. TiN_x Samples were grown using DC (Direct Current) sputtering method because has shown in previous experimentation the formation of crystallographic grains in (111) orientation [1], most desired to enhance physical film properties such as electro migration lifetime [2-4]. The objective of this investigation is to compare chemical, compositional profiles and grain structure formation in Titanium nitride coatings grown on Si and MgO substrates. Grazing incidence X-ray diffraction (GIXRD) measurements were used to analyze the texture development in the TiN coatings. Residual stress was calculated with this non-destructive technique to analyze micro structural details and thin film properties.[5] Scanning electron microscopy (SEM) and Energy Dispersive X-ray Spectroscopy (EDAX) are used to analyze the grain formation, size and chemical information of the TiN coatings. The results are presented and discussed.

Introduction

Titanium nitride exhibits an exceptional combination of chemical, physical, mechanical and electrical properties, such as a high degree of hardness, chemical stability, high thermal conductivity, immunity to wear and corrosion, chemical inertness and biocompatibility. The properties of thin films and/or coatings such as preferred orientation of lattice plane and electrical resistance, grown by physical and chemical vapor deposition (PVD) methods are highly dependent on many factors. Gas pressure, reactive gases, deposition rate, temperature and substrate material conditions will make resultant properties of thin films suitable for a wider range of applications if the material properties are tuned right [6-8]. The better understanding of the complex thin film properties lies the in comparative research analysis of samples grown in different set of conditions.

Methodology

Titanium nitride (TiN) films were deposited by DC- sputtering using a Ti metal target in N_2-Ar mixtures onto silicon (Si) and magnesium oxide (001) (MgO) substrates. The samples were grown with different thicknesses values varying in the range of 5-100 nm. The samples were characterized by grazing incidence X-ray diffraction (GIXRD) and scanning electron microscopy (SEM). The GIXRD enhances the diffracted signal coming from the thin film, by

keeping a fixed low angle of incidence between the X-rays and the sample surface. This insures penetration into the coating allowing measurement of residual stresses within concentrated parts of the film [3,4]. It also reveals crucial information about the crystal structure and chemical composition of the coating. SEM measurements allowed us to analyze the grain size and morphology with respect to time and temperature.

Results and Discussion

The SEM images of TiN coatings are shown in Fig. 1. The imaging analysis demonstrates fully grown grains on DTRA 59 sample with an average grain size ~24 nm. In Fig. 2, SEM images DTRA 56 sample are shown. It is evident that the samples exhibit grain morphology with an average grain size ~16 nm.

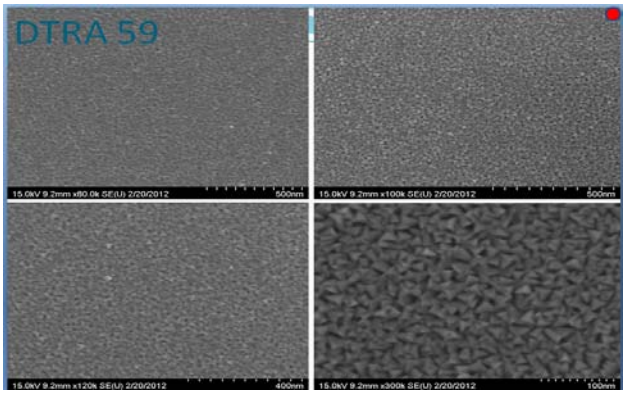

Fig. 1. SEM pictures depicting fully grown grains on DTRA 59 sample zoomed at 80 K, 100 K, 120 K and 300 K. Average grain size 24 nm.

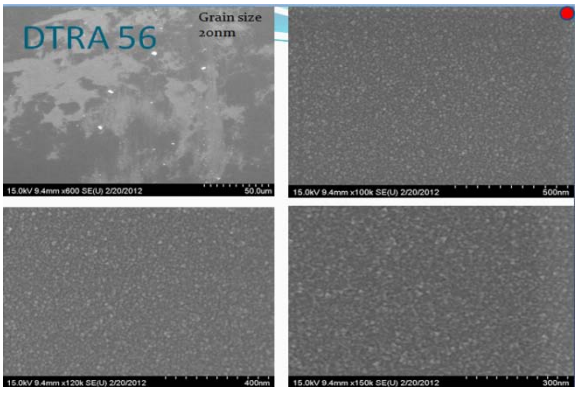

Fig. 2. SEM pictures depicting grain crystals on DTRA 56 sample, zoomed at 80 K, 100 K, 120 K and 150 K. Average grain size 16 nm.

XRD and GIXRD results demonstrate the TiN coatings exhibit a preferred (111) orientation under equilibrium conditions. TiN crystals are found in a face centered cubic structure. Figure 3 shows the XRD data of TiN coatings. In Fig. 3, the residual stress is calculated using a modified sin2ψ based in the measurement of lattice parameters determined from a fixed Bragg reflection at different tilting angles (chi ψ= -10,25) [5].

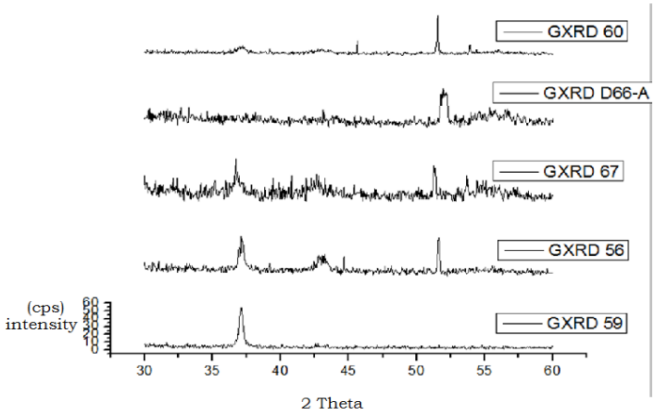

Fig. 3. GAXRD scan of silicon samples Coated with Titanium nitrate. It can be observed the characteristic (111) orientation peak around 2 Theta= 36°

Using a new experimental method for calculating residual stress using the grazing-incidence X-ray diffraction in the reference peak it was calculated that the residual stress to be 6.22 MPa in compression.

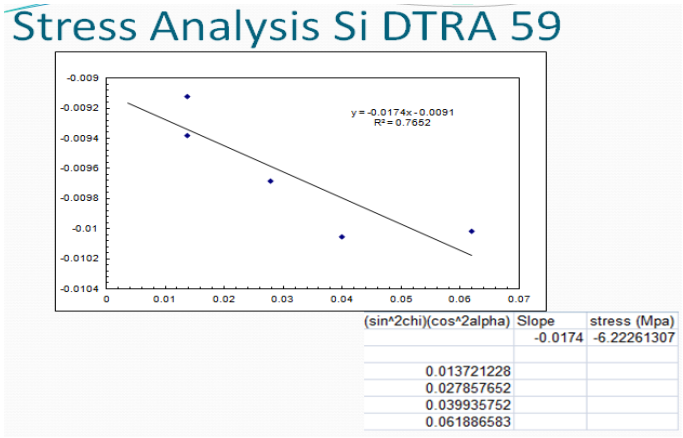

Fig. 4. The residual stress is calculated to be -6.22 MPa

Conclusion

TiN coatings with different thicknesses were grown. The effect of the variation of growing conditions and their effect on the chemical, physical and mechanical properties of the films were studied by using XRD and SEM. The analysis showed that nano-crystalline films are governed by the preferred orientation in (111). A compressive stress across the interface exists for the coatings grown on Si while the magnitude is slightly higher for those grown on MgO.

References

[1] K. D. Preston & G. H. Haertling "Microstructural investigation of acetate-derived PLZT films". Integrated Ferroelectrics, Volume 1, Issue 1, 1992.

[2] H. Onoda, M. Kageyama, K. Hashimoto, J. Appl. Phys. 77 (1995) 885.

[3] D.B. Knorr, S.M. Merchant, M.A. Biberger, J. Vac. Sci. Technol., B 16(1998) 2734.

[4] J.S. Chun, I. Petrov, J.E. Greene, J. Appl. Phys. 86 (1999) 3633.

[5] C.-H. Maa,, J.-H. Huangb, Haydn Chena "Residual stress measurement in textured thin film by grazing-incidence X-ray diffraction" *Thin Solid Films,* 418 (2002) 73–78.

[6] R. Roth, J. Schubert, M. Martin, E. Fromm, Thin Solid Films,1995, 270, 320.

[7] J. E. Sundgren, Thin Solid Films 1985, 128, 21.

[8] Z. Y. Chen, A. W. Castleman, Jr., J.Chem.Phys. 1993, 98,231.

NOVEL CONTROL TECHNIQUE FOR CADMIUM SULFIDE CHEMICAL BATH DEPOSITION USING REAL TIME MONITORING OF CADMIUM ION MOLARITY

Farhana Anwar*, Rafael Ordonez, Heber Prieto, and David Zubia
[1] Electrical Engineering & Computer Science, Nano Materials Integration Laboratory, University of Texas at El Paso, El Paso, TX 79968, USA
*(fanwar@utep.edu)

Keywords: *Chemical Bath Deposition, Cadmium sulfide thin film, solar cell*

ABSTRACT

Cadmium sulfide (CdS) Chemical-bath-deposition (CBD) parameters are modified to allow, for the first time, real time and in-situ monitoring of cadmium ion molarity using a commercially available cadmium ion Ion-Selective-Electreode at 60°C. This modification involves alterations to typical deposition parameters that eliminate the formation of cadmium hydroxide and keep cadmium ion molarity above 10^{-7}M which allows in situ monitoring of CdS CBD. Additionally, the new parameters favor non-porous film formation. The optical and structural characterization of the film proves it's applicability in solar cells.

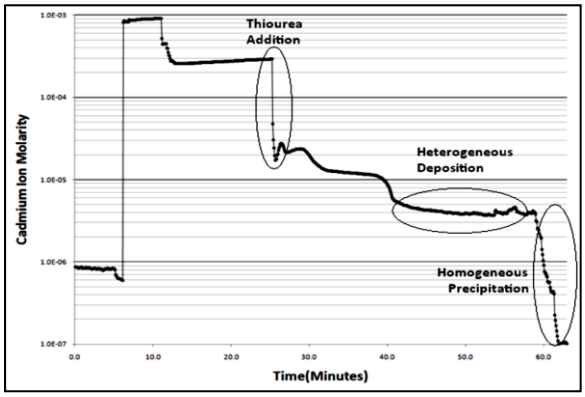

Fig.1. In situ Monitoring of CdS CBD deposition.

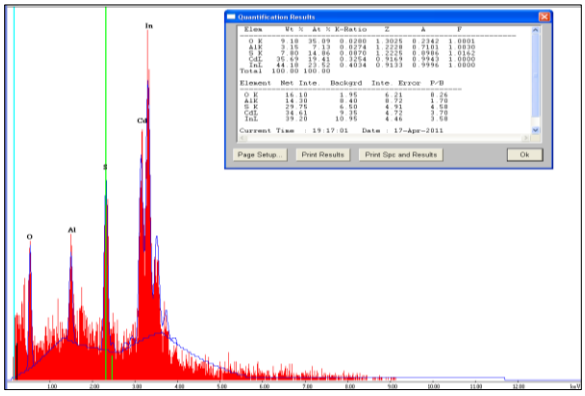

Fig.2. EDX analysis of CdS film.

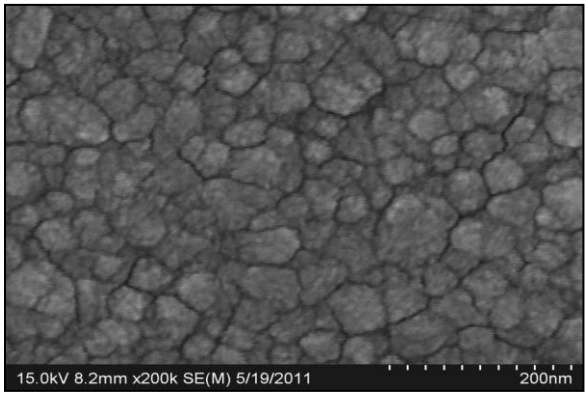

Fig.3. SEM surface morphology of CdS film.

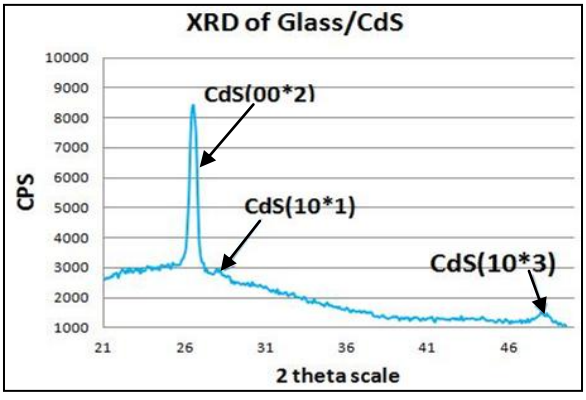

Fig.4. XRD of CdS film on glass substrate.

Table 1:Typical and New Cadmium sulfide CBD parameter comparison

	Kitaev et al. [3] parameters	Chu et al.[4] parameters	New Parameters in this work for CBD Cadmium Ion Monitoring
Cadmium salt	20mM to 0.1M	1mM Cadmium Acetate	1mM Cadmium Acetate
Thiourea	At least twice the molarity of Cd-salt	5mM	5mM
Temperature	50°C to 90°C	85°C	60°C
P^H	At least 11.0	9.1	8.9
Ammonia	At least 1M	0.4M	0.05M
Buffering Salt	None	20mM Ammonium Acetate	10mM Ammonium Acetate

Table 2: Bandgap of CdS films with different thickness

Sample	Thickness(nm)	Bandgap
3	15	2.49
4	25	2.46
5	35	2.44
6	40	2.43
7	48	2.39

1. Introduction:

Cadmium sulfide is a direct band gap semiconductor material used as a thin film layer in solar cells since 1955. Chemical bath deposition (CBD) is a method known for being relatively inexpensive and simple to execute but a thorough understanding of how nucleation and crystal growth can be controlled with this process is lacking. [1] Of special interest is the ability to monitor and control the deposition rate in-situ and in real time. Moreover the ability to monitor and suppress homogeneous precipitation is important to achieve dense films, free of cluster growth. In 2004, Voss et al. [2] used a Quartz Crystal Microbalance and theoretical equilibrium reactions of CBD CdS to more accurately explain reaction kinetics and concluded that during porous film formation free cadmium ions (Cd^{2+}) are consumed in solution. Thus, a Cd^{2+} Ion-Selective-Electrode (ISE) can also be used to monitor formation of the porous films. However the CBD parameters developed by Kitaev et al. [3] results in Cd^{2+} molarity below the detection limits of the ISE. In this work, we present parameters that are set to monitor and control freeCd^{2+} in-situ and in real-time as well as prevent porous film formation using an Ion-Selective-Electrode. This in situ monitoring also shows possibility of controlling and measuring deposition rate which is significant for manufacturing CdS films.

2. Deposition Parameters:

Typical cadmium sulfide CBD parameters involve high concentrations of the cadmium salt, ammonia, and thiourea. These cadmium and pH values produce cadmium hydroxide precipitate, justifying the need for modified deposition parameters. 1st and 2nd column of Table 1 compares the two different CBD parameters reported in the literature, and 3rd column presents new parameters used in this paper that allows monitoring of cadmium ion molarity during CBD. The Chu et al. [4] parameters appear to be applicable for CBD cadmium ion monitoring since they do

not produce cadmium hydroxide precipitate. However, they are performed at 85°C which is above the recommended operating temperature of the ISE. For this work, the deposition temperature was 60°C within the operating range of the ISE.

Using the parameters mentioned in Table 1, it is found that at pH = 7.6, the decomposition of thiourea is suppressed, and at pH = 8.9, the decomposition is so fast that the reaction starts to produce porous film within a minute after thiourea is added. Therefore, thiourea decomposition time can be controlled with pH, and a pH value between 7.6 and 8.9 should decompose thiourea slowly enough to delay porous film formation that is caused by fast thiourea decomposition. Fig. 1 shows cadmium ion molarity vs. time graph at pH=8.2 which shows both homogenous (porous) and heterogeneous (non-porous/dense) deposition. From the experiments it is found that pH=8.4 decompose thiourea slowly enough to favor non-porous deposition of cadmium sulfide.

3. CdS film characterization:

The grain size, shape and crystal orientation of the CdS grains greatly affect the electrical properties of solar cells. Fig. 2 shows energy-dispersive X-ray spectroscopy (EDX) analysis which gives the percentage of Cd and S present in the deposited film. The surface morphologies of CdS films were observed by SEM. Fig. 3 shows an SEM photograph of the CdS surface. The CdS films consisted of small grains of size <10nm and had a smooth surface. Fig. 4 shows the X-ray diffraction pattern of the CdS film which shows peaks at 2θ positions of 26.8°, 28.5° and 48.5° corresponding to the (00•2), (10•1) and (10•3) planes of the hexagonal phase with a preferred orientation in the (00•2) direction.

Cadmium sulfide is a semiconductor transparent to light energies below 2.42eV or light wavelengths above than 512nm. Therefore, analyzing transmittance from 400nm to 600nm can be used to find the actual bandgap of the cadmium sulfide samples produces in this work. A Cary 5000 double beam spectrophotometer manufactured by Varian Inc. was used to measure the transmittance of the CdS film. Table 2 shows the bandgap measurement of CdS samples of different thickness deposited on glass substrate. Thicknesses of the CdS films were measured by Filmetrics F20 Thin-Films Analyser. The average bandgap found is 2.44eV, and it is in very good agreement with the 2.42eV band gap of single crystal cadmium sulfide.

4. Conclusion:

For the first time, a commercially available cadmium ion selective probe is used to characterize, monitor and control cadmium sulfide Chemical-Bath-Deposition. The optical and structural characterization of the film shows that the procedure produces high quality film suitable for optoelectronic device application.

5. References:

[1] Rieke, C P and B, Bentjen S. "*Deposition of Cadmium Sulfide Films by Decomposition of Thiourea in Basic Solutions*". *Chemistry of Materials.* 1993, Vol. 5, 1, pp. 43-53.

[2] Voss, C, et al. "*Growth Kinetics of Thin-Film Cadmium Sulfide*". *Journal of The Electrochemical Society.* 2004, Vol. 151, 10, pp. C655-C660.

[3] Kitaev, G A, Uritskaya, A A and Mokrushin, S G. "*Conditions for the chemical deposition of thin films of cadmium sulphide on a solid surface*". *Russian Journal of Physical Chemistry.* 1965, Vol. 39, 8, pp. 1101-1102.

[4] Chu, T L, et al. "*Solution-Growth Cadmium Sulfide Films for Photovoltaic Devices*".*Journal of Electrochemical Society.* 1992, Vol. 139, 9, pp. 2443 - 2446

CONTROL STUDY OF HIERARCHICAL STRUCTURAL FIBER FOR ELECTROCHEMICAL ENERGY STORAGE

Md Ashiqur Rahaman Khan [1]*, Miguel Mendoza[1], Mohammad Arif Ishtiaque Shuvo[1], Matthew Garcia and Yirong Lin [1]
[1] Department of Mechanical Engineering, The University of Texas at El Paso, El Paso, TX, 79968; USA
* Corresponding author (mrkhan3@miners.utep.edu)

Keywords: Nanowire, energy storage, battery, supercapacitor, ZnO

ABSTRACT

With the ever-increasing demand in extending duration of mobile devices, technologies related to improve the performance of electrochemical storage device such as battery and supercapacitor have received extensive attention in the past few years. Due to the excellent mechanical and electrical properties and high specific surface area, nanowire is an ideal candidate for electrode material in battery or supercapacitor. There are various studies performed to increase the specific energy density and cyclic performance using metal oxide nanowires. However, most of them are randomly dispersed with limited performance enhancement while those aligned ones are grown on relatively weak mechanical substrate thus provides very limited or none mechanical strength to the devices. Multifunctional material is a new group of material developed to provide structural load bearing functionality and system performance related functionalities. The advantage of using this type of material lies in reducing complexity and enhancing performance without sacrificing mechanical strength or inducing extra weight of the whole system. Therefore, using multifunctional material is ideal for building a novel energy storage device with an excellent combination of mechanical, electrical, specific energy density. This letter will introduce the fundamental study of developing a hierarchical multifunctional structural fiber with ZnO nanowire coated on carbon fiber. Coating electrodes with zinc oxide nanowires can increase performance of energy storage devices, as the change of surface area will affect the electron charge/discharge rate of electrodes. Zinc oxide nanowire growth is achievable using low temperature hydrothermal synthesis. Growth time, temperature and the use of surfactant will all control the geometry of nanowire thus the structure-property relation can be determined in the future. The success of controlling the geometry of the nanowire will lead to determine the optimal performance for structural and energy storage.

1.0 Introduction

One-dimensional nanostructure such as nanowire, nanorod and nanotube is drawing much research interest in recent years because of their possible applications in nano-scale devices. Nanowires have very high surface area with tunable dimension and crystal morphology. Thermal, mechanical and electrical properties of nanostructure vary depending upon many factors such as temperature, duration of reaction, pressure, molar concentrations of chemicals used in different synthesis procedures. Zinc oxide is n type semiconductor which has electrical, optical, piezoelectrical, optoelectrical and many other important applications because of its wide band gap (3.37 eV) and high electron hole binding energy (60 eV)[1,2].

Zinc oxide has piezoelectric, pyroelectric properties and appropriate doping makes it electrically conductive. Zinc oxide is also biocompatible, biodegradable and nontoxic which extends the area of its biological application [3]. Carbon-zinc oxide and graphene-zinc oxide nanocomposites are suitable for energy storage applications. In this paper zinc oxide nanowires are grown by varying growth reaction time and using polyethylenemine as surfactant on carbon fiber and graphene. The diameter, length, crystal structure is analyzed by scanning electron microscopy (SEM) and X-ray diffraction (XRD).

2.0 Experimental procedure

2.1. ZnO seed particles

Zinc acetate dehydrate (12.5 mM) has been dissolved in ethanol at 50 °C under vigorous stirring by magnetic stir bar. After completely dissolved the solution is brought to room temperature and diluted to a concentration of 1.4 mM by adding ethanol. Another sodium hydroxide (20 mM) ethanol solution is prepared at 60 °C under vigorous stirring. After cooling to room temperature, additional ethanol is added in order to dilute to make a concentration of 5.7 mM. These two solutions are mixed at a ratio of 18:7 at a temperature of 55 °C for 30 minutes. Substrates washed with acetone and isopropanol are dipped in the seed solution for 5 minutes and subsequently annealed on a hot plate at 150 °C for 10 minutes to enhance adhesion between the fiber and nanoparticles.

2.2 ZnO nanowires: Hydrothermal growth

Zinc oxide nanowires are grown by low temperature hydrothermal method [4]. An aqueous solution of 25 mM zinc nitrate hexahydrate [$Zn(NO_3)_2.6H2O$, 99.9% purity], 25 mM hexamethylenetetramine (HMTA) ($C_6H_{12}N_4$, 99.9% purity) and 5-7 mM Polyethylenemine (PEI, Branched, molecular weight 800 gm/mol) are prepared at room temperature. Carbon fibers are immerged in growth solution when the temperature is at 85/90 °C. The growth is done in a glass beaker and solution temperature is maintained constant by using a thermocouple and hot plate. Three different time duration of 2 hours, 4 hours and 6 hours for the growth is studied. For longer reaction time growth solution is change after every 2 hours. After the reaction is complete, samples are taken out of the solution to rinse with de-ionized water and dried at 100 °C on a hot plate.

3.0 Results and Discussion

All samples of ZnO nanowires are grown on carbon fibers and previously synthesized graphene. Prepared samples are analyzed by X-ray Diffraction. Figure 1 shows XRD pattern of ZnO nanowires coated over carbon fiber. The peaks are well defined and match with standard results. Figure 2a-c shows SEM images of ZnO NWs grown on carbon fibers without using PEI. The nanowires grown for 2 hours have an aspect ratio of 32. As the reaction time increased to 4 hours and 6 hours, aspect ratio decreased to slightly less than 19 and just over 17 respectively. It is observed from the SEM images that diameters and lengths of the nanowires are increased as reaction time increased from 2 hours to 4 hours but decreased for 6 hours which does not convenient with the previous research work. The reason is the carbon fibers which were in the middle of the tow had not enough zinc oxide ions available around them. Figure 2d show SEM image of ZnO NWs grown on graphene for 2 hours. The diameters of NWs grown on carbon fiber and graphene for 2 hours are 39 nm and 34 nm approximately justifies that this method is very stable and steady. Figure 3a-d shows NWs grown for 2 hours using 5-7 mM PEI. It is found that length and diameter of NWs

increased with increase of PEI concentration from 5 to 7 and aspect ratio is found 37, 40 and 40 respectively.

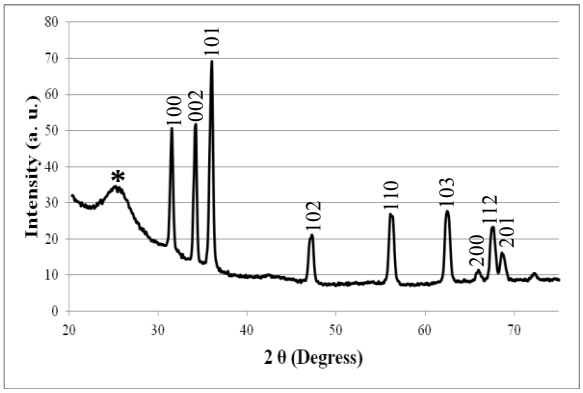

Figure 1. XRD pattern for ZnO NWs grown on carbon fiber. Asterisk marked peak is for carbon fiber.

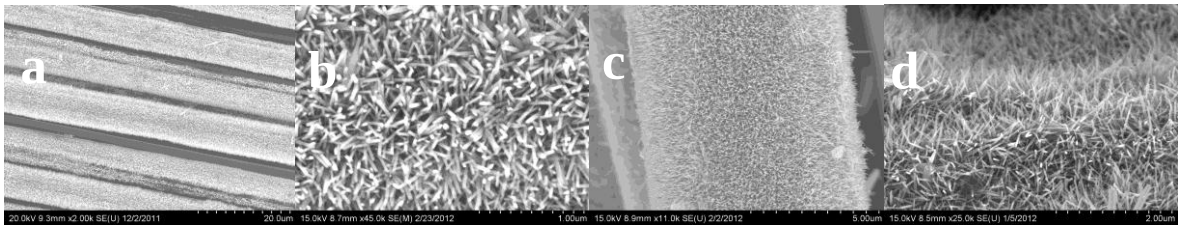

Figure 2. SEM images of ZnO NWs grown on carbon fiber for 2h at different scale (a) 20µm (b) 1 µm; (c) for 4h, scale 5 µm; (d) ZnO NWs grown on graphene for 2h, scale 2 µm; reaction temp 90 °C.

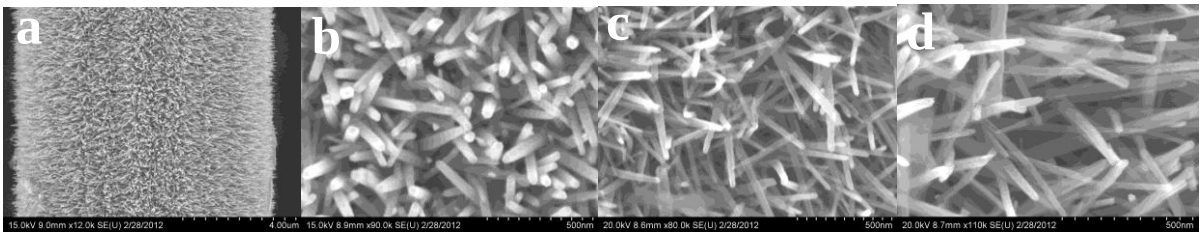

Figure 3. SEM images of ZnO NWs grown on carbon fiber for 2h with 5 mM PEI at different scale (a) 4 µm (b) 500 nm; (c) 6 mM PEI scale 500 nm; (d) 7 mM PEI scale 500 nm ; reaction temp 85 °C.

4.0 Conclusion

ZnO nanowires are grown on carbon fiber and graphene by hydrothermal method. Nanowires with different size and aspect ratio are achievable by changing reaction time, reaction temperature and surfactant in different concentrations. Consistent growth sizes allow growing nanowires on different substrates in the process of nanocomposites synthesis for improving capability and performance of energy storage devices such as lithium ion battery and supercapacitor.

References:

[1] *Zinc Oxide Bulk, Thin Films and Nanostructures*; Jagadish, C., Pearton, S. J., Eds.; Elsevier: New York, 2006.

[2] Heo, Y. W.; Norton, D. P.; Tien, L. C.; Kwon, Y.; Kang, B. S.; Ren, F.; Pearton, S. J.; LaRoche, J. R. ZnO *Nanowire Growth and Devices*. Mater. Sci. Eng. 2004, 47, 1–47.

[3] Wang, Z. L, *Splendid One-Dimensional Nanostructures of Zinc Oxide: A New Nanomaterial Family for Nanotechnology*; Mater. Sci. Eng. 2008; VOL. 2; NO. 10;1987–1992.

[4] R. A. McBride, J. M. Kelly, D. E.McCormack, J. Mater. Chem. 2003, 13, 1196.

INVESTIGATION OF THERMAL CONDUCTIVITY AND MECHANICAL PROPERTIES OF HAFNIA-ZIRCONIA BASED THERMAL BARRIER COATINGS

M. Noor-A-Alam, A.R. Choudhuri and C.V. Ramana*

Department of Mechanical Engineering
University of Texas at El Paso, El Paso, Texas 79968, USA
* Corresponding author (rvchintalapalle@utep.edu)

Keywords: Thermal barrier coatings, gas turbines; hafnia, zirconia

ABSTRACT

Hafnia-zirconia based thermal barrier coatings (TBC) were grown using RF magnetron sputtering technique. The composition of hafnia and zirconia were varied to fabricate the coatings keeping the yttria content constant at 7.5mol%. The coatings were grown onto different substrates namely inconel-738 and SS-403. Thermal conductivity of the coatings was measured using photo-acoustic (PA) method. The thermal conductivity of yttria stabilized hafnia (YSH) coatings was found in the range of 0.89-1.30 (±0.03) W/m-K. Mechanical properties investigated using nano-indentation technique indicate that the YSH coatings exhibit higher mechanical strength compared to that of yttria stabilized hafnia-zirconia (YSHZ) coatings. Residual stress analysis was performed using the X-ray diffraction pattern. The $Sin^2\psi$ technique was followed to calculate the residual stress. The results demonstrate very high compression stress within the coatings.

1 Introduction

Thermal barrier coatings (TBCs) are critical to protect the metallic surface from high temperature oxidation and erosion in gas turbine systems. The coating is a multifunctional thick film consisting of three layers the top of which makes insulation between the components and very high temperature environment. In this way, TBCs help use high operating temperature which consequently increases the efficiency of gas turbine power plants operating in diversified fuel environment. Extensive efforts have been directed towards the improvement of the quality of TBCs in last two decades [1-5]. Since the TBC system has to function in an environment of very high temperature and high velocity diverse gas compositions thermal conductivity and mechanical properties of TBC are the key concerns provided that the coating is structurally and thermodynamically stable at the operating temperatures. In this work, these two fundamental properties of TBC were investigated thoroughly for various compositions of yttria stabilized hafnia-zirconia coatings.

2 Experimental

YSH and YSHZ targets of 2″ diameter and 0.125″ thickness were used to fabricate the TBCs onto Inconel-738 and SS-403 substrates. Commercially available YSH target and YSHZ targets prepared in the laboratory were employed as targets. Materials were by solid state reaction using mixed proportions of HfO_2 and ZrO_2 stabilized by Y_2O_3. The composition of the target material is varied by varying the ratio of HfO_2 and ZrO_2 while keeping the Y_2O_3 stabilizer content constant (7.5 mol%). Coatings were grown using RF magnetron sputtering technique at variety of operating parameters to optimize the deposition conditions. Photo-acoustic (PA) method was used to evaluate the thermal conductivity of the coatings and nano-

indentation technique was used to investigate the mechanical properties. Residual stress analysis was performed using the X-ray diffraction pattern following the $Sin^2\psi$ method.

3 Results

3.1 Thermal Conductivity

The thermal conductivity of YSH coatings grown on Inconel-738 is shown in Fig. 1. The results indicate that the thermal conductivity of YSH coatings increases with increasing growth temperature. This can be attributed to the increasing grain size with the increase of growth temperature the result of which is the decrease in phonon scattering. The maximum value obtained at 500 ^{0}C growth temperature is 1.3 W/m.K which in general is lower than that of pure hafnia coating or bulk hafnia material.

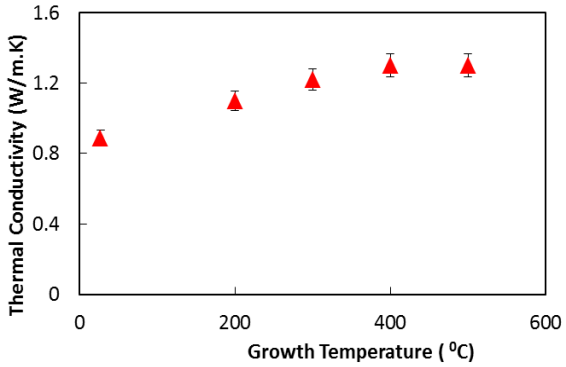

Fig. 1: Thermal conductivity of YSH coatings with respect to growth temperature when grown on Inconel-738

2.2 Mechanical Properties

Figure 2 shows the mechanical properties YSH and YSHZ coatings. Hardness and modulus of elasticity were measured using the nano-indentation technique. A triangular shape diamond tip nano-indenter was used as the tool for indentation and the results are plotted against various compositions of hafnia and zirconia in the coatings. YSH coatings grown on SS-403 and inconel-738 show the similar hardness and modulus of elasticity values. The hardness values for YSH on both of these two substrates are about 18 GPa. YSHZ coatings show lower hardness (6-11GPa) compared to YSH coating. Among all the compositions (4:1, 2:1, 1:2 and 1:4) of YSHZ the 4:1 ratio of hafnia and zirconia exhibits the maximum hardness which is 11.4 GPa. Modulus of elasticity is always higher in YSH coating.

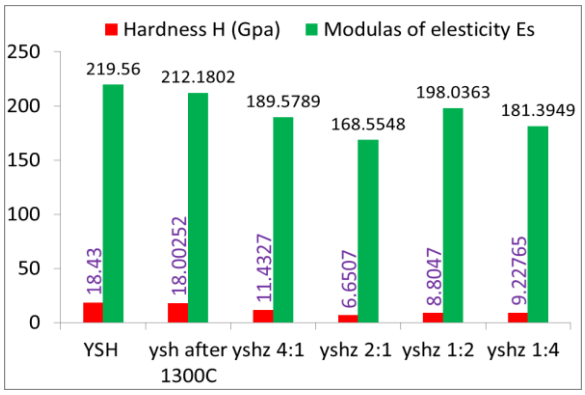

Fig. 2: Hardness and modulus of elasticity of YSH and YSHZ coatings.

2.3 Residual Stress

The residual stresses calculated for YSH and YSHZ coatings are shown in Fig. 3. YSH shows the similar residual stress on both the ss-403 and inconel-738. The as grown YSH coating shows a compressive residual stress of ~ 2GPa on both the ss-403 and inconel-738 substrates. YSHZ shows lower residual stress compared to YSH which is less than 1GPa. The YSH samples which was exposed to hot gas at 800 ^{0}C shows lower compressive residual stress (1.37 GPa) compared to as grown YSH coatings.

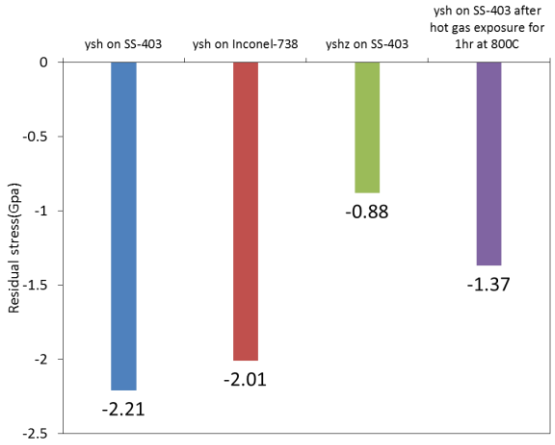

Fig.3 Residual stresses calculated for YSH and YSHZ coatings

3 Conclusions

The low thermal conductivity of YSH coating is demonstrated. Hardness and Young's modulus of YSH coatings are higher than those of YSHZ coatings. Among all the compositions of YSHZ 4:1 ratio of hafnia to zirconia shows the maximum value of hardness while 1:2 ratio of hafnia to zirconia shows maximum modulus of elasticity. Both YSH and YSHZ coatings show very high compressive stress within the coatings. Further investigation is needed to understand the effect of substrate on residual stress in coatings.

References

[1] Gurrappa, A. Sambasiva "Thermal barrier coatings for enhanced effi-ciency of gas turbine Engines". *Surface Coating Technology,*Vol. 201, pp 3016–3029, 2006.

[2] N.P. Padture, M. Gell, E.H. Jordan "Thermal barrier coatings for gas– turbine engine applications" *Science*, Vol. 296 pp. 280–284,2002.

[3] A.G. Evans, D.R. Mumm, J.W. Hutchinson, G.H. Meier, F.S. Pettit, "Mechanisms controlling the durability of thermal barrier coatings", *Progress in Materials Science*, Vol. 46 pp. 505–553, 2001.

[4] G. Soyez, J.A. Eastman, L.J. Thomson, G.R. Bai, P.M. Baldo, A.W. McCormick, R.J. DiMelfi, A.A. Elmustafa, M.F. Tambwe, D.S. Stone, "Grain-size-dependent thermal conductivity of nanocrystalline yttria sta-bilized zirconia films grown by metal-organic chemical vapor deposition", *Applied Physics Lletters*, Vol. 77, pp. 1155–1157, 2000.

[5] N. Wang, C. Zhou, S. Gong, H. Xu, "Heat treatment of nanostructured thermal barrier coating", *Ceramic International*, Vol. 33, pp. 1075–1081, 2007.

TWO-DIMENSIONAL LASER SPECTEROSCOPY TO STUDY ULTRAFAST DYNAMICS IN MATERIALS

C. Li[1]*
[1] Department of Physics, The University of Texas at El Paso, El Paso, TX 79968, USA;
* Corresponding author (cli@utep.edu)

Keywords*: Femtosecond, Laser, Spectroscopy*

ABSTRACT

In both natural light harvesting systems and artificial photovoltaic cells, research on the charge and energy transfer dynamics has brought great interest. This information is critical to improve our understanding the physics and provide guidance for future development. These dynamical processes happen in the time scale of femtosecond to picosecond. Ultrafast laser spectroscopy is commonly used to detect this information. In this paper, we focus on how two-dimensional (2D) laser spectroscopy can provide an incisive tool to probe the electronic transitions, and energetic evolutions that must be understood to describe photosynthetic light-harvesting and photovoltaic charge transfer. We demonstrate its application to the study of organic dye Coumarin 102. We illustrate several capabilities of 2D spectroscopy including monitoring energy level broadening, observing energy level evolution. This information will help to determine the energy and charge transfer pathways.

1 Introdu ction

Ultrafast laser spectroscopy has been developed to probe carrier and energy transfer processes in both photovoltaic cells and photosynthetic proteins [1,2]. Typically two femtosecond (10^{-15}s) or picosecond (10^{-12}s) laser pulses are used to pump and probe the interested system to study the processes with femtosecond/picosecond time scale. Two-dimensional (2D) laser spectroscopy utilizes three or four femtosecond pulses to probe the system and gives more information on the dynamics. For example Fleming and co-workers had used 2D spectroscopy to measure electronic couplings and carrier transportation in a molecular complex, the Fenna–Matthews–Olson photosynthetic light-harvesting protein [2]. The striking discovery is the coherent energy transfer pathway in such a complicated molecular system. In most experiments non-collinear optical pulses with an appropriate phase matching condition were used to implement the experiment and obtain the nonlinear optical signal. In this approach it is difficult to implement more laser beams due to the constraint of the phase matching requirement. By contrast, 2D nuclear magnetic resonance (NMR), which serves in most ways as the inspiration for these methods, always uses collinear pulses with well-defined inter-pulse phases to resolve the structure of complex molecules. In a recent work the direct (collinear geometry, phase-cycled) optical analog of 2D NMR had been realized with an acoustic optic pulse shaper on a Rubidium atomic vapor system [4]. Therefore, the purpose of this experiment is to develop collinear 2D spectroscopy to study the complex molecular systems such as organic solar cells.

2 Results and Discussion

The experimental setup is shown in Fig. 1. The dashed line represents the optical light path and the solid line represents electronic signal. Amplified 80 fs pulses were generated by a Ti:sapphire laser system(Coherent Vitesse and RegA 9050 system) with a pulse energy of 7 μJ at a repetition rate of 20 kHz. A series of collinear phase coherent three-pulse sequences are needed to yield a 2D spectrum. Each collinear three-pulse sequence was generated from a single input laser pulse using an Acouto-Optic Pulse Shaper (AOPS). Then this pulse sequence is shot into the sample cell. The fluorescence from Courmarin dye was collected from the side by a photo multiplier tube (PMT).

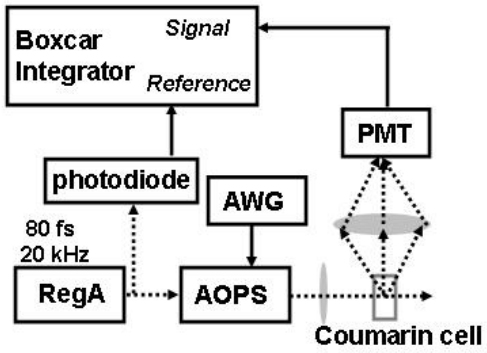

Fig.1. Experimental setup for 2D spectroscopy. AOPS: acousto-opto pulse shaper, AWG: arbitrary waveform generator, PMT: photo multiplier tube.

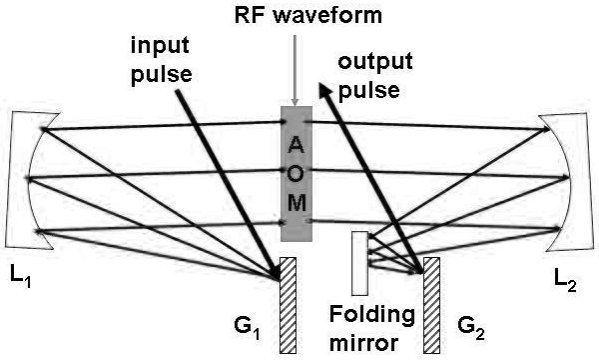

Fig.2. Acousto-optic pulse shaper setup. AOM: acousto-optic modulator. G1, G2: gratings, L1, L2: focusing mirrors.

To describe pulse shaping in frequency domain, the frequency domain expression of optical pulses is used. First the frequency components of the femtosecond pulse are spread in space. Each component will be modulated individually in a parallel scheme. The mathematical equation for this modulation is

$$E_{out}(\omega) = E_{in}(\omega)\, M(\omega) \tag{1}$$

where $E_{in}(\omega)$ is the input pulse spectrum, $M(\omega)$ is the modulation function, $E_{out}(\omega)$ is the output pulse spectrum. Fig 2 shows the schematic setup of the frequency domain pulse shaping. G_1 and G_2 are two gratings with the same grove spacing. L_1 and L_2 are two focusing mirrors with the same focus length. AOM is the spatial light modulator. The modulation function $M(\omega)$ is loaded into the AOM. L_1 and L_2 are 2-inch diameter gold coated spherical mirrors. G_1 and G_2 are gold coated gratings with 1200 groves/mm.

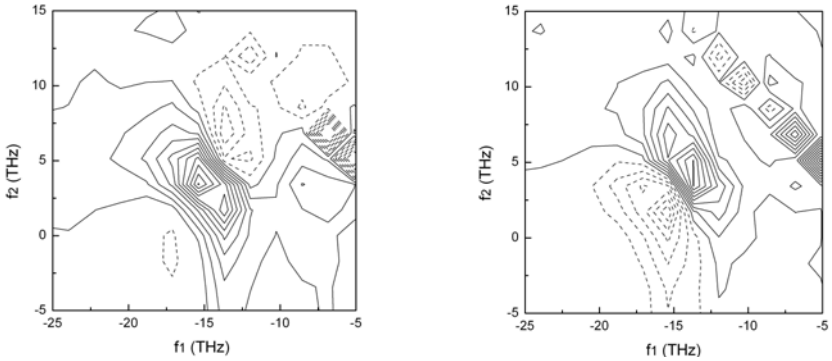

Fig.3. Real (left), and imaginary (right) 2D spectra of Coumarin 102.

Fig 3 shows the obtained 2D (real and imaginary) spectra obtained from the 2D experiment of Coumarin 102. The spectrum shows a photon echo peak at Δf_1=-15.4 THz, Δf_2=3.4 THz. In this experiment, the laser center wavelength is 803 nm. From the peak position and laser center frequency we know we are accessing the initial energy level at 762.6 THz corresponding to a 393.4 nm wavelength. The solid lines represent positive regions and the dashed lines are negative. The contour lines are plotted at increments of 10% of the real spectrum's maxima. In the real 2D spectrum, the full width at half maximum (FWHM) along the anti-diagonal direction is 5.2 THz via Gaussian fitting, while along the diagonal direction it is only 2.4 THz. As mention in a previous discussion, the inhomogeneous linewidth definition depends on experimental timescale. Since the total experiment time is nearly 600 fs, some rapid moves may freeze out as inhomogeneities which show as homogeneous dynamics in the conventional spectroscopy.

We have demonstrated the ability to perform collinear 2D laser spectroscopy on the organic dye, Coumarin 102. The future work is to create increasingly more complex optical pulse sequences, which will allow for the extraction of increasingly detailed molecular electronic information, such as coupling between transitions.

References

[1] T.M. Clarke and J.R. Durrant "Charge Photogeneration in Organic Solar Cells". *Chem. Rev.*, Vol. 110, pp 6736-6767, 2010.

[2] Y.C. Cheng and G.R. Fleming "Dynamics of Light Harvesting in Photosynthesis". *Annu. Rev. Phys. Chem.*, Vol. 60, pp 241-262, 2009.

[3] W. Wagner, C. Li, J. Semmlow and W.S. Warren "Rapid Phase-cycled Two-dimensional Optical Spectroscopy in Fluorescence and Transmission Mode". *Optics Express*, Vol. 13, pp 3697-3706, 2005.

Thermoelectric Properties of Carbon Nanotubes, CNTs

A S M Arifur Rahim Chowdhury[1], Onasis Garcia[2], Dr. Mujibur R. Khan[3], Luisa A. Cabrera[4]*
Department of Mechanical Engineering, University of Texas at El Paso, El Paso, Texas 79968

Abstract

We have investigated the thermoelectric properties of both Singlewall Carbon Nanotubes (SCWNTs) and Multiwall Carbon Nanotubes (MCWNTs). These nanotubes consisted of approximately 60% semiconducting and 40% metallic tubes. Nanotubes were randomly dispersed on a nonconductive glass substrate and thermoelectric properties were tested by creating a temperature difference. Voltage (mV), current (μA) and resistance (Ω) were taken with respect to temperature difference (°C). Seeback coefficient and power factors were also calculated. The seeback coefficient of SWNTs was approximately 0.124±0.008 (mV/ºC). On the other hand, for the MWCNTs that was about 0.06±0.007 (mV/ºC). Moreover, as temperature difference increased resistance decreased for both SWCNTs and MWCNTs; however, SWCNTs showed lower resistance than MWCNTs. The experiment results validated that SWNTs displays better thermoelectric properties than MWNTs.

Introduction: Carbon nanotubes show good thermoelectric responses at temperature difference. For example, at room temperature the thermal conductivity of Copper is 385 $W.m^{-1}.K^{-1}$ where at room temperature thermal conductivity of SWCNTs is 3500 $W.m^{-1}.K^{-1}$ [1]. Meanwhile, metallic carbon nanotubes have an electrical density 4×10^{9} A/cm^2 that is 1000 times greater than metals like Copper [2]. Energy harvesting and energy efficiency is a burning question in today's world. However, application of carbon nanotubes for adequate output is very important. It is a great challenge to achieve the highest output by using the right materials for the right purpose. Because of the very good thermoelectric responses of the carbon nanotubes, lots of researches are going on to investigate the thermal behavior of carbon nanotubes. As an example, thermal stability of CNTs was investigated. Investigation revealed that [3] SWCNTs have better thermal stability than MWCNTs. That investigation also indicated that shorter CNTs are able to withstand higher thermal loads. Moreover, Young's modulus of CNTs is at least as high as graphite and can be even higher for small SWNTs [4]. It also showed that Young's modulus for MWCNTs are dependent upon the degree of order within the tube walls. Because of significant thermoelectric responses carbon nanotubes are currently being used as reinforcement to strengthen and stiffen polymers. For example, SiC does not display any thermoelectric responses. However, it was revealed that [5] a SiC and SWCNTs mixture showed thermoelectric responses in temperature difference. Carbon nanotubes are also being considered as possible conductors of electricity in advanced nanoelectronic devices. Moreover, the use of Carbon Nanotubes as materials for novel sensors, superconductor, solar cell, light bulb filament, etc. can be a great option.

Experimental Procedure**:** SWCNTs and MWCNTs were procured from cheap tubes. The average diameter for the SWCNTs was approximately 1.2 nm, and the length was approximately 1-15 micrometer. On the other hand, the average diameter for MWCNTs was approximately 4-12 nm and the length was 3-10 micrometer. The procured nanotubes were composed of 40% metallic and 60% semiconductor. Both SWCNTs and MWCNTs were in powder form. SWCNTs and MWCNTs were randomly dispersed on the nonconductive glass substrate and junctions were created at hot and cold side. Then voltage (mV), resistance (Ω) and current (μA) was measured using multimeter. Seeback coefficient and power factors were also calculated. For dispersing SWCNTs on the glass substrate, SWCNTs solution was prepared. SWCNTs solution was prepared by adding 50 mg of SWCNTs into 50 mL of 95% alcohol. The SWCNTs and alcohol mixture was sonicated for 14 minutes at 70% intensity as shown in figure 1. Afterwards, SWCNTs solution was placed on a nonconductive glass substrate and heated so that the ethanol vaporized.

Figure 1: Sonication of SWCNTs

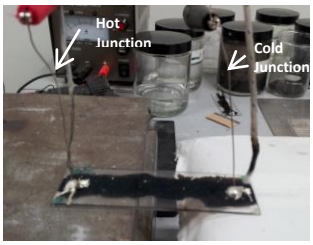

Figure 2: Hot junction and cold junction

The result was randomly distributed SWCNTs on the nonconductive glass substrate. Then the junction was created on the hot side and the cold side as figure 2. Alumel (Ni-Al) was used for making the junctions. For the experiment, temperature difference was created between two junctions by keeping the hot side on the hotplate and the cold side on the ice. The highest temperature difference achieved in the experiment was approximately $\Delta T = 180$ ºC. The same procedures were followed for MWCNTs experiments.

Results and discussion**:** The thermoelectric properties of SWCNTs and MWCNTs were investigated in this research. When carbon nanotubes were randomly dispersed on the nonconductive glass substrate, nanotube junctions were created. Nanotubes junctions are shown in figure 3. Carbon nanotubes display a very good electrical response along to axial direction of the nanotube. However, it does not show significant electric response on the radial direction. That is one of the unique properties of carbon nanotubes. Carbon nanotubes displayed significant thermoelectric response on the temperature difference. As shown in figure 4, as temperature difference was increasing voltage was increasing for SWCNTs and MWCNTs. However, SWCNTs displayed higher voltage than MWCNTs. Moreover, seeback coefficient of SWCNTs was about 0.124±0.008 (mV/ºC), whereas seeback coefficient of MWCNTs was about 0.06±0.007 (mV/ºC). Meanwhile, as temperature difference was increasing

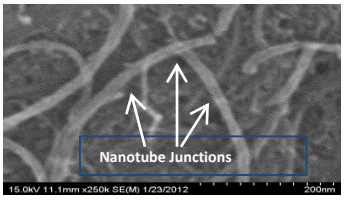

Figure 3: Nanotubes junctions

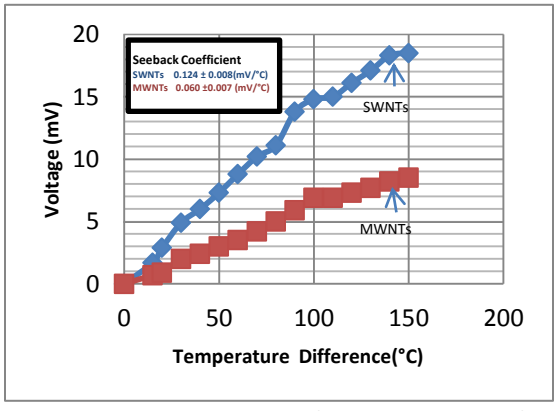

Figure 4: Voltage vs. Temperature (SWCNTs and MWCNTs)

current flow was increasing for SWCNTs and MWCNTs. However, as displayed in figure 5 SWCNTs showed better current flow than MWCNTs at temperature differences. As shown in figure 6 the resistance slightly decreased for both SWCNTs and MWCNTs as temperature difference increased. In general, resistance supposed to increase as temperature difference increased. However, the experiment displayed different results. It's because of the composition of CNTs that was used for the experimental purposes. The carbon nanotubes were composed of 40% metallic and 60% semiconductor. It was revealed that [6] carbon nanotubes resistance at temperature difference depends on the composition of metallic and semiconductor composition. Since carbon nanotubes were composed of 60% semiconductor, resistance showed a decreasing trend. Power factors ($P.F = \frac{S^2}{\rho}$) were also calculated. Power factors for SWCNTs and MWCNTs are shown in table 1.

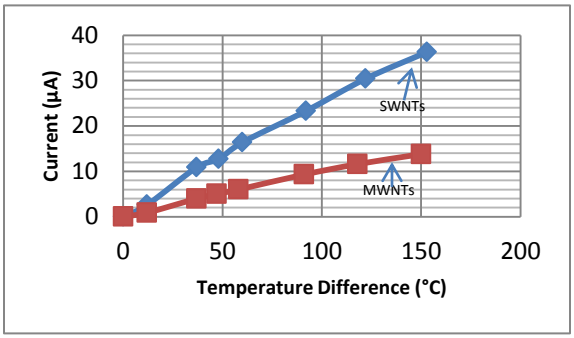

Figure 5: Current vs. Temperature (SWCNTs and MWCNTs)

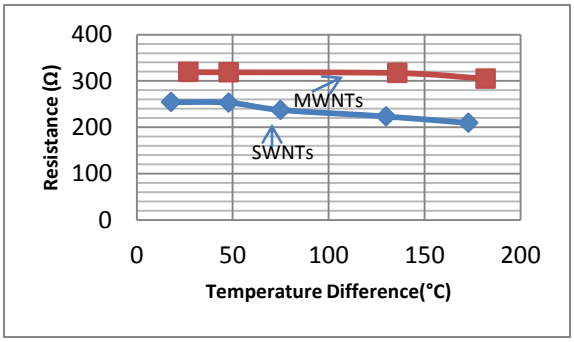

Figure 6: Resistance vs. Temperature (SWCNTs and MWCNTs)

Table: 1

	Seeback Coefficient	Power factors
SWCNTs	0.124±0.008 (mV/ºC)	5.2×10^{-7} W.K^{-2}m^{-1}
MWCNTs	0.06±0.007 (mV/ºC)	0.11×10^{-7}W.K^{-2}m^{-1}

Conclusion: From our experimental result we can summarize that as temperature difference increased the current as well as voltage increased for both SWCNTs and MWCNTs, and resistance decreased. However, if we analyze the results of current, voltage and resistance for both SWCNTs and MWCNTs, we can see that SWCNTs displayed better thermoelectric properties than MWCNTs. The higher seeback coefficient of SWCNTs demonstrated that SWCNTs have higher thermoelectric voltage response than MWCNTs.

Acknowledgements: The author would like to thank Mechanical Engineering department of UTEP and University research grant for their support.

References:

[1] Pop, Eric et al; Mann, David; Wang, Qian; Goodson, Kenneth; Dai Hongije "Thermal conductance of an individual single wall carbon nanotube above room temperature"

[2] Hong, Seunghun; Myung "Nanotubes Electronics: A flexible approach to mobility"

[3] G. E. Begtrup1, 2, K. G. Ray1, 3, B. M. Kessler1, T. D. Yuzvinsky1, 2, 3, H. Garcia1, and A. Zettl*, 1, 2, 3 "Extreme thermal stability of carbon nanotubes"

[4] J.-P. Salvetat*, J.-M. Bonard, N.H. Thomson, A.J. Kulik, L. Forr´o, W. Benoit, L. Zuppiroli "Mechanical properties of carbon nanotubes" 29 July 1999

[5] Luisa A. Cabrera[1*], Onasis Garcia[1], Mujibur Khan[1], Arifur R. Chowdhury[1] "Investigation of Thermoelectric Properties of SiC+ SWCNTs" March 2012

[6] Cheng Yung Kuo, Chia Lang Chan, Chie Gau, Chien-Wei Liu, Shiuan Hua Shiau, and Jyh-Hua Ting "Nano Temperature Sensor Using Selective Lateral Growth of Carbon Nanotube Between Electrodes" JANUARY 2007

Investigation of Thermoelectric Properties of SiC+ SWCNTs

Luisa A. Cabrera[1], Onasis Garcia[1], Mujibur Khan[1], Arifur R. Chowdhury[1]*
[1]Department of Mechanical Engineering, University of Texas at El Paso, El Paso, Texas 79968

Abstract

A mixture of SiC (silicon carbide) nanoparticles and SWCNTs (single walled carbon nanotubes) was randomly distributed using a direct deposition of particles on a glass substrate and the thermoelectric properties were measured and analyzed. The nanotubes were 0, 10, 25 and 50 wt% respectively for different SiC+SWCNTs samples. Voltage (mV), current (μA) and resistance (Ω) were measured and Seebeck coefficients(*S*) and power factors (P.F) were calculated for different categories of samples. It has been observed that SiC nanoparticles did not show any significant thermoelectric properties. However, SiC when infused with SWCNTs showed significant thermoelectric effects. Even though the seebeck coefficient was in identical range with different wt% of SWCNTs, current, resistance and P.F. changed with wt% of SWCNTs. Current and P.F. increased substantially with the increase of SWCNTs in the samples. Finally, the structures created were analyzed in a SEM (scanning electron microscope). It has been revealed that fiber like SWCNTs created a randomly distributed network inside the SiC matrix and infused the thermoelectric properties in the combined SiC+SWCNTs material system.

Introduction

Although SWCNTs have been shown to exhibit excellent mechanical, electrical and thermal properties [1], they cannot sustain high-temperature environments, for which their application in certain surroundings has been limited. Silicon Carbide is described as an attractive material for high temperature applications, along with having a low density (suitable for lightweight applications), and good mechanical properties; however, its electrical characteristics correspond to those of a semiconductor. If these mentioned properties of SWCNTs were to be combined with the higher resistance to oxidation of silicon carbide the resultant material's application would lie in the field of energy conservation, as materials with effective thermal and electric properties are sought to improve industrial processes where transfers are essential, such as turbines, where a high temperature environment. The thermoelectric properties of each have been studied in the past [2,3] but so far the combined effects of these materials have not been recorded in this manner. It is desirable to find an ideal percentage combination of these materials for a specific application according to its working temperature and energy-distributing properties. Single-walled nanotubes (SWCNTs) of 99% purity were thoroughly mixed with Silicon Carbide nanoparticles and their thermoelectric properties were studied and recorded. The thermal conductivity of SWCNTs is found to be 3500 W/m.K along their long tube axis, and 1.52 W/m.K along the radial axis, a huge difference in values; they are stable up to 2900 °C. The thermal conductivity of silicon carbide is 300 W/m.K, maintaining stability up to 2730 °C. The electrical properties of SWCNTs include a resistivity of E-6 Ω.cm, a capability to carry a current density of 4 E9 A/cm^2, and a band gap varying from 0 to 2 eV. The electrical properties of SiC consist of a resistivity varying from E 2 to E6 Ω.cm, with a band gap varying from 2.36 to 4.9 eV; silicon carbide is considered to be a semiconducting material.

Experimental Procedure

Silicon Carbide and SWCNT particles are distributed according to the amount of ethanol solution that is to be used; a certain amount of milligrams of particles is to be dissolved into the same amount of milliliters. A solution of 95% ethanol 5% water is added to the measured particles. The mixture is placed and adjusted on a sonifier, which is then operated at 70% of its capacity for 15 minutes; two minutes of continuous sonication are added. The sonication process ensures that the particles are thoroughly distributed in the substance for later

Figure 1 – Deposition of mixture on glass substrate.

study. A small amount of the mixture is taken with a clean pipette and carefully placed onto the working substrate, in this case glass; this is shown on figure 1. Once the SWCNTs-Silicon Carbide mixture is evenly distributed, it is to be carefully placed on a hot plate, previously heated to 100 °C. The leftover ethanol will then evaporate and the substrate will be left with a thin layer of pure mixture; this process is to be repeated several times until one can see a clear, full line of product. Once the sample is finished, electrodes must be created to allow for testing; these are constituted of silver epoxy and small alumel wires. The recording of values will be done with the help of two multimeters. Alligator clips are placed on each electrode, and the former are connected to the first measuring device; a thermocouple wire is connected to the second recording device, which will be destined for temperature-measuring purposes only. With this setup, one end of the thermocouple is placed on the hot plate (which is initially at room temperature), while the other is put on an ice pack, to create the temperature difference. The initial cold junction temperature is recorded, and the thermocouple is placed on the hot junction for the rest of the experiment. The temperature is allowed to rise on the hot plate up to a maximum of 200 °C; appropriate measurements are taken during this time. This process is repeated for different samples and combinations of Silicon Carbide and SWCNTs. For further study, the sample is analyzed on the SEM to observe how links are made at nanoscale.

Results & Discussion

A silicon carbide sample was created to record its values and compare them to those of the samples containing SWCNTs. According to previous literature, isolated Silicon Carbide particles are shown to exhibit no thermoelectric effect [4]. The performed experiments coincide with this statement; as shown in figure 2, the measured Seebeck coefficient for a SiC-only sample is found to be zero, corresponding to no voltage difference with temperature increase. Additionally, no current was found during the experiment, and resistance was found to be very large. The results shown below correspond to samples created with 50 wt%, 25 wt% and 10 wt% concentration of SWCNTs. Voltage is measured to linearly increase in every test. Those performed on these samples act accordingly; nevertheless, while the 50 wt% concentration sample shows higher values than the 25 wt% sample, the 10 wt% specimen rises above the values of the latter and thus does not complete the predicted trend. With these values, the Seebeck Coefficient is calculated for each sample. This number will give a measurement of thermoelectric power; in this case, its value was calculated by measuring the slope of each voltage-temperature line. The results are shown to be somewhat similar to each other, indicating that the slopes are close as well, as one can see in figure 3. The values for the Seebeck coefficients are depicted in table 1.The found power factors can also be seen in this figure, related to the Seebeck coefficients in a proportional manner according to the formula — . Current is shown to increase linearly for each of the samples measured; the value of the slope differs according to each concentration, however. The measured quantities correspond to micro amperes, which show that the value of current will not be significant, yet it is still existent. Figure 4 shows the values and slopes from these measured currents. According to the tests performed, resistance is shown to increase when the quantity of carbon nanotubes decreases; this result corresponds to standards set by previous knowledge as the conductivity of the former is much greater than that of SiC. If one observes figure 6, the sample with 10 wt% concentration of

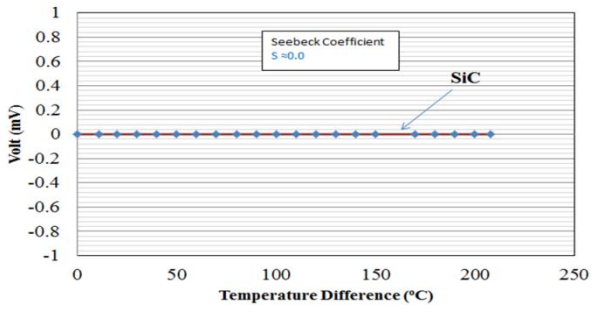

Figure 2-Voltage vs. Temperature Difference for SiC

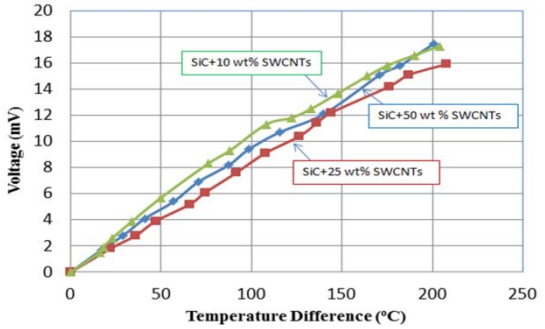

Figure 3- Voltage vs. Temperature Difference for SWCNTs

SWCNTs has a resistance in the 11000 ohms, while the 50 wt% concentration is shown to be between 600 and 800 ohms. It is also to be noted that resistance in individual samples has been observed to linearly decrease as the temperature difference between junctions increases. The samples were analyzed in the SEM for a thorough observation of their link-forming properties; as one can see in figure 5 the size difference between both materials causes an easy identification of each; the paths that the nanotubes create are randomized, and there appears to be an even distribution of materials. Nevertheless, this might not be the case in the complete sample, and alternative methods must be sought to standardize and analyze this composition.

Table 1

Type of Sample	Seebeck Coefficient, S (mV / ^{O}C)	P.F (W.K^{-2}m^{-1})
SiC+10 wt% SWCNTs	0.084±0.007	0.06×10^{-7}
SiC+ 25 wt% SWCNTs	0.080±0.008	0.3×10^{-7}
SiC+50 wt% SWCNTs	0.085±0.008	0.8×10^{-7}

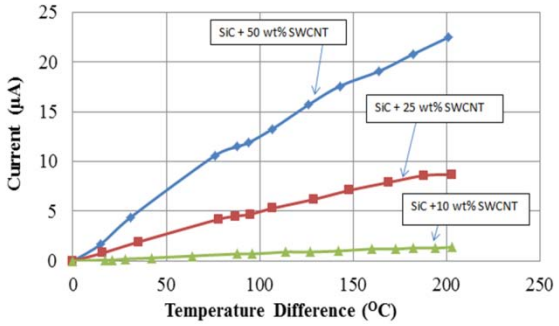

Figure 4-Current vs. Temperature difference curve

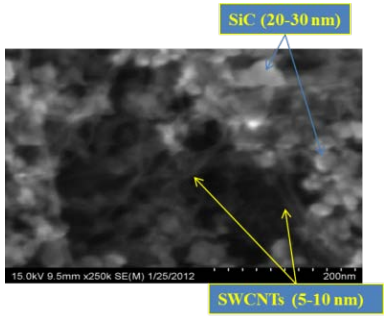

Figure 5-Sample as seen in the SEM

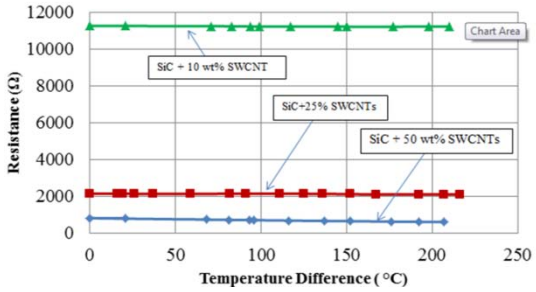

Figure 6-Resistance vs. Temperature difference curve

Conclusion

As the graphs indicate, the thermoelectric properties of SiC-SWCNTs samples are found to greatly increase with the addition of the latter particles. Although there is no great change for the Seebeck coefficient in the three performed tests, further experimentation must be performed in order to contrast this to other weight percentages. The ideal mixture ratio of a material composed of these two kinds of particles will consist of the required thermoelectric properties for a specified application. Additionally, further experimentation could be performed to test the mechanical values of this mixture.

Reference

1. A. Fereidoon, M. Ghorbanzadeh Ahangari, M.D. Ganji, M. Jahanshahi, Density functional theory investigation of the mechanical properties of single-walled carbon nanotubes, Computational Materials Science, Volume 53, Issue 1, February 2012, Pages 377-381,

2. Mavrinskiy, A., Baitinger, E., & , (2008). Thermoelectric power in carbon nanotubes. *Semiconductors*, *43*(4), 480-484
3. Jiang, J., Wang, J., & Li, B. (2011). A nonequilibrium green. *Journal of Applied Physics*, *109*, doi: 10.1063/1.3531573
4. Garcia, O. (2011). *Experimental study of thermoelectric properties for randomly distributed carbon nanotubes and silicon carbide nanoparticles*. (Master's thesis, The University of Texas at El Paso).

SYNTHESIS AND CHARACTERIZATION OF GRAPHENE AEROGEL FOR HIGH PERFORMANCE ENERGY STORAGE APPLICATION

Mohammad Arif Ishtiaque Shuvo, Miguel Mendoza, Md Ashiqur Rahaman Khan and Yirong Lin[1]*
Department of Mechanical Engineering, The University of Texas at El Paso, El Paso, TX, 79968
* [1] Corresponding Author: Yirong Lin (ylin3@utep.edu)

Keywords*: Graphene, Aerogel, Energy Storage, Lithium ion battery*

ABSTRACT

Graphene, the progenitor of all Graphitic components, has become one of the most exhilarating topics in both academia and industry for being highly promising in various technological applications. A single layer of Graphite with sp^2 bonded carbon atoms densely packed in a honeycomb crystal lattice is known as Graphene. The excellent mechanical, electrical, thermal –and nontoxic properties of graphene have intrigued the researcher to incorporate this material in space craft design (for having breaking lengths of 5000–6000 km at sea level and can conduct electrical power), lithium-ion-batteries (LIBs), super capacitors, solar cells and many other hi-tech propositions. Its high specific area, strong nano-filler adhesion properties have made it not only an excellent choice for composites with excellent mechanical properties but also the high charge carrier and concentrations properties have made it promising candidate for nano-electronic devices. However, synthesizing single layer graphene is still a problem and very few methods have been developed for its mass production thus limits its further application in industrial scale devices. Therefore, we report a scalable method to synthesize graphene by modified Hummer's method and graphene aerogel using freeze-drying. Scanning Electron Microscopy and X-Ray Diffraction, Brunauer-Emmett-Teller (BET) surface area testing were used for the characterization of graphene and graphene aerogel. Different parameters in centrifuge and horn sonication are used to control the geometry information of graphene and graphene aerogel. Due to the high specific surface area and robust mechanical strength, this synthesized graphene and graphene aerogel have the potential to be used for electrode materials for electrochemical energy storage devices such as lithium-ion battery, super-capacitor to further enhance the specific energy density for the next generation mobile devices.

1.0 Introduction

Graphene, the recently discovered two dimensional materials, is a hot research topic in the nano-research world for having variegated material properties within itself and thus pacifies many research demands. The scientific community has been fascinated by its distinct difference with carbon nanotube (CNT) and fullerene, and exhibition of unique properties. Quantum Hall effect at room temperature, an ambipolar field effect along with ballistic conduction of charge carriers, tunable band gap and high elasticity are the important properties of graphene [4]. Instead of flat surface, undulated graphene surface is obtained because of thermal fluctuation and the rippled magnitude is about one nanometer [1]. Based on

number of layers, graphenes have been defined as Single layer graphene (SG), Bi-layer graphene (BG) and few-layer graphene (number of layers ≤ 10) [4].

In periodic table we find C in IV A and therefore have 4 valence electrons with similar energies which facilitate easy hybridization. Out of 6 total electrons of carbons, 2 inner shell electrons belong to a spherically symmetric 1s orbital that is tightly bound and has energy far from the Fermi energy of Carbon. Rest 4 electrons give rise to 2s, $2p_x$, $2p_y$ and $2p_z$ orbitals. Distinct hybridization capability sets carbon apart from other materials and this allows carbon to form 0D, 1D, 2D and 3D structures [5]. Thus carbon has the ability to form 2D Graphene.

2.0 Experimental Section

2.1 Graphene Synthesis

In our way of research, we used chemical oxidation method for synthesizing graphene. At first, we added 12mL of H_2SO_4 slowly to Graphite powder (3g 300 meshes, 99%), $K_2S_2O_8$ (2.5g), and P_2O_5 (2.5g) mixture. The solution was poured into a bottle and heated at 80°C for 4.5 hours using a hotplate keeping it inside a water bath. After heating the solution was brought back to room temperature and was subjected to sonication for 2 hours. Then the solution was diluted with 0.5L of de-ionized (DI) water and filtered using a 0.2 micron Nylon Millipore filter to remove the residual acid. The product is dried under ambient condition overnight. After this pre-oxidation the mixture is subjected to Hummers Method. Then the pre-treated graphite powder and 120mL of concentrated Sulphuric Acid were stirred together in an ice-bath. Later 15g. of potassium permanganate ($KMnO_4$) was added to the suspension maintaining vigorous agitation. The temperature was monitored during addition process so that the temperature would not exceed 20°C. Removing the ice bath the suspension temperature is brought 35±3° for 2 hours and then diluted with DI water (250ml). As addition of water evolved heat, it is then again kept in ice bath to keep the temperature below 50°C. The mixture was then heated for 2hours at 90°C. The diluted mixture then turns into brown color. It is then further diluted with 0.7 liters of water and for reduction 30% hydrogen peroxide (20ml) was added which made residual permanganate and manganese dioxide to colorless soluble manganese sulfate. Peroxide treatment made the suspension bright yellow and upon filtration yellow-brown filter cake was found. To avoid precipitation of the slightly soluble mellitic acid salt which was formed during reaction, the warm suspension was filtered and washed with 1:10 HCl aqueous solution (1L) to remove metal ions followed by 1L DI water to remove the acid. The obtained Graphite oxide was subjected to 0.5 wt% dispersion followed by dialysis to completely remove salts and acids. Then exfoliation was carried out by using digital horn sonicator for 30 mintues. The dispersed solution was subjected to centrifugation at 3000 r.p.m. to remove any un-exfoliated graphite oxide for another 30 minutes which centrifuge has a rotor diameter of 14cm. Then we will freeze the solution bellow 0° and applying fridge drier we will get dry Graphene Oxide (GO). [1], [2]

2.2 Reduction: The prepared Graphene Oxide is heated in a tube furnace up to 600°C with a heating rate of 5°C/min in Nitrogen atmosphere and kept there for 2h for the complete reduction of GO to Graphene.

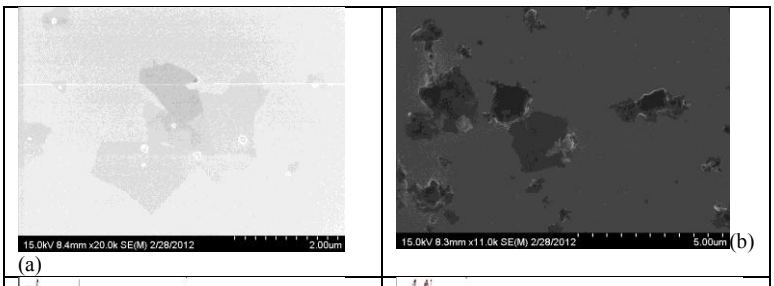

Figure 1. (a) SEM image of single layer graphene overlapping each other (b) SEM image of few layer graphene.

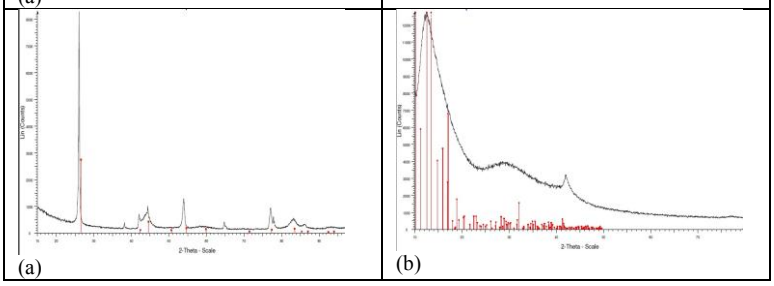

Figure 2. XRD pattern of (a) Pure Graphite (b) Oxidized Graphite.

3.0 Results and Discussion

Scanning Electron Microscopy (SEM) was performed for understanding the degree of exfoliation. From the SEM image in Figure 1(a) it is clearly visible that single graphene layer is overlapping each other and Figure 1(b) shows few layer graphene stacking together. X-Ray diffraction (XRD) was used for understanding the degree of oxidation. As pure graphite was bonded with oxygen after oxidation, the interlayer distance was increased which can be understood by observing the pick shift in XRD patterns. 2θ value for the pick in graphite oxide decreased.

4.0 Conclusion

Research has been done for synthesizing this single layer graphene in a mass basis which will be incorporated into making nano-composites with excellent mechanical properties and electrode materials for energy storage devices. Sonication time and energy have impact on dispersion and exfoliation of the graphene nano sheet.

References

[1] W. S. Hummers and R. E. Offeman. "*Preparation of Graphitic Oxide*", J.Amer. Chem. Soc., Vol. 80, pp. 1339-1339, 1958.
[2] Yuxi Xu, Hua Bai, Gewu Lu, Chun Li and Gaoquan Shi. "*Flexible Graphene Films via the Filtration of Water-Soluble Noncovalent Functionalized Graphene Sheets*"
[3] Jinhong Yu, Xingyi Huang, Chao Wu and Pingkai Jiang. "*Permittivity, Thermal Conductivity and Thermal Stability of Poly(vinylidene fluoride)/Graphene Nanocomposites*"
[4] C.N.R. Rao, A. K. Sood, K. S. Subrahmanyam and A. Govindaraj. "*Graphene the new two dimensional nanomaterials*"
[5] Saito, R., G. Dresselhaus, et al. "*Physical Properties of Carbon Nanotubes*", 1998.

CENTRAL FINITE-VOLUME SCHEMES IN GLOBAL ATMOSPHERIC MODELS

K. Katta[12*], R. Nair[1], V. Kumar[2]
[1]National Center for Atmospheric Research, Boulder CO 80305, USA
[2] Computational Science Program/Mechanical Engineering, El Paso, TX 79968, USA;
* kkkatta@miners.utep.edu

Keywords: *conservative transport; central finite-volume; non-oscillatory; positivity preservation; cubed-sphere; deformational flow; high-order WENO*

ABSTRACT

Central finite-volume (FV) schemes are a subset of Godunov-type methods for solving hyperbolic conservation laws, widely known for their simplicity. Among the advantages of these schemes are that they do not require Riemann solvers or characteristic decomposition and grid staggering. These characteristics make them different from upwind schemes so that they can be used for solving a wide range of problems governed by conservative systems, including geoscience problems. In this work we demonstrate the performance of four different schemes, which are based on the central FV framework. The four central schemes considered for linear transport problems are the Kurganov-Petrova (KP), a third-order central Weighted Essentially Non-Oscillatory (WENO-33), a fifth-order dimension-splitting WENO (WENO-5), and a combination of WENO-33 and WENO-5 (WENO-35). For numerical modeling of the transport of trace constituents in atmospheric models positivity-preserving solution is essential. However, WENO schemes are not strictly positivity-preserving and can produce minor spurious oscillations in the numerical solution. In order to address this issue a bound-preserving filter along with an additional flux correction step are employed. Both these techniques are inexpensive and effective. These FV schemes are semi-discrete, and the time integration is performed with a third-order or fourth-order strong-stability preserving Runge-Kutta scheme, depending on the order of the spatial discretization. The numerical schemes are evaluated with several benchmark tests, on a 2D Cartesian plane and the cubed-sphere geometry, which accentuate accuracy and conservation properties.

1. Research Description:

1.1. Motivation:

Atmospheric numerical modeling has been going through drastic changes over the past decade, mainly to utilize the massive computing capability of the petascale systems. This obliges the modelers to develop grid systems and numerical algorithms that facilitate exceptional level of scalability on these systems. The numerical algorithms that can address these challenges should have the local properties such as the high on-processor operation count and minimum parallel communication i.e. high parallel efficiency, it should also satisfy the following properties such as inherent local and global conservation, high-order accuracy, geometric flexibility, non-oscillatory advection, positivity preservation.

1.2. Central Finite Volume Schemes: A Possible Solution

To address the above-mentioned properties, I considered high-order Central Finite-Volume (FV) schemes. Central FV schemes are a subset of Godunov-type methods for solving hyperbolic conservation laws, widely known for their simplicity. The FV methods offer inherent conservation property and geometric flexibility to adapt to complex grid systems, and have the potential to exploit current massively parallel petascale computers. The

advantages of these types of schemes include, free from Riemann solvers or characteristic decomposition and grid staggering. Note that exact Riemann solvers do not exist for many practical problems, and they are often computationally expensive. These characteristics make them different from upwind schemes, and universal methods, which can be used for solving a wide range of problems governed by conservative systems (partial differential equations) that can be written in integral control-volume form over a domain including geosciences problems. Design or choice of the grid system for the computational domain also plays a vital role in overall efficiency of the modern FV based model. For example, the global FV climate model based on conventional latitude-longitude spherical grid system has stringent limitation to scale to massively parallel machines. Because of the computational problems (including scalability issues) associated with the polar singularities, latitude-longitude grid system is not considered for the next generation global modeling. Other choices for global grid systems that can provide quasi-uniform grid structures (control-volumes) are icosahedral hexagonal grid, Yin-Yang grid and cubed-sphere grid. However, the cubed-sphere grid system is very well suited for FV discretization, because the underlying control-volumes (grid cells) are logically rectangular, facilitating an easy implementation. Moreover, the cubed-sphere grid system is free of polar singularities, and its grid uniformity leads to excellent parallel efficiency. Due to the characteristics of the cubed-sphere grid, it has been adopted for the proposed global FV transport schemes.

2.3 Current Research

High-order central finite-volume schemes for linear transport problem and Shallow-water model on the cubed-sphere.

In my work, I demonstrated the performance of four different schemes, which are based on the central FV framework. The four schemes considered are Kurganov-Petrova (KP) (see Kurganov and Petrova 2001), a compact central Weighted Essentially Non-Oscillatory (WENO-33) (see Levy *et al.* 2000), a fifth-order WENO (WENO-5) (see Byron and Levy 2006), combination of WENO-33 and WENO-5 (WENO-35), for a linear transport problem on the sphere. For numerical modeling of the transport of trace constituents in atmospheric models, a non-oscillatory, positivity preserving solution is essential. WENO schemes produce spurious oscillations in the numerical solution; to address this issue a Bound-Preserving filter is employed, to further achieve strictly positive-definite solution an additional flux correction step is implemented. Both the techniques are inexpensive and effective. A third-order or fourth-order Strong Stability Preserving Runge-Kutta time stepping scheme based on the order of the spatial discretization is used. The numerical schemes are evaluated with several benchmark tests, on a 2D Cartesian plane and cubed-sphere geometry, which accentuate accuracy and conservation properties.

The above-mentioned central FV schemes are then extended to a full shallow water model on the cubed-sphere in curvilinear coordinates. The shallow water equations (SWE) are the simplest form of the equations of motion used to describe the evolution of an incompressible fluid in response to gravitational and rotational accelerations on the surface of the sphere. The SWE are derived from the Navier-Stokes equations, which describe the motion of fluids. Accuracy tests are then performed for the SWE for the test problems as proposed in the climate simulation community which include Global steady state nonlinear geostropic flow, Steady state zonal geostropic flow with compact support, Forced nonlinear system with a translating low, Zonal flow over isolated mountains, Rossby-Haurwitz wave. My contributions include the demonstration of the above-mentioned schemes for atmospheric modeling, which are implemented for the first time on a cubed-sphere. The results obtained from the experiments are quite impressive (The results from the moving vortices test are shown in the figure below, the error norms can be compared to many schemes being developed, like Nair and Lauritzen (2010), Putman and Lin (2007), etc.). This may give the

opportunity to better understand the atmosphere and can achieve accurate prediction of the future climate.

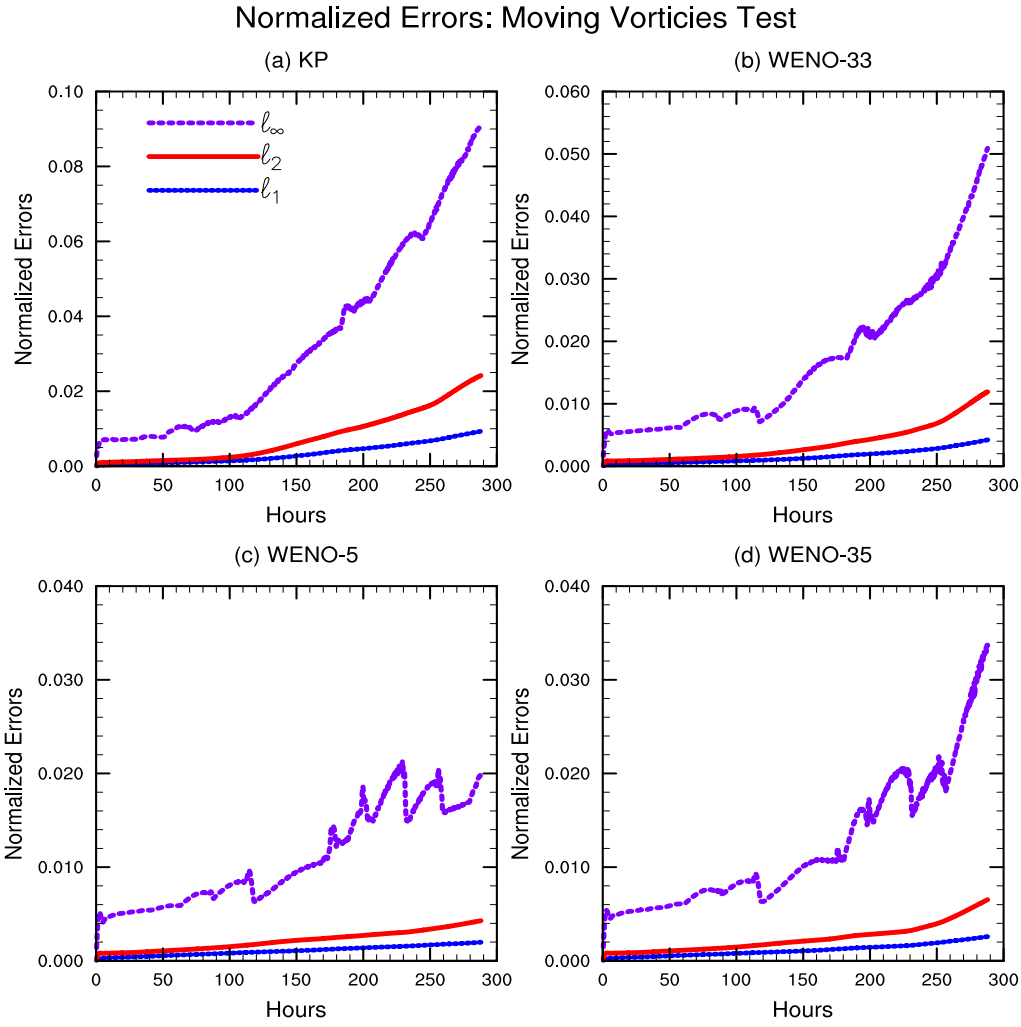

References

[1] Kurganov A, Petrova G. 2001. A third-order semi-discrete genuinely multidimensional central scheme for hyperbolic conservation laws and related problems. *Numerische Mathematik* **88**: 683–729.

[2] Levy D, Puppo G, Russo G. 2000. Compact central weno schemes for multidimensional conservation laws. *SIAM J. Sci. Comput.* **22**: 656–672.

[3] Jiang GS, Shu CW. 1996. Efficient implementation of weighted eno schemes. *J. Comput. Phys.* **126**: 202–228.

[4] Nair RD, Lauritzen PH. 2010. A class of deformational flow test cases for linear transport problems on the sphere. J. Comput. Phys. 229: 8868-8887.

[5] Katta K, Nair RD, Kumar V. 2011. High-order central finite-volume schemes for linear transport problems on the cubed-sphere. Submitted to QJRMS.

MODELING OF A PIPE FLOW DISTRIBUTOR FOR SINGLE TANK THERMOCLINE THERMAL STORAGE SYSTEM

S. Afrin[1], V. Kumar[1]*
[1] Mechanical Engineering, University of Texas at El Paso, El Paso, TX 79968, USA;
* Corresponding author (vkumar@utep.edu)

Keywords: *Thermal Energy storage, Concentrated Solar Power, Thermocline, Flow distributor*

ABSTRACT

Single tank thermocline thermal storage system (TES) is such a system in which both hot and cold heat transfer fluid flows simultaneously. The temperature gradient zone is named as thermocline. Maintenance of this thermocline region in a single tank TES system during the charging and discharging cycles for a concentrating solar power (CSP) plant depends on the uniformity of the velocity profile at any horizontal plane. We check the velocity distribution for a pipe flow distributor influenced by the dimension which includes the diameter of the main pipe, distributor pipes, holes, distance between holes, number of holes and holes position in the distributor pipe. Our research focuses on the computational analysis of the dynamics Hitec® molten salt as a heat transfer fluid for various distributor configurations using the commercial software GAMBIT 2.4.6 FLUENT 6.1. Our objective is to optimize uniformity of velocity distribution to maintain the hot and cold thermal fronts by varying the geometry of different types of flow distributor. We compared the standard deviation of the velocity field at various positions of the tank height for each configuration to assess the uniformity of velocity distribution and mixing of the cold and hot region.

Introduction

Advanced research on thermal energy storage (TES) coupled with renewable energy pulling its concern to concentrated solar power (CSP). Solar energy that we get from sun is the most available convenient sources of energy. It is abundant to meet the current demand of energy. But because of its intermittent nature solar energy can only be utilized at sunny day. So it needs to be stored for continual supply during peak demand and to stabilize the fluctuations of energy. TES, employed by CSP, is the solution to reserve solar energy and enabling it to produce electricity when the sunlight is not available.

TES comprises a number of technologies for storing solar power on heavy scale which can be stored for later use and single tank thermocline is one of them. In single tank thermocline system both the hot and cold fluid placed in the same tank. In this system the two regions - hot and cold temperature region is disjoined for all operating period. These two regions separated by a temperature gradient known as thermocline. The hot fluid positioned at the top and the cold fluid at the bottom of the tank. When the system is charged the cold fluid is

drained from the bottom of the tank, heated up by the solar field and returned through the top of the tank. In the discharging period the hot fluid drawn from the top of the tank and cooled down while passing through the power conversion equipment [1].

Theory

We analyze the pipe flow distributor of different geometry to check the velocity distribution. Fig.1 shows the schematic diagram of pipe flow distributor and single tank storage system .

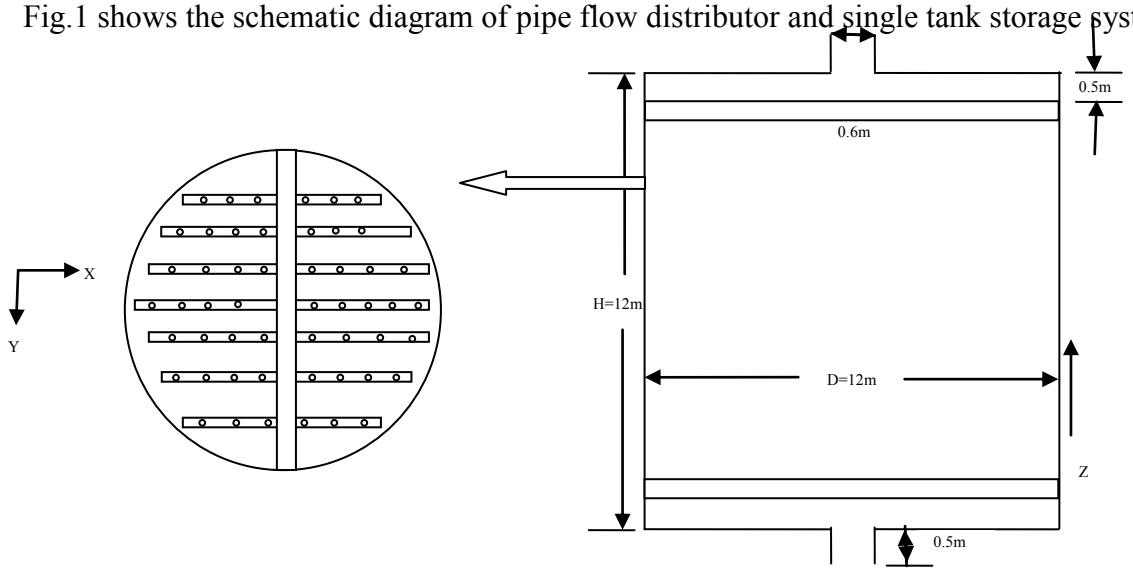

Fig.1. Schematic diagram of pipe flow distributor and single tank storage system

The dimension of the single tank is $12m$ height and $12m$ diameter [2]. For pipe flow distributor the inlet diameter is $0.6m$. The main pipe diameter varies by $1.0m$ and $0.8m$, distributor pipe diameter is $0.6m$ and the hole diameter is $0.3m$. The number of holes and distance between holes are varied along with the different number of distributor pipes. The hot fluid comes in from the top of the tank, which is inlet and the cold fluid goes out from the bottom of the tank which is outlet.

The average velocity is calculated by the following formula

$$v_a = v_i * \left(\left(\frac{d_{in}}{d_t}\right)^2 \right)$$

The inlet velocity of the fluid should be $0.2\ m/s$ for the tank height and diameter $12m$. To be fully charged by 6 hours.

Velocity at any point is compared to the average velocity. From the variation of these two velocities, percentage deviation of velocity can be obtained by the following formula

$$\delta V = \left(\frac{\sum_{i=1}^{n} \sqrt{(v - v_a)^2}}{N} \right) * 100\%$$

Near the inlet and outlet this deviation will be high and at the middle of the tank the desired value will be lower. So the thermocline region will be conserved on this way. A MATLAB code is developed to compare the results for all cases within a plot.

Result and Discussion

We did the computational analysis of different configuration of pipe flow distributor. We varied the number of distributor pipes by 6, 7, 8 & 9; distributor holes by 88, 104, 120, 140, 144 &168; holes position at the top of the distributor pipe near the inlet and at the bottom neat the outlet and the other way around. The percentage velocity deviation varied from 0.28% to 0.59% for different cases. From the result, that we got by doing the computational analysis using the commercial software FLUENT 6.3, we analyzed the performance of the distributor. In ideal case the velocity at the middle of the tank is assumed to be equal to the average velocity $0.0005 m/s$. We compared the results with ideal case and come up an end that the performance of the flow distributor is influenced by the geometry of the distributor. The following Fig.2 represents the graphical picture of the percentage deviation of velocity distribution at different height of the single tank.

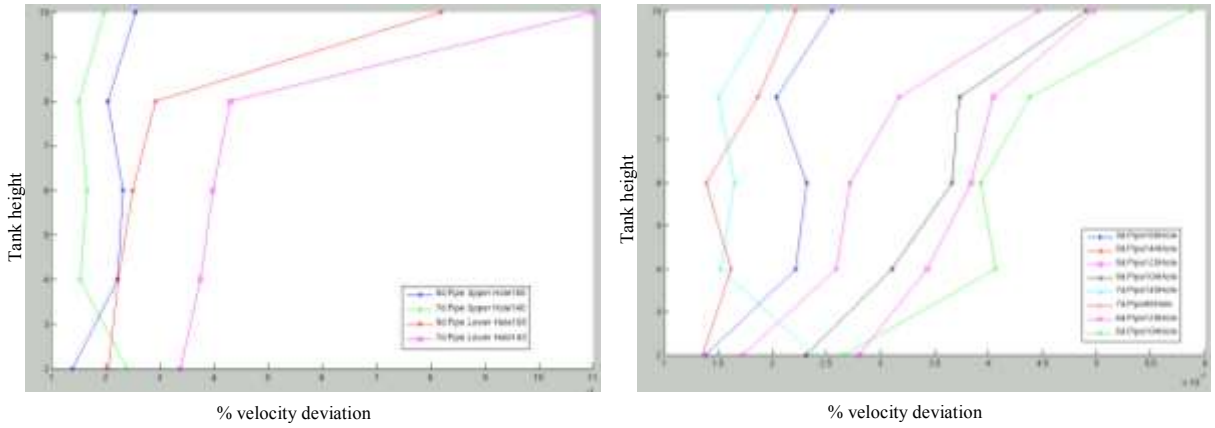

Fig.2. %Velocity deviation vs. height of the tank

Conclusion

To maintain the hot and cold thermal front in a single tank TES system we have studied different geometry of flow distributor considering different parameter and observed the numerical results to make a comparison with the theoretical values. We get to know that the velocity distribution is influenced by the number of distributor pipes, number of holes and holes position. It has also been influenced by the dimension of the pipes. In our future work we will check the velocity distribution contour for these cases to determine effective parameter for designing a flow distributor, impact of turbulence and the thermal effect.

References

[1] Parabolic Trough Thermal Energy Storage Technology, National Renewable Energy Laboratory,January 2010, <http://www.nrel.gov/csp/troughnet/thermal_energy_storage.htm>.

[2] Yang Z. and Garimella S.V., Molten_salt thermal energy storage in thermoclines under different environmental boundary conditions, (2010). CTRC Research Publications. Paper 138.

BACTERIALLY-MEDIATED PRECIPITATION OF FERRIC IRON MINERALS DURING THE LEACHING OF BASALTIC ROCKS

K. Schnittker[1a], J. Navarrete[1b], I. Cappelle[1c], D. M. Borrok[1d]
[1]Department of Geological Sciences, cSETR-Geology, El Paso, TX 79968, USA
kschnittker3@gmail.com[a], jnavarrete2@miners.utep.edu[b], ijcappelle@miners.utep.edu[c], dborrok@utep.edu[d]

Keywords: *T. ferrooxidans*, bioleaching, iron oxidation, basaltic rocks, acidic conditions

ABSTRACT

The bacterially-mediated oxidation of ferrous iron [Fe(II)] in environments where its oxidation is otherwise unfavorable (i.e., acidic and/or anaerobic conditions) results in the formation of ferric iron [Fe(III)] precipitates. The mineralogy and morphologies of these precipitates are dictated by the solution biochemistry. In this study, we evaluated Fe(III) precipitates that formed during aerobic bioleaching experiments with T*hiobacillus ferrooxidans* (T. *ferrooxidans*) and ilmenite ($FeTiO_3$) and Lunar or Martian basaltic stimulant rocks. During the experiments, the bacteria actively oxidized Fe(II) to Fe(III), resulting in the formation of white and yellow-colored precipitates. In our initial experiments with both ilmentite and basalt, High-Resolution Scanning Electron Microscopic (HRSEM) analysis indicated that the precipitates were less than 5μm and mostly nanometer-scaled, white, and exhibited a platy texture. Networks of mineralized bacterial biofilm were also abundant. In these cases the white precipitates coated the bacteria, forming rod-shaped minerals 5-10μm long by about 1μm in diameter. Energy Dispersive Spectra (EDS) analysis showed that the precipitates were largely composed of Fe and phosphorous (P) with an atomic Fe:P ratio of ~1. Additional experiments were performed where the growth media was altered to determine differences in the resulting precipitates. HRSEM/EDS analysis confirmed the presence of minerals with much higher Fe:P ratios (~2) and much smaller Fe:S ratios (~0.15). This suggests that the change in growth media chemistry was reflected in precipitates that were rich in S and poorer in P. Our results have implications for the interpretation of solution chemistries and precipitation mechanisms associated with biologically-mediated Fe(III)-minerals on Earth, but might also provide insights into possible biosignatures in extraterrestrial systems.

1. Introduction

For future space exploration the ability to extract resources from other planets, moons, and asteroids will become important. A possible alternative to high-temperature combustion and reduction methods for producing desirable metals from basaltic rocks and ilmenite is bioleaching[1]. Leaching experiments were conducted with *T. ferrooxidans* and basaltic rocks (Lunar and Martian simulant rock) and the mineral ilmenite ($Fe^{II}TiO_3$) under acidic conditions. All the Fe(II) for chemical energy was supplied by the mineral or rock. Our goals were to (1) explore bioleaching technologies for the in-situ resource utilization of planetary materials; (2) provide insights into possible biosignatures formations, and (3) provide new insights into terrestrial weathering processes under acidic pH conditions.

2. Background

2.1 *T. ferrooxidans* Metabolism

T. ferrooxidans is a Gram-negative, autotrophic (self-nourishing) bacterium. The bacteria are also known as *Acidithiobacillus ferrooxidans* (*A. ferrooxidans)* because they grow best under acidic conditions (acidophilic) [2]. Unlike plants that utilize light energy, these bacteria oxidizes inorganic compounds like Fe(II) to acquire chemical energy[3]. In this case, atmospheric oxygen is reduced to water as a byproduct; however, we envision that ultimately we will utilize iron-

oxidizing bacteria that use alternate electron acceptors. Because oxidized iron is largely insoluble, this process can result in the production of Fe(III)-oxide, -sulfate, or –phosphorous minerals depending upon the solution chemistry.

2.2 Heap Bioleaching

Heap leaching involves crushed ore being piled onto an impermeable base and an acidic leach solution like sulfuric acid (H_2SO_4) percolating through the system. The crushed ore is aerated to promote the microbial oxidation of iron and sulfur compounds, this is also called biomining[1]. Metals are recovered from these acidic solutions and are further refined by processes such as solvent extraction and electro plating. Microbes present in the heap increase the amounts and rates of mineral dissolution and metal solubilization. For example, the presence of *T. ferrooxidans* can enhance leaching by more than 100 fold compared to leaching absent of bacteria[5].

3. Objectives

- To determine whether the small amounts of Fe(II) in minerals like pyroxene and olivine within Lunar and Martian simulant basaltic rocks and the mineral ilmenite can support the metabolism and growth of *T. ferroxidans*.
- To determine whether more iron could be extracted from the rock in biotic systems than in biotic systems.
- To determine the minimal amount of growth nutrients needed to support the growth of bacteria in the experimental systems.
- To characterize any Fe(III)-minerals that formed as a result of the experimental leaching.
- To determine how the character and mineralogy of Fe(III)-minerals changed with changes in the experimental growth media.

4. Results

4.1 ICPOES Data. The graphs in Fig.1 show that Fe(II) was removed from the experimental solutions in the presence of iron-oxidizing bacteria, confirming metabolic activity.

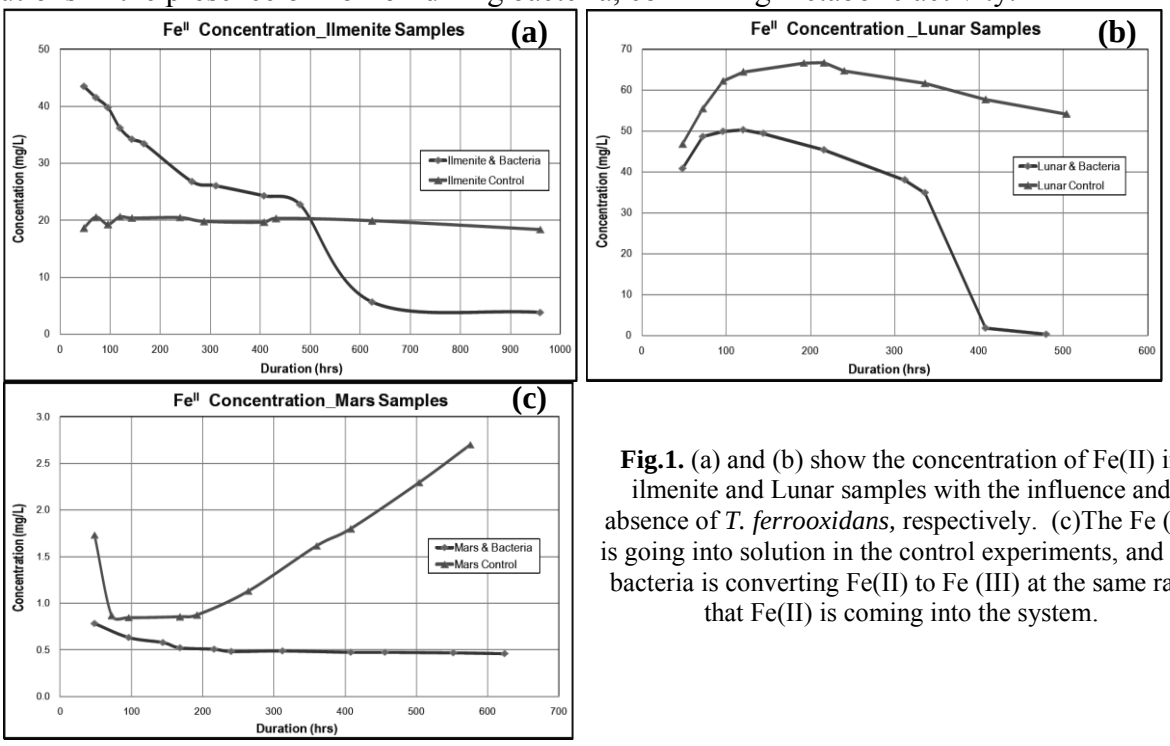

Fig.1. (a) and (b) show the concentration of Fe(II) in ilmenite and Lunar samples with the influence and absence of *T. ferrooxidans,* respectively. (c)The Fe (II) is going into solution in the control experiments, and the bacteria is converting Fe(II) to Fe (III) at the same rate that Fe(II) is coming into the system.

4.2 HRSEM/EDS Results. The photographs below show a variety of Fe(III)- precipitates that formed during leaching experiments. Depending upon the growth media conditions and pH, Fe(III)-phosphate, - sulfate, and –oxide minerals were formed.

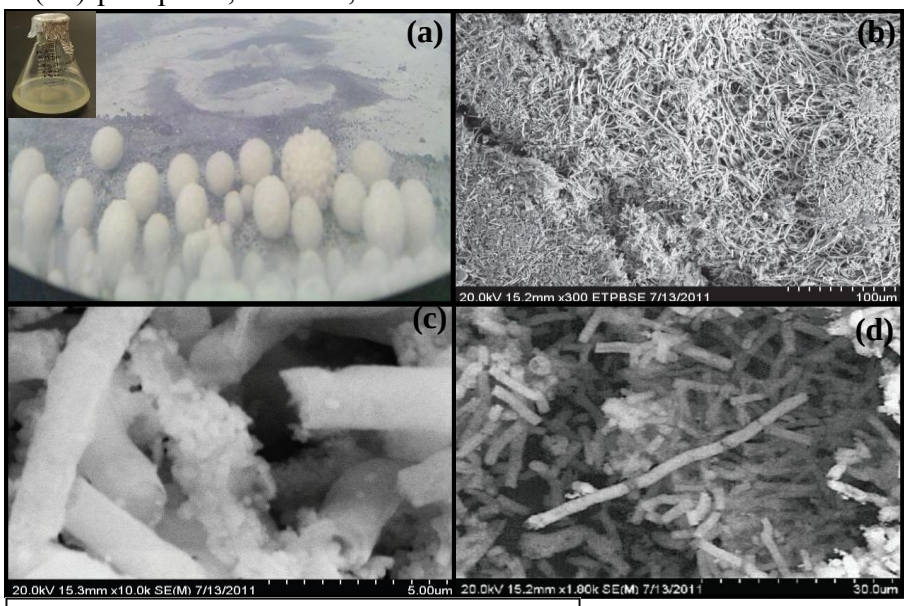

Fig.2. (A) Photograph of Fe(III)-phosphate and bacterial spheres that formed during leaching of ilmenite. (B-D) HRSEM images of the Fe(III)-phosphate biominerals. Bacteria strands are coated with Fe(III)-phosphate.

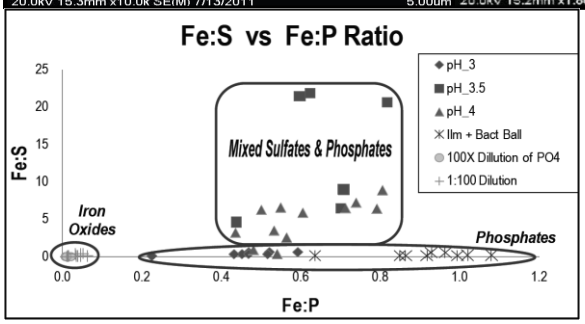

Fig.3. HRSEM EDS data from Fe(III)-precipitates for the original growth media, different pH levels, the P was diluted by an order of magnitude, and the overall growth media was limited. Precipitates could be broken into 3 different fields based on their Fe:P and Fe:S ratios. to lower.

4. Conclusions

- The small amounts of Fe(II) available in basaltic rocks (and ilmenite) supported the metabolism of *T. ferroxidans*.
- We were able to track this microbial activity even in systems that were severely-nutrient limited.
- A variety of Fe(III)-minerals were formed, depending upon the chemistry of the experimental solutions.
- Regardless of the Fe(III)-precipitates formed, they all had in common morphological features suggestive of bacterially-mediated growth. These morphological features may be useful as biosignatures.

5. Future Work

- Electron diffraction analysis will be performed to better identify mineral phases. We will create a working bio-reactor for these systems and test systems where the mineral apatite [$Ca_5(PO_4)_3(OH,F,Cl)$] is the only P nutrient source for bacterial growth.

6. References

[1] J. W. Evans and L.C. De Jonghe "*The Production and Processing of Inorganic Materials".* The Minerals, Metals, and Materials Society (TMS), 2002.

[2] D. E. Rawlings and T. Kusano "Molecular Genetics of *Thiobacillus ferroxidans". Microbiological Reviews,* Vol. 58, No. 1, pp. 39-55, 1994.

[3] T. Yamanaka "*Chemolithoautotrophic Bacteria: Biochemistry and Environmental Biology*". Springer, Japan, 2008.

[4] R. Näveke, "Bacterial leaching of ores and other materials". *Institut für Mikrobiologie*, Technische Universität, Braunschweig, Fed. Rep. Germany, 1986.

FLUENT SIMULATIONS FOR FLUID FLOW IN POROUS MEDIA FOR CARBON SECUESTRATION APPLICATION

E. Cordero[1]*, J. Ortega[1*], P. Delgado[1], V. Kumar[1], D. Crandall[2], G. Bromhal[3]

[1]University of Texas at El Paso, El Paso, TX
[2]Contractor, National Energy Technology Laboratory, Morgantown, WV
[3]National Energy Technology Laboratory, Morgantown, WV

*ecordero6@miners.utep.edu
*jdortega4@miners.utep.edu

Abstract

Fluid flow through porous medium at pore-scales is investigated. For the porous media grid building, a set of CT-scans were taken from a sandstone sample from an oil reservoir. These CT-scans were taken with the help of a medical imaging machine, so that the outcome would be a stack of the previously mentioned images or CT-scans. Simulation of imbibitions and drainage were also performed on simpler geometries, so that the physics and behavior could be proven correct, following the capillary pressure and conductance resistances principles.

A three dimensional computational model was produced using Image J™ and Scan IP™. Two-phase Volume of Fluid (VOF) simulations were performed using Fluent™ code. A good comparison of the model was obtained using a pore network for the drainage. The contact angle was found to have a significant impact on the micro scale physics in the numerical Fluent imbibition simulations. Plans for future work are also presented.

1 Introduction

1.1 Application and Objective

The carbon dioxide (CO_2) sequestration has the potential to significantly reduce the amount of pollutants released to the atmosphere, and by consequence reducing the greenhouse effect on the global climate. This technique is very proficient for enhanced oil and natural gas

recovery. To predict the behavior of the motion of CO_2 on the geologic repositories, accurate models for single phase and two phase flow in porous media under various conditions need to be constructed. The primary objective of this work is to improve the methods used to study flow motion in the micro-scale, so that the models can be used to determine and predict potential processes within CO_2 reservoirs.

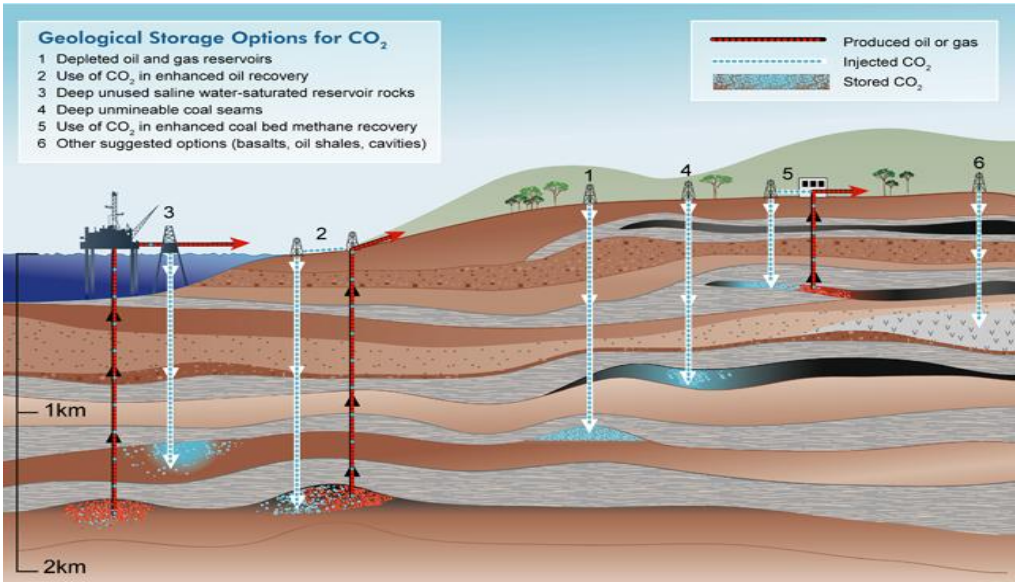

Figure 1. Schematic of the Geological Storage options for CO2

2 Procedure

2.1 Image Pre-processing

For the image pre-processing the freeware Image J was used. The stack of CT-scans was received in grayscale. After performing some smoothening, of these images the thresholding can be done, which will help to process the images as binary data for the following step. It is also important to do some scaling and cropping to eliminate the regions that are not of interest, in order to avoid memory limitation issues. As a parameter for future comparison, a three dimensional reconstruction of the model can be made in this software.

2.2 Image processing and Meshing

In the first case, the Iso2Mesh (1) was to process the binary images obtained from Image J and used to generate a surface mesh on the structure while extracting the information of the location of nodes and faces. This information was then written in form of a Journal file. This file provides commands to Gambit to plot the nodes and create the faces of the structure. Once the structure is re-created in Gambit a volume can be created and disconnected space can be deleted. The final meshing process can proceed and boundary conditions can be applied before in order to output a case file for Fluent.

For the second case, the processing and the meshing of the images obtained from Image J, was performed with help of the software Scan IP was used. In this step the unconnected space throughout the rock is deleted and then the three dimensional model is constructed. Once the reconstruction is completed a smoothening process is very helpful to obtain a better resolution of

the 3-D model. The meshing process is also done with this software which gives the user the freedom of choosing the solver that will be used for the simulation, which in this study was Fluent, and many other parameters for the volume and face meshes before the final case file for Fluent is produced.

2.3 Numerical Solver

The numerical solver used for these simulations was Fluent 5/6. Various simulations were performed with both air and water to better understand and describe the physics and behavior of fluid flow through a porous medium. Simple boundary conditions were used in the process such as a velocity inlet plane at the bottom of the rock and a pressure outlet set at the top plane of the model. All the cases were performed under the condition of steady state and only using single phase flow.

In an effort to perform a two phase flow simulation on this type of rocks, it was necessary to confirm the physics of the model at the micro scale. Consequently, imbibition and drainage unsteady flow simulations were performed on a two dimensional grid consisting of two parallel throats of different diameters, where it could be observed if the fluid was following the correct path as theory and previous experimental result dictate.

2.4 Post-Processing and Results.

For post-processing Fluent was also used. As it was very complicated to visualize the 3-D single phase flow simulation, cross-sectional planes were created starting from the inlet and swept in the z-axis direction to better understand the behavior of the velocities and pressures of the flowing fluid with respect to the geometry of the rock. As for the two phase flow simulation, successful results of the imbibition and drainage models were obtained which assured the reliability of the Fluent results for a 3-D multiphase flow model.

4. Conclusion and Future Work

With positive results obtained for the single phase flow simulations, there is more confidence in the process developed to be able to further study and investigate multiphase flows through a porous medium. Currently, two phase flow models are being developed and investigated. Since it is necessary to produce a model in the micro-meters scale, the meshing process becomes more complex and several iterations had to be tested in order to find a model that could be good for the CFD simulation. This meshing process is being investigated in order to produce a mesh of the model that can be useful without having to modify parameters. Nonetheless several more complex 2-D and 3-D models are being developed in order to assure that the case set-up is correct before it is implemented on a complex geometry such as a porous medium.

References:

1) Qianqian Fang and David Boas, "**Tetrahedral mesh generation from volumetric binary and gray-scale images**," Proceedings of IEEE International Symposium on Biomedical Imaging 2009, pp. 1142-1145, 2009

2) Crandall, D. (2007). TWO-PHASE FLOW IN POROUS MEDIA AND FRACTURES. 203.

Powering Large Manufacturing Facilties using Renewable Energy: Assessment on Reliability and Cost

Jesus Jimenez[1], Tongdan Jin[2], Saul Villarreal[3], Mauricio Cabrera-Rios[4]

[1,2,3]*Ingram School of Engineering, Texas State University-San Marcos, San Marcos TX, 78666*
[4]*Dept. of Industrial Engineering, University of Puerto Rico at Mayagüez, Mayagüez PR 00681A*

Keywords: *wind energy, solar Photovoltaics, net metering, loss-of-load probability, stochastic optimization, lifecycle assessment*

Abstract

A semiconductor manufacturing facility typically consumes 300-400 MWh electricity in the daily operation. Integrating wind and solar energy into the production process reduces the carbon footprint and sustains the business growth. A key challenge in deploying the renewable technologies is the power volatility. We investigate a grid-connected distributed generation system comprising wind and solar power to accommodate the daily electricity needs in a wafer fabrication environment. The study shows the renewable energy is cable of mitigating the carbon emission, enhancing the energy stability, and achieving cost savings in regions where the wind speed is above 4.8m/s or the overcast days are less than 35% of the year.

1. Introduction

Semiconductor wafer fabrications, also known as wafer fabs, consume a large amount of electricity in daily production. As smart grid initiatives, distributed generation (DG) systems comprising wind turbines (WT) and solar Photovoltaic (PV) systems emerged a promising technology to meet the growing energy needs in the next 20-30 years. Deploying DG systems in wafer fabs is able to control and reduce the greenhouse gases emission. However, a key challenge in deploying WT and solar PV systems is the power intermittency as the energy yield depends on the wind speed, weather condition, and geographical locations [1].

2. The Research Objective

Although the direct greenhouse gases emission from wafer fabs is less than 10% in the global carbon emission, the semiconductor industry is proactively and voluntarily reducing its emissions on a global basis. The transition towards to a sustainable manufacturing paradigm creates great opportunities for wafer fabs to contribute to a green society either directly or indirectly.

Wafer fabs can make direct contributions to the green society through energy saving. These include: 1) designing green semiconductor products that use less energy; 2) using environmentally benign materials to make semiconductor device; and 3) building sustainable

fabs that use less energy to make chips. The ITRS has set aggressive goals for the semiconductor industry to decrease the energy from the current 1.9 k Wh/cm^2 to 1.2 k Wh/cm^2 by 2016 [2]. Indirect contributions to the protection of the environment include: 1) providing products that enable customers and society to save energy during the operation; and 2) designing products that enable energy savings at the assembly and final system level.

This research aims to conduct a lifecycle cost assessment which guides the modeling, analysis, and integration of a cost-effective DG system in large wafer fabs. The DG system comprises WT units, solar PV panels, a net metering system, and a substation connected to the main grid. Figure 1 shows the grid-unconnected DG system under study.

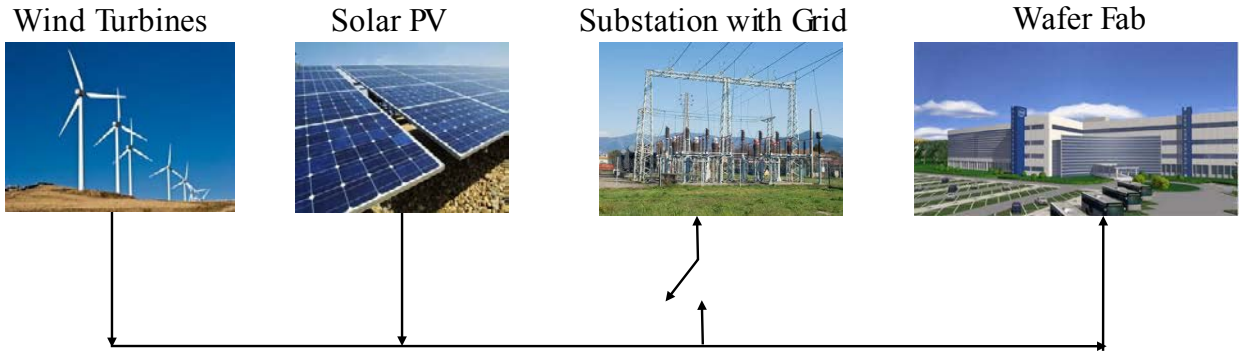

Figure 1. A grid-connected DG system integrated with renewable power.

The objective of the study is to determine the types and capacity of WT, solar PV, and substation such that the lifecycle cost of the DG system is minimized subject to a loss-of-load probability (LOLP) constraint. It is assumed that WT generate electric power during the day and night; the solar PV system produces power from 7 am to 7 pm each day. The net metering system allows the wafer fab to sell the surplus renewable electricity back to the utility company if the renewable power exceeds the load. The substation is used as a contingency when the load exceeds the total alternative power. The lifecycle costs include the DG installation, operations, maintenance, and utility bills. The system profit includes tax credits and the revenues generated when selling surplus alternative energy through the net metering. Wafer fabs located in Dallas TX, Phoenix, AZ, and Portland, WA are used to compare how different locations and weather conditions affect the energy yield of the DG system.

3. The Research Methodology

To solve this highly non-linear mixed integer stochastic programming, a computer simulation model implemented by WITNESS simulation software is developed to mimic the wind speed and solar radiation, based on which the actual energy production is predicted. The output of WT and solar PV is a stochastic process as the energy production depends on the weather condition, the clock time, and calendar date. The simulation model coupled with a simulation-based optimization algorithm is used to determine DG type and sizing to minimize the cost over the 20-year horizon. The algorithm has five controllable factors: choice of 1 MW WT, 2 MW WT, 3 MW WT, the capacity of PV system, and the capacity of the substation. The simulation-based

algorithm uses linear regression to approximate the desired configuration for the wafer fab, followed by a Central Composite Design (CCD). After obtaining values through the CCD for the determined setting, the best solution is chosen as an incumbent. A metamodel is then created, and it is subject to optimization using the Generalized Reduced Gradient Algorithm on Excel Solver under a multiple starting point scheme. After a potential minimum is obtained, three stopping criteria are checked: 1) the potential minimum belongs to the original CCD; 2) the R squared is 100%; or 3) a predefined maximum number of iterations have been achieved.

The software used in this study includes Excel Solver, Minitab, and Matlab, for the simulation-based algorithm. WITNESS simulation software was used for modeling and predicting the instantaneous power and annual energy production of the distributed generation system.

4. Preliminary Results

The results show that from purely economic point of view, integrating the solar PV technology into wafer fabs implies 20-25% of additional cost on top of the baseline cost. The major cost component is the capital investment on PV systems. Current PV cost is $4-5/W which is more than twice higher than the wind technology. The study indicates that WT technology is more attractive as energy can be produced 24 hours a day across the year. Our analysis shows that if the average wind speed exceeds 4.8 *m/s* in a region, WT becomes a reliable and affordable alternative energy resource to power the manufacturing facility.

A direct benefit of adopt WT and PV technology is to improve the LOLP performance. The study shows that if 20% of the load is supplied by renewable power such as PV or WT, the LOLP drops by 50%. It is also worth of mentioning that the system cost in our studies may be overestimated. If the wafer fabs simply decides to meet the baseline LOLP, the minimum substation capacity needed is lower than the current baseline. Hence the total DG system cost is expected to decrease owning to the reduced installation cost of the substation.

5. Conclusion

In summary, this study proposed a probabilistic-based method to design a sustainable DG system to supply the electric energy for large manufacturing facilities such as wafer fabs. The probabilistic method blended within a simulation model is developed to characterize the power volatility and load uncertainty. The results show that if we consider the growing trend of the utility price and uncertain fossil fuel for the next 20-30 years, the decision on installation of WT and solar PV becomes more supportive. This will absolutely increase motivation for those chip manufacturers seeking to build environmentally friendly facilities which are self-sustained and cost-effective in a long-term perspective.

References:

[1] C. Novoa, T. Jin, "Reliability centered planning for distributed generation considering wind power volatility," Electric Power Systems Research, vol. 81, no. 8, 2011, pp. 1654-1661.

[2] International Technology Roadmap of Semiconductors (ITRS). Environmental, Safety and Health Chapter. [Online]. Available http://www.itrs.net, last accessed on January 27, 2011.

[3] S. Villarreal, J.A. Jimenez, T. Jin, M. Cabrera-Rios, "Designing a sustainable and distributed generation system for semiconductor wafer fabs," Texas State University Working Paper, 2012.

CHALLENGES ON BIO-FUELS DISTRIBUTION NETWORK IN THE US

German Reyes[1], Hansuk Sohn[1]*
[1] Industrial Engineering, New Mexico State University, Las Cruces, NM 88003, USA;
* Corresponding author (hsohn@nmsu.edu)

Keywords: *Bio-fuels, Distribution*

ABSTRACT

This research aims at studying decision support tools which can handle the infrastructure of bio-fuels supply chain. Though there have been several models developed to analyze productions of bio-fuels and feedstock based on certain criteria, literature review suggests that there have been minimal attempts to develop research on the supply and delivery issues of these sources. To handle this issue, we will take the first step at better identifying the distribution factors that play a key role in developing and refining the infrastructure necessary to deliver bio-fuels, and then develop a simulation model for evaluating a range of future biofuels distribution scenarios.

1 Goals and Objectives

Increased demand for, and volatile cost of, fossil fuels has augmented the interests in developing technologies that can leverage alternative energy sources, including bio-fuels. A wide spectrum of organizations, from established research firms to new startups, are investigating the feasibility of different stocks and process technologies in producing bio-fuels [1] – [9]. However, research on the supply and delivery issues of these sources has been minimal. Aside from a handful of government reports and one practitioner conference, formal investigation of supply chain and distribution issues of bio-fuels is essentially absent.

This research study has two major aims. First, we take the first step at better identifying the distribution factors that play a role in developing and refining the infrastructure necessary to deliver alternative fuels. Clearly there are many process stages to produce and deliver bio-fuels. For example, whether large and centralized or small and decentralized processing plants are more viable for a specific fuel is critical to its success in the marketplace. Second, unlike other studies on the topic acknowledging the fact that traditional sources of fuel (i.e. petroleum, natural gas, etc.) will not readily disappear from the competitive landscape, we focus on the dynamic nature of how the "new" and "old" energy sources may ultimately co-exist by adjusting their geographic product offerings based on production costs and energy content. We intend to do so by developing simulation model that allows for simultaneous analysis of the distribution network of various sources of energy.

2 Research Method

This research aims to study a simulation modeling of overlapping distribution system for transportation fuel. We believe that an important and missing element on the viability of fossil fuels can be remedied through simultaneous analysis of distribution systems for various sources of transportation fuel. We will first investigate scenarios various independent distribution systems for delivering alternative fuels throughout the contiguous United States. Then we will extend our model to handle several different fuels at various BTU contents, and different sources of crop growth. Viable range and necessary infrastructure will be determined based the field research of the project. Furthermore, supply systems become more advanced as product/process/distribution and transport innovations standardize or streamline the value chain steps. As such, the system can be changed to reflect technological advances, system overlaps (i.e. standardized elements, uniform materials, interchangeable equipment of different distribution systems). For example, a basic question that can be answered using this model is the following: Assuming the cost competitiveness of Nebraska ethanol and assuming successful development of algae-based ethanol in Southern New Mexico, what size plant/processing and distribution infrastructure would be justified in Alamogordo?

3 Potential Impact

There are three key potential impacts from this study [10]. First, the modeling allows for studying alternative distribution scenarios where locations of processing and distribution points are more astutely determined. We believe that considering the effect of other fuels distribution networks provides a unique (and often ignored) factor in distribution modeling of this type. Second, this study can help innovative newcomers to the energy market to dynamically consider the competitive effect of incumbent firms and existing fuel sources in their channel and distribution decisions. Third, we believe the simulation program can be made such that it can provide suggested geographic distribution networks for any of the following markets:

- Commercial or private airplane (based on airport locations)
- Fleet Trucks (based on delivery and distribution of diesel fuel)
- Home heating (kerosene, etc.)
- Military base needs
- Other fuel markets.

4 References

[1] M. Jacobson, "Review of solutions to global warming, air pollution, and energy security", *Energy and Environment Science*, Vol. 2, pp 148-173 2009.

[2] National Algal Biofuels Technology Roadmap, US Department of Energy Office of the Biomass Program, Available from: http://www1.eere.energy.gov/biomass/pdfs/algal_biofuels_roadmap.pdf; Retrieved March 2012.

[3] J. Benemann, P. Pursoff, and W. Oswald, (1978). Engineering Design and Cost Analysis of a Large-Scale Microalgae Biomass System. *Final Report to the US Energy Department*, NTIS# HCP/T, 1605(UC-61), 91.

[4] T. Milne, R. Evans, and N. Nagle, "Catalytic conversion of microalgae and vegetable oils to premium gasoline, with shape-selective zeolites", *Biomass*, Vol. 21, No. 3, pp 219-232, 1990.

[5] J. Sheehan, T. Dunahay, J. Benemann and P. Roessler, (1998). A look back at the U.S. Department of Energy's aquatic species program-Biodiesel from algae, Available from:

www.nrel.gov/docs/fy04osti/34796.pdf; Retrieved March 2012.

[6] R. Perlack, L. Wright, A. Turhollow, R. Graham, B. Stokes, and D. Erbach, (2005). *Biomass as feedstock for a bioenergy and bioproducts industry: the technical feasibility of a billion-ton annual supply*, ORNL/TM-2006/66, Oak Ridge National Laboratory, Oak Ridge, TN..

[7] Chisti, Y., "Biodiesel from microalgae", *Biotechnology Advances*, Vol. 25, No. 3, pp 294–306, 2007.

[8] L. Rodolfi, Z. Chini, N. Bassi, G.Padovani, N. Biondi, G. Bonini, and M. Tredici, "Microalgae for oil: strain selection, induction of lipid synthesis and outdoor mass cultivation in a low-cost photobioreactor", *Biotechnol Bioeng*, Vol. 102, No. 1, pp 100–112, 2008.

[9] Biomass Multi-Year Program Plan, US Department of Energy Office of the Biomass Program, Available from: http://www1.eere.energy.gov/biomass/pdfs/mypp_april_2011_section1.pdf; Retrieved March 2012.

[10] A. Azadegan and H. Sohn, "Bio-fules and their distribution challenges: Modeling a stratified energy network in the US", working paper, 2012.

A CENTRAL VS DISTRIBUTED MICRO-STORAGE MANAGEMENT USING GAME THEORY AND EVOLUTIONARY TECHNIQUES

Nicolas Lopez, Karla Gutierrez and Jose F. Espiritu
Department of Industrial, Manufacturing & Engineering, The University of Texas at El Paso, El Paso, TX 79968, USA;

ABSTRACT

A micro-grid storage system is analyzed using a centralized approach for balancing the proper battery-schedule to store and release energy. The system is compared to a de-centralized approach where the batteries act individually as agents that try to optimize their response to the environment. The optimization is done utilizing a Genetic Algorithm. The agent based utilizes Game Theory techniques to incorporate the agents. The results show that the centralized method finds more accurate solutions than the de-centralized, which is modular.

1 Introduction

Electricity prices as well as the demand in the U.S. is rising [1][5], and the forecasts show that independent of the 3 main possible economic scenarios (high economic growth, medium economic growth or low economic growth) the quantity of electricity being generated by means of renewable sources will at least duplicate[1]. The variability of these new technologies calls for storage methods to deal with the stochastic behavior of such supplies. The best way to find answers to such questions is a mathematical model that relates the information (Graham, Hollands, 1990), which can be resolved via iterations or simulations until a proper educated solution is obtained.

2 Methodology

A central genetic algorithm and a de-centralized agent based method were developed to approximate the optimal energy storage schedule that minimizes the cost of supplying electricity to a micro-grid. The problem was formulated as a minimization where the cost of electricity varies according to the electric-demand. The batteries have 3 options for each time step: store electricity, release electricity and do nothing. In the centralized approach, a single GA is used to calculate the schedules for all batteries while in the agent-based (de-centralized) method, a game theory approach was utilized: a non-cooperative game where each battery is a player trying to minimize according to the von Neumann and Morgestern[3] utility functions.

3 Problem Formulation

We present our mathematical formulation of our approach to the Micro-Storage Energy Integration Problem.

Objective function:

(1)

Subject to:

(2)
(3)
(4)
(5)
(6)
(7)
(8)
(9)

The objective function (1) represents the minimization of the total cost of the project calculated as the integral of the individual cost of energy for all time steps of the project length. Equation (2) states that the instantaneous system balance must be positive to avoid blackouts. Equation (3) defines the total supply and (4) the demand or load. Equation (5) represents the total electricity changes in the system due to the individual contributions of the storage systems. The capacity of the individual storage systems is limited by a constant k in equation (6). Equations (7), (8) and (9) state the cost of electricity according to different demand levels.

4 Numerical Example

The methodology was tested using the following information:

Table 1: Hourly demand in (kW) for the day:

Hour	1	2	3	4	5	6	7	8	9	10	11	12	13	14	15	16	17	18	19	20	21	22	23	24
Demand	6	8	7	5	8	8	9	10	7	13	19	24	25	23	13	13	9	8	6	8	10	6	9	11

The 5 batteries considered are: 1) Battery Model: Vision CP12240D, 12V, 24Ah approximate charge/discharge capacity 0.288kWh. 2) USB US-305, 6V, 305Ah, approximate charge/discharge capacity 1.83kWh. 3) Trojan L16P, 6V, 360Ah, approximate charge/discharge capacity 2.16kWh. 4) Vision 6FM55D, 12V, 55Ah, approximate charge/discharge capacity 0.66kWh. 5) Vision 6FM200D, 12V, 200Ah, approximate charge/discharge capacity 2.4kWh. The genetic algorithm parameters are population size = 50, number of generations = 50, maximum number of games = 100, crossover method = roulette. For the agent based simulation: Equilibrium criteria: when 4 games in a row don't change. Allowance: cycling values of ±1 are understood as not changing. Each game was defined as a day: 24 hours conform 1 day. The agents played series of games (days) by presenting their best answers (solutions) obtained by utilizing genetic algorithms. At the end, the solutions of the agents were combined by a central agent who "measured" the overall cost of the system. This means that the fluctuations in demands created by the agents were "seen" or observed at the end of each game, when the evaluation function for the system is called.

5 Results and Conclusions

The algorithm was encoded in Matlab and run on an Intel® Pentium® processor P6100 for an approximated running time of 238.6s, and obtaining the following results: The agents converged to 43 generations after 9 games, and obtained the following store/release schedule: We can see that the overall demand is "smoother" than the original particularly noticing that the highest peak

is 16.9 kWh as compared to the 25 kWh that were originally served while the smallest demand is of 5.7 kWh as compared to 5.0 kWh from the original demand, in the agent-based case.

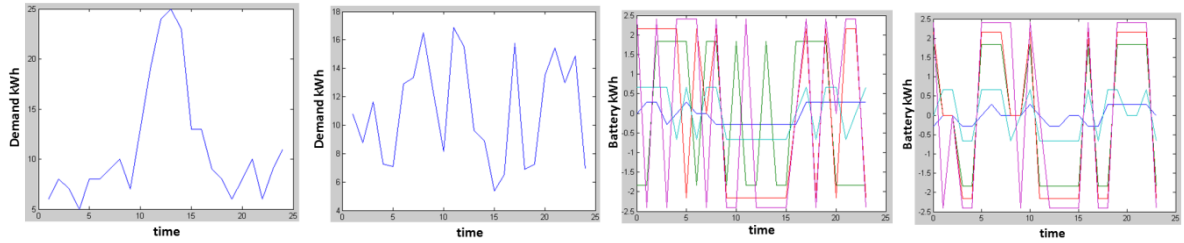

Fig 1. a) Original demand b) final demand (c) de-centralized schedule (d) centralized storage schedule

The savings for this de-centralized method schedule are of $0.4718, representing a modest reduction of 1.48% from the original initial cost of demand = $ 31.83 per day for the overall system. We can see that it is somewhat synchronized as they store and release energy in similar fashion while remaining not entirely equal as expected. The central genetic algorithm achieved better results rendering savings of $0.9692, representing a lowering of 3.05% in costs, and a more aggressive and synchronized schedule among the batteries: It appeared to run faster also, approximately (6.3 seconds), although in reality the 5 agents could run in parallel.

References

[1] EPA(2010) "Smart Grid and Clean Energy for Local Governments", U.S. Environmental Protection Agency. April 29, 2010.

[2] Borbely AM, Kreider JF, (2001) Distributed Generation: The Power Paradigm for the New Millennium, CRC Press, ISBN: 0849300746

[3] Yoav Shoham, Kevin Leyton-Brown " Multi-Agent Systems Algorithmic, Game-Theoretic, and Logical Foundations" revision 1.1 PDF version. Standford University & University of British Columbia, 2010.

[4] Jose F. Espiritu, Nicolas Lopez, Emmanuel Gurrola "Solving the Renewable Energy System Integration Problem Considering Multiple Objectives", Industrial Engineering Research Conference, Reno Nevada, 2011.

[5] R. Gueso, A. Dalla Valle, M. Guidolin " World Depletion Models: Price effects compared with strategic or technological interventions", Technological Forecasting and Social Change. Volume 74, Issue 4, May 2007. Pages 452-469.

[6] Steven J. Davis, Ken Caldera, H. Damon Matthews "Future CO2 Emissions and Climate Change from Existing Energy Infrastructure". Science Vol. 329 no. 5997 pp. 1330-1333. ISSN 0036-8075. 10 September 2010.

[7] National Grid (2012) "Metered half-hourly electricity demand" Demand Data, July-Dec 2011. National Grid. Available at: http://www.nationalgrid.com/uk/Electricity/Data/Demand+Data/

[8] Zareipour H., Janjai A., Leung H., Motamedi A., Schellenberg A., "Classification of Future Electricity Market Prices" Transactions on Power Systems IEEE, Volume 26, Issue 1, pages 165-173, ISSN 0885-8950, February, 2011.

[9] DOE/EIA (2011) "Annual Energy Outlook 2011 with projections to 2035" U.S. Department of Energy, U.S. Energy Information Administration, DOE/EIA-0383(2011), April, 2011.

[10] Rahaman S., Pipattanasomporn M., " Smart Grid Information Clearinghouse: Active content collection and knowledge discovery model" Intelligent System Application to Power Systems (ISAP), 2011 16th International Conference, IEEE, ISBN 9781457708077, November 18, 2011.

[11] Perukrishnen Vytelingum, Thomas D. Voice, Sarvapali D. Rachmurn, Alex Rogers, Nicholas R. Jennings "Agent-based Micro-Storage Management for the Smart Grid" School of Electronics and Computer Science, University of Southampton, UK

[12] Yang, Kong-Yu, Shi, Hui-Juan "Review and latest progress on multi-modal genetic algorithms" Beijing Xinxi Keji Daxue Xuebao (Journal of Beijing Information Science & Technology University). Vol. 26, no. 1, pp. 6-10. Jan 2011.

[13] L. Exarchakos, M. Leach, G. Exarchakos "Modelling electricity storage systems under the influence of demand-side management programmes". International Journal of Energy Research, 33(1):62-67, 2009.

SUSTAINABLE COMMODITY WOOD PLASTIC COMPOSITE MATERIALS FROM CHILE FIBERS AND PLASTICS

Haytham Alodan[1], Steven Hespeler[1], Jorge Soltero[1], Basilio Garcia[1], and Delia J. Valles-Rosales[1*]
[1]Department of Industrial Engineering, Espina St. MSC 4230 ECIII Room 288, Las Cruces, New Mexico, USA
* Corresponding author (dvalles@nmsu.edu)

Keywords: *Chile Pepper Fibers, Mechanical Properties, and Wood plastic Composites*

ABSTRACT

Wood plastics are novel material composites made of plant biomass and polymer blends that exhibit useful properties that surpass those of the individual components, and are predicted to play important roles in sustainable markets. This study focuses on a new wood plastic composite based on pre-dried New Mexico's red chile peper stems and leafs with high density polyethylene. The effects of proportions and particle sizes on the strength of the resulted blend were studied. A series of experiments were designed showing that wood fiber length, geometry, and content strongly affect the microcellular structure of the new sustainable material. It was found that larger particle sizes of wood fiber showed higher mechanical properties.

1 Introduction

Wood plastic composites exhibit useful properties that surpass those of the individual components, and are predicted to play important roles in sustainable markets. Some WPCs use recycled materials and can actually be recycled. They resist decay and insect attack and the weathering capabilities excel over individual components such as wood. They are dimensionally stable which results in little to no splintering, cracking or warping. WPCs can be produced in engineered profiles by any thermosets or thermoplastic processing techniques i.e. injection molding processing or compression molding processing [1 and 2].

Although wood plastic composites are biomaterials with many benefits and advantages over other materials currently used in the market, they do present some challenges. This study shows some of the challenges when processing WPCs. The combination of a hygroscopic (biomass) and hydrophobic (plastic) materials can cause issues in the compatibilization process of wood-fiber plastic composites [3]. The melting index of plastic can also cause molding difficulties as well as the blending of additives which are known to increase proper fiber dispersion, increase outdoor performance, and increase mechanical properties [4, 5, 6, 7, 8, 9, and 10].

Fiber length, ratio of fiber to plastic, and additives in a composite material are a concern when it comes to processing WPCs to obtain useful properties. Not only the fiber length, but

the geometry and content can strongly affect the microcellular structures of these composite materials [9]. Dispersing fibers throughout the plastic matrix can be difficult. Orientations of fibers have a very important effect on the physical and mechanical properties of the material. Different processing techniques will disperse the fibers in different directions and that is usually due to the processing parameters [11 and 4].

This study focuses on a new wood plastic composite based on pre-dried New Mexico's red chile stems and leafs with high density polyethylene. The effects of proportions and particle sizes on the strength of the resulted blend were studied. Three types of wood fibers particle sizes were analyzed at different weights (25, 50, 75, and 0%). ASTM 638-9 specimens were manufactured using injection molding. This study introduces chile leafs and stems which represent a potential source of fibers. Chile pepper is a major crop in New Mexico, West Texas and East Arizona, 40% of chile crops are produced in New Mexico. Wood fibers represent 40% to 60% of an average size chile plant which represent approximately 51% of chile wood fibers after drying [4, 12, and 13].

2 Methodology and Experimentation

A series of experiments were designed showing that wood fiber length, geometry, and content strongly affect the microcellular structure of the new sustainable material. A 3^6 design of experiment was performed with different factors categorized in two groups: materials and process parameters. ASTM 638-9 specimens were produced using injection molding and tested mechanically for tensile strength. Processing parameters include barrel temperature, nozzle temperature, injection time, and mold temperature controlled at 120°F. Material humidity and weight were controlled at 89% and 244.98 grams respectively. Chile leafs and stem wood were dried in an oven 24 hours at 70°C and grinded to various mesh sizes. Finally, dried wood was mixed with recycled polyethylene with various proportions.

3 Results

Comparisons between various proportions of wood and plastics and were done using the results of mechanical tests. Results show that the proportion 75% rPE and 25%wood fibers has the highest ultimate tensile strength (UTS) of 18.639 which is still lower than the presented by 100% recycled polyethylene. However, the average yield stress for the proportion 75% rPE and 25%wood fibers is slightly higher than the presented by the 100% rPE. In addition, the standard deviation of the UTS for the proportion 50% rPE and 50% wood is the highest among all proportions. Cause for this difference is assumed to be affected by the low number of samples due to the difficulties raised when processing them with 120mesh wood size which were tinny and small that the particles did not mix properly with plastic grains.

4 Conclusions

In this investigation, the authors analyzed the effects of reinforced recycled polyethylene combined with five types of chile wood particles grain sizes. Three types of wood fibers grain sizes were analyzed at different weights (25, 50, 75, and 0%). It can be observed that wood fiber length, geometry, and content strongly affect the microcellular structure of the WPC specimens. Due to a finer microcellular structure, the larger grain sizes of wood fiber samples showed higher mechanical properties also pointed out by Bledzki and Faruk [4].

One major problem faced was the dispersion of wood particles throughout the matrix. Wood particles burned on the sides of the barrel of the injection molding machine due to the light weight of the particles and improper mixing. In many cases, the melting index of plastic was higher than the degrading temperature for wood. This can cause potential burning and degrading of the wood fiber, which could also limit the mechanical performance of the composite material. Future research will focus on improving the mixing process of the melt.

References

[1] Klyosov, A. A. 'Wood-Plastic Composites." John Wiley & Sons, Inc., Hoboken, NJ, USA, 2007

[2] Wolcott, M. P. and Englund, K. "A Technology Review of Wood-Plastic Composites." 33rd. Particleboard / Composite Materials Symposium. Wood Plastic Information Center, 1996.

[3] English, B. W. and Falk, R. H. "Factors that Affect the Application of Woodfiber-Plastic Composites." USDA Forest Services. Forest Prod. Lab., Madison, Wisconsin. Forest Products Society, No. 7293, 189-194, 1996.

[4] Bledzki, A. K. and Faruk, O. "Microcellular Injection Molded Wood Fiber-PP Composites: Part II- Effect of Wood Fiber Length and Content on Cell Morphology and Physico-mechanical Properties." Journal of Cellular Plastics, Vol. 42, 77-88, 2006.

[5] Soury, E., Behravesh , A.H., Rouhani Esfahani, E., and Zolfaghari, A. "Design, optimization and manufacturing of wood–plastic composite pallet." Materials and Design. Vol. 30, 4183–4191, 2009.

[6] Faruk, O. and Matuana, L. M. "Nanoclay reinforced HDPE as a matrix for wood-plastic composites." Composites Science and Technology, Elsevier, Vol. 68, No. 9, 2073-2077, 2008.

[7] Rowell, R. M. "Advances and Challenges of Wood Polymer Composites," Proceedings of the 8th Pacific Rim Bio-Based Composites Symposium: Advances and Challenges in Biocomposites. Kepong, Malaysia: Forest Research Institute Malaysia, 2-11, 2006.

[8] Lu, J. Z., Wu, Q., and Negulescu, I. I. "Wood-Fiber/High-Density-Polyethylene Composites: Coupling Agent Performance," Wiley InterScience, Vol. 96, No. 1, 93-102, 2005.

[9] Markarian, J. "Additive developments aid growth in wood-plastic composites reports for Plastics Additives & Compounding." Plastics Additives & Compounding, Vol. 4, No. 11, 18-21, 2002.

[10] Li, R. "Environmental degradation of wood ±HDPE composite." Polymer Degradation and Stability, Vol. 70, No. 2, 135-145, 2000.

[11] Migneault, S., Koubaa, A., Erchiqui, F., Chaala, A., Englund, K., and Wolcott, M. P. "Effects of processing method and fiber size on the structure and properties of wood–plastic composites." Composites, Vol. 40, No. 1, 80-85, 2008.

[12] Funk, P.A., Walker, S.J. "Green Chile Pepper Harvest Mechanization." Proceedings of theN American Society of Agricultural and Biological Engineers (ASABE). Reno, Nevada, June 21 - June 24, 2009.

[13] National Agricultural Statistics Service, Agricultural Statistics Board, U.S. Department of Agriculture Editors, 2006, Report: Acreage. Released June 30, 2006.

Targeted delivery of Drug using Novel Photo voltaic Devices.

Mohammod K Bhuyan,

Department of Mechanical Engineering, University of Texas at El Paso, El Paso, TX-79968

Keywords: photovoltaic cell (PV), photo sensation,

A B S T R A C T

Conventional Drug D elivery S ystems (DDS) for can cer t reatments contain several constraints such as limited acce ssibility o f drugs to the tumor tissues, inaccurate targeting a nd biocirculation as well as severe toxicity. Therefore, to improve the DDS with minimal exposure and t oxicity, novel t echnique is e ssential. Recent investigation o f employing p hoto r esponsive photovoltaic (PV) cells revealed that PV cells work as coated drug carriers capable of delivering charged dr ug to the beleaguered region. Positive charge P oly-L-Lysine a nd negative c harge Bovine serum a lbumin attached th e negative s ide and po sitive side of a solar c ell respectively. Experimental d ata shows t hat t he P V cells e ffectively can release t he c harged molecules upo n external p hoto stimulation, w hich suggests t he P V for targeted drug delivery will pave the way for the development and introduction of innovative, targeted therapies with improved efficacy.

1. I ntroduction

Due to the limitations (inadequate accessibility of dr ugs, severe t oxicity a nd development of multi-drug resistance) of t herapeutic agents' delivery t o can cer t umors, approximately 50% cancer patients d ie e ach year [37] and leading one o f t he major cau ses o f d eath in USA [36]. The main c auses o f d ecease ar e metastases, owing to without initial control of t he crucial cancer cells. There is hence a n u rgent n eed t o triumph ov er death a nd impediments of conventional d rug d elivery system and as a result DDS h as g ained significant at tention (importance) in last t wo d ecades. Various types o f dr ug de livery systems have been introduced to ai d t argeted D DS s uch as ; nanomedicine for dr ug de livery and i maging [1],carbon no notubes, v iral nanoparticles, macromolecules, v esicles, p articles as c arriers for t herapeutics [38–42] and thermally responsive water s oluble polymers [2]. However, eac h o ne has its own limitations, such as nanoparticles are instable in movement, toxic and target is not accurate. There are also challenge lie s in t he d esign o f nanoparticles to overcome t he t umor wall. Thermoresponsive polymeric technique believed t o be ve ry potential mo dality f or D DS, but it is in v ery infancy level a t t he s ame t ime designing the thermal responsive medicine and engineering the t ransition t emperature i s critical. In a ll previous researches, t he e ffectiveness o f t he treatment is directly r elated t o the t reatment's ability t o target an d t o k ill t he c ancer ce lls while affecting as few healthy cells as possible. Therefore, f or t he ca ncer t reatment an important g oal o f t argeted dr ug de livery is t o minimize t he exposure o f normal t issues t o the drugs w hile preserving their t herapeutic concentration in diseased parts of the body [3]. [3]. Existing methodologies used for can cer treatments are not yet perfect; accordingly, new strategies for targeted drug delivery are needed.

In our present study for novel DDS, simple PV cells been used w hich carry special

features; with the presence of light PV converts lights into electricity as well as induces charge transfer by photovoltaic effect (PVE) [3]. And using the PVE, light or laser can release drug to the targeted tissue without hampering healthy cells or tissue.

Near-IR (NIR) or laser source that can penetrate 2 cm-10cm through human skin tissue [4] are also employed with PV cell for photo sensation. Motivated by the special features of PV, we have hypothesized that a PV might be served as a new DDS to carry cancer chemotherapeutic drugs and release them upon external photo stimulation (NIR or laser). Our ultimate goal is to develop a targeted chemotherapeutic drug delivery methodology based on NIR activated micro-PV devices. That's why first we need to demonstrate if the charged molecules can be effectively released from the PV device when exposed to photon stimulation. As a proof of principle, we have first conducted experiment by commercially available PV devices with positively charged poly-l-lysine and negatively charged bovine serum albumin (BSA) and tested the release of the molecules upon photo stimulation. These molecules were physically absorbed onto the surface of the PVs before exposed to an IR LED illuminator, which was used as an external light source.

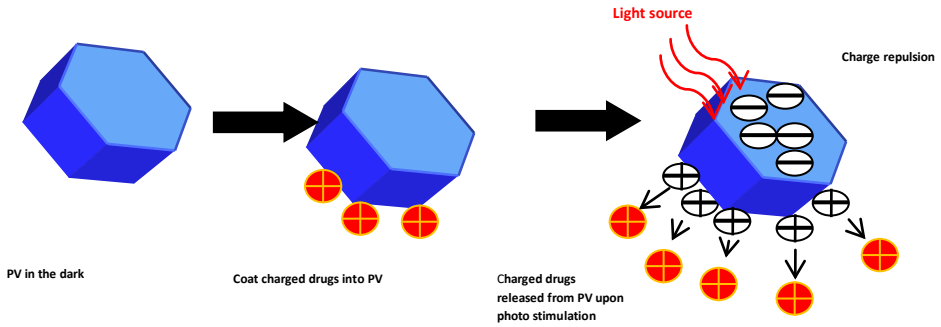

Fig.1. Systematic illustration of drugs release from photovoltaic device (PV) upon light exposure

2.0 Material and methods
2.1. Materials

2.1.1 Photo voltaic cell

PVE is a basic physical process through which a PV cell converts sunlight into electricity and transport inside a semiconductor material, of positive and negative electric charges, through the action of light. This material features two regions, one exhibiting an excess of electrons, the other an electron deficit, respectively referred to as *n*-type doped and *p*-type doped [4]. When the junction of *n*-type and *p*-type doped is

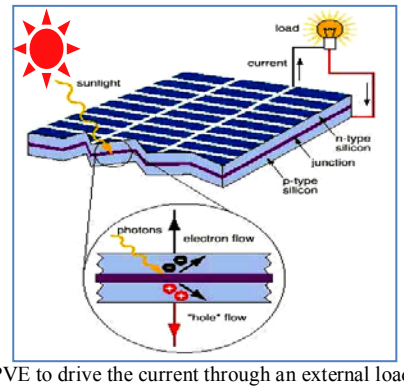

Fig.2. PVE to drive the current through an external load

illuminated, photons yield their energy to the atoms, each photon causing an electron to move from the valence band to the conduction band,

leaving behind a hole, which also able to move around the material, thus giving rise to an electron-hole pair (Fig. 2). Because of the circuit at the cell's terminals, electrons from the *n* region migrate back to the holes in the *p* region, and it raises the potential difference: the electric will current passes through circuit [5]

2.1.2 PV cells preparation

PV cells were obtain from RadioShack® (Custom assembled in USA with circuit voltage 0.55VDC in full sun light, maximum voltage 0.484V and maximum current 0.25-

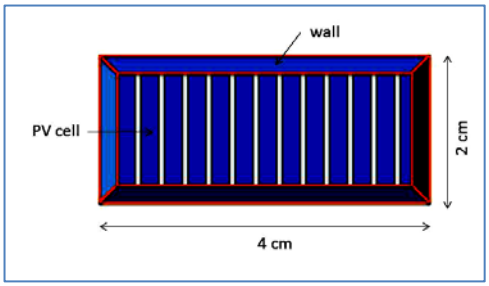

Fig. 3.Top view of PV cell with wall (Glue) around the edges.

0.275 amps. Nontoxic glue (Prym Consumer USA Inc. ®) wall was made surrounding the cells to protect the drugs from leaking out of PV cells (Fig. 3). For external photo stimulation a 2.1 watts regular table lamp (Model no. – 288741, American Fluorescent®,) with input voltage 12V, and current 0.175 amp was used. To read the amount of drug release eppendorf ® BioPhotometer been used at absorbance of 260 nm wavelength.

2.1.3 Preparation of BSA

Negative charged BSA composed of large globular protein (mol wt. 66,000 Dal) with essential amino acid profile was obtained from Sigma-Aldrich® (Product no. A2153) and has assay of ≥96% (agarose gel electrophoresis), pH 6.5-7.5 (1% in 0.15 M sodium chloride). Total 16ml of 25 mg/ml solution was made with distilled water and preserved it in tube at 2-8 ºC

2.1.4 Preparation of Poly-l-lysin

Poly-L-Lysine is a synthetic amino acid chain that carries positive charge and widely used as a coating to enhance cell attachment and adhesion to both plastic ware and glass surfaces [35]. For the experiment, 0.1 % (w/v) concentrated Poly-l-lysine (Sigma-Aldrich®, Product no. P8920) diluted to 0.05% by mixing with distilled water to use as coating.

2.2.1 Coating of Charge molecule

After cleaning the cells with distilled water and dry them using tissue paper, put cells into dark for at least 12 hours to remove existing charges from PV cells. During this time make 16 ml, 25 mg/ml concentrated negative charged BSA [6] solution and refrigerate at 8^0C. After

discharging of PV cells, add 1.5 ml of BSA solution on n-type surface (top part) of PV cells using eppendorf ® 1000 µL pipettes in completely dark room. Keep these solar cells in the dark for 5 hours to attach molecules on PV cells. The procedure of coating and attaching negative charged poly-l-lysine is similar to BSA.

2.2.2 Releasing of drug molecules upon photo simulation.

During these 5 hours poly-l-lysine and BSA will attach to PV cells. Wash the cells with distilled water to remove unbounded drug. Divide cells in two equal groups. The first group (4 PV cells) kept under light for external photo stimulation and the second group (4 PV cells) still in the dark. Place these cells for 3 hours in their respective environment. After 3 hours, take a 500 µL drug

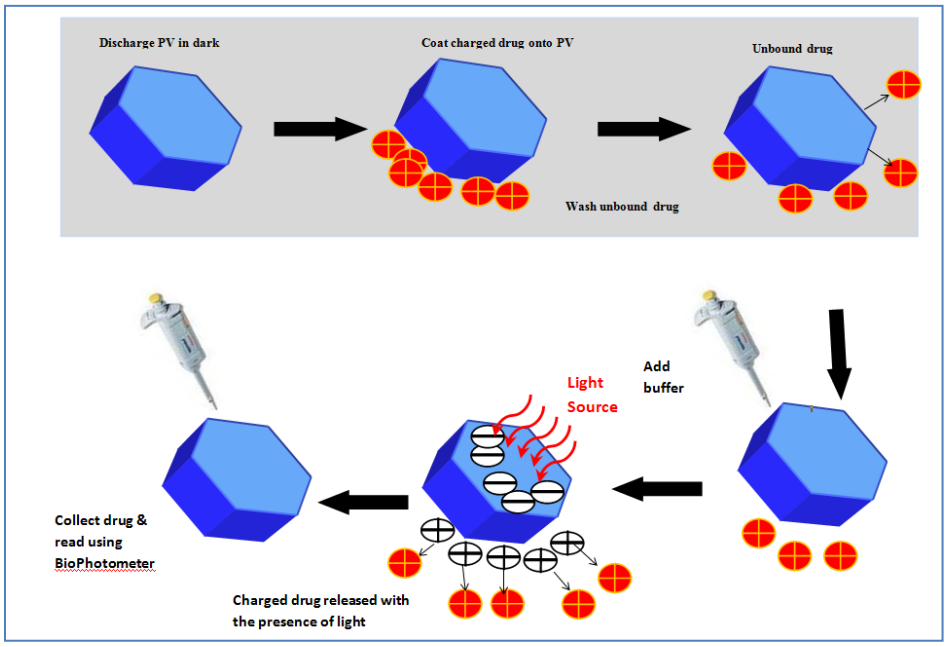

Fig. 4. Schematic diagrams showing step-by-step procedure of the experiment

from each PV cell into UVette® and read the absorbance of these samples using eppendorf ® BioPhotometer ® at 260 nm wavelength. Plot the graph in Microsoft Excel 2010® as amount of drug release on the Y axis vs. stimulation and without stimulation on the X axis. While plotting the graph change the OD values to µg/ml unit. The step-by-step schematic representation of coating and releasing of poly-l-lysin from PV cells is shown in figure 4.

3.0 Result

3.1 Negatively Charged BSA

From the experiment it was found that a large amount of molecules released upon external photo stimulation. Fig. 5 shows that 14.7234 µg/ml of molecules were released during external photo

stimulations compared to 2.1119 µg/ml during non-stimulation. It was found that the amount of molecule released using BSA is significantly greater than poly-l-lysine.

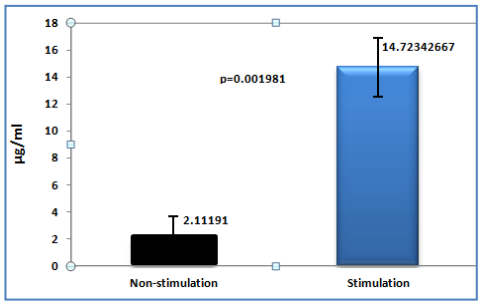

Fig. 5. Release of BSA when discharge on *n*-type surface

3.2 Positively charged Poly- l-lysin

Significant amount of Positively charged poly-l-lysine molecules also released ($p > 0.05$) upon external photo stimulation. It was found that 4.2496 µg/ml of molecules were released during external stimulations in compared to 3.8399 µg/ml during non-stimulation.

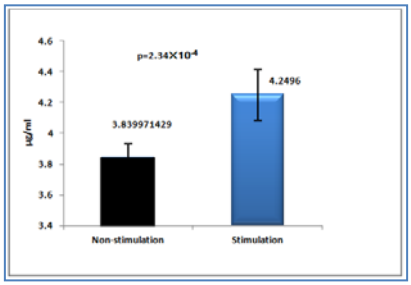

Fig. 6. Release of poly-l-lysine when discharge on *p*-type surf

3.3 BSAFT-IR Spctroscopy test

Fig.7 depicting absorption spectra in the Amides region of a BSA sample in native (room temperature) and aggregated and this suggests that nitrogen remained within the core of the protein, that are inaccessible to the solvent in the native form (2 hrs of incubation at 58^0 C). BSA also exhibits an intense Amide I band centered at approximately 1650 cm^{-1} in agreement

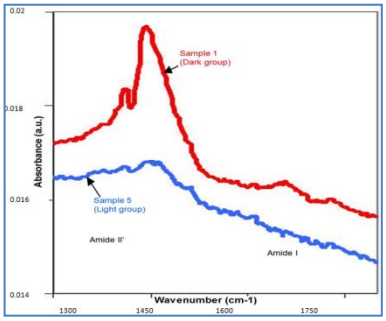

Fig. 7. IR absorption spectra of BSA

with the reported percentage of α-helix structure. Both Amide II and Amide I spectral contributions are present.

3.4 Microscopic Observation

PV cells coated with BSA are observed under the Optical Microscope. The FTIR spectra are collected from the BSA coated solar panel with and without photo stimulation. It is found that, more BSA protein aggregation was on the surface of PV cells which are kept in the dark and less BSA protein aggregation when PV cells kept for light stimulation. The PV cells surface boundaries are more clear and visible in the light group, while in the dark group cells are unsmooth and bumpy, as shown in Fig. 8 and Fig.9 respectively.

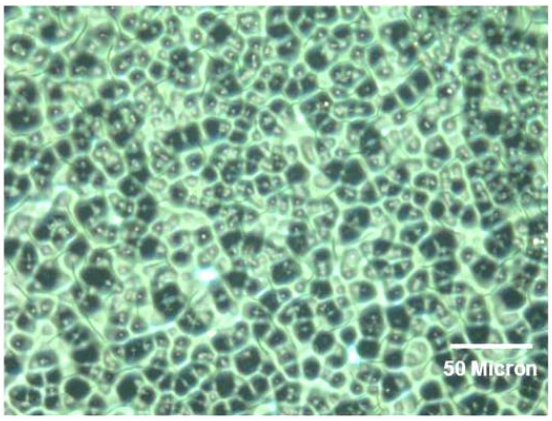

Fig. 8. Dark group: More protein aggregation left on solar panel to form bumpy surfaces

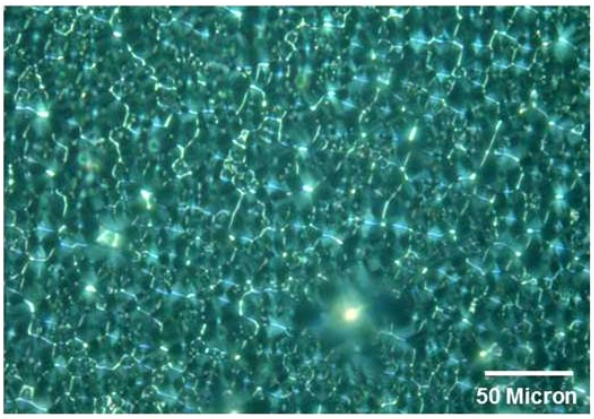

Fig. 9. Light group: The underlying solar panel grain boundaries are more visible and clear

4.0Discussion

4.1 Current Targeted DDS systems

Chemotherapy, a major treatment of cancer generally employs invasive technique including application of catheters to allow chemotherapy. Initial chemotherapy shrinks cancer existence, surgery to then eliminate the tumor(s) if feasible, followed by more chemotherapies and radiations. Researchers devoted hard working regarding the development of chemotherapy over the past decades has achieved improvement; however it is not significant. The advances in treatment of cancer are progressing. Several approaches are being practiced currently to develop the toxicity of anticancer curative [8], [9], [10]. The most commonly used method is antibody-or ligand-mediated targeting of anticancer therapeutic. Major treatment of therapeutics is that the targeted delivery of antineoplastic drugs to cancer-affected or tumor tissues such as tumor vasculature can be enhanced by incorporating the drug-molecules together to bind with receptors or antigens that are expressed or over expressed on target cells compared with normal tissues. This permits the precise release of treatments to cancer cells [11],[12] ,[13],[14],[15].

Of late, targeted therapeutics in nanomedicine has been widely explored. Nanocapsules or nanoparticles associated DDS suggest massive advantages [16],[17], [18] as examples: reduction of side-effects, guarantees the pharmaceutical effects and minimize dosage ; prevents

drugs from degradation and boosts drug strength[19]. Nanoparticles have also easy access to cells through small capillaries, which can release accurate drug accumulation to indented sites for a longer period of time even for few weeks. Beside nanomedicine, on the basis of nanosystems, various types of DDS have been evolved, for example, polymeric nanoparticles of poly(D,L-lactide-*co*-glycolide) (PLGA), micelles, liposomes, dendrimers, and silica nanoparticles [20], [21], [22].

McCarthy *et al*. synthesized a new type of a nanoparticles delivery method for *in vivo* application based on clinically used bio compatible PLGA encapsulated as photosensitizer [23]. Upon cellular internalization, the photosensitizer is released from the nanoparticles and becomes highly phototoxic to kill the cancer cells. Farokhzad *et al* [24] developed new type of bioconjugates nanoparticle-aptamer; docetaxel-encapsulated pegylated PLGA. These bioconjugated nanoparticles attaching with cancerous epithelial cells enhance toxicity kill cancer cells [25], [26], [27].

Nanoparticles are also used in magnetic drug carriers for cancer cure without causing severe side effects usually found in conventional chemotherapy. Alexiou *et al* used iron oxide nanoparticles covered by starch derivative with phosphate group [8]. Ferrofluid and starch encapsulated iron oxide nanoparticle are injected to body and externally strong-magnetic-field induces the gathering of nanoparticles, and ferrofluids in tumor tissue and tumor cells. Dendrimer possess unique characteristics for drug carrier to cancer cells [26], [27] for that reason Kukowska Latallo *et al*. have produced folate-conjugated dendrimer nanoparticles combined with methotrexate [27]. Due to high express levels of the folate, 4 days after their administration these nanoparticles build up in human KB tumors and livers. Kukowska *et al* also studied the internalization of these nanoparticles into tumor cells and demonstrated that this targeted dendrimer nanoparticles show a high antitumor activity and a marked toxicity to kill cancer cells.

4.2 Light associated Drug delivery

Over the past decades researchers designed drug and DDS with external stimuli such as light and ionizing radiation, which adjoins advance efficacy in biomedical applications. Photodynamic therapy (PDT) is a minimally invasive therapeutic modality approved for medical treatment of several types of cancer and non-oncological disorders. Using fibre-optic systems, light can be targeted accurately into many parts of the body for the treatment cancer cells. PDT consists in the application of a photo sensitizer (PS), which selectively accumulates in the tumor tissue, followed by subsequent exposition to light of an appropriate wavelength (generally in the red spectral region, wave length 600 nm or more, as red light penetrates deeper into tissues). Energy from the light-excited PS is transferred to the O_2 to give single oxygen ($1O_2$) and other highly reactive oxygen species (ROS). These cytotoxic photoproducts, generated upon illumination, start a cascade of biochemical events that induces damage and death of neoplastic cells [28]. PDT can be applied either alone or in combination with other therapeutic modalities, such as chemotherapy, surgery, radiotherapy or immuno -therapy. Near-infrared (NIR) radiation has established to be a potential tool for both *in vivo* imaging and photothermal cancer treatment. A major benefit to using light in the NIR window, ca. 650–900 nm, is its minimal absorbance by

skin and tissue. This window is bounded at the low end by the absorbance of hemoglobin and at the high end by the absorbance of water [29], [30]. Between these limits, light can penetrate tissue on the order of hundreds of micrometers to centimeters, enabling, for example, whole-body optical imaging [31]. UV and visible wave length light have also been used to trigger drug delivery. Comparison with longer wavelengths, light in the UV and visible regions suffers a number of drawbacks. It is strongly absorbed by skin and tissue and therefore cannot be used for deep-tissue triggering. Moreover, it damages tissue at much lower powers than NIR. [32] Nevertheless, tissues such as skin, the ear, or the back of the eye are excellent candidates for treatment, so long as the irradiation power is safe. Numerous chemical changes, such as bond cleavage and isomerization, can only be achieved with light in the UV or visible range.

4.3 PV devices and its potential for Target DDs

So far, numerous types of DDS have been developed for cancer treatment and PV solar cells DDS have been considered one of the most innovative, effective and promising options. A photovoltaic cells (PV) is a system that converts lights into electricity as well as induces charge transfer by photovoltaic effect [3]. A PV can serve as a new drug delivery system to carry cancer chemotherapeutic drugs and release them upon external photo stimulation (NIR or laser). The near-IR (NIR) or laser source can penetrate 2 - 10 cm through human skin tissue [4]. The ultimate goal of this project is to develop a targeted chemotherapeutic DDS based on NIR activated micro-photovoltaic devices. In this pilot study, we investigated if the charged molecules can be effectively released from the PV device when exposed to photon stimulation. As proof of principle, we have first experimented coating by commercially available photo voltaic devices with positively charged poly-l-lysine and negatively charged bovine serum albumin (BSA) and tested the release of the molecules upon photo stimulation depicting figure 6. These molecules were physically absorbed onto the surface of the PVs before exposed to an IR LED illuminator, which was used as an external light source.

4.4 Future direction of PV associated drug delivery

Researchers at Sandia National Laboratories, Albuquerque, NM developed micro scale solar cells. When the cells are below a millimeter, it rejects the heat so efficiently that it does not need any cooling systems which makes smaller solar cells are more efficient at dissipating heat. The thickness ranges from 14 to 20 micrometers thick (a human hair is approximately 70 micrometers thick), they are 10 times thinner than conventional 6-inch-by-6-inch brick-sized cells, and perform at about the same efficiency. Sandia makes these cells from silicon that has been processed using conventional chemical methods. The cells are carve out of this silicon using a chemical etching technique that creates negligible waste, and then treat the surface of the wafer to create the electrical properties necessary for a functioning cell. The resulting cells are about 20 micrometers thick but have the same efficiency as conventional cells, converting about 14.9 percent of sunlight into electrical energy. Usually, the cells are made in hexagonal shape, which makes the most of the available area without wasting much silicon [33].

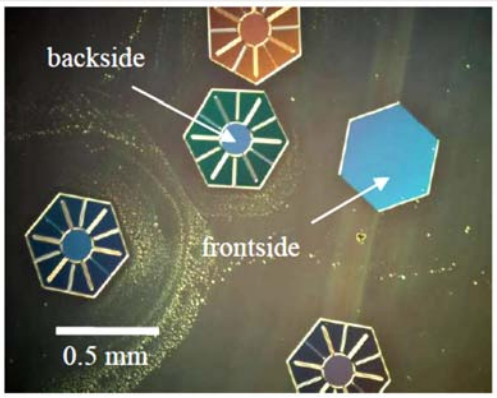

Fig. 10. Optical image of 500 micron wide, 20 micron thick Micro Solar Cells [32].

Similarly, Semprius, a NC based company, has developed a novel micro printing technology. Semprius's solar modules contain arrays of square cells that measure just 600 micrometers on each side. These cells have three semiconducting layers--each of which is based on gallium arsenide and absorbs a different band of sunlight--and they are made using a combination of chemical etching and printing, which means fewer raw materials are wasted. They can operate under sunlight concentrated 1,000 times using cheap optical systems. According to the National Renewable Energy Laboratories, the efficiency of the resulting modules ranges from 25 to 35% [34].

4.5 Traditional Solar PV

The worldwide demand for energy is steadily increasing, doubling every 15 years. To sustain this growth without causing irreversible harm to the environment, solar energy and PV cells have rapidly grown as a clean and renewable source of energy. The first practical application of photovoltaics was to power orbiting satellites and other spacecraft, but today the majority of photovoltaic modules are used for grid connected power generation. Due to the growing demand for renewable energy sources, the manufacturing of solar cells and photovoltaic arrays has advanced considerably in recent years. There is a smaller market for off-grid power for remote dwellings, boats, recreational vehicles, electric cars, roadside emergency telephones, remote sensing, and cathodic protection of pipelines. Grid-connected solar PV is the fastest growing energy technology in the world, with 50% annual increases in cumulative installed capacity in 2006 and 2007, to an estimated 7.7 GW, making it the world's fastest-growing energy technogy.

5.0 Conclusion

Our studies have developed a breakthrough technology in the DDS using of PV solar panels. To accomplished the research *in* advanced level, biodegradable and bio compatible micro solar cell required . At present, bio compatible and biodegradable solar cell manufacturing are in research level in different research institutes , however, BioSolar, Inc, CA, has developed bio-based materials from renewable plant sources to produce PV solar panels. Clearly, further formulation optimization studies are needed to improve the efficiency DDS. Extensive research and development of attaching and releasing more drugs from PV cell also need to developed both *in vitro* and *in vivo* prior to implement to living body.

Acknowledgments

References

[1] Yiyao Liu, Hirokazu Miyoshi,Michi hiru Nakmura Nanomedicine for drug delivery and imaging: A promising avenue for cancer therapy and diagnosis using targeted functional nanoparticle Article first published online: 27 MAR 2007 DOI :10: 1002/ijc.22709

[2] Ashutos Chikoti, Mathew R Dreher, Dan E. Meysr and Drazen Raucher. Targeted drug delivery by thermally responsive polymers 2. Juzeniene A, Peng Q, Moan J (2007) Mileston

[3] Wim H De Jong, P.J.B., *Drug Delivery and Nanoparticles: Applications ans Hazards.* International Journal of Nanomedicine, 2008.

[4] Califano, F.P., *Current Utilization of Photovoltaic Effect.* Chimica & L Industria, 1975. **57**(4): p. 293- 293.

[5] Chen, L.J., et al., *Photovoltaic effect in a periodically poled lithium niobate Solc-type wavelength filter.* Applied Physics Letters, 2006. **88**(12)

[6] Alfred V. Elgersma, R.L.J.Z., Willem Nordea and Johannes Lyklema, *The adsorption of bovine serum albumin on positively and negatively charged polystyrene latices* Elsevier 2004.

[7] Langer R. Drug delivery: drugs on target. *Science* 2001; **293**: 58–9.

[8] Alexiou C,Schmid RJ,Jurgons R,Kremer M,Wanner M,Bergemann C,Huenges E,Nawroth T,Arnold W,Parak FG. Targeting cancer cells: magnetic nanoparticles as drug carriers. *Eur Biophys J* 2006; **35**: 446–50.

[9] Nobs L,Buchegger F,Curny R,Allemann E. Current methods for attaching targeting ligands to liposomes and nanoparticles. *J Pharm Sci* 2004; **93**: 1980–92.

[10] Allen TM. Ligand-targeted therapeutics in anticancer therapy. *Nat Rev Cancer* 2002; **2**: 750–63.

[11] Ding BS,Dziubla T,Shuvaev VV,Muro S,Muzykantov VR. Advanced drug delivery systems that target the vascular endothelium. *Mol Interv* 2006; **6**: 98–112.

[12] Ehrhardt C,Kneuer C,Bakowsky U. Selectin—an emerging targeting for drug delivery. *Adv Drug Deliv Rev* 2004; **56**: 527–49.

[13] Eliceiri BP,Cheresh DA. Adhesion events in angiogenesis. *Curr Opin Cell Biol* 2001; **13**: 563–88.

[14] Dagar S,Sekosan M,Lee BS,Rubinstein I,Onyuksel H. VIP receptors as molecular targets of breast cancer: implications for targeted imaging and drug delivery. *J Controlled Release* 2001; **74**: 129–34.

[15] Arap W,Pasqualini R,Ruoslahti E. Cancer treatment by targeted drug delivery to tumor vasculature in a mouse model. *Science* 1998; **279**: 377–380.

[16] Sahoo SK,Labhasetwar V. Nanotech approaches to drug delivery and imaging. *Drug Discov Today* 2003; **8**: 1112–20

[17] Fahmy TM,Fong PM,Goyal A,Saltzman WM. Targeted for drug delivery. *Nanotoday* 2005: 18-20

[18] Fahmy TM,Samstein RM,Harness CC,Saltzman WM. Surface modification of biodegradable polyesters with fatty acid conjugates for improved drug targeting. *Biomaterials* 2005; **26**: 5727–36

[18] Couvreur P,Barratt G,Fattal E,Legrand P,Vauthier C. Nanocapsule technology: a review. *Crit Rev Ther Drug Carrier Syst* 2002; **19**: 99–134.
[20] Cegnar M,Premzl A,Zavasnik-Bergant V.Kristl J. Kos J.Poly (lactide-co-glycolide) as a carrier system for delivering cysteine protease inhibitor cystatin into tumor cells. *Exp Cell Res* 2004; **301**: 223–31
[21] Farokhzad OC,Jon S,Khademhosseini A,Tran TN,Lavan DA,Langer R. Nanoparticle-aptamer bioconjugates: a new approach for targeting prostate cancer cells. *Cancer Res* 2004; **64**: 7668–72.
[22] Fonseca MJ,Jagtenberg JC,Haisma HJ,Storm G. Liposome-mediated targeting of enzymes to cancer cells for site-specific activation of prodrugs: comparison with the corresponding antibody-enzyme conjugate. *Pharm Res* 2003; **20**: 423–8.
[23] McCarthy JR,Perez JM,Bruckner C,Weissleder R. Polymeric nanoparticle preparation that eradicates tumors. *Nano Lett* 2005; **5**: 2552–6.
[24] Farokhzad OC,Cheng J,Teply BA,Sherifi I,Jon S,Kantoff PW,Richie JP,Langer R. Targeted nanoparticle-aptamer bioconjugates for cancer chemotherapy *in vivo*. *Proc Natl Acad Sci USA* 2006; **103**: 6315–20.
[25] Cheng J,Teply BA,Sherifi I,Sung J,Luther G,Gu FX,Levy-Nissenbaum E,Radovic-Moreno AF,Langer R,Farokhzad OC. Formulation of functionalized PLGA-PEG nanoparticles for in vivo targeted drug delivery. *Biomaterials* 2007; **28**: 869–76.
[26] Patri AK,Kukowska-Latallo JF,Baker JRJr. Targeted drug delivery with dendrimers: comparison of the release kinetics of covalently conjugated drug and non-covalent drug inclusion complex. *Adv Drug Deliv Rev* 2005; **57**: 2203–14.
[27] Kukowska-Latallo JF,Candido KA,Cao Z,Nigavekar SS,Majoros IJ,Thomas TP,Balogh LP,Khan MK,Baker JRJr. Nanoparticle targeting of anticancer drug improves therapeutic response in animal model of human epithelial cancer. *Cancer Res* 2005; **65**: 5317–24.
[28] Moan J, Berg K (1991) The photodegradation of porphyrins in cells can be used to estimate the lifetime of singlet oxygen. Photochem Photobiol 53:549–553
[29] R. Weissleder , *Nat. Biotechnol.* **2001** , *19* , 316 .
[30] C. R. Simpson , M. Kohl , M. Essenpreis , M. Cope , *Phys. Med. Biol.* **1998** , *43* , 2465 .
[31] V. Ntziachristos , J. Ripoll , L. H. V.Wang , R.Weissleder , *Nat.Biotechnol.* **2005** , *23*, 313
[32] Gregory N. Nielson, M.O., Paul Resnick, Jose L. Cruz-Campa, Tammy Pluym, Peggy J. Clews, Elizabeth Steenbergen, Vipin P. Gupta, *MICROSCALE C-SI (C)PV CELLS FOR LOW-COST POWER.* IEEE, 2009(Sandia National Laboratories).
[33] F.C.Krebs, J.A., H.Spanggaard,K.Larsen,E.Kold, *Production of large-area polymer solar cells by industrial silk screen printing, lifetime considerations and lamination with lyethyleneterephthalate.* Sol.Energy Mater.Sol.Cells, 2004.
[34] C. A. Bower, E.M., P. E. Garrou, *Transfer Printing: An Approach for Massively Parallel Assembly of Microscale Devices.* IEEE 2010(Semprius, Inc.).
[35] Ning-Ping Huang, R.M., Janos Voros, Marcus Textor, Rolf Hofer, Antonella Rossi, Donald L. Elbert,
Jeffrey A. Hubbell, and Nicholas D. Spence, *Poly(l-lysine)-g-poly(ethylene glycol) Layers on Metal*
Oxide Surfaces: Surface-Analytical Characterization and Resistance to Serum and Fibrinogen
Adsorption. American Chemical Society, 2001.

[36]. http://seer.cancer.gov/, Surveillance epidemiology and end results, (2002)..

[37] R.K. Jain, Delivery of molecular medicine to solid tumors. *Science*, **271** (1996), pp. 1079–1080.

38. V.P. Torchilin, Polymer-coated long-circulating microparticu- late pharmaceuticals, J. Microencapsul. 15 (1998) 1–19.
[39] R. Duncan, Drug–polymer conjugates: potential for im proved chemotherapy, Anticancer Drugs 3 (1992) 175–210
[40 T.M. Allen, Liposomal drug formulations—rationale for development and what we can expect in the future, Drugs 56 Con(
1998) 747–756.
41. R. Langer, Drug delivery and targeting, Nature 392 (1998) 5-10
42. M. Jones, J. Leroux, Polymeric micelles—a new generation of colloidal drug carriers, Eur. J. Pharm. Biopharm. 48 (1999) 101–111.

EFFECTS OF VARIATION IN THE MATERIAL BEHAVIOR ON INDENTATION DERIVED ELASTIC MODULUS AND HARDNESS

Hasan Faisal[1]* and Rafiqul Tarefder[2]
[1]Graduate Research Assistant, Department of Civil Engineering, University of New Mexico, Albuquerque, NM 87131
[2]Associate Professor, Department of Civil Engineering, University of New Mexico, Albuquerque, NM 87131
* Corresponding author (hfaisal@unm.edu)

Keywords: *Nanoindentation, Finite Element Analysis, Mechanical Property, Sinking-in, Pile up*

ABSTRACT

Nanoindentation, a depth sensing indentation technique, is used in this study to investigate the effects of indentation-driven material properties for the variation of different input of elastic properties and plastic properties; the plastic properties include different yield strengths as well as the strain hardening behaviors. A finite element 2-D axisymmetric model is used to simulate nanoindentation load displacement behavior. In the investigation the indentation derived elastic recovery is found strictly a function of elastic behavior as well as the strain hardening behavior of the material. However, the hardness of the material is found to a function of the plastic behavior of the material only. The elastic modulus of the material increases as the indentation depth increases, since the substrate imparts contact stiffness of the material; however substrate effect on the hardness of the material is negligible. Piling up of material around the indenter is found evident for low strain hardening material and sinking in found in the case of high strain hardening material. As the E/Y ratio increases the piling up of material increases and the sinking in effect decreases and in opposite the piling up of material decreases and sinking in increases with decrease in the E/Y ratio.

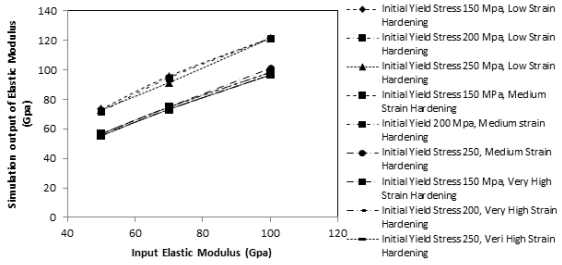

Fig.1. Simulation output of Elastic Modulus as a function of elasticity

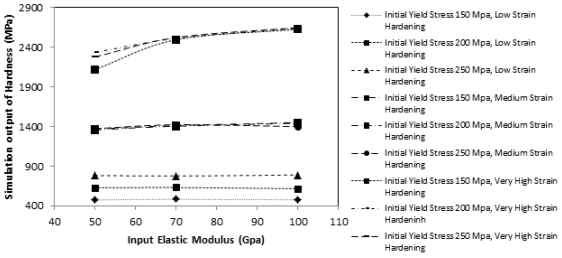

Fig.2: Simulation output of Hardness as a function of elasticity and the plasticity

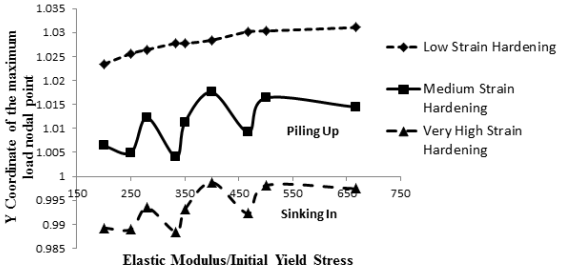

Fig.3. Sinking in and piling up of material at the maximum load, as a function of E/Y and strain hardening

1 Model Description:

A finite element model input file has been constructed for simulating the nanoindentation on a thin film material resting on a thick substrate. The 2-D model is axisymmetric and to simulate a conical indenter similar to Berkovich indenter, typically used for nanoindentation tests, with a semi angle of 70.3°. In the model a 1µm thin film is attached to a 100µm thick silicon substrate system. The width of the model is also fixed in 100µm. The left boundary of the model is allowed to move only in the Y-direction, whereas the bottom boundary is allowed to move only in the X-direction. In the model the right boundary is not constrained and the top boundary is free to move when it's not in contact with the indenter. The coefficient of friction between the indenter and the film is taken to be 0.1. The indenter is used in the model is rigid. The model is generated in such a way that it can be used for the ABAQUS extended functionality 10.2. In the simulation the loading is prescribed in a depth controlled way. Therefore, the resulting load is the reaction in the Y direction acting on the indenter. To investigate the effect on the elastic modulus and the hardness determined from the load displacement curve for nanoindentation 3 different elastic modulus along with 3 different initial yield stress and 3 strain hardening behavior are used. The model is able to identify and quantify the effect of variable material property on the pile up and sink in effect around the indenter in the thin film.

2 Results & Discussions:

The finite element simulations are ran for a specific material property to generate load displacement curve for nanoindentation. The load displacement curve consists of two parts, the loading part and the unloading part. The reduced elastic modulus of the material and the indenter is calculated from the initial slope of the unloading curve. The value of calculated elastic modulus shows a small deviation from the original value. The discrepancy in the obtained elastic modulus is due the coarser mesh in the model. To investigate the effects of various elastic moduli, plasticity introduced in the form of variation of initial yield strength and strain hardening on the simulation output of elastic modulus curves are plotted as shown in Fig.1. The figure shows the simulation output of elastic modulus as a function of input elastic modulus. The curves are plotted for different initial yield stress and strain hardening behavior of the material. The load displacement curve successfully qualitatively generated the same trend of increase in the output elastic modulus as in the input. For the case of quantity, it can be noted that the upper three curves represents the low strain hardening behavior, which refers to the perfectly plastic case in this study. The different three curves represent the three initial yield stress value of the material. However, for all the yield stress in perfectly plastic material the indentation produced elastic modulus simply followed the same line, i.e. upper three. It can be concluded that the obtained

elastic modulus are not a function of initial yield stress for the material. The same conclusion can be obtained from the nanoindentation logic of a material, since the elastic material is obtains from the unloading portion of the nanoindentation curve, which is nothing but the elastic recovery of the material.

Fig.2 shows the variation of indentation derived hardness as a function of elasticity and plasticity which involves initial yield stress as well as strain hardening. The figure shows the lower three curves related with perfect plasticity or low strain hardening of the material, shifting upward with increase in the initial yield stress of the material property. The middle three curves represents the same strain hardening behavior, i.e. the medium strain hardening behavior and with three different initial yield stress. In this case they followed the same line of action. The topmost three lines represent very high strain hardening and three different initial yield stress. In this case also the curves followed the same line of action. For all the cases the indentation derived hardness is found to be a function of plasticity, not as a function of the elasticity behavior of the material. However, at the very high strain rate the statement is not quite true, but in this study it considered as constant for a specific plastic behavior. From the nanoindentation technique the hardness is derived from the ratio of maximum load and the area under maximum load. The area is calculated from the radius of the impression, which is fully accountable for plastic deformation of the material. At low strain hardening or perfect plasticity the hardness of the material increase only due to the increase in the initial yield stress of the material behaviour, as with the increase in the maximum load as well as with the decrease in the indentation radius. For the simulation in the depth controlled mode the indenter required more load to overcome the initial yield and to enter into the plastic regime. However, with the strain hardening behavior the plasticity dominated with the medium and very high strain hardening behavior, the effect initial yield stress become negligible in these cases. The indentation derived hardness is higher in case of very high strain hardening behavior of the material as higher load is required to obtain the same indentation depth.

Fig.3 shows the piling up and sinking in of the material around the indenter is also found to be a function of E/Y. As the E/Y ratio increases the piling up of the material increases, whereas the sinking in of the material decreases. However, sinking in is evident for material with high strain hardening behavior as they can absorb higher energy compared with the low strain hardening materials, which shows piling up of the material around the indenter boundary.

3 References

[1] Cheng, Y., and Cheng, C. (1998). "Can stress-strain relationships be obtained from indentation curves using conical and pyramidal indenters?" J. of Mater. Res., 14(9), 3493–3496.
[2] Doerner, M. F., and Nix, W. D. (1986). "A Method for interpreting the data from depth-sensing indentation instruments." J. Mater. Res., 1(4), 601–609.
[3] Fischer-Cripp, A. (2004). "Nanoindentation." Mechanical engineering series, 2nd Ed., Springer, New York.
[4] Oliver, W. C., and Pharr, G. M. (1992). "An improved technique for determining hardness and elastic modulus using load and displacement sensing indentation experiments." J. Mater. Res., 7(6), 1564–1583.
[5] Shen, Y.-L. (2010). "Constrained Deformation of Materials." Devices, Heterogeneous Structures and Thermo-Mechanical Modeling, Springer, New York.

DYNAMIC MODULUS TESTING OF NEW MEXICO ASPHALT MIXTURES

Mekdim T. Weldegiorgis[1]* and Rafiqul A. Tarefder[2]
[1] Department of Civil Engineering, Graduate Research Assistant, University of New Mexico, Albuquerque, NM 87106, USA
[2] Department of Civil Engineering, Associate Professor and Regents' Lecturer, University of New Mexico, Albuquerque, NM 87106, USA
* Corresponding author (mteshome@unm.edu)
Keywords: Dynamic Modulus, Witczak Model

ABSTRACT

In this research laboratory testing is conducted to determine the dynamic modulus and phase angle of New Mexico asphalt mixtures. Testing is conducted on two different asphalt mixtures collected from an actual construction sites in New Mexico. To develop mastercurves, dynamic modulus testing is performed at five temperatures and six different loading frequencies at each temperature. Data from each test is processed using the GCTS software and Microsoft Excel program to determine the dynamic modulus and develop mastercurves respectively. Witczak predictive model is implemented to predict the dynamic modulus and resulting master curves are compared with mastercurves from actual testing. Dynamic modulus values of SPII mix is found to be higher than SPIII mix regardless of temperature and frequency. The sigmoidal function used to fit the mastercurve is found to provide a very good fit to the laboratory testing data. Predicted dynamic modulus values, using Witczak model, are found to be less than laboratory test results for SP-II mix.

1. Introduction

1.1.Definition

Complex modulus is a function used to describe linear viscoelastic material property under small dynamic loading. There is a linear relationship between dynamic stress and dynamic strain with the complex modulus as a proportion factor. Complex modulus is a function of frequency and the linear relationship between dynamic loading and dynamic strain is expressed by equation (1)[4].

$$\sigma(\omega, t) = E^*(i\omega)\varepsilon(\omega, t) \quad (1)$$

$where$: $\sigma(\omega, t)$ is dynamic stress which is a function of frequency ω or time t; $E^*(i\omega)$ is complex modulus which is a function of frequency ω; $\varepsilon(\omega, t)$ is dynamic strain which is a function of frequency ω or time t

The dynamic modulus is defined as the absolute value of complex modulus. This value can mathematically be expressed by ratio of the stress amplitude and strain amplitude as shown in equation (2) [4].

$$|E^*| = \frac{\sigma_o}{\varepsilon_o} \quad (2)$$

$where$: $|E^*|$ is dynamic modulus; σ_o is stress amplitude; ε_o is strain amplitude

1.2.Significance

The current state of practice for mix design of HMA in USA is Superpave, which is a result of the late 1980's endeavor to develop new specification and performance tests by the Strategic Highway Research Program (SHRP). The three recommended steps in Superpave mix design constitute binder and aggregate selection taking into account environmental factors, aggregate blending, and volumetric analysis. Superpave presumes good performance of compacted HMA through volumetric mix design

and material selection without going through strength tests and models. However, these methods are not reliable to ensure good performance [1]. To fill in this gap in Superpave mix design criteria, HMA Dynamic modulus test is recommended as a simple performance test in the recent findings of the National Cooperative Highway Research Program (NCHRP) projects. In the same vein, Mechanistic-Empirical pavement Design Guide (MEPDG) takes dynamic modulus as the most important material characterization parameter in the design inputs [3].

1.3.Modeling

Witczak Predictive Model is the most widely accepted model to predict dynamic modulus of asphalt concrete. This model is based on a database of 2750 dynamic modulus measurements from 205 different asphalt mixtures tested over the last 30 years in the laboratories of the Asphalt Institute, the University of Maryland, and the Federal Highway Administration. This model can predict the dynamic modulus of mixtures using both modified and conventional asphalt cements [2].

$$\log|E^*| = -1.249937 + 0.029232\rho_{200} - 0.001767(\rho_{200})^2 - 0.002841\rho_4 - 0.058097V_a - 0.802208\left(\frac{V_{beff}}{V_{beff}+V_a}\right) + \frac{3.871977 - 0.0021\rho_4 + 0.003958\rho_{38} - 0.000017(\rho_{38})^2 + 0.00547\rho_{34}}{1 + e^{(-603313 - 0.313351\log(f) - 0.393532\log(\eta))}} \quad (3)$$

where: $|E^*|$ is dynamic modulus, 10^5psi; η is bitumen viscosity, 10^6 Poise; f is loading frequency, Hz; V_a is air void content, %; V_{beff} is effective bitumen content, % by volume; ρ_{34} is cumulative % retained on the 19-mm (3/4-in.) sieve; ρ_{38} is cumulative % retained on the 9.5-mm (3/8-in.) sieve; ρ_4 is cumulative % retained on the 4.76-mm (No. 4) sieve; ρ_{200} is % passing the 0.075-mm (No. 200) sieve.

2. Experimental Design

Asphalt mix for testing is collected from an actual road reconstruction project in the state of New Mexico. The Project is widening of I-25 from two to three lanes each way from Tramway Boulevard on Albuquerque's north side to the southern exit at Bernalillo with a total length of 7.7 miles. The asphalt mixes used for this research are SP-III and SP-II mixes. The maximum aggregate size and binder PG-grade for SP-II mix is 1.5″ and PG 64-22 while the maximum aggregate size of SP-III mix is 1.0″ mixed with a binder grade of PG 70-22. The Gyratory compaction machine is used to compact a 6 inch diameter sample from which the 4 inch diameter sample is cored out for conducting dynamic modulus test.

3. Test Results

The computed dynamic modulus were used to construct mastercurves for each mixtures tested. A sigmoidal function shown in equation (4) is used to fit the individual dynamic modulus data to the mastercurve. Fitted model parameters are presented in Table 1.

$$\log(|E^*|) = \delta + \frac{\alpha}{1 + e^{\beta - \gamma\log(f_r)}} \quad (4)$$

where: δ is the minimum value of E*; $\delta + \alpha$ is the maximum value of E*; β, γ are parameters describing the shape of the sigmoidal function; f_r is reduced frequency of loading at reference temperature

Table 1: Mastercurve parameters for dynamic modulus test (ref. Temp = 21 ºC)

Asphalt mix	Master curve parameters			
	α	β	δ	γ
SP-II	2.9	-1.2	1.7	-0.4
SP-III	2.4	-0.8	2.0	-0.5

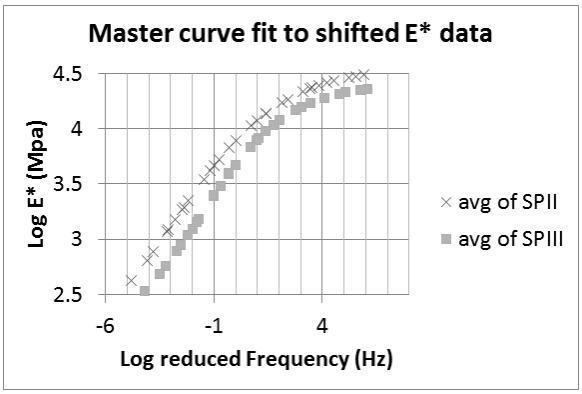

Fig. 1: Mastercurves for SP-II and SP-III Mixes

4. Predicting E* using Witczak model

The Witczak model is implemented to predict mastercurves of asphalt mixtures tested in this research. The results from the analysis show that the Witczak equation showed poor prediction performance for SP-II mix as depicted in Fig. **2**. Moreover, the Witczak predictive model is found to under predict the modulus values compared with test data values.

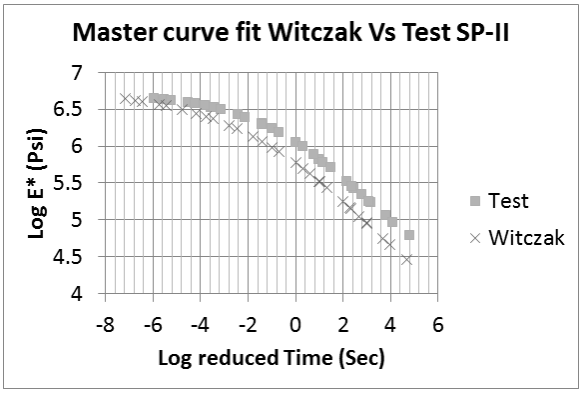

Fig. 2: Witczak Model Mastercurve Prediction for SPII mix

5. Conclusion

Based on the results on this study the following conclusions are drawn: Dynamic modulus values of SPII mix is found to be higher than SPIII mix regardless of temperature and frequency. The sigmoidal function used to fit the mastercurve is found to provide a very good fit to the laboratory testing data. The Witczak model was found to give poor prediction of the dynamic modulus mastercurve of SP-II asphalt mix. Predicted dynamic modulus values, using Witczak model, are found to be less than laboratory test results.

6. Reference

[1] Brown, R., Kandhal, P., and Zhang, J. (2001). "Performance Testing for Hot Mix Asphalt." NCAT Report No. 2001-05A, National Center for Asphalt Technology, Auburn, AL.

[2] Garcia, G., and Thompson, M., (2007). "HMA dynamic modulus - Temperature relations" Research Report FHWA-ICT-07-006, Illinois Center for Transportation, Department of Civil and Environmental Engineering, University of Illinois, 205 North Mathews – MC-250 Urbana, IL 61801.

[3] Tashman, L. and Elangovan, M. A. (2004). "Dynamic Modulus Test – Laboratory Evaluation and Future Implementation in the State of Washington." Final research report, Washington State University (WSU), Transportation Research Center (TRAC), Pullman, WA 99164-2910.

[4] Y.M. Haddad "Viscoelasticity of engineering materials".1st edition, Chapman & Hall, 2001.

DEVELOPMENT OF TiO_2 NANOWIRES ON CARBON FIBER SUBSTRATE UTILIZING DIFFERENT TITANIUM PRECURSORS

M. Mendoza, A. Khan, M. Shuvo, and Y. Lin
Department of Mechanical Engineering, The University of Texas at El Paso, El Paso, TX 79968, USA
mmendoza11@miners.utep.edu

Keywords: *Nanowires, Titanium Oxide, Carbon Fiber, Energy Storage*

ABSTRACT

Development of metal oxide nanowires for electrochemical applications is widely studied in academia and industry due to their excellent electrical and mechanical properties suitable for applications as an anode material in high energy density devices such as lithium-ion batteries, photovoltaic cells, and supercapasitors. The benefits of implementing nanowires as anode materials include a higher specific surface area and shorter diffusion lengths, features capable of improving the performance of electrochemical devices. Previously, various metal oxide nanowires grown on different substrates have been developed in order to increase specific capacities and charge/discharge rates. This paper introduces the development and characterization of TiO_2 nanowires grown on a carbon fiber fabrics substrate utilizing different titanium precursors. With this growth setting, the mechanical strength of the carbon fiber is intended to counteract with the high specific surface area of the nanowires. Nanowires are synthesized through a low temperature hydrothermal based method and its crystal structure and morphology are characterized by X-ray diffraction (XRD) and scanning electron microscopy (SEM). Growth conditions such as temperature and time are adjusted in order to analyze and control morphological features such as diameter, length, and density. TiO_2 nanowires with lengths of 6.5~15 μm and diameters above 150 nm are obtained.

1. Introduction

Synthesis of one-dimensional (1D) semiconducting oxide nanomaterials have grown over the past few years due to their mechanical and electrical properties as well as their applications in photovoltaic cells, photocatalysis, sensors, and pigments [1,2]. Due to their morphology, 1D nanomaterials own remarkable properties for electrochemical applications. The high specific surface area of nanomaterials is capable of improving the interaction of devices and media during charge transfer processes, while their shorter diffusion length enhances electron's flow [3]. Among all the metal oxides, titanium oxide (TiO_2) is a semiconducting material with potential applications in energy storage devices such as lithium-ion batteries, dye sensitize solar cells (DSSC), and supercapacitors. Besides its low cost, easy synthetic process, and eco-friendly characteristics, TiO_2 is capable of providing high energy density, excellent charge/discharge rates, and avoid the formation of the solid electrolyte interface (SEI) while used as an anode material for lithium-ion batteries, DSSCs, and supercapacitors [4,5]. In this paper, the authors present a simple hydrothermal method to synthesize TiO_2 nanowires on a carbon fiber fabrics substrate for anode material applications. In order to analyze the compatibility and growth characteristics of the TiO_2 nanowires on the substrate, three different titanium precursors were analyzed during this experimentation (titanium n-butoxide, titanium isopropoxide, and titanium tetrachloride). Previously, 1D nanowires have been grown on different substrates such as silicon

glass, fluorine-doped tin oxide (FTO), and tin-doped indium oxide (ITO) [6]. Carbon fiber fabrics implementation responds to the need of developing a conductive contact and improving the mechanical strength of the material. TiO_2 nanowires were synthesized following a hydrothermal method similar to the one developed by Kumar et al.[7]. Experiments with different reaction temperatures and periods are performed in order to analyze the morphology and density of the nanowires.

2. Experimental

The nanowires were synthesized following a simple hydrothermal method. In order to remove organic impurities, carbon fiber fabrics were ultrasonically cleaned successively in acetone, isopropyl alcohol (IPA), and deionized (DI) water for a period of 15 minutes each. Carbon fibers were transferred to a 250mL Pyrex glass screwtop bottle and mixed with a 50mL solution containing DI water and concentrated (37%) hydrochloric acid (HCl) on a 1:1 ratio. Subsequently, 2.5mL of the titanium precursor were added dropwise to this solution. The glass bottle was placed inside and aluminum cylinder and transferred into an oven were different growing temperatures (120-170˚C) and periods (2-6h) were tested. The resulting materials were rinsed several times with DI water and dried at 90˚C for 30 minutes. The as-prepared samples were characterized using powder X-ray diffraction (XRD, B8 Discover, Bruker) and scanning electron microscopy (SEM, S-4800, Hitachi).

3. Results

The analysis of the crystal structure of the nanowires is shown in Fig1. According to the XRD patterns, TiO_2 nanowires exhibited high diffraction peaks in the 2-Theta values of 27˚, 36˚, and 54˚. The as-prepared nanowires matched the tetragonal rutile phase of TiO_2 with *a* and *b* values of 4.59 Å and *c* of 2.96 Å [8]. XRD data demonstrates that an increment in reaction's temperature and time will result in higher peaks and a better crystallinity of the samples. Fig 2 shows SEM images of the samples. Better results were obtained when temperatures of 160 and 170˚C and periods of 4 and 6h were implemented during the hydrothermal process. Among all the three precursors, titanium tetrachloride and titanium n-butoxide exhibited remarkable results, being the samples made out of titanium tetrachloride the ones that displayed a better alignment of the nanowires with respect to the substrate as well as better densities and dimensions. The as-prepared nanowires displayed lengths of 6.5~15 μm and diameters of 150~200 nm.

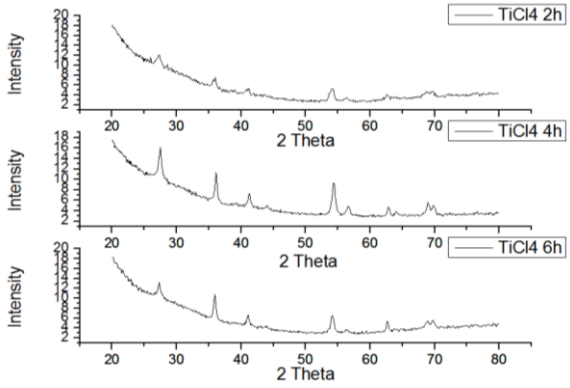

Fig 1. XRD patterns for TiO_2 nanowires grown at 170˚C utilizing different reaction periods.

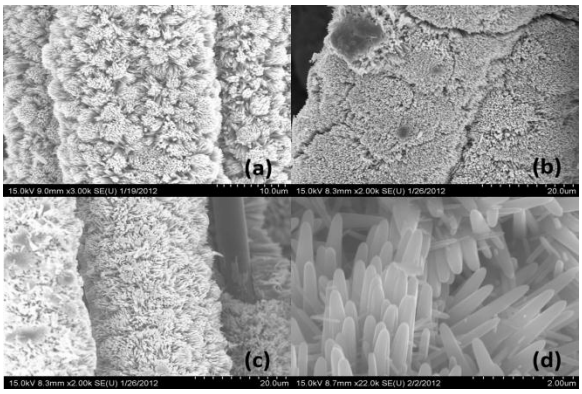

Fig 2. Corresponding SEM images of the as-prepared TiO2 nanowires (a) titanium n-butoxide 170˚C / 4h (b) titanium tetrachloride 160˚C / 4h (c) titanium tetrachloride 170˚C / 6h (d) titanium tetrachloride 170˚C / 6h.

4. Conclusions

A simple hydrothermal method was implemented to synthesize TiO_2 nanowires on a carbon fiber substrate. This method demonstrated the feasibility of growing large amounts of nanowires on this substrate. Growth of vertically aligned nanowires is feasible when hydrothermal temperatures above 160˚C are implemented. Three different titanium precursors were analyzed, being titanium tetrachloride ($TiCl_4$) the one that exhibited best results. The as-prepared nanowires displayed diameters between 150~200 nm and a maximum length of 15 μm. Future electrochemical testing will demonstrate the functionality of these nanowires on energy storing devices such as lithium-ion batteries, DSSCs, and supercapasitors.

References

[1] Y.X. Zhang, G.H. Li, Y.X. Jin, Y. Zhang, J. Zhang and L.D. Zhang "Hydrothermal synthesis and photoluminescence of TiO_2 nanowires". *Chem. Phys. Lett.*, Vol. 365, pp 300-304, 2002.

[2] W. Zhou, H. Liu, R.I. Boughton, G. Du, J. Lin, J. Wang and D. Liu "One-dimensional single-crystalline Ti-O based nanostructures: properties, synthesis, modifications and applications". *J. Mat. Chem.*, Vol. 20, pp 5993-6008, 2010.

[3] C. Altavilla and E. Ciliberto,eds "Inorganic nanoparticles: synthesis, applications, and perspectives". 1st edition, CRC Press, 2011.

[4] F. Wu, X. Li, Z. Wang, H. Guo, X. Xiong and X. Wang "A novel method to synthesize anatase TiO_2 nanowires as an anode material for lithium-ion batteris". *J. Alloy Compd*., Vol. 509, pp. 3771-3715, 2011.

[5] Myung "Nanostructured TiO_2 and its application in lithium-ion storage". *J. Adv. Funct. Mater*., Vol. 21, pp. 3231-3241, 2011.

[6] L.E. Greene, M. Law, J. Goldberger, F. Kim, J.C. Johnson, Y Zhang, R.J. Sykally and P. Yang "Low-temperature wafer-scale production of ZnO nanowire arrays" *Angew. Chem., Int. Ed.,* Vol. 42, pp. 3031-3034, 2003.

[7] A. Kumar, A.R. Madaria and C. Zhou "Growth of aligned single-crystalline rutile TiO_2 nanowires on arbitrary substrates and their application in dye-sensitized solar cells". *J. of Phys. Chem., C.* Vol. 114, pp. 7787-7792, 2010.

[8] K. Thamaphat, P. Limsuwan and B. Ngotawornchai "Phase characterization of TiO_2 powder by XRD and TEM". *Kasetsart J. (Nat. Sci.),* Vol. 42, pp. 357-361, 2008.

SYNTHESIS AND STRUCTURE EVALUATION OF YTTRIA-STABILIZED HAFNIA NANO-COATINGS

A. Garcia, C. Barraza, M. Noor-A-Alam and C.V. Ramana
Mechanical Engineering, University of Texas at el Paso, El Paso, TX 79968

Keywords: *Thermal Barrier Coatings, Yttrium stabilized Hafnia (YSH), X-Ray Diffraction (XRD), Scanning Electron Microscope (SEM)*

ABSTRACT

Yttrium stabilized Hafnia (YSH) coatings (TBC) were grown on two different substrates, Sapphire and Si-100, using RF magnetron sputtering. The coatings were grown under variable temperature and thickness. The characterization and analysis of the coatings was performed using grazing incidence X-ray diffraction and scanning electron microscopy. The phase evolution and residual stress in the coatings is evaluated as a function of temperature and thickness.

1. Introduction

Thermal barrier coatings are protective coating systems with low thermal conductivity. TBC's act as protective wall on the surface of a material achieving long term effectiveness in the high temperatures oxidation environment and increase the material's resistance to thermal fatigue[1-5]. TBC's are likely to have a thermal expansion coefficient that differs from the component to which it is applied. TBC's are most commonly used in turbine engines where combustion temperatures approach the material deformation point.

2. Experimental

Yttria stabilized hafnia (YSH) thin coatings were fabricated on sapphire and silicon substrates with an increasing variation of time. The coatings were grown using a RF magnetron sputtering to maintain the discharge and avoid charge build-up. The deposition was made in a vacuum chamber with a pressure controlled gas flow (Ar: 20 sccm) and a constant power (80 W). During the sputtering process time parameters were modified to create variant thickness in the resulting coatings. Similarly, the coatings were grown at various temperatures. For the characterization of the grown YSH coatings, grazing incidence X-ray diffraction (GIXRD) and scanning electron microscopy (SEM) were used. The GIXRD enhances the diffracted signal coming from the thin film, by keeping a fixed low angle of incidence between the X-rays and the sample surface. This insures penetration into the coating allowing measurement of residual stresses within concentrated parts of the film[6]. It also reveals crucial information about the crystal structure and chemical composition of the coating. SEM measurements allowed us to analyze the grain size and morphology with respect to time and temperature. Grazing Incidence X-Ray Diffraction (GIXRD) analysis was performed on six different substrates with an increase in time variance. InTable1, the different parameters for the YSH characterization are presented.

400C^{o} YSH GIXRD Samples		
Sample #	**Sputtering Time**	**Power/Flow**
1.	6hrs	80W/20sccm
2.	4hrs	80W/20sccm
3.	3hrs	80W/20sccm
4.	1 hr	80W/20sccm
5.	30 min	80W/20sccm

Table1. Sample Parameters for YSH Characterization

3. Results and Discussion

Figure 1 presents the GIXRD patterns obtained for YSH coatings for variable deposition times. Curves shown are for samples starting with 30 min sputtering and subsequently the samples with a time increase of one hour each up to 6 hours.

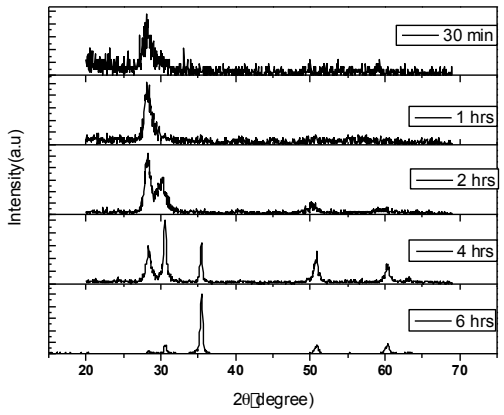

Fig.1. YSH GIXRD Data

YSH coatings grown for 30 min shows a clear dominant monoclinic crystalline structure, is not until the 2 hrs sample that the monoclinic peak starts decreasing and cubic structure becomes visible. As the time increases cubic structure becomes the dominant peak. At 6hrs the monoclinic structure has completely disappeared and the plane has shifted to the right. Another noticeable change as time increases is the intensity of each peak, indicating the coating probable thickness.

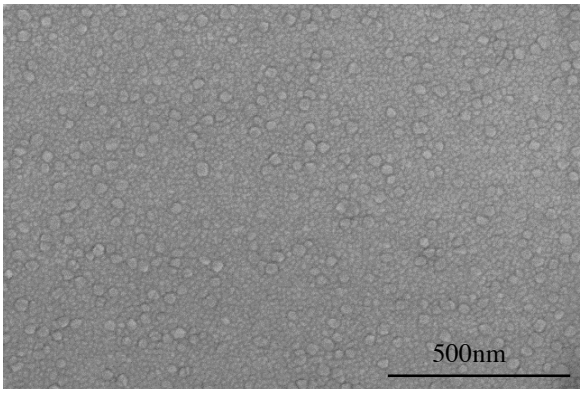

Fig.2. SEM image of YSH (400 °C; 1 hr) coatings

Figures 2 shows SEM- micrographs of the top of the surface of the YSH samples sputtered in a vacuum at temperature 400 C° for 1 hr. Images present grain sizes from 15 nm and the bigger particles being 34 nm.

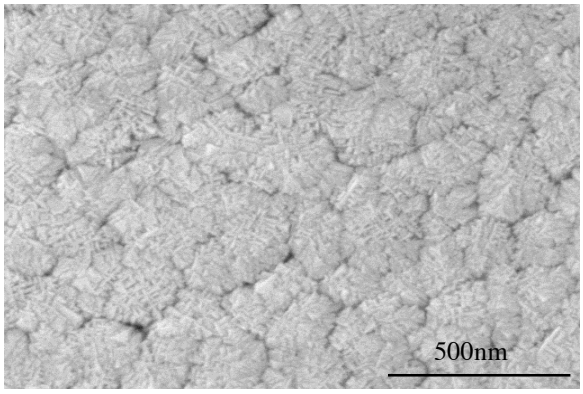

Fig.3. SEM image of YSH coatings (400 °C; 6 hr)

Figure 7 shows SEM- micrographs of the top of the surface of the YSH samples sputtered in a vacuum at temperature 400 C° for 6hrs, showing rod shape grains size of 60nm. This image presents a notorious increase in crystallization compared to the 1 hr. sample. It also shows a big increase in particle size. In this particular sample particles go up to 240nm.

4 Conclusion

The characterization of YSH coatings grown on Si-100 substrates is performed using GIXRD and SEM analyses. The effect of deposition time i.e., coating thickness on the structure is studied. Monoclinic structure was dominant at the early stages of deposition while crystallization and transformation is progressive with thickness leading to the stabilization of cubic phase.

5. References

[1] M. Noor-A-Alam, A. R. Choudhuri, C.V. Ramana "Effect of composition on the growth and microstructure of hafnia–zirconia based coatings". *Surface & Coatings Technology*, Vol. 206, pp. 1628–1633, 2011

[2] Gurrappa, A. Sambasiva "Thermal barrier coatings for enhanced efficiency of gas turbine Engines". *Surface Coating Technology.* Vol. 201, pp. 3016–3029, 2006.

[3] N.P. Padture, M. Gell, E.H. Jordan "Thermal barrier coatings for gas– turbine engine applications". *Science*, Vol. 296 pp. 280–284, 2002.

[4] A.G. Evans, D.R. Mumm, J.W. Hutchinson, G.H. Meier, F.S. Pettit, "Mechanisms controlling the durability of thermal barrier coatings". *Progress in Materials Science*, Vol. 46 pp. 505–553, 2001.

[5] G. Soyez, J.A. Eastman, L.J. Thomson, G.R. Bai, P.M. Baldo, A.W. McCormick, R.J. DiMelfi, A.A. Elmustafa, M.F. Tambwe, D.S. Stone, "Grain-size-dependent thermal conductivity of nanocrystalline yttria sta-bilized zirconia films grown by metal-organic chemical vapor deposition". *Applied Physics Lletters*, Vol. 77, pp. 1155–1157, 2000.

[6] C.-H. Ma, J.-H. Huang, Haydn Chen "Residual stress measurement in textured thin film by grazing-incidence X-ray diffraction". *Thin Solid Films*, Vol. 418, pp. 73–78, 2002

HAFNIUM OXIDE – COBALT FERRITE COMPOSITE FOR USE IN HIGH DENSITY ENERGY CAPACITORS

S. Wells[1]*, C.V. Ramama[1]
[1] Mechanical Engineering Department, University of Texas at El Paso, El Paso, TX 79968, USA;
* sjwells@miners.utep.edu

Keywords*: Electrical energy storage, Capacitors, dielectrics, Hafnium, Cobalt, Ferrite*

ABSTRACT

Efficient use of energy in modern technology can be highly depended on high density electrical capacitors. These in turn are dependent on the dielectric materials in the capacitors. A new ceramic composite (Hf_2O and Cobalt Ferrite) has been developed for use in capacitors, and its properties and microstructure are examined.

1 Introduction

Ferrite ceramic materials have been the subject of numerous investigations for many years due to their wide range of applications in the fields of electronics, optoelectronics, magentics, magneto-electronics, and electrochemical science and technology. Cobalt (Co) ferrites, particularly, have been studied extensively in recent years due to their remarkable properties such as high saturation magnetization, large permeability at high frequency, and remarkably high electrical resistivity. Due to their low eddy current losses, there exist no other materials with such wide ranging value to electronic applications in terms of power generation, conditioning, and conversion. These properties also make them unique for application in microwave devices which require strong coupling to electromagnetic signal. Recently, ferrite compounds have drawn considerable attention for their potential application as electrode materials in Li-ion batteries and solid oxide fuel cells. It has been reported that the transition metal ferrites with spinel structure such as $NiCo_2O_4$, $NiFe_2O_4$ and $CoFe_2O_4$, $CuFe_2O_4$ were used as candidates for cathode materials of lithium batteries.

The goal of the present work is to study the effect of hafnium (Hf) doping on the structure, electrical and dielectric properties of Co ferrite. The obvious relevance of the work is to examine whether the dielectric constant of these materials can be enhanced compared to pure Co ferrite while retaining their insulating nature.

2 Preparation

$CoFe_{2-x}Hf_xO_4$, ceramic materials were prepared employing the conventional solid state chemical reaction method. The starting materials were 99.99% pure CoO, Fe_2O_3, and HfO_2. Powders of the starting materials were ground in a mortar and pestle for one hour and the mixtures were heat treated in air at 1200 ^oC for 12 hours. The powders were made into

pellets and then sintered at 1250 ^{o}C in air for 12 hours. The composition of the ceramics were varied to obtain Hf concentration (x) in the range of 0-0.2. Specifically, $CoFe_{2-x}Hf_xO_4$ ceramics with six different compositions yielding x values of 0, 0.05, 0.075, 0.10, 0.15 and 0.20 were synthesized. The resulting ceramic materials were then used for further investigation to characterize the microstructure evolution and dielectric property as a function of Hf-concentration. The crystal structure of the ceramics was investigated using a Bruker D8 Discover X-ray diffractometer employing Cu K_α radiation of wavelength 1.5406 Å. Dielectric measurements were carried out at room temperature employing a LCR meter.

3 Results

The XRD pattern pure Co ferrite ($CoFe_2O_4$) is shown in Fig. 1. The calculated pattern after the Rietveld refinement carried out using the GSAS program is also shown (Fig. 1). The wrp (weighted refined parameter) and the χ^2 (goodness of the fit) values of the fitting are as indicated. XRD data indicate that the synthesized $CoFe_2O_4$ ceramic crystallizes in the inverse spinel phase without any impurity phase present. The lattice constant determined from XRD is 8.374 Å, which agrees with that of the reported value for $CoFe_2O_4$.[1] The XRD data of HfO_2 can be used as calibration check for the $CoFe_{2-x}Hf_xO_4$ ceramics in terms phase purity, homogeneity and secondary phase growth (if any). The SEM images of the samples are shown in Fig. 2 as a function of varying Hf-concentration.

Figure 1, XRD data of Hf-Co ferrite composites.

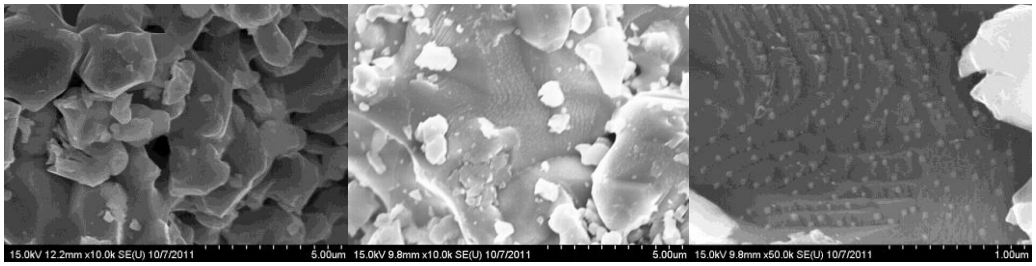

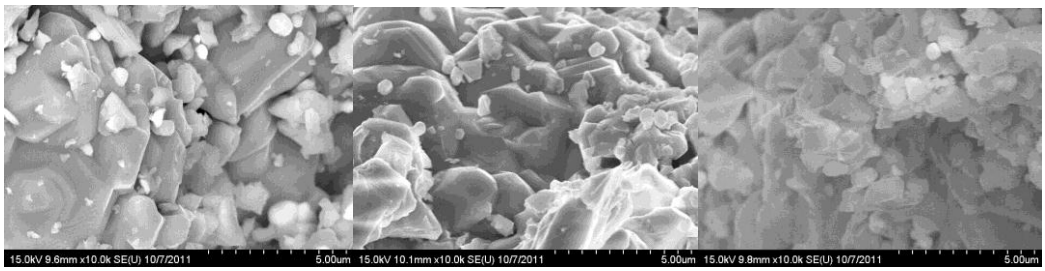

Figure 2 SEM scans

The frequency variation of the dielectric constant (ε′) of Hf substituted Co ferrites are presented and compared with that of pure Co ferrite in Fig. 3. It can be seen (Fig. 3) that ε′ decreases with increasing frequency. The decrease of ε′ with increasing frequency as observed for $CoFe_{2-x}Hf_xO_4$ materials is a typical dielectric behavior of spinel ferrites. At 100 Hz, ε′ in Hf-substituted cobalt ferrites is in general higher than that of pure cobalt ferrite. In addition, ε′ increases from $15.13x10^4$ to $17.04x10^4$ with increasing Hf concentration from x = 0.05 to 2.0. The increase in the dielectric constant with the inclusion of Hf could be due to the fact that, with the inclusion of Hf, the Co ferrite lattice is distorted and increase in Fe (Hf) – O bond lengths at B site giving rise to increase in the atomic polarizability subsequently the dielectric constant. In addition to that, formation of small amounts of the respective HfO_2 phases at the grain boundaries, leads to the accumulation of charges at the grain boundaries resulting the interfacial polarization, which contributes to the additional increase in ε′. A decrease in ε′with increasing frequency is due to the fact the dipole lags behind the applied field at higher frequencies.

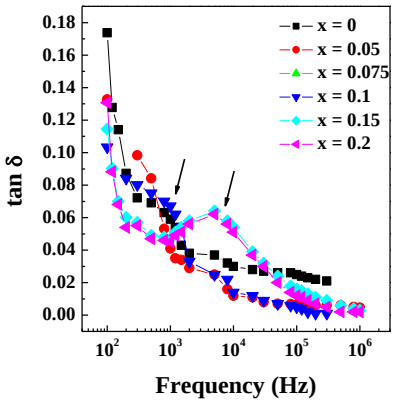

Figure 3, Real dielectric constant and dielectric loss factor vs frequency

References

[1] K. Kamala Bharathi, G. Markandeyulu, and C. V. Ramana "Structural, Magnetic, Electrical, and Magnetoelectric Properties of Sm- and Ho-Substituted Nickel Ferrites". *J. Phys. Chem. C* 2011, *115,* 554–560

SELECTIVE GROWTH OF CDTE THIN FILMS ON MICRO AND NANO PATTERNED CDS SUBSTRATES FOR SOLAR CELL APPLICATIONS

B. Aguirre[1], J. L. Cruz-Campa[2], R. Ordonez[1], Farhana Anwar[1], J. C. McClure[3], G. Nielson[2] Zubia[1]*

[1] Department of Electrical and Computer Engineering, University of Texas at El Paso, El Paso, TX 79968, USA;

[2] Sandia National Laboratories, Albuquerque, 87123 NM, USA;

[3] Department of Metallurgical and Materials Engineering, University of Texas at El Paso, El Paso, TX 79968 USA

* Corresponding author (dzubia@utep.edu)

Keywords:*CdTe, solar cell, selective growth, nanoheteroepitaxy*

ABSTRACT

Selective growth of CdTe on glass/ITO/CdS/SiO_2 substrates was achieved in this work at the micro and nanoscale level to increase the efficiency of CdTe-based solar cells. Substrates were patterened with optical and nano imprint lithography before CdTe was deposited using close space sublimation. Preliminary results show that confinement of CdTe crystals at the nano scale eliminates the number of subgrains and improves the crystal quality of CdTe compared to non-patterned CdS substrates. Scanning electron microscopy (SEM) is used to confirm the selective growth and to analyze the micro and nano structure of CdTe islands on glass/ITO/CdS/SiO_2 substrates for improving the efficiency of CdTe solar cells.

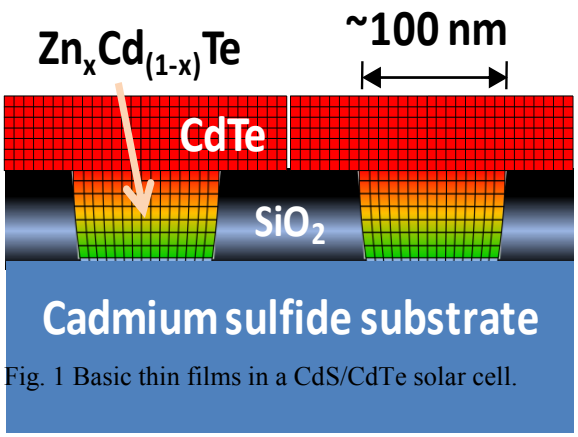

Fig. 1 Basic thin films in a CdS/CdTe solar cell.

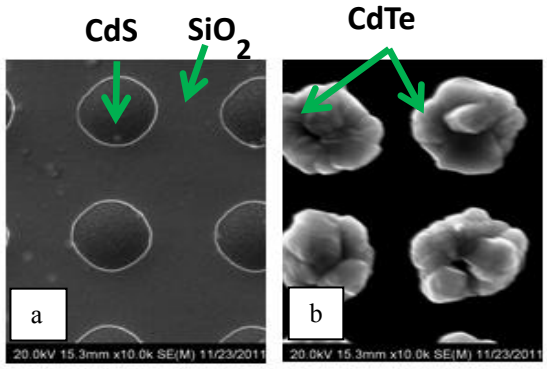

Fig. 2a) 2 µm-feature size CdS/SiO_2 patterned substrate b) CdS/SiO_2 substrate with selective growth of CdTe

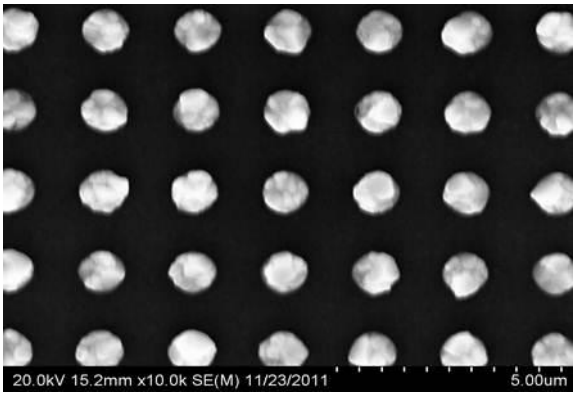

Fig. 3 1 µm -feature size CdS/SiO_2 patterned substrate with CdTe selectively grown (@10K mag.).

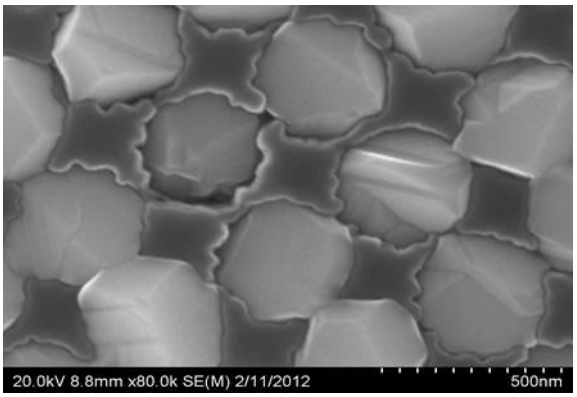

Fig. 4 350 nm-feature size CdS/SiO_2 patterned substrate with CdTe selectively grown (@ 80K mag).

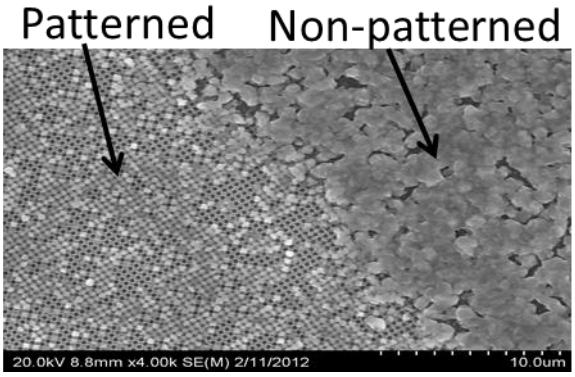

Fig. 5 CdTe grown on a patterned (350 nm feature size) and nonpatterned CdS substrate.

1 Introduction

CdTe solar cell efficiencies have been around 16 % for the last 17 years. This low efficiency makes photovoltaic (PV) power 2-4 times the cost of power from the grid. In order to make solar energy a feasible source of power and contribute to the nation's economic growth, PV systems must reach $1 per watt and PV modules are expected to have efficiencies above 20% in the next decade. Reducing the number of defects in CdTe would contribute to improve the CdTe based solar cell efficiencies and as a consequence to reduce the cost of power produced by PV's. The problem with CdTe solar cells is in the grain boundaries of the CdTe layer as well as in the large lattice mismatch between the CdS and the CdTe layers (~10%) that result in defects and recombination centers that lower the overall efficiency. While much research has focused on increasing the efficiency, the fundamental problem of the high density of defect due to the lattice mismatch and polycrystallinity of the films has not been addressed directly. Instead methods that passivate the defects such as $CdCl_2$ treatment have been used which only indirectly mitigate the problem. This research work focuses on increasing the crystal perfection of CdTe thin films for solar cell applications by selectively growing CdTe on patterned glass/ITO/CdS/SiO_2 substrates. A cross-sectional

schematic view of the patterned thin films in a CdS/ZnCdTe solar cell is shown in Figure 1. Micro and nano patterned glass/ITO/CdS/SiO_2 substrates were used to control the selective growth of CdTe at the micro and nano scale to reduce the stress formed at the CdS/CdTe heterointerface and therefore prevent the formation of defects

2 Experimental Procedure

80 nm-thick CdS thin films were grown using chemical bath deposition on top of 4 inch glass/Indium Tin Oxide (ITO) substrates. A temperature of 70 °C and a pH of 8.4 were maintained during deposition. After CdS films were grown, a 200 nm-thick SiO_2 layer was deposited on top of the CdS films using plasma enhanced chemical vapor deposition (PECVD). The purpose of the SiO_2 layer is to make a mesh or in other words, an array of micro/nano windows out of it using lithography processes. The micropattern was transferred to the SiO_2 film using optical lithography and the nanopattern using nano-imprint lithography (NIL). Feature sizes of 1 and 2 μm were transferred to the SiO_2 film using optical lithography and ~350 nm features sizes were transferred using NIL. After substrates were micro and nano-patterned, dry etching was used to finalize the patterning process. Close space sublimation was used afterwards to selectively grow CdTe on the patterned substrates. The best deposition parameters to accomplish CdTe selectivity were T_{sub} =500 °C , T_{source} = 550 °C for micro pattern and 540 °C for nanopattern, He flow = 0.13 SLPM and a pressure = 5 Torr at 1.1 mm distance.

3 Results and Discussion

Selective growth of CdTe in glass/ITO/CdS/SiO_2 substrates was achieved using the close-space deposition technique. Figures 2a) and 2b) show SEM pictures of the micropatterned glass/ITO/CdS/SiO_2 substrates before and after CdTe selective growth. It can be seen that CdTe is only deposited inside the SiO_2 windows where contact needs to be done with the CdS film to form a p-n junction. Improvement in the CdTe crystal quality is expected if the feature size of the micropattern windows is reduced further in order to grow a single CdTe crystal in each of the SiO_2 windows. Figure 3 shows a reduction of the feature size down to 1 μm and figure 4 a further reduction to 350 nm in which single crystals of CdTe are grown inside each nano-window. Having single crystals of CdTe grown as shown in Figure 4 is very important because defects are reduced and a better interface with the CdS layer is obtained; resulting into less recombination centers and higher efficiency in CdTe solar cells. From Figure 4 it can be seen that CdTe is still grown selectively but its structure has changed to single crystal when compared to the micro pattering where a lot of crystals having grain boundaries fill up each of the micro-windows. Figure 5 shows a comparison of the micro/nano structure of CdTe when it is grown selectivity using a nanopatterned SiO_2/CdS substrates and when no pattering is used at all. In the nanopatterned substrate, single, uniform, ordered high quality CdTe grains are grown inside each SiO_2 window whereas on the planar side, CdTe is grown with a lot of grain boundaries, no-order and with lack of uniformity.

Department of Mechanical Engineering | Engineering Annex, Suite 126
The University Of Texas At El Paso | 500 W. University Avenue | El Paso, Tx. 79968-0521
Ph (915) 747 5450 | Fax (915) 747 5019 | Http://me.utep.edu/
Mechanical@utep.edu | Meug@utep.edu | Megrad@utep.edu